Prior Information in Inverse Boundary Problems

Garde, Henrik

Publication date:
2016

Document Version
Publisher's PDF, also known as Version of record

Prior Information in Inverse Boundary Problems

Henrik Garde

Kongens Lyngby 2016

PhD thesis:	Prior information in inverse boundary problems
Author:	Henrik Garde Department of Applied Mathematics and Computer Science Technical University of Denmark Kgs. Lyngby, Denmark
Thesis submitted:	February 29th, 2016
PhD supervisor:	Associate Professor Kim Knudsen Department of Applied Mathematics and Computer Science Technical University of Denmark Kgs. Lyngby, Denmark
PhD committee:	Associate Professor Nuutti Hyvönen Department of Mathematics and Systems Analysis Aalto University Helsinki, Finland
	Lecturer Bangti Jin Department of Computer Science University College London London, England
	Professor Michael Pedersen Department of Applied Mathematics and Computer Science Technical University of Denmark Kgs. Lyngby, Denmark

Technical University of Denmark
Department of Applied Mathematics and Computer Science
Richard Petersens Plads, building 324,
2800 Kongens Lyngby, Denmark
Phone +45 4525 3031
compute@compute.dtu.dk
www.compute.dtu.dk

PHD-2016-409
ISSN 0909-3192

Preface

This thesis was prepared in partial fulfilment of the requirements for the PhD degree at the Technical University of Denmark (DTU). The work was carried out between March 1st 2013 and February 29th 2016, in the Section for Scientific Computing at the Department of Applied Mathematics and Computer Science, DTU, under the supervision of Associate Professor Kim Knudsen.

The aim of the thesis is to present and document my work on inclusion detection in electrical impedance tomography; it consists of a summary of the results documented in both published peer-reviewed journal papers and unpublished manuscripts (all attached in the appendix, labelled Paper A-E):

(A) H. Garde and K. Knudsen. Depth dependent bounds on distinguishability of inclusions in electrical impedance tomography. Submitted manuscript (2016). Available from: `http://arxiv.org/abs/1602.03785`

(B) H. Garde and S. Staboulis. Convergence and regularization for monotonicity-based shape reconstruction in electrical impedance tomography. Submitted manuscript (2016). Available from: `http://arxiv.org/abs/1512.01718`

(C) H. Garde. Comparison of linear and non-linear monotonicity-based shape reconstruction using exact matrix characterizations. Submitted manuscript (2016). Available from: `http://arxiv.org/abs/1602.04053`

(D) H. Garde and K. Knudsen. Sparsity prior for electrical impedance tomography with partial data. Inverse Probl. Sci. Eng., 24 (2016), pp. 524–541. DOI: 10.1080/17415977.2015.1047365.

(E) H. Garde and K. Knudsen. 3D reconstruction for partial data electrical impedance tomography using a sparsity prior. Proceedings of the 10th AIMS International Conference on Dynamical Systems, Differential Equations and Applications, American Institute of Mathematical Science (AIMS), November 2015, pp. 495–504. DOI: 10.3934/proc.2015.0495.

Additional unpublished results are also presented, in particular on depth-weighted regularization, that combines the concepts of depth dependence and sparsity regularization from two different publications.

Finally, it is remarked that the author, during his PhD studies, also has co-authored another paper not included in this thesis:

- Y. Dong, H. Garde and P. C. Hansen. R^3GMRES: including prior information in GMRES-type methods for discrete inverse problems. Electronic Transactions on Numerical Analysis, 42 (2014), pp. 136–146.

The above paper is also concerned with implementing prior information into algorithms for solving inverse problems, however it deals with general linear and finite dimensional inverse problems. It was therefore found to be thematically too different from the other publications that focus on inclusion detection in electrical impedance tomography.

This version of the thesis has been revised after the PhD defence. The revisions address minor non-essential corrections and typographical errors pointed out by the assessment committee.

Acknowledgments

I would foremost like to thank my advisor Associate Professor Kim Knudsen. He has given much freedom for me to decide what I wanted to focus on during my PhD, and has always had time to discuss my work and ask the critical questions that help push my work in the right direction.

I would also like to thank Professor Per Christian Hansen and all the members of the HD-tomo and HybridData projects; there is always a positive attitude and the projects bring more togetherness to the Section of Scientific Computing. The weekly HD-tomo seminars have provided an excellent way to both present my own work and to learn about the work of everyone involved in the projects.

As the projects encompass members with various backgrounds, the seminars often leads to interesting discussions and novel ideas that I would normally not have considered.

I was on an external research stay in Finland during the last four months of 2014, visiting Professor Samuli Siltanen at University of Helsinki. I would like to thank everyone in Samuli's group for their hospitality during my stay. During the stay I also visited Associate Professor Ville Kolehmainen at the University of Eastern Finland (UEF) in Kuopio, and was allowed to perform measurements with their KIT4 equipment. I would in particular like to thank Paula Kaipio (UEF at the time) and Stratos Staboulis (now at DTU Compute) for helping to plan and perform the measurement experiments.

Finally, I would like to acknowledge the Otto Mønsted Foundation for partially funding my external research stay and trips to several conferences. Furthermore, I would like to acknowledge that my PhD has been funded by the advanced grant no. 291405 HD-tomo from the European Research Council.

Kgs. Lyngby
February 29th, 2016

Henrik Garde

Abstract (English)

This thesis gives a threefold perspective on the inverse problem of inclusion detection in electrical impedance tomography: depth dependence, monotonicity-based reconstruction, and sparsity-based reconstruction.

The *depth dependence* is given in terms of explicit bounds on the datum norm, which shows the change in distinguishability of inclusions (support of an inhomogeneity) as they are placed closer towards the measurement boundary. This is done by determining eigenvalue bounds for differences of pseudodifferential operators on the boundary of the domain. Ultimately, the bounds serves as insight into how much noise that can be allowed in the datum before an inclusion cannot be detected.

The *monotonicity method* is a direct reconstruction method that utilizes a monotonicity property of the forward problem in order to characterize the inclusions. Here we rigorously prove that the method can be regularized against noise with a uniform regularization parameter, and that the method can be generalized to discrete electrode models. We give examples in 2D and 3D with noisy simulated data as well as real measurements, and give a comparison of reconstructions based on a non-linear and a linear formulation of the method.

Sparsity-based reconstruction is an iterative method, that through an optimization problem with a sparsity prior, approximates the inhomogeneities. Here we make use of prior information, that can cheaply be obtained from the monotonicity method, to improve both the contrast and resolution of the reconstruction. Numerical examples are given in both 2D and 3D for partial data using noisy simulated data as well as real measurements.

Abstract (Danish)

Denne afhandling giver et trefoldigt perspektiv på det inverse problem at detektere inklusioner i elektrisk impedanstomografi: Dybdeafhængighed, monotonicitetsbaseret rekonstruktion og sparsitetsbaseret rekonstruktion.

Dybdeafhængigheden er angivet i form af eksplicitte grænser på normen af dataen, hvilket viser ændringen i *distinguishability* (skelnen) af inklusioner (støtten af en inhomogenitet) når de placeres tættere og tættere på randen hvor målingerne foretages. Dette gøres ved at bestemme egenværdigrænser for differenser af pseudodifferentialoperatorer på randen af domænet. I sidste ende tjener grænserne som indsigt til hvor meget støj der kan tilføjes dataen, før at en inklusion ikke længere kan detekteres.

Monotonicitetsmetoden er en direkte rekonstruktionsmetode der anvender en monotonicitetsegenskab af forward-problemet til at karakterisere inklusionerne. Vi giver et stringent bevis for at metoden kan regulariseres mod støj ved brug af en uniform regulariseringsparameter, samt at metoden kan generaliseres til diskrete elektrodemodeller. Der gives eksempler i 2D og 3D med både støjfyldte simulerede data og med faktiske målinger, og der gives en sammenligning af rekonstruktioner fra en ikke-lineær og en lineær formulering af metoden.

Sparse rekonstruktion er en iterativ metode, der gennem et optimeringsproblem med en sparsitets-prior, approksimerer inhomogeniteterne. Her gør vi brug af forhåndsviden, der billigt kan beregnes med monotonicitetsmetoden, til at forbedre både kontrasten og opløsningen af rekonstruktionen. Der gives numeriske eksempler i både 2D og 3D med brug af delvis og støjfyldt randdata samt målte data.

Contents

Chapter 1

Introduction

Inverse problems form a field of mathematics that cover a wide range of tools from linear algebra, PDEs, pseudodifferential operators, regularization strategies and to numerical aspects such as noise models, quadrature, and efficient implementation of reconstruction algorithms. Many inverse problems are related to a practical problem based on a physical formulation, prominently for tomography problems. Here structural information is inferred by imaging a parameter in the interior of an object or a person, only from non-invasive and indirect measurements taken at the boundary. Therefore, practical measurements are often involved. This implies an interplay between applied mathematics and engineering in the sense that the mathematical models need to balance between model problems with well-understood theory to, in practice, models more aligned with real measurements that does not necessarily possess attractive properties such as uniqueness of solutions or provable regularizing reconstruction methods. Furthermore, inverse problems are often ill-posed and therefore require some form of regularization to stably solve them. Such regularization imparts a priori knowledge about the solution into the reconstruction algorithm, and it is therefore worth considering what prior information that is appropriate for reconstruction; firstly so that the modified problem can be solved and secondly whether that kind of prior information is obtainable.

The particular inverse problem of interest in this thesis is the inverse problem of *electrical impedance tomography* (EIT), also known as the *Calderón problem* in

recognition of Calderón's famous seminal paper [17]. The problem consists of reconstructing the electrical conductivity in an object or person from several pairs of electrostatic current-voltage measurements taken at surface electrodes. Applications include medical imaging, in particular monitoring patient lung function and early detection of cancer, geophysics, and industrial tomography for instance for non-destructive imaging of cracks in concrete [35, 1, 71, 19, 27, 67, 46, 45]. EIT is considered high-contrast as different types of soft tissues have distinct and well-separated conductivity values, this also holds for different rock types (shale, clay, granite, etc.) [10] which makes it a good imaging modality for the above applications. On the other hand, EIT is very ill-posed due to the diffusive nature of electric fields, and imaging leads to low resolution characterized by smoothed edges and often regions that are difficult to correctly segment and separate. The numerical results in this thesis show that when reconstructing sufficiently small (preferably convex-shaped) inclusions it is possible to obtain reasonably sharp edges and separation of the inclusions, if the background conductivity is assumed known. This is furthermore shown for noisy data and locally when only part of the boundary is used for measurements.

For a general inverse problem there is, of course, a corresponding forward problem. Suppose that we have two Banach spaces X and Y, where X is the *parameter space* which should contain the parameter x that we seek to reconstruct from the inverse problem. Y is the *measurement space* where we are able to measure data y that in some way depends on the unknown x. A map $F : D(F) \subseteq X \to Y$ is called *the forward map* if it is the mathematical model that, in the case of no modelling errors and noise, predicts what data $y = F(x)$ that would be measured for a parameter x. In the case of EIT x is the electrical conductivity and y is a current-to-voltage (or voltage-to-current) pseudodifferential operator that is determined from solving elliptic PDEs with various boundary conditions. Another example is for instance computed tomography (CT) where x denotes the attenuation coefficients and y are the line integrals of x through the domain, which in some geometries corresponds to the Radon transform or X-ray transform of x. Typically, the forward map is a model of the physics behind the problem, in EIT by prescribing currents and measuring voltages at surface electrodes, and in CT by measuring intensity drops from X-rays after they have passed through the object and recorded by a detector. In most cases the forward problem is *well-posed*, meaning that F is well-defined and continuous, i.e. the forward map F can reliably be evaluated numerically without having to worry much about truncation errors or small perturbations to x.

The inverse problem of determining x from the measurement y, however, is typically *ill-posed* meaning that either F^{-1} does not exist or it is discontinuous. Mostly the existence of a solution x to the inverse problem is implied, and in practice this makes sense as the data y must come from some parameter x. However, for noisy data $\tilde{y}$ that may also be influenced by modelling errors, we

may have that $\tilde{y} \notin R(F)$, where $R(F)$ is the range of F. Therefore, we may have to make do for some numerical approximation to a solution from the data $P(\tilde{y})$ projected onto $R(F)$. What remains are three important questions, that each constitute a major field of research on their own:

(i) Uniqueness: is F injective, i.e. can we define an inverse $F^{-1} : R(F) \to X$?

(ii) Stability: is F^{-1} continuous, or under what assumptions on X is it continuous?

(iii) Reconstruction: is there an algorithm for evaluating F^{-1} or some regularized approximation?

A uniqueness proof does not necessarily imply an algorithm for evaluating F^{-1} as it requires the proof to be constructive. For EIT constructive uniqueness proofs only exists when regularity assumptions are applied, and the most general uniqueness proofs are not constructive [7, 57]. In particular for partial data there are several uniqueness proofs but in most geometries, and types of partial data, there is no actual algorithm for reconstruction [16, 47, 48, 72, 42]. Stability, of course, directly implies uniqueness, though similar to reconstruction it is often necessary to have additional assumptions on the regularity of x and on the dimension or geometry of the domain to be able to prove some form of stability. In that case we call the stability *conditional*.

The ill-posedness of an inverse problem is either that there is no uniqueness, or that there is uniqueness but no stability. The latter case holds for EIT in very general cases, though it is possible to obtain conditional log stability [4, 5, 55] or in the partial data case conditional log-log stability [34]. While the problem is then technically well-posed, EIT is often called *severely ill-posed* due to the poor modulus of continuity from logarithmic stability. More precise would be to call it *severely ill-conditioned*, as similar to inverting a matrix with very high condition number, the inverse problem of EIT suffers from the issue that very small noise perturbations or modelling errors can lead to very large perturbations in the reconstruction. It is therefore always required to utilize some kind of regularization in order to stably reconstruct an approximation to the solution. The purpose of using prior information, in the form of regularization, is to put enough assumptions on the parameter space X that it becomes small enough to reduce the ill-posedness/ill-conditioning of the inverse problem. A few examples of such regularization are Tikhonov regularization (standard 2-norm prior), sparsity (1-norm prior), smoothing priors (requirements on differentiability), piecewise constant priors (total variation and Perona-Malik type regularization). For a few examples related to EIT see [43, 30, 11, 68, 10, 26].

For reconstruction in the inverse problem of EIT there is a strange duality: all provable regularization strategies are direct (non-iterative) reconstruction methods [50, 49, 62, 57] using so-called *complex geometric optics solutions*. However, the direct reconstruction methods are often so rigid that prior information about the solution, or the desired form of regularization, might not be applicable to the reconstruction method. The more flexible iterative least-squares output methods are only able to guarantee some local optimum of a cost functional, and not necessarily the sought solution, however they tend to be more noise robust. Depending on the applied regularization the iterative methods can lead to sharper edges, improved contrast and better separation of inclusions compared to the counterpart of the direct reconstruction methods. As such it is difficult to discuss what can reliably be reconstructed in EIT, and one way to somewhat circumvent this duality is to use a direct reconstruction to get a reasonable starting guess for an iterative method, see for instance [26].

In this thesis the focus is mostly on reconstruction in the inverse problem of EIT. The common theme of Papers A-E is inclusion detection, a simpler problem than the general inverse problem of EIT, where perturbations/inhomogeneities from a known or uninteresting background conductivity are reconstructed. The thesis is composed of a general introduction to EIT and some of its forward models, and subsequently the thesis is split into three parts:

(i) Depth dependence, which will be a summary of paper A, on the forward map's dependence on inclusions, in particular on their distance to the boundary. The subject is thematically similar to the concept of signal-to-noise ratio, as depth dependent bounds on the so-called *distinguishability* of the inclusions are determined in the unit disk geometry in 2D.

(ii) The monotonicity method, which will be a summary of papers B and C, that focus on a direct reconstruction method that characterize the inclusion (location of the perturbation/inhomogeneity) through monotonicity properties of the forward map. Paper B generalizes the method from the standard continuum model to more precise electrode models. It is shown that the method can be regularized, both in terms of noise and in terms of the change in forward model, with a regularization parameter that is uniform with respect to the involved test balls. Both noisy simulated and real measurement data reconstructions are given in 2D, as well as some 3D reconstructions from simulated data. Paper C gives a comparison of two different variations of the monotonicity method in a unit disk geometry in 2D; one linear the other non-linear, where the comparison makes use of exact matrix characterizations of the involved operators.

(iii) Sparsity-based reconstruction, which will be a summary of papers D and E, that will be concerned with iterative reconstruction of the actual per-

turbation (not only its location) by the use of a sparsity prior. Here we consider the problem of partial data EIT where measurements are taken on a small subset of the boundary. We make use of a spatially varying regularization parameter to implement prior information that, for instance, can be cheaply obtained from the monotonicity method. Examples with noisy simulated data are given in both 2D and 3D. Furthermore, some additional examples not present in the papers are given from real measurements using a depth-weighted regularization parameter.

In terms of notation, there may be discrepancies between the summary and the papers; the reason is that I seek to have a unified notation in the thesis which is not necessarily the case across the different papers. In particular for the forward models there will be a different notation than in paper B. The notation there was chosen in consensus with what is often used for direct reconstruction methods in inclusion detection for the Neumann-to-Dirichlet map and for approximation results using the complete electrode model. For many papers on other direct and iterative methods the notation is consistent with this thesis. A few specific notes on notation: for normed spaces X and Y, the space of bounded and linear operators from X to Y is denoted $\mathcal{L}(X, Y)$, with $\mathcal{L}(X) \equiv \mathcal{L}(X, X)$. Furthermore $\|\cdot\|$ is the standard L^2-norm, and $\langle \cdot, \cdot \rangle$ is either the L^2-inner product or a dual pairing, depending on the context. For integration we use dx as the usual Lebesgue measure, and ds as the boundary measure (whether in 2D or 3D).

All numerical examples are computed in Python, and solutions to PDEs are found using the finite element method (FEM) with the Python library FEniCS [54].

1.1 Electrical impedance tomography

In EIT the electrical conductivity γ is reconstructed from current-voltage measurements taken at electrodes on the surface of an object, modelled by a bounded simply connected Lipschitz domain $\Omega \subset \mathbb{R}^d$ for $d \geq 2$. The problem is governed by the *conductivity equation*

$$\nabla \cdot (\gamma \nabla u) = 0 \text{ in } \Omega, \tag{1.1}$$

where u is the electrical potential. The equation (1.1) is derived from Maxwell's equations under the assumption that there are no internal sources or sinks of electricity [10].

In this thesis we assume, for simplicity, that the conductivity γ is real-valued

and isotropic (scalar-valued) in $L^\infty_+(\Omega)$, where

$$L^\infty_+(\Omega) \equiv \{w \in L^\infty(\Omega) : \operatorname{ess\,inf} w > 0\}.$$

Other generalizations exists such as complex-valued admittivities and anisotropic (matrix-valued) conductivities/admittivities. Isotropic γ is often assumed since it can be proven that for anisotropic γ the underlying inverse problem does not have a unique solution, there is only uniqueness up to a diffeomorphism which is the identity on the boundary [8].

1.1.1 Forward models

Various models for EIT exists, the most prominent being the *continuum model* (CM) and the *complete electrode model* (CEM). The CM assumes that the entire boundary can be accessed and that a continuous boundary current or potential can be applied. This leads to the original formulation from Calderón's seminal paper [17]

$$\nabla \cdot (\gamma \nabla u) = 0 \text{ in } \Omega, \quad u|_{\partial\Omega} = f \text{ on } \partial\Omega, \tag{1.2}$$

for boundary potential $f \in H^{1/2}(\partial\Omega)$. Here and onwards $u|_{\partial\Omega}$ denotes the trace operator applied to u. Standard elliptic theory gives rise to a unique solution $u \in H^1(\Omega)$ and thereby implies the existence of a well-defined Dirichlet-to-Neumann (DN) operator

$$\Lambda(\gamma) : H^{1/2}(\partial\Omega) \to H_\diamond^{-1/2}(\partial\Omega), \quad u|_{\partial\Omega} \mapsto \nu \cdot \gamma \nabla u|_{\partial\Omega}.$$

Here ν is an outwards pointing unit normal, and

$$H_\diamond^{-1/2}(\partial\Omega) \equiv \{w \in H^{-1/2}(\partial\Omega) : \langle w, \mathbb{1} \rangle = 0\},$$

where $\mathbb{1} \equiv 1$ on $\partial\Omega$ and $\langle \cdot, \cdot \rangle$ denotes the $(H^{-1/2}, H^{1/2})$-dual pairing. That the current $\nu \cdot \gamma \nabla u|_{\partial\Omega}$ is in $H_\diamond^{-1/2}(\partial\Omega)$ is due to the total conservation of current at the boundary, and can also be directly derived from the conductivity equation (1.1).

Another formulation makes use of a Neumann problem where a boundary current is applied

$$\nabla \cdot (\gamma \nabla u) = 0 \text{ in } \Omega, \quad \nu \cdot \gamma \nabla u|_{\partial\Omega} = g, \quad \int_{\partial\Omega} u \, ds = 0, \tag{1.3}$$

where $g \in H_\diamond^{-1/2}(\partial\Omega)$ is the applied current pattern (up to a sign). The latter condition in (1.3) is a grounding condition of the total electrical potential at the boundary, and is a sufficient condition to uniquely solve (1.3), since the

Neumann condition only gives uniqueness up to a scalar. The unique solution to (1.3) is $u \in H^1_\diamond(\Omega)$, where

$$H^{1/2}_\diamond(\partial\Omega) \equiv \left\{ w \in H^{1/2}(\partial\Omega) : \int_{\partial\Omega} w\, ds = 0 \right\},$$
$$H^1_\diamond(\Omega) \equiv \{ w \in H^1(\Omega) : w|_{\partial\Omega} \in H^{1/2}_\diamond(\partial\Omega) \}.$$

This gives rise to the Neumann-to-Dirichlet (ND) map

$$\mathcal{R}(\gamma) : H^{-1/2}_\diamond(\partial\Omega) \to H^{1/2}_\diamond(\partial\Omega), \quad \nu \cdot \gamma \nabla u|_{\partial\Omega} \mapsto u|_{\partial\Omega}.$$

It is clear that $\mathcal{R}(\gamma)$ and $\Lambda(\gamma)$ are each others inverses when $\Lambda(\gamma)$ is restricted to $H^{1/2}_\diamond(\partial\Omega)$. Here it should be noted that $\Lambda(\gamma)$ generally has the non-trivial null-space $\operatorname{span}\{\mathbb{1}\}$, and the aforementioned restriction to $H^{1/2}_\diamond(\partial\Omega)$ corresponds to removing that null-space. In many cases, including the Papers A-C, it is sufficient to restrict $\mathcal{R}(\gamma)$ to $L^2_\diamond(\partial\Omega)$ where

$$L^2_\diamond(\partial\Omega) \equiv \left\{ w \in L^2(\partial\Omega) : \int_{\partial\Omega} w\, ds = 0 \right\}.$$

In that case $\mathcal{R}(\gamma)$ becomes a compact and self-adjoint operator in $\mathcal{L}(L^2_\diamond(\partial\Omega))$.

The knowledge of $\Lambda(\gamma)$ or $\mathcal{R}(\gamma)$ is equivalent to the knowledge of all possible current-voltage measurement pairs at $\partial\Omega$, and is the maximal obtainable datum for EIT. Therefore, the non-linear maps $\gamma \mapsto \Lambda(\gamma)$ and $\gamma \mapsto \mathcal{R}(\gamma)$ are called *forward problems* for the CM. The corresponding *inverse problem* of EIT, when using the CM, is to reconstruct γ given Ω and either $\Lambda(\gamma)$ or $\mathcal{R}(\gamma)$. Virtually all existing theory on uniqueness of the inverse problem in EIT is formulated through the CM [64, 57, 59, 58, 7, 25].

Another model we will use is the CEM, which is a finite dimensional and discrete electrode model. This model is often used for reconstruction from practical measurements and is known to accurately predict current-voltage measurements [63]. The model is formulated as

$$\nabla \cdot (\gamma \nabla v) = 0 \text{ in } \Omega, \tag{1.4}$$
$$\nu \cdot \gamma \nabla v = 0 \text{ on } \partial\Omega \setminus \cup_{j=1}^k \overline{E_j}, \tag{1.5}$$
$$v + z_j \nu \cdot \gamma \nabla v = V_j \text{ on } E_j, \;\; j = 1, 2, \ldots, k, \tag{1.6}$$
$$\int_{E_j} \nu \cdot \gamma \nabla v\, ds = I_j, \;\; j = 1, 2, \ldots, k, \tag{1.7}$$

where the E_j-sets are connected and mutually disjoint subsets of $\partial\Omega$ that model the position of the physical electrodes. The boundary condition (1.7) is the

total applied current I_j through electrode E_j, and (1.5) implies that there is no current flux outside the electrodes. Finally, the condition (1.6) is the measured boundary voltage V_j at electrode E_j, and the terms $z_j > 0$ are the *contact impedances* that model the resistive layer between object and electrode. It was proved in [63] that for any current pattern I in the hyperplane

$$\mathbb{C}^k_\diamond \equiv \left\{ W \in \mathbb{C}^k : \sum_{j=1}^{k} W_j = 0 \right\},$$

there is a unique solution $(v, V) \in H^1(\Omega) \oplus \mathbb{C}^k_\diamond$. This gives rise to the current-to-voltage map (or measurement map), analogous to the ND map, given by

$$R(\gamma) : \mathbb{C}^k_\diamond \to \mathbb{C}^k_\diamond, \quad I \mapsto V.$$

As γ is real-valued then $R(\gamma)$ is self-adjoint and it can be shown [63] that $R(\gamma)$ is an $\mathbb{R}^{k\times k}$-matrix, or if represented through a real-valued basis for $\mathbb{C}^k_\diamond$ it is an $\mathbb{R}^{(k-1)\times(k-1)}$-matrix. I will generally suppress the dependence of the contact impedances z for $R(\gamma)$ as they are assumed to be known. The values of z can, to some degree, be estimated through calibration, however we shall also estimate them concurrently with the conductivity for some real measurement data in Section 4.2.

1.1.2 Fréchet derivatives

In reconstruction, either direct or iterative, it is often necessary to evaluate the derivative of the forward map. Consider $F : U \to Y$ with open subset $U \subset X$ for Banach spaces X and Y, then F is Fréchet differentiable at $x_0 \in U$ if there exists a bounded linear map $F'(x_0) : X \to Y$, called the Fréchet derivative of F at x_0, such that

$$\lim_{\|\eta\|_X \to 0} \frac{\|F(x_0) + F'(x_0)\eta - F(x_0 + \eta)\|_Y}{\|\eta\|_X} = 0.$$

Here all the forward maps considered

$$\begin{aligned}
\Lambda &: L^\infty_+(\Omega) \to \mathcal{L}(H^{1/2}(\partial\Omega), H^{-1/2}_\diamond(\partial\Omega)),\\
\mathcal{R} &: L^\infty_+(\Omega) \to \mathcal{L}(H^{-1/2}_\diamond(\partial\Omega), H^{1/2}_\diamond(\partial\Omega)),\\
R &: L^\infty_+(\Omega) \to \mathcal{L}(\mathbb{C}^k_\diamond),
\end{aligned}$$

are Fréchet differentiable everywhere. Let $\gamma_0 \in L^\infty_+(\Omega)$, then the Fréchet derivatives at γ_0 are given by the following: let u_f be the solution to (1.2) with Dirichlet condition $f \in H^{1/2}(\partial\Omega)$, w_g is the solution to (1.3) with Neumann

condition $g \in H_\diamond^{-1/2}(\partial\Omega)$, and v_I is the solution to (1.4)-(1.7) with current pattern $I \in \mathbb{C}_\diamond^k$, all with the conductivity $\gamma = \gamma_0$, then for any $\eta \in L^\infty(\Omega)$

$$\begin{aligned}
\langle \Lambda'(\gamma_0)[\eta]f, \tilde{f}\rangle &\equiv \int_\Omega \eta \nabla u_f \cdot \overline{\nabla u_{\tilde{f}}}\, dx, \\
\langle \mathcal{R}'(\gamma_0)[\eta]g, \tilde{g}\rangle &\equiv -\int_\Omega \eta \nabla w_g \cdot \overline{\nabla w_{\tilde{g}}}\, dx, \\
\langle R'(\gamma_0)[\eta]I, \tilde{I}\rangle_{\mathbb{C}^k} &\equiv -\int_\Omega \eta \nabla v_I \cdot \overline{\nabla v_{\tilde{I}}}\, dx.
\end{aligned}$$

In fact, the forward maps are all analytic (see for instance the appendix of Paper B), however the higher derivatives are rarely used as they are very costly to evaluate, while the above first order derivatives of the boundary operators only depend on the interior solutions to the PDE for the conductivity γ_0. Furthermore, the first order derivatives hold information on the singularities in the conductivity that can be used for reconstruction [31, 32]. Generally the n'th order Fréchet derivative of the boundary operators can be written as combinations of Fréchet derivatives up to order $n-1$ of u, w, or v.

1.1.3 Partial data

When considering partial data we deal with two connected subsets Γ^{D} and Γ^{N} of the boundary $\partial\Omega$, to encompass the partial Dirichlet- and Neumann-data, respectively. For instance with the ND map, we define the partial ND map as the operator with the graph

$$\{(g, f) : g \in H_\diamond^{-1/2}(\partial\Omega),\ \operatorname{supp} g \subseteq \Gamma^{\mathrm{N}},\ \ f = (\mathcal{R}(\gamma)g)|_{\Gamma^{\mathrm{D}}}\}.$$

In this case we will also choose the grounding condition in (1.3) as

$$\int_{\Gamma^{\mathrm{D}}} u\, ds = 0.$$

Uniqueness has been proven for various choices for Γ^{D} and Γ^{N} [16, 47, 48, 72], in many cases involving the entire boundary with Γ^{D} and Γ^{N} being a slightly overlapping partition of $\partial\Omega$. We are in particular interested in *local Cauchy data* $\Gamma = \Gamma^{\mathrm{D}} = \Gamma^{\mathrm{N}}$, i.e. where the current and voltage measurements are taken on the same, possibly small, part of the boundary. In 2D uniqueness has been proven generally for local Cauchy data for an arbitrarily small subset Γ [40], while in 3D uniqueness for local data has only been proven for certain geometries. For partial data in 3D we use the unit ball geometry, for which there is uniqueness for local data [42].

For the CEM one might consider labelling it as partial data since measurements are only taken at the discrete electrodes. This is often misleading, since reconstructions using CEM with electrodes equidistantly placed on the whole boundary are typically similar to the CM counterpart. However, reconstructions from partial data using the CM and for CEM with electrodes restricted to a small subset Γ have very different characteristics in terms of how stably γ can be reconstructed, compared to the full boundary reconstructions. In the partial data case it is often only possible to detect/reconstruct inclusions close to the measurement boundary from noisy measurements, see in particular Paper D and E.

It is possible from the CEM measurement map $R(\gamma)$ to construct an operator $\mathcal{R}_h(\gamma)$ using the concept of *extended electrodes*, that extends the physical electrodes to cover all of $\partial\Omega$. For extended electrodes of size h then $\mathcal{R}_h(\gamma)$ gives a linear approximation to $\mathcal{R}(\gamma)$ in terms of h [36] (we will return in more detail to this construction in Section 3.2). Consider the example $\Omega = \mathbb{D}$ the unit disk in $\mathbb{R}^2$, and suppose that we place k electrodes of size π/k equidistantly on $\partial\mathbb{D}$. Thus, in total, half of $\partial\mathbb{D}$ is covered by electrodes no matter what k we choose. Furthermore the extended electrodes will have size $h = 2\pi/k$. Thus, if we double the number of electrodes k then h is being halved. This implies that we can approximate the full ND map $\mathcal{R}(\gamma)$ arbitrarily well by only covering, in total, half of the boundary with sufficiently small electrodes. The key concept here is to think of CEM as partial data in terms of how densely the electrodes cover the boundary, not how much of the boundary that is covered; this is tantamount to the size h of the extended electrodes. One could consider for local data on a set Γ (which contains all the physical electrodes) to construct the operator $\mathcal{R}_h$ such that the extended electrodes only extends to Γ, and in turn approximate the partial ND map instead.

1.2 Inclusion detection

Due to the severe ill-posedness (or ill-conditioning) of the inverse problem in EIT, it is not always of interest to perform a full-scale reconstruction of the conductivity γ. Instead one can consider the easier problem of reconstructing inclusions from a known or uninteresting background conductivity γ_0. Consider the open non-empty subset $\mathcal{D} \subset \Omega$ and assume that $\gamma_0 \in L^\infty_+(\Omega)$ is known, then we assume that the conductivity is of the form

$$\gamma = \gamma_0 + \kappa\chi_{\mathcal{D}}, \tag{1.8}$$

where $\chi_{\mathcal{D}}$ is a characteristic function on the sought inclusion $\mathcal{D}$ that we seek to reconstruct, and κ is a perturbation on $\mathcal{D}$ which for instance could be in $L^\infty_+(\Omega)$,

in which case we call $\mathcal{D}$ a *positive* or *definite inclusion*. Similarly we could have negative inclusions by using $-\kappa$ instead of κ, or even indefinite inclusions (both positive and negative values of κ).

In Part I the review of Paper A will show depth dependent bounds on the *distinguishability* for the inclusion $\mathcal{D}$. This is thematically related to the signal-to-noise ratio, and shows how much influence $\mathcal{D}$ has on the data $\Lambda(\gamma)$ or $\mathcal{R}(\gamma)$ depending on the distance of $\mathcal{D}$ to the boundary, and if we can expect to reconstruct the inclusion from noisy data.

Specialized reconstruction methods exist for reconstructing (or obtaining estimates) on the inclusion $\mathcal{D}$ in (1.8), for instance some direct methods that all involve repeated but cheap testing of criteria, such as the *factorization method* [14, 15, 53], the *enclosure method* [37, 38], and *one-step linearization* [31]. In Part II we review one such method known as the *monotonicity method* that relies on the monotonicity properties of $\gamma \mapsto \mathcal{R}(\gamma)$, such that for any open ball $B \subset \Omega$ we can characterize $\mathcal{D}$ by

$$\begin{aligned} B \subseteq \mathcal{D} \qquad & \text{if and only if} \qquad \mathcal{R}(\gamma_0 + \beta^{\text{nonlin}}\chi_B) - \mathcal{R}(\gamma) \geq 0 \\ & \text{if and only if} \qquad \mathcal{R}(\gamma_0) + \beta^{\text{lin}}\mathcal{R}'(\gamma_0)\chi_B - \mathcal{R}(\gamma) \geq 0, \end{aligned}$$

for admissible values of β^{nonlin} and β^{lin}. There we summarize the results of Papers B-C that also generalize the method to handle noisy data and electrode models such as CEM.

Finally, in Part III we summarize Papers D-E where we not only seek to reconstruct $\mathcal{D}$ but instead we approximate the perturbation $\delta\gamma \equiv \kappa\chi_{\mathcal{D}}$ with an iterative method. Here a sparsity assumption is used for reconstruction in both 2D and 3D with local data, and spatially varying regularization is applied to further include prior information about the location of $\mathcal{D}$, for instance obtained through the monotonicity method. The actual reconstruction is done by iteratively solving an optimization problem

$$\delta\gamma \simeq \operatorname*{argmin}_{\delta\sigma \in \mathcal{A}_0} \left(\frac{1}{2} \sum_{k=1}^{K} \|\mathcal{R}(\gamma_0 + \delta\sigma)g_k - f_k\|^2_{L^2(\Gamma)} + \sum_{j=1}^{\infty} \alpha_j |\langle \delta\sigma, \psi_j \rangle_{H^1(\Omega)}| \right)$$

on a convex subset $\mathcal{A}_0 \subset H^1_0(\Omega)$, for K pairs of Cauchy data $\{(g_k, f_k)\}_{k=1}^K$ taken on the subset $\Gamma \subset \partial\Omega$, the spatially varying regularization parameter α_j, and the ℓ^1-sparsity term on the coefficients in an appropriate basis $\{\psi_j\}_{j=1}^\infty$.

Part I

Depth dependence

Chapter 2

Depth dependence in EIT

For a compact and self-adjoint Hilbert space operator $F : X \to X$, then F has discrete real-valued eigenvalues that can be ordered from the largest magnitude to the smallest magnitude

$$|\lambda_1| \geq |\lambda_2| \geq \dots$$

By the min-max theorem (see e.g. [60]) the eigenvalues can be found by

$$|\lambda_n| = \sup \left\{ \frac{|\langle Fx, x\rangle_X|}{\|x\|_X^2} : x \neq 0, \;\; x \perp \operatorname{span}\{x_1, x_2, \dots, x_{n-1}\} \right\},$$

where $x_1, \dots, x_{n-1}$ are the eigenvectors to the largest $n-1$ eigenvalues (counting multiplicity), and the supremum is attained for $x = x_n$. The eigenvectors constitute an orthonormal basis for X, so if $V_n \equiv \operatorname{span}\{x_1, \dots, x_{n-1}\}^\perp$, then we obtain

$$|\lambda_n| = \|F|_{V_n}\|.$$

This gives rise to the concept of *distinguishability* of inclusions in EIT. Suppose the unknown conductivity is of the form $\gamma = 1 + \chi_{\mathcal{D}}$, where we seek to reconstruct $\mathcal{D}$ from the noisy ND map $\mathcal{R}^\delta(\gamma) \equiv \mathcal{R}(\gamma) + E^\delta$ with additive noise $\|E^\delta\|_{\mathcal{L}(L^2_\diamond(\partial\mathbb{D}))} = \delta$. To guarantee that $\mathcal{R}^\delta(\gamma)$ is not data coming from the background data $\mathcal{R}(1)$ that has been influenced by noise, we need

$$\|\mathcal{R}(\gamma) - \mathcal{R}(1)\|_{\mathcal{L}(L^2_\diamond(\partial\Omega))} > \delta.$$

Therefore, the largest eigenvalue of $\mathcal{R}(\gamma)-\mathcal{R}(1)$ determines how much noise that can be added to $\mathcal{R}(\gamma)$, before we can no longer determine if $\mathcal{R}^\delta(\gamma)$ originates from just the background conductivity, or if there is something else that may be reconstructed or approximated. The eigenfunctions to the largest eigenvalues of $\mathcal{R}(\gamma) - \mathcal{R}(1)$ are, in this sense, the optimal choice for orthonormal current patterns for measurements as they maximise the distinguishability.

Distinguishability in EIT was considered in [41, 18], where examples were given for concentric ball inclusions in the unit disk $\mathbb{D} \subset \mathbb{R}^2$. In Paper A we consider non-concentric ball inclusions in the disk, and do not obtain the actual eigenvalues but rather lower and upper bounds on the eigenvalues that depend on how far the inclusion is from the boundary.

2.1 Möbius transformations of the forward problem

We consider the unit disk domain $\mathbb{D} \subset \mathbb{R}^2$ and use harmonic morphisms, transformations that preserve harmonic functions (see [70, 29, 39, 51, 52, 3, 61] for other applications in EIT), to determine the eigenvalue bounds. We identify $(x_1, x_2) \in \mathbb{R}^2$ by $x_1 + ix_2 \in \mathbb{C}$.

All harmonic morphisms of the disk are given by Möbius transformations, which are uniquely given by (up to rotation)

$$M_a(x) = \frac{x-a}{\overline{a}x-1}, \quad x \in \mathbb{D}, \tag{2.1}$$

for $|a| < 1$. These transformations satisfy $M_a : \mathbb{D} \to \mathbb{D}$ and $\partial\mathbb{D} \to \partial\mathbb{D}$. The particular choice of rotation in (2.1) implies that M_a is an *involution*, meaning

$$M_a^{-1} = M_a.$$

Denoting $a \equiv \rho e^{i\zeta}$ with $0 \leq \rho < 1$ and $\zeta \in \mathbb{R}$, then for any $0 < r < 1$ the Möbius transformation M_a maps the concentric ball $B_{0,r}$ to a ball $B_{C,R}$ with centre C and radius R given by

$$C = \frac{\rho(r^2-1)}{\rho^2 r^2 - 1} e^{i\zeta}, \qquad R = \frac{r(\rho^2-1)}{\rho^2 r^2 - 1}.$$

On the other hand, given $C \equiv ce^{i\zeta}$ with $0 \leq c < 1$ and $\zeta \in \mathbb{R}$, and let $0 < R < 1 - c$. Then there is a unique $a \in \mathbb{D}$ such that M_a maps $B_{C,R}$ to a concentric

ball $B_{0,r}$ satisfying

$$r = \frac{1 + R^2 - c^2 - \sqrt{((1-R)^2 - c^2)((1+R)^2 - c^2)}}{2R}, \qquad a = \frac{C}{1 - Rr}.$$

The connection above between a concentric ball $B_{0,r}$ and non-concentric ball $B_{C,R}$ will be used throughout, and is also illustrated in Figure 2.1. Here it is also noted that applying M_a to $B_{0,r}$ gives a non-concentric ball $B_{C,R}$ such that $a \in B_{C,R}$ along the same direction as the centre, but slightly closer to the boundary.

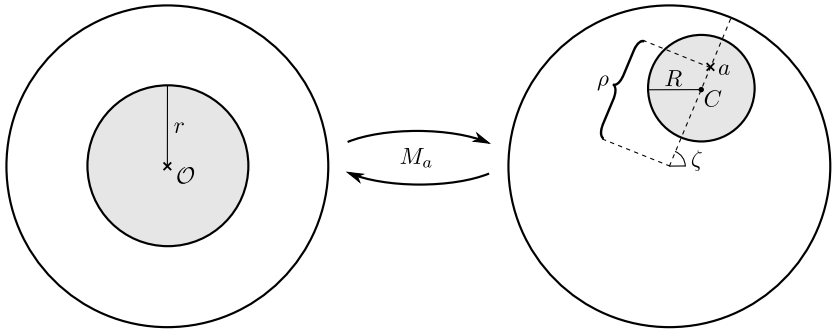

Figure 2.1: Illustration of the action of M_a on ball inclusions in the unit disk.

To apply the Möbius transformation to the DN and ND maps we denote the change of variables with M_a by

$$\mathcal{M}_a f \equiv f \circ M_a,$$

where either $f : \mathbb{D} \to \mathbb{C}$ or $f : \partial\mathbb{D} \to \mathbb{C}$. For distributions in $H^{-1/2}(\partial\mathbb{D})$ we use the natural generalization

$$\langle \mathcal{M}_a g, f \rangle \equiv \langle g, J_a^{1/2} \mathcal{M}_a f \rangle, \;\; g \in H^{-1/2}(\partial\mathbb{D}), f \in H^{1/2}(\partial\mathbb{D}),$$

where $J_a^{1/2}$ is the Jacobian determinant for the change of variables on $\partial\mathbb{D}$

$$J_a^{1/2}(e^{i\theta}) = \frac{1 - \rho^2}{1 + \rho^2 - 2\rho\cos(\theta - \zeta)}.$$

The notation used for $J_a^{1/2}$ is because it is the square root of the Jacobian determinant on $\mathbb{D}$.

Using the short notation

$$\gamma_{C,R} \equiv 1 + A\chi_{B_{C,R}}, \tag{2.2}$$

where $A > -1$ and $\chi_{B_{C,R}}$ is a characteristic function on $B_{C,R}$, we can write up the DN and ND maps for a non-concentric ball inclusion by

$$\Lambda(\gamma_{C,R}) = \Lambda(\mathcal{M}_a\gamma_{0,r}) = J_a^{1/2}\mathcal{M}_a\Lambda(\gamma_{0,r})\mathcal{M}_a, \tag{2.3}$$

$$\mathcal{R}(\gamma_{C,R}) = \mathcal{R}(\mathcal{M}_a\gamma_{C,R}) = P\mathcal{M}_a\mathcal{R}(\gamma_{0,r})J_a^{1/2}\mathcal{M}_a, \tag{2.4}$$

where $P : L^2(\partial\mathbb{D}) \to L^2_\diamond(\partial\mathbb{D})$ is an orthogonal projection, and $J_a^{1/2}$ is understood as the multiplication operator $f \mapsto J_a^{1/2}|_{\partial\mathbb{D}} f$. To better see the symmetry of (2.3) and (2.4) one could use that $\Lambda(\gamma)$ has the null-space span$\{1\}$ to write (2.3) as

$$\Lambda(\gamma_{C,R}) = J_a^{1/2}\mathcal{M}_a\Lambda(\gamma_{0,r})P\mathcal{M}_a.$$

This is a particularly simple expression, because if we consider $P\mathcal{M}_a$ and $J_a^{1/2}\mathcal{M}_a$ as operators on $L^2_\diamond(\partial\mathbb{D})$ they are the adjoint of one another. It is furthermore noted that $\gamma_{C,R}$ and $\gamma_{0,r}$ can be interchanged in (2.3) and (2.4).

2.2 Bounds on distinguishability

While $\Lambda(\gamma)$ is generally an unbounded operator on $L^2(\partial\mathbb{D})$, the difference operator $\Lambda(\gamma_{C,R}) - \Lambda(1)$ becomes infinitely smoothing because $\gamma_{C,R} = 1$ in a neighbourhood of the boundary. In fact $\Lambda(\gamma_{C,R}) - \Lambda(1)$ extends to a compact and self-adjoint operator on $L^2(\partial\mathbb{D})$ (see Lemma 3.2 of Paper A for more details). When restricting $\mathcal{R}(\gamma)$ to $L^2_\diamond(\partial\mathbb{D})$ the ND map is a compact self-adjoint operator in $\mathcal{L}(L^2_\diamond(\partial\mathbb{D}))$. So in either case of the DN or ND maps we can investigate the distinguishability in terms of the eigenvalue of largest magnitude.

Now lower and upper bounds on the distinguishability can be derived from the expressions (2.3) and (2.4), where it is recalled that $\rho = |a|$ determines how close $B_{C,R}$ is to $\partial\mathbb{D}$.

Theorem 2.1 *There are the following distinguishability bounds:*

$$\frac{1-\rho}{1+\rho} \leq \frac{\|\Lambda(\gamma_{0,r}) - \Lambda(1)\|_{\mathcal{L}(L^2(\partial\mathbb{D}))}}{\|\Lambda(\gamma_{C,R}) - \Lambda(1)\|_{\mathcal{L}(L^2(\partial\mathbb{D}))}} \leq \sqrt{\frac{1-\rho^2}{1+\rho^2}},$$

$$\frac{1-\rho}{1+\rho} \leq \frac{\|\mathcal{R}(\gamma_{0,r}) - \mathcal{R}(1)\|_{\mathcal{L}(L^2_\diamond(\partial\mathbb{D}))}}{\|\mathcal{R}(\gamma_{C,R}) - \mathcal{R}(1)\|_{\mathcal{L}(L^2_\diamond(\partial\mathbb{D}))}} \leq \frac{\sqrt{1+\rho^2}}{1-\rho^2}.$$

Note that as $\rho \to 1$ we have $R \to 0$, i.e. the non-concentric inclusion shrinks as it is moved closer to the boundary. For the DN map it is evident that the

coefficients of both lower and upper bounds tends to 0 as $\rho \to 1$, which implies that $\|\Lambda(\gamma_{C,R}) - \Lambda(1)\|_{\mathcal{L}(L^2(\partial\mathbb{D}))}$ tends to infinity. This makes sense as the requirement for $\Lambda(\gamma_{C,R}) - \Lambda(1)$ to be compact is that $\gamma_{C,R} = 1$ in a neighbourhood of $\partial\mathbb{D}$, so as the inclusion is moved closer to $\partial\mathbb{D}$ the spectrum becomes unbounded. For the upper bound of the ND map we see the opposite; here the coefficient for the upper bound tends to infinity as $\rho \to 1$ to counter that $\|\mathcal{R}(\gamma_{C,R}) - \mathcal{R}(1)\|_{\mathcal{L}(L^2_\diamond(\partial\mathbb{D}))} \to 0$, since $\mathcal{R}(\gamma)$ is generally a compact operator.

Using monotonicity-properties of Λ we can obtain the following upper bound, where the radius of the inclusion is kept fixed for $|C| \leq 1 - r$:

$$\|\Lambda(\gamma_{0,r}) - \Lambda(1)\|_{\mathcal{L}(L^2(\partial\mathbb{D}))} \leq \sqrt{\frac{1-\rho^2}{1+\rho^2}} \|\Lambda(\gamma_{C,r}) - \Lambda(1)\|_{\mathcal{L}(L^2(\partial\mathbb{D}))}. \tag{2.5}$$

So for a fixed size inclusion the distinguishability is increasing as it is moved closer to the boundary, as we intuitively expect.

2.2.1 Verification of bounds

To numerically verify the bounds, and to test how tight they are, matrix characterizations of $\Lambda(\gamma_{C,R}) - \Lambda(1)$ and $\mathcal{R}(\gamma_{C,R}) - \mathcal{R}(1)$ are determined. The matrix characterizations make use of bases modified from the standard Fourier basis $\{f_n\}_{n\in\mathbb{Z}}$ for $L^2(\partial\mathbb{D})$ given by

$$f_n(\theta) \equiv \frac{1}{\sqrt{2\pi}} e^{in\theta}, \quad \theta \in (-\pi, \pi). \tag{2.6}$$

The bases used are orthonormal in weighted inner products

$$\langle f, g \rangle_{1/2} \equiv \int_{\partial\mathbb{D}} f\overline{g} J_a^{1/2}\, ds, \quad \langle f, g \rangle_{-1/2} \equiv \int_{\partial\mathbb{D}} f\overline{g} J_a^{-1/2}\, ds.$$

These will be natural choices of inner products to make use of the known spectrum of $\Lambda(\gamma_{0,r}) - \Lambda(1)$ and $\mathcal{R}(\gamma_{0,r}) - \mathcal{R}(1)$, when using the expressions (2.3) and (2.4).

Now the difference operators of DN and ND maps can be characterized using the following two theorems.

Theorem 2.2 *Let $\hat{\lambda}_n$ be the n'th eigenvalue of $\Lambda(\gamma_{0,r}) - \Lambda(1)$. Define the orthonormal basis $\{\phi_n\}_{n\in\mathbb{Z}}$ by*

$$\phi_n \equiv \mathcal{M}_a f_n, \quad f_n(\theta) \equiv \frac{1}{\sqrt{2\pi}} e^{in\theta}, \quad n \in \mathbb{Z}.$$

Then $\Lambda(\gamma_{C,R}) - \Lambda(1)$ *is represented in this basis via the following tridiagonal matrix:*

$$\mathcal{A}_{m,n} \equiv \langle (\Lambda(\gamma_{C,R}) - \Lambda(1))\phi_m, \phi_n \rangle_{1/2} = \begin{cases} \frac{1+\rho^2}{1-\rho^2}\hat{\lambda}_m, & m = n, \\ \frac{-a}{1-\rho^2}\hat{\lambda}_m, & m - n = 1, \\ \frac{-\overline{a}}{1-\rho^2}\hat{\lambda}_m, & m - n = -1, \\ 0, & \text{else.} \end{cases}$$

Theorem 2.3 *Let either* $H(\gamma) \equiv \mathcal{R}(\gamma)$ *or* $H(\gamma) \equiv \mathcal{R}(\gamma) - \mathcal{R}(1)$*. Let* $\hat{\lambda}_n$ *be the n'th eigenvalue of* $H(\gamma_{0,r})$*, and denote by* h_n *the n'th Fourier coefficient of* $J_a^{1/2}$ *given by*

$$h_n = \begin{cases} 1 & n = 0, \\ \overline{a}^{|n|} & n > 0, \\ a^{|n|} & n < 0. \end{cases}$$

Define the orthonormal basis $\{\psi_n\}_{n \in \mathbb{Z} \setminus \{0\}}$ *by*

$$\psi_n \equiv J_a^{1/2} \mathcal{M}_a f_n, \quad f_n(\theta) \equiv \frac{1}{\sqrt{2\pi}} e^{in\theta}, \ \ n \in \mathbb{Z} \setminus \{0\}.$$

Then $H(\gamma_{C,R})$ *is represented in this basis via the following matrix:*

$$\mathcal{A}_{n,m} \equiv \langle H(\gamma_{C,R})\psi_m, \psi_n \rangle_{-1/2} = \hat{\lambda}_m (h_{n-m} - \overline{h_m} h_n), \ \ m, n \neq 0.$$

The above matrices are used to efficiently and accurately evaluate the eigenvalues of $\Lambda(\gamma_{0,r}) - \Lambda(1)$ and $\mathcal{R}(\gamma_{0,r}) - \mathcal{R}(1)$, without errors from finite element discretization and numerical integration. Figure 2.2 shows the bounds from Theorem 2.1 for various choices of radii r, evaluated using the matrices from Theorems 2.2 and 2.3.

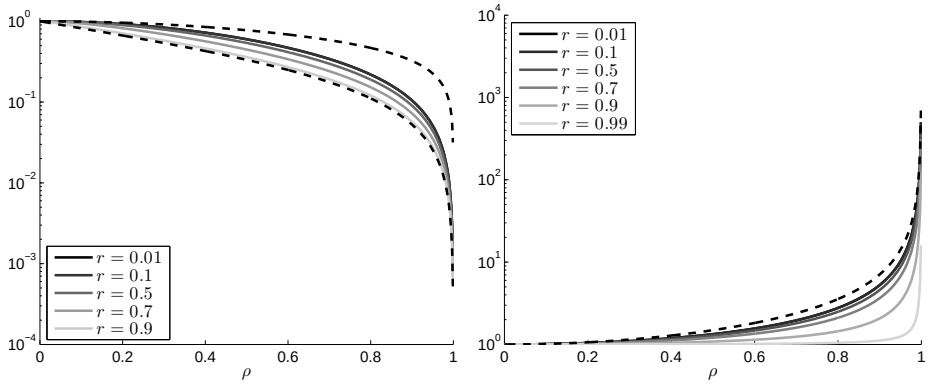

Figure 2.2: **(a):** Ratio $\|\Lambda(\gamma_{0,r}) - \Lambda(1)\|/\|\Lambda(\gamma_{C,R}) - \Lambda(1)\|$ for $|a| = \rho \in [0, 1)$, along with the bounds (dashed lines) from Theorem 2.1. **(b):** Ratio $\|\mathcal{R}(\gamma_{0,r}) - \mathcal{R}(1)\|/\|\mathcal{R}(\gamma_{C,R}) - \mathcal{R}(1)\|$ for $|a| = \rho \in [0, 1)$, along with the upper bound (dashed line) from Theorem 2.1.

2.3 Conclusions/discussion

While the bounds in Theorem 2.1 are not optimal, they are reasonably close, for instance for the DN maps for large inclusions, or either close to the centre or to the boundary. While for the ND maps the upper bound is reasonable for small inclusions. For the DN maps it is seen that for fixed radius r in (2.5) the distinguishability is increasing the closer the inclusions is to the boundary. The same does not follow directly for the ND map, though it can be confirmed to also be the case through numerical examples (see the appendix of Paper A).

The distinguishability bounds can also in some sense be related to stability. Suppose that there is a stability estimate

$$\|\gamma_1 - \gamma_2\|_{L^\infty(\mathbb{D})} \leq \omega\left(\|\Lambda(\gamma_1) - \Lambda(\gamma_2)\|\right), \tag{2.7}$$

where $\omega : [0, \infty) \to [0, \infty)$ is an increasing function satisfying $\lim_{t\to 0} \omega(t) = 0$. If such an estimate holds for the $\gamma_{C,R}$-conductivities then we obtain:

$$\begin{aligned}\|\gamma_{C,R} - 1\|_{L^\infty(\mathbb{D})} &= \|\gamma_{0,r} - 1\|_{L^\infty(\mathbb{D})} \\ &\leq \omega\left(\|\Lambda(\gamma_{0,r}) - \Lambda(1)\|\right) \\ &\leq \omega\left(\sqrt{\frac{1-\rho^2}{1+\rho^2}}\|\Lambda(\gamma_{C,R}) - \Lambda(1)\|\right).\end{aligned} \tag{2.8}$$

Thus, the stability in (2.8) is strictly better than inserting $\gamma_{C,R} - 1$ directly into (2.7), and the bound becomes tighter as $\rho \to 1$ i.e. as the inclusion is placed closer to the boundary. This shows the inherent depth dependence in EIT, and why we can expect to much more stably reconstruct inclusions close to the measurement boundary.

The bounds are only found for the 2D problem in the unit disk. One could also consider a similar analysis on the unit ball domain in 3D. Here it should be noted that harmonic morphisms in 3D are only translations and orthogonal transformations such as rotations and reflections in planes, and Möbius transformations in 3D are generally not harmonic morphisms [56]. Instead one could use *Kelvin transforms*, which also preserve harmonic functions and can be used to move ball inclusions around in the unit ball (see e.g. [28]). The Kelvin transforms are not harmonic morphisms as they are not only a change of variable, but there is a scaling that ensures that it preserves harmonic functions. Due to the scaling a Kelvin transform will not map a Neumann condition to a Neumann condition, but instead to a Robin condition. So it is likely that the counterparts to (2.3) and (2.4) in 3D will include a linear combination of both DN and ND maps for the concentric inclusion.

Part II

Monotonicity-based shape reconstruction

Chapter 3

The monotonicity method

Suppose that the conductivity is of the form

$$\gamma = \gamma_0 + \kappa\chi_{\mathcal{D}},$$

where $\mathcal{D}$ is the unknown inclusion that we seek to reconstruct, and $\kappa \in L^\infty_+(\Omega)$ is the perturbation on $\mathcal{D}$ from the known background conductivity $\gamma_0 \in L^\infty_+(\Omega)$. The monotonicity method is mainly based on the CM [32, 65, 66] with some theory on stability of reconstructions when using the CEM [33], in the sense of how large pixels one should use in the discretization to guarantee detection of an inclusion. The method is formulated either using a non-linear method that is numerically quite slow or through the faster linear formulation.

Since $\kappa \in L^\infty_+(\Omega)$ we call κ a positive perturbation, and as it is bounded from below by a positive scalar, there is a singularity on $\partial\mathcal{D}$ in γ. By having the singularity at $\partial\mathcal{D}$ makes it possible to avoid regularity assumptions on κ, although it is possible to use a more complicated variant of the method if there is no singularity when κ is piecewise continuous [32]. It should be noted that the method can also be formulated for negative perturbations, and for perturbations with both positive and negative values, and the following results naturally extend to these formulations.

The contributions of Paper B comprises new regularization theory for the monotonicity method and generalizations to the CEM that lead to convergence of

reconstructions from the CEM to the CM reconstruction, when the boundary is densely covered by electrodes. In Paper C a numerical comparison of the non-linear and linear formulation of the monotonicity method shows that there is essentially no difference in the reconstructions, which is quite useful in the light that the linear method has a much lower computational complexity.

3.1 The monotonicity method for the continuum model

The reconstructions of the monotonicity method will be based on a noisy ND-map $\mathcal{R}^\delta(\gamma) \equiv \mathcal{R}(\gamma) + E^\delta$ for a compact and self-adjoint noise perturbation $E \in \mathcal{L}(L^2_\diamond(\partial\Omega))$ with noise level $\|E\|_{\mathcal{L}(L^2_\diamond(\partial\Omega))} = \delta$. The reconstructions with the CM are done using either of the following non-linear and linear formulations:

$$\mathcal{T}_{\alpha,\delta} \equiv \left\{ B \subseteq \Omega \text{ open ball} : \mathcal{R}(\gamma_0 + \beta^{\text{nonlin}}\chi_B) + \alpha \operatorname{Id} - \mathcal{R}^\delta(\gamma) \geq 0 \right\}, \tag{3.1}$$

$$\mathcal{T}'_{\alpha,\delta} \equiv \left\{ B \subseteq \Omega \text{ open ball} : \mathcal{R}(\gamma_0) + \beta^{\text{lin}}\mathcal{R}'(\gamma_0)\chi_B + \alpha \operatorname{Id} - \mathcal{R}^\delta(\gamma) \geq 0 \right\}, \tag{3.2}$$

where α is a regularization parameter, and the inequalities are in the sense of positive semi-definiteness. In Section 3.2 we return to admissible choices of α that will lead to convergence when the noise level tends to zero.

The monotonicity method is based on the following monotonicity relations for the ND map: for any $\gamma, \tilde{\gamma} \in L^\infty_+(\Omega)$ it holds (see e.g. [32])

$$\int_\Omega \frac{\tilde{\gamma}}{\gamma}(\gamma - \tilde{\gamma})|\nabla \tilde{u}|^2 \, dx \leq \langle (\mathcal{R}(\tilde{\gamma}) - \mathcal{R}(\gamma))g, g \rangle \leq \int_\Omega (\gamma - \tilde{\gamma})|\nabla \tilde{u}|^2 \, dx, \tag{3.3}$$

where $g \in L^2_\diamond(\partial\Omega)$ is arbitrary and $\tilde{u} \in H^1_\diamond(\Omega)$ is the solution to (1.3) with Neumann condition g and conductivity $\tilde{\gamma}$.

Under the assumptions that Ω has smooth boundary, γ_0 is piecewise analytic, and $\overline{\mathcal{D}} \subset \Omega$, then it follows from (3.3) and theory on localized potentials [32] that

$$\mathcal{D} \subseteq \cup\mathcal{T}_{0,0} \subseteq \mathcal{D}^\bullet \quad \text{if} \quad 0 < \beta^{\text{nonlin}} \leq \operatorname{ess\,inf} \kappa, \tag{3.4}$$

$$\mathcal{D} \subseteq \cup\mathcal{T}'_{0,0} \subseteq \mathcal{D}^\bullet \quad \text{if} \quad 0 < \beta^{\text{lin}} \leq \operatorname{ess\,inf} \left(\frac{\gamma_0 \kappa}{\gamma} \right), \tag{3.5}$$

where $\mathcal{D}^\bullet$ has the rather technical definition

$$\mathcal{D}^\bullet \equiv \overline{\Omega} \setminus \cup\{ U \subseteq \mathbb{R}^d \setminus \mathcal{D} \text{ open and connected} : U \cap \partial\Omega \neq \emptyset \}.$$

In very general cases where $|\mathcal{D}| = |\overline{\mathcal{D}}|$ in terms of measure, then $\mathcal{D}^\bullet$ can be interpreted as filling out the holes of $\mathcal{D}$ (see also Figure 3.1). In particular if $\mathcal{D}$ has connected complement (no holes) then $\mathcal{D}^\bullet = \overline{\mathcal{D}}$.

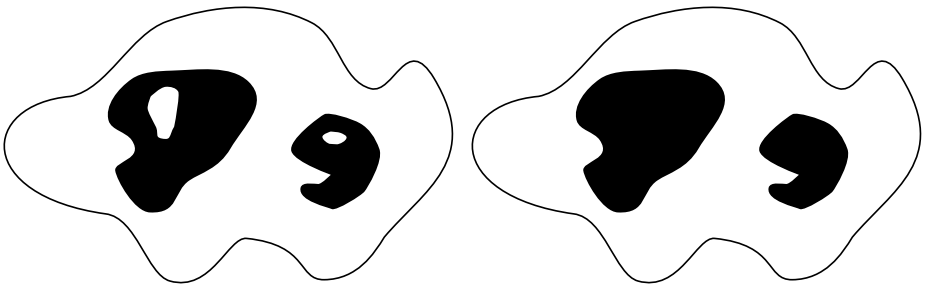

Figure 3.1: Illustration of an example of $\mathcal{D}$ (black regions on the left) and the corresponding upper bound $\mathcal{D}^\bullet$ (black regions on the right).

For positive bounds $\beta_0^{\mathrm{L}} \leq \gamma_0 \leq \beta_0^{\mathrm{U}}$ and assuming prior knowledge of positive bounds on the perturbation $\beta^{\mathrm{L}} \leq \kappa \leq \beta^{\mathrm{U}}$, then it is possible to choose admissible β-values in (3.1) and (3.2) as

$$\beta^{\mathrm{nonlin}} \equiv \beta^{\mathrm{L}}, \quad \beta^{\mathrm{lin}} \equiv \frac{\beta_0^{\mathrm{L}} \beta^{\mathrm{L}}}{\beta_0^{\mathrm{U}} + \beta^{\mathrm{U}}}.$$

Thus it is typically necessary to assume both lower and upper bounds on κ when using the linear method, while the non-linear method only requires a lower bound.

3.1.1 Comparison of linear and non-linear reconstruction

To compare the reconstructions (3.1) and (3.2) we make use of Möbius transformations in the unit disk $\mathbb{D} \subset \mathbb{R}^2$, and a background conductivity $\gamma_0 \equiv 1$ (see Section 2.1 for notation). Thus we use M_a to relate a conductivity $\gamma_{0,r}$ to $\gamma_{C,R}$, where similar to (2.2) the conductivities are

$$\gamma_{C,R} \equiv 1 + \beta \chi_{B_{C,R}}.$$

The matrix characterizations from Section 2.2.1 cannot directly be used in the monotonicity tests in (3.1) because the bases used depend on the transformation M_a of each ball $B_{C,R}$. However we need a fixed basis, the same used to represent the datum $\mathcal{R}(\gamma)$, and here we make use of the standard Fourier basis $\{f_n\}_{n \in \mathbb{Z} \setminus \{0\}}$ for $L^2_\diamond(\partial\mathbb{D})$, defined in (2.6). The main idea is to find matrix representations of

$J_a^{1/2}\mathcal{M}_a$ and $P\mathcal{M}_a$ in the Fourier basis, which is done using a matrix H_a and its adjoint $(H_a)^*$ defined in the following theorem.

Theorem 3.1 *Recall that $a = \rho e^{i\zeta}$ and define the matrix H_a by*

$$(H_a)_{n,m} \equiv \langle f_m, \mathcal{M}_a f_n \rangle, \;\; n, m \in \mathbb{Z} \setminus \{0\},$$

then H_a has the following properties (note in particular that (iv)-(vii) *explicitly defines the entire matrix):*

(i) H_a *is a matrix representation of* $J_a^{1/2}\mathcal{M}_a$.

(ii) $(H_a)^*$ *is a matrix representation of* $P\mathcal{M}_a$.

(iii) H_a *is involutory, i.e.* $H_a = H_a^{-1}$.

(iv) $(H_a)_{n,m} = e^{i(m-n)\zeta}(H_\rho)_{n,m}, \;\; \forall n, m.$

(v) H_a *is centrohermitian, i.e.* $(H_a)_{n,m} = \overline{(H_a)_{-n,-m}}, \;\; \forall n, m.$

(vi) H_a *is block diagonal with* $(H_a)_{n,m} = 0$ *for* $n < 0, m > 0$ *and for* $n > 0, m < 0$.

(vii) There is the following formula for $n > 0, m > 0$*:*

$$(H_\rho)_{n,m} = \sum_{k=\max\{n-m,0\}}^{n} (-1)^{n-k} \binom{k+m-1}{k+m-n} \binom{n}{k} \rho^{2k+m-n}.$$

The H_a-matrices are closely related to the matrix formulations in Theorems 2.2 and 2.3. In fact, Theorem 3.1 directly implies:

(i) H_a is the basis change matrix from/to orthonormal basis $\{J_a^{1/2}\mathcal{M}_a f_n\}_{n\in\mathbb{Z}\setminus\{0\}}$ of the weighted space $(L^2_\diamond(\partial\mathbb{D}), \|\cdot\|_{-1/2})$ to/from orthonormal basis $\{f_n\}_{n\in\mathbb{Z}\setminus\{0\}}$ of $(L^2_\diamond(\partial\mathbb{D}), \|\cdot\|)$.

(ii) $(H_a)^*$ is the orthonormal basis change matrix from/to basis $\{P\mathcal{M}_a f_n\}_{n\in\mathbb{Z}\setminus\{0\}}$ of the weighted space $(L^2_\diamond(\partial\mathbb{D}), \|\cdot\|_{1/2})$ to/from orthonormal basis $\{f_n\}_{n\in\mathbb{Z}\setminus\{0\}}$ of $(L^2_\diamond(\partial\mathbb{D}), \|\cdot\|)$.

In the same vein the Fréchet derivative for ball inclusions can be found using the following proposition.

Proposition 3.2 *Denote by A' the matrix representation of $\mathcal{R}'(1)[\chi_{B_{C,R}}]$, i.e.*

$$A'_{n,m} \equiv \langle \mathcal{R}'(1)[\chi_{B_{C,R}}] f_m, f_n \rangle, \;\; n, m \in \mathbb{Z} \setminus \{0\},$$

then

(i) A' *is Hermitian, i.e.* $A' = (A')^*$.

(ii) A' *is centrohermitian, i.e.* $A'_{n,m} = \overline{A'_{-n,-m}}$.

(iii) A' *is block diagonal with* $A'_{n,m} = 0$ *for* $n < 0, m > 0$ *and for* $n > 0, m < 0$.

(iv) There is the following formula for $n > 0, m > 0$*, recalling that* $C = ce^{i\zeta}$*:*

$$A'_{n,m} = -e^{i(m-n)\zeta} \sum_{k=0}^{\min\{n,m\}-1} \frac{1}{k+1} \binom{m-1}{k} \binom{n-1}{k} c^{m+n-2k-2} R^{2k+2}.$$

So using the expression (2.4), along with the properties of Theorem 3.1 and Proposition 3.2 the matrix structures A of $\mathcal{R}(\gamma_{C,R})$ and A' of $\mathcal{R}'(1)\chi_{B_{C,R}}$ are:

$$A = \begin{pmatrix} \mathcal{J}\overline{(H_a^+)^* D^+ H_a^+}\mathcal{J} & 0 \\ 0 & (H_a^+)^* D^+ H_a^+ \end{pmatrix}, \quad A' = \begin{pmatrix} \mathcal{J}\overline{A'^+}\mathcal{J} & 0 \\ 0 & A'^+ \end{pmatrix},$$

where D is the diagonal matrix holding the eigenvalues of $\mathcal{R}(\gamma_{0,r})$, $\mathcal{J}$ is the *exchange matrix* (zeroes in all entries except on the anti-diagonal, from bottom left to top right, where its entries equal 1), and D^+, H_a^+, and A'^+ are the lower right parts of D, H_a, and A', respectively.

Now we have representations of $\mathcal{R}(1)$, $\mathcal{R}'(1)\chi_B$, and $\mathcal{R}(1+\beta\chi_B)$ for any ball $B \subset \Omega$, and the reconstructions (3.1) and (3.2) can be compared for various noise levels δ. A few examples are given in Figure 3.2 (see Paper C for more noise levels).

The instability of EIT is evident, and even for noiseless data we are not able to perfectly reconstruct $\mathcal{D}$. This is because we have to use a finite N-term approximation of A and A', and as such we only use the operators

$$P_N \mathcal{R}(1) P_N, \quad P_N \mathcal{R}'(1)[\chi_B] P_N, \quad P_N \mathcal{R}(1+\beta\chi_B) P_N,$$

where P_N is the orthogonal projection onto $\operatorname{span}\{f_n\}_{|n|=1,2,\ldots,N}$.

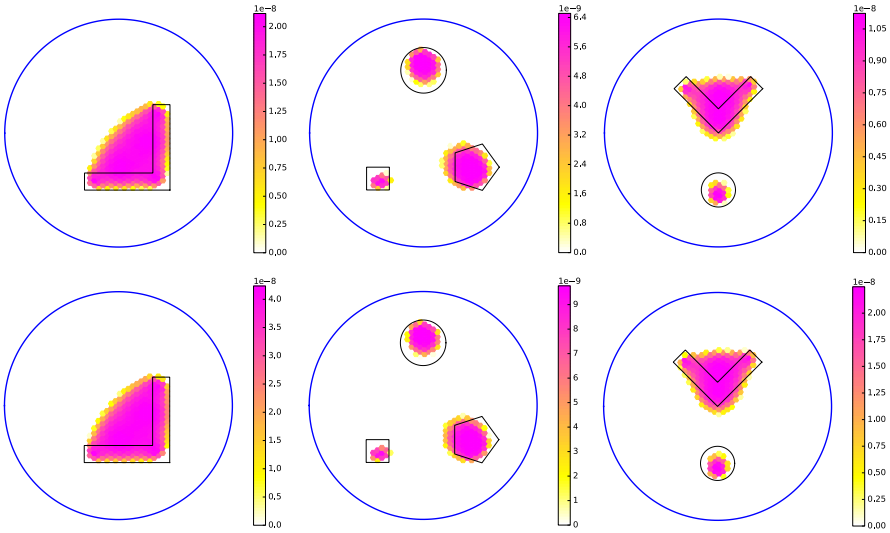

Figure 3.2: Monotonicity-based reconstructions from simulated data using 32 current patterns and with a noise level of $\delta = 10^{-4}$ (see Paper C for more details). The linear method is used for the top row and the non-linear method for the bottom row. The ground truth inclusions are outlined with a black line, with $\gamma_0 = 1$ and $\kappa = 4$. The plots show the smallest eigenvalue for each ball that gave a positive semi-definite operator.

3.2 Generalizations to electrode models

Here we summarize the regularization and convergence results of Paper B. The main idea is to generalize (3.1) and (3.2) to other forward models, in particular the CEM. Thus we assume to have approximate compact self-adjoint operators $\{\mathcal{R}_h(\gamma)\}_{h>0}$, and replace $\mathcal{R}(\gamma)$ with the approximation $\mathcal{R}_h(\gamma)$:

$$\mathcal{T}_{\alpha,\delta,h} \equiv \left\{ B \subseteq \Omega \text{ open ball} : \mathcal{R}_h(\gamma_0 + \beta^{\text{nonlin}}\chi_B) + \alpha \operatorname{Id} - \mathcal{R}_h^\delta(\gamma) \geq 0 \right\},$$
$$\mathcal{T}'_{\alpha,\delta,h} \equiv \left\{ B \subseteq \Omega \text{ open ball} : \mathcal{R}_h(\gamma_0) + \beta^{\text{lin}}\mathcal{R}'_h(\gamma_0)\chi_B + \alpha \operatorname{Id} - \mathcal{R}_h^\delta(\gamma) \geq 0 \right\}.$$

Here we assume that there is the following type of estimate

$$\|\mathcal{R}(\gamma) - \mathcal{R}_h(\gamma)\|_{\mathcal{L}(L^2_\diamond(\partial\Omega))} \leq \omega(h)\|\gamma\|_{L^\infty(\Omega)}, \tag{3.6}$$

where $\omega : [0,\infty) \to [0,\infty)$ with $\lim_{h\to 0} \omega(h) = 0$. Similarly for the linearisation we assume

$$\|\mathcal{R}'(\gamma)\eta - \mathcal{R}'_h(\gamma)\eta\|_{\mathcal{L}(L^2_\diamond(\partial\Omega))} \leq \omega(h)\|\eta\|_{L^\infty(\Omega)}\|\gamma\|_{L^\infty(\Omega)}. \tag{3.7}$$

It is worth noting that $\mathcal{T}_{\alpha,\delta,0} = \mathcal{T}_{\alpha,\delta}$ and $\mathcal{T}'_{\alpha,\delta,0} = \mathcal{T}'_{\alpha,\delta}$, from (3.1) and (3.2). Now we can formulate the regularization of the monotonicity method for an admissible choice of regularization parameter, where σ below denotes the spectrum of compact and self-adjoint operators on $L^2_\diamond(\partial\Omega)$.

Theorem 3.3 *Let $\alpha = \alpha(h,\delta) \in \mathbb{R}$ satisfy*

(i) $\delta - \inf_{B\in\mathcal{T}_{0,0}} \inf \sigma\left(\mathcal{R}_h(\gamma_0 + \beta^{\text{nonlin}}\chi_B) - \mathcal{R}_h(\gamma)\right) \leq \alpha(h,\delta)$,

(ii) $\lim_{h,\delta\to 0} \alpha(h,\delta) = 0$.

Then for any $\lambda > 0$ there exists an $\epsilon_\lambda > 0$ such that

$$\mathcal{T}_{0,0} \subseteq \mathcal{T}_{\alpha,\delta,h} \subseteq \mathcal{T}_{\lambda,0},$$

for all $h, \delta \in (0, \epsilon_\lambda]$.

Theorem 3.3 implies that it is possible to regularize the monotonicity method using the same regularization parameter for all balls $B \subset \Omega$. Furthermore, it states that the reconstruction from the approximative forward model $\mathcal{R}_h(\gamma)$, even when influenced by noise, is interlaced between two reconstructions from the CM, both noiseless: one with no regularization and one with regularization $\alpha = \lambda$. So the choice of regularization parameter in Theorem 3.3 implies that the approximative model always gives an overestimate of the inclusion $\mathcal{D}$, i.e. that the inclusion is guaranteed to be detected.

We furthermore obtain the set-theoretic limit when $\alpha(h,\delta)$ is chosen as in Theorem 3.3

$$\lim_{h,\delta\to 0} \mathcal{T}_{\alpha,\delta,h} = \mathcal{T}_{0,0},$$

and as such we have convergence, from above, to the reconstruction from the CM with no noise or regularization.

An analogous result holds for the linear method.

Theorem 3.4 *Let $\alpha = \alpha(h,\delta) \in \mathbb{R}$ satisfy*

(i) $\delta - \inf_{B\in\mathcal{T}'_{0,0}} \inf \sigma\left(\mathcal{R}_h(\gamma_0) + \beta^{\text{lin}}\mathcal{R}'_h(\gamma_0)\chi_B - \mathcal{R}_h(\gamma)\right) \leq \alpha(h,\delta)$,

(ii) $\lim_{h,\delta\to 0} \alpha(h,\delta) = 0$.

Then for any $\lambda > 0$ there exists an $\epsilon_\lambda > 0$ such that

$$\mathcal{T}'_{0,0} \subseteq \mathcal{T}'_{\alpha,\delta,h} \subseteq \mathcal{T}'_{\lambda,0},$$

for all $h, \delta \in (0, \epsilon_\lambda]$.

For the approximative operator $\mathcal{R}_h(\gamma)$ we would like to use the CEM, as it is a precise electrode model to use for real measurements. Here the concept of *extended electrodes* is applied, which was introduced in [36]. Recall the CEM from (1.4)-(1.7), and define mutually disjoint extended electrodes $\{E_j^+\}_{j=1}^k$ that cover all of the boundary:

$$E_j \subseteq E_j^+ \subseteq \partial\Omega, \quad \bigcup_{j=1}^k \overline{E_j^+} = \partial\Omega, \quad \min_{j=1,\dots,k} \frac{|E_j|}{|E_j^+|} \geq c, \tag{3.8}$$

for a scalar $c > 0$ independent of the electrodes. The first two conditions in (3.8) means, as the name implies, that the extended electrodes E_j^+ artificially extends the physical electrodes to cover the whole boundary. The latter condition in (3.8) is used in the estimates below, and implies that there must be a relation between the size of the physical electrodes $|E_j|$ and the number of electrodes k in order to estimate the ND map using the CEM. That is, if we reduce the size of $|E_j|$ sufficiently we also need to increase the number of electrodes in order to densely cover the boundary.

This gives rise to the extension operator $Q : \mathbb{R}^k \to L^2(\partial\Omega)$ and its adjoint $Q^* : L^2(\partial\Omega) \to \mathbb{R}^k$ given by

$$QW \equiv \sum_{j=1}^k W_j \chi_j^+, \quad (Q^* f)_j \equiv \int_{E_j^+} f \, ds,$$

where χ_j^+ is a characteristic function on E_j^+. Thus, there is the following relation between the ND map $\mathcal{R}(\gamma)$ and the measurement map for CEM $R(\gamma)$, where the first estimate (3.9) is a restatement of the estimate in [36] and the estimate for the linearisation (3.10) was proven in Paper B.

Theorem 3.5 *Let $L : L^2(\partial\Omega) \to L^2_\diamond(\partial\Omega)$ be an orthogonal projection, and let $P : L^2(\partial\Omega) \to \mathbb{R}^k$ be defined as*

$$(Pf)_j \equiv \frac{1}{|E_j|} \int_{E_j} f \, ds.$$

For mutually disjoint extended electrodes $\{E_j^+\}$ satisfying (3.8)*, with maximal diameter on $\partial\Omega$ given by $h \equiv \max_j \operatorname{diam}(E_j^+)$, assume that there is the Poincaré inequality-type estimate*

$$\|(\mathrm{Id} - QP)f\|_{L^2(\partial\Omega)} \leq Ch \inf_{c\in\mathbb{R}} \|f + c\|_{H^1(\partial\Omega)},$$

for all $f \in H^1(\partial\Omega)$ and constant $C > 0$ independent of h. If γ is C^∞-smooth near $\partial\Omega$ and $\eta \in L^\infty(\Omega)$ is compactly supported in Ω, we have

$$\|\mathcal{R}(\gamma) - LQ(R(\gamma) - Z)Q^*\|_{\mathcal{L}(L^2_\diamond(\partial\Omega))} \leq Ch\|\gamma\|_{L^\infty(\Omega)}, \tag{3.9}$$

$$\|\mathcal{R}'(\gamma)\eta - LQ(R'(\gamma)\eta)Q^*\|_{\mathcal{L}(L^2_\diamond(\partial\Omega))} \leq Ch\|\eta\|_{L^\infty(\Omega)}\|\gamma\|_{L^\infty(\Omega)}, \tag{3.10}$$

where $C > 0$ is independent of γ, η, and h. Here $Z \in \mathbb{R}^{k\times k}$ is the diagonal matrix holding the non-zero entries $Z_{j,j} \equiv z_j/|E_j|$.

A simple explanation of the approximation $LQ(R(\gamma)-Z)Q^*$ applied to a current pattern $f \in L^2_\diamond(\partial\Omega)$, is that Q^* takes the total current through each extended electrode E_j^+ and passes it on to $R(\gamma)$ that assumes it comes from the smaller physical electrodes E_j. The contribution from the contact impedances in $R(\gamma)$ is subtracted as they are not part of the CM. The corresponding voltages are then extended by Q to a simple function on the extended electrodes, and L ensures that the same grounding level is used as in the CM. That the estimate holds for $h \to 0$ is intuitive as simple functions are dense in L^2.

Here it is straightforward to see that $\mathcal{R}_h(\gamma) = LQ(R(\gamma) - Z)Q^*$ with Fréchet derivative $\mathcal{R}'_h(\gamma)\eta = LQ(R'(\gamma)\eta)Q^*$ satisfies the requirements from (3.6) and (3.7), and therefore the CEM can be used in the monotonicity method. It is furthermore possible to use the monotonicity method directly using the measurement map $R(\gamma)$ instead of $LQ(R(\gamma) - Z)Q^*$, because it holds that $A \geq 0$ if and only if $LQAQ^* \geq 0$ for any $A \in \mathbb{R}^{k\times k}$.

Due to similar monotonicity relations to (3.3) for the CEM it is possible to simplify the choice of regularization parameter in Theorems 3.3 and 3.4 to $\alpha \geq \delta$. The monotonicity method was implemented and tested for both 2D and 3D reconstruction using the linear formulation with the CEM. The examples in Figures 3.3 and 3.4 shows that the monotonicity method is numerically viable when using the CEM. See Paper B for more details on the choice of current patterns and discretization.

For real measurements (see Figure 3.5) a slight modification to the reconstruction was done, by not using one β-value, but instead a series of increasing β-values and for each ball $B \subset \Omega$ it is counted for how many β-values it yields a positive semi-definite operator. This approach seems to be more stable, and rather than giving a binary reconstruction of *B is inside $\mathcal{D}$* or *B is outside $\mathcal{D}$*, it shows how reliably we can expect the reconstruction to be at various points in the domain. The modification was necessary as the method is quite sensitive with respect to the background conductivity γ_0 which was estimated from the measurements.

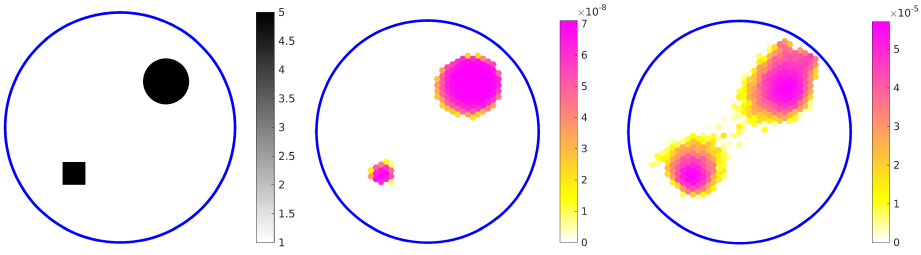

(a) (b) (c)

Figure 3.3: 2D monotonicity-based reconstruction using the CEM with 16 equidistant electrodes. The plots show the smallest eigenvalue for the monotonicity tests that yielded a positive semi-definite operator. **(a):** Numerical phantom. **(b):** Reconstruction from noiseless simulated data. **(c):** Reconstruction from noisy simulated data with approximately 0.5% noise. See Paper B for further details.

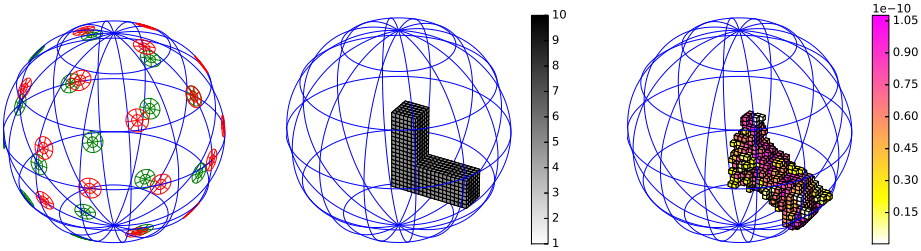

(a) (b) (c)

Figure 3.4: 3D monotonicity-based reconstruction using the CEM with 32 equidistant electrodes. **(a):** Electrode placement on the sphere; electrodes marked as red are on the front side (facing the camera) of the sphere and green electrodes are placed on the back of the sphere. **(b):** Numerical phantom. **(c):** Reconstruction from noiseless simulated data. The plot shows the smallest eigenvalue for the monotonicity tests that yielded a positive semi-definite operator.

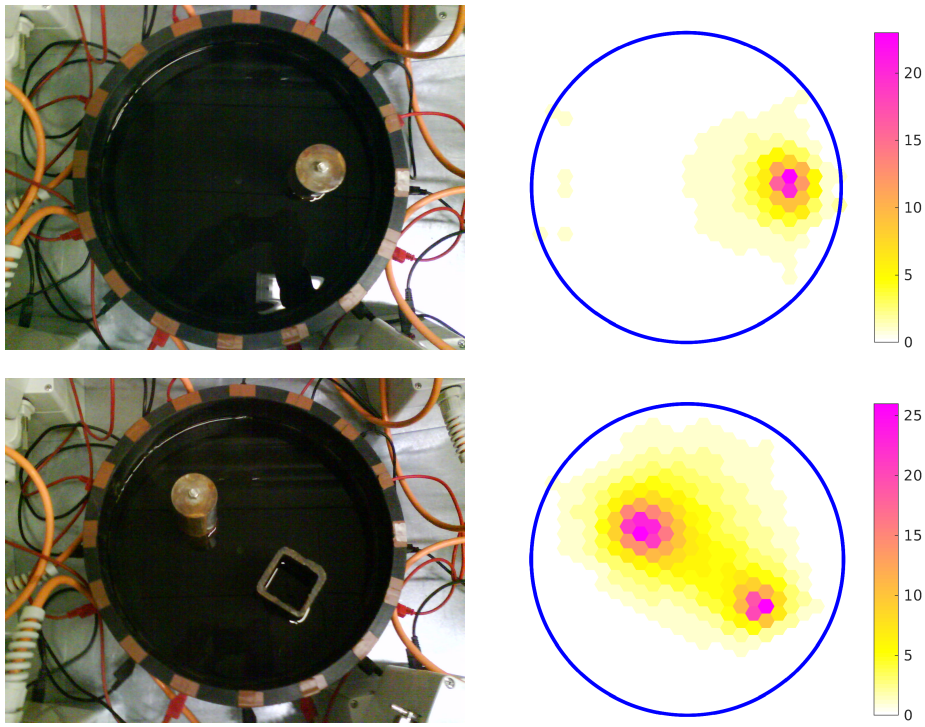

Figure 3.5: 2D monotonicity-based reconstruction using the CEM with 16 equidistant electrodes. The measurement equipment is the KIT4 measurement device from the University of Eastern Finland, see Paper B for further details. **Left:** Measurement setup with metal objects submerged in tap water. **Right:** Reconstruction based on counting how many times a monotonicity test succeeds for increasing β-values.

3.3 Conclusions/discussion

From the comparison of the linear and non-linear monotonicity method it is no surprise that they give similar results when no noise is added, due to (3.4) and (3.5) where it is seen that the Fréchet derivative can be used to determine the singularities of γ. It is however a bit surprising that the linear and non-linear method performs equally well for noisy data, especially in light of the resolution guarantees found in [33] that are much more pessimistic for the linear approach. It should however be noted that the estimates found in [33] are not shown to be optimal and are also based on the CEM and not the CM. It is very useful that there is not much difference in using the non-linear and linear approach since, in other geometries than the unit disk, the non-linear method is far more computationally demanding: the non-linear method requires an evaluation of the ND map for each ball that is used in the monotonicity tests. If the ND map is approximated using N current patterns, it is required to solve N linear systems of equations from the FEM discretization of (1.3) for each ball that is tested, which depending on resolution and dimension may be several hundreds to several thousands of monotonicity tests. However, for the linear approach it is only needed to solve N such systems once, as solutions to (1.3) are used for both $\mathcal{R}(\gamma_0)$ and $\mathcal{R}'(\gamma_0)$. Therefore, the linear monotonicity method is amongst the fastest reconstruction methods in EIT, and compared to an iterative gradient-based reconstruction method, the computational complexity is equivalent to one iteration with one evaluation of the forward map and its derivative. Furthermore, it is often possible to evaluate $\mathcal{R}(\gamma_0)$ and $\mathcal{R}'(\gamma_0)$ beforehand, and reuse them for several reconstructions, in which case it is possible to perform real-time reconstructions in 3D on a regular laptop. The method is, however, less noise robust (similar to other direct reconstruction methods) than for instance the sparsity-based method in Part III, and is especially sensitive with regards to inaccuracies in the background conductivity [33].

In terms of efficient implementation, if the linearisation is evaluated with respect to the test balls so each column in the matrix representation is the linearisation on a ball, then the matrix for the Fréchet derivative can be split into smaller parts; one part for each core on the computer system. In that way the reconstruction can be run in parallel as the monotonicity tests are completely independent of one another, and it is also a way to run the method on systems without enough memory to hold the full linearisation.

While it was speculated in [32, 33] that it is possible to regularize and use the CEM with the monotonicity method, it was not proved that a uniform regularization parameter could be used nor that the reconstructions would converge as noise and approximation errors decayed. This is the contribution from Paper B,

and is one of few proven convergence results for reconstruction methods using the CEM, which makes it thematically comparable to what was done with the factorization method in [53]. It is expected that other direct reconstruction methods can be extended to use the CEM, with convergence theory based on the estimates in Theorem 3.5.

In [32] it was outlined how to prove the monotonicity method for the CM based on partial data, in particular with local data. The proof of Theorems 3.3 and 3.4 can straightforwardly be adapted to use the partial ND map by changing the estimates (3.6) and (3.7) accordingly, to estimates on $L^2_\diamond(\Gamma)$ for a subset $\Gamma \subset \partial\Omega$. The author has not performed any numerical tests with the monotonicity method for partial data, and it is subject to future research.

Part III

Sparsity-based reconstruction

Chapter 4

Sparse reconstruction from local Cauchy data

This chapter outlines the work in Papers D and E on sparsity-based reconstruction using the CM in 2D and 3D, where it is assumed that measurements are only taken on a part of the boundary. The work is based on [44, 43] that applied ℓ_1-sparsity based reconstruction to EIT with full boundary data for the CM, that was later adapted to the CEM in [23, 24].

Furthermore, a spatially varying regularization parameter is used in Papers D and E to be able to apply prior information about the location of inhomogeneities directly into the algorithm. Additional unpublished results will also be shown for depth-weighted regularization using the theory from Part I, and apply it to real measurements.

4.1 Sparse reconstruction in EIT

Here we reconstruct, or approximate, a perturbation $\delta\gamma$ (and not only its support as in the monotonicity method), from a known background conductivity γ_0, i.e. γ is on the form

$$\gamma = \gamma_0 + \delta\gamma.$$

For a fixed $c \in (0,1)$ we assume that $\gamma_0 \in H^1(\Omega)$ with $c \leq \gamma_0 \leq c^{-1}$, and furthermore that the perturbation $\delta\gamma$ is in the following convex set

$$\mathcal{A}_0 \equiv \left\{\delta\sigma \in H_0^1(\Omega) : c \leq \gamma_0 + \delta\sigma \leq c^{-1} \text{ a.e. in } \Omega\right\}.$$

We use K real-valued current patterns for partial data measurements, meaning Cauchy data taken on subsets Γ^{D} and Γ^{N} (see Section 1.1.3 for details), given by

$$\left\{(g_k, f_k) : g_k \in H_\diamond^{-1/2}(\partial\Omega),\ \operatorname{supp} g_k \subseteq \Gamma^{\mathrm{N}},\ f_k = (\mathcal{R}(\gamma)g_k)|_{\Gamma^{\mathrm{D}}}\right\}_{k=1}^{K}.$$

The sparse reconstruction of $\delta\gamma$ is formulated in terms of an optimization problem, to minimize the following Tikhonov functional on $\mathcal{A}_0$:

$$\Psi(\delta\sigma) \equiv \sum_{k=1}^{K} J_k(\delta\sigma) + P(\delta\sigma),\ \ \delta\sigma \in \mathcal{A}_0, \tag{4.1}$$

with

$$J_k(\delta\sigma) \equiv \frac{1}{2}\|\mathcal{R}(\gamma_0 + \delta\sigma)g_k - f_k\|^2_{L^2(\Gamma^{\mathrm{D}})}, \quad P(\delta\sigma) \equiv \sum_{j=1}^{\infty} \alpha_j |\langle \delta\sigma, \psi_j\rangle_{H^1(\Omega)}|,$$

where $\alpha_j > 0$ is the regularization parameter and $\{\psi_j\}_{j=1}^{\infty}$ is an orthonormal basis for $H_0^1(\Omega)$, chosen such that $\delta\gamma$ is sparse in that basis i.e. well approximated by only few basis functions. Ideally, the basis is chosen such that there exists a finite index set $\mathcal{I} \subset \mathbb{N}$ such that

$$\delta\gamma = \sum_{j\in\mathcal{I}} \langle \delta\gamma, \psi_j\rangle_{H^1(\Omega)}\psi_j.$$

Prior information about the sparsity of $\delta\gamma$ can be directly included in the algorithm by choosing α_j significantly lower for the basis functions that are expected to be in the expansion of $\delta\gamma$. In that way the basis coefficients that are expected to be non-zero are penalized less in the optimization problem, and are allowed to attain larger values, cf. Figure 4.1.

A local optimum of the optimization problem $\operatorname{argmin}_{\delta\sigma\in\mathcal{A}_0} \Psi(\delta\sigma)$ can be obtained by use of the soft thresholding map with threshold $\beta > 0$

$$\mathcal{S}_\beta(x) \equiv \operatorname{sgn}(x)\max\{|x| - \beta, 0\},\ \ x \in \mathbb{R},$$

by iteratively evaluating (cf. [12, 13, 44, 43, 22])

$$\delta\gamma_{i+1} \equiv P_{\mathcal{A}_0}\left(\sum_{j=1}^{\infty} \mathcal{S}_{s_i\alpha_j}(\langle \delta\gamma_i - s_i G(\delta\gamma_i), \psi_j\rangle_{H^1(\Omega)})\psi_j\right), \tag{4.2}$$

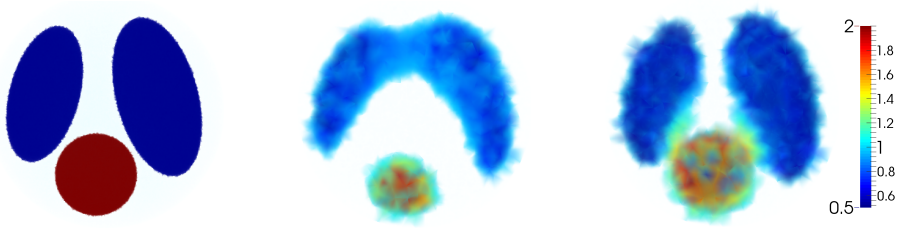

(a) (b) (c)

Figure 4.1: 3D sparsity-based reconstruction in the unit ball, using noisy simulated data from 35 current patterns given by spherical harmonics and $\gamma_0 = 1$. The plots show volumetric representations of the reconstructions **(a):** Numerical phantom. **(b):** Reconstruction from full boundary data. **(c):** Reconstruction from full boundary data assuming the support of $\delta\gamma$ is given on a 10% dilation of the true support.

where $P_{\mathcal{A}_0}$ is a projection of $H_0^1(\Omega)$ onto $\mathcal{A}_0$, s_i is a step length parameter for the i'th iterate, and $G(\delta\gamma_i)$ is a gradient of $J \equiv \sum_{j=1}^{K} J_k$ evaluated at the i'th iterate. The method is initialized with $\delta\gamma_0 \equiv 0$ and a Barzilai-Borwein step size estimate [9] is used to evaluate s_i.

Define the map $F_g : \delta\sigma \mapsto u$, where u is the solution to (1.3) with Neumann condition g and conductivity $\gamma_0 + \delta\sigma$, then the Fréchet derivative $J'(\delta\sigma)$ can be identified with a function, which we denote by the same symbol, given by

$$J'(\delta\sigma) = -\sum_{k=1}^{K} \nabla F_{g_k}(\delta\sigma) \cdot \nabla F_{\chi_{\Gamma^D}(\mathcal{R}(\gamma_0+\delta\sigma)g_k - f_k)}(\delta\sigma).$$

In 2D it is necessary to assume that the current patterns satisfy $g \in L^p(\partial\Omega) \cap H_\diamond^{-1/2}(\partial\Omega)$ for some $p > 1$ to have the Fréchet derivative in terms of $H_0^1(\Omega)$. In 3D we need $p \geq \frac{8}{5}$ and furthermore that c in $\mathcal{A}_0$ is sufficiently close to 1, meaning that the perturbation $\delta\gamma$ cannot be too large. The gradient G used in (4.2) is the $H_0^1(\Omega)$-function that through Riesz' representation theorem gives $J'(\delta\sigma)$ by

$$J'(\delta\sigma)\eta = \langle G(\delta\sigma), \eta \rangle_{H^1(\Omega)}, \quad \eta \in H_0^1(\Omega),$$

which in practice corresponds to the solution of the homogeneous Dirichlet problem

$$(-\Delta + 1)v = J'(\delta\sigma) \text{ in } \Omega, \quad v|_{\partial\Omega} = 0 \text{ on } \partial\Omega. \tag{4.3}$$

So for each iteration it is required to solve $K + 1$ elliptic PDEs to obtain the gradient G (and possibly additional evaluations when determining the step size),

where in the first K it is possible to reuse the factorization of the FEM system matrix as only the boundary conditions change, and the last problem (4.3) remains unchanged throughout the iterations.

4.1.1 Reconstructions

All reconstructions considered in Papers D and E are for local data

$$\Gamma = \Gamma^{\mathrm{D}} = \Gamma^{\mathrm{N}}.$$

Similar to what is done in [43, 23], a FEM basis $\{\psi_j\}_{j=1}^N$ for piecewise affine elements is used, which is a bit heuristic as it is not orthonormal in terms of the $H^1(\Omega)$-inner product. The corresponding functional becomes

$$\Psi(\delta\sigma) \equiv \frac{1}{2}\sum_{k=1}^{K}\|\mathcal{R}(\gamma_0+\delta\sigma)g_k - f_k\|^2_{L^2(\Gamma)} + \sum_{j=1}^{N}\alpha_j|\delta\sigma(x_j)|, \tag{4.4}$$

where $\{x_j\}_{j=1}^N$ are the mesh nodes in the FEM mesh used for reconstruction, and $\{\delta\sigma(x_j)\}_{j=1}^N$ are the corresponding basis coefficients for $\delta\sigma$.

It is evident from (4.4) that including prior information via the regularization parameter α_j corresponds to knowledge about the support of perturbation $\delta\gamma$. Such information can, for instance, be found using the monotonicity method (see Part II) during the first iteration where the ND map and its derivative at γ_0 is evaluated. Thereby, the spatially varying regularization can be performed at almost no additional computational cost.

The regularization parameter is chosen as

$$\alpha_j \equiv \alpha\beta_j\mu_j,$$

where α corresponds to a general regularization parameter, that is chosen from assumptions on the general sparsity of $\delta\gamma$, and is not related to prior information on the location of $\delta\gamma$. The μ_j-values correspond to the prior information on the location of $\delta\gamma$ as they are chosen as 1 where no prior information is given, and as a smaller scalar (in the numerical examples as 10^{-2}) where the support of $\delta\gamma$ is assumed. The β_j-values are chosen such that the penalty term approximates a weighted L^1-norm

$$\alpha\int_\Omega \mu(x)|\delta\sigma(x)|\,dx \simeq \alpha\sum_{j=1}^{N}\beta_j\mu_j|\delta\sigma(x_j)|, \tag{4.5}$$

where $\mu(x_j) = \mu_j$. This makes it possible to choose α independently of how fine the FEM discretization is. Partial data examples for noisy simulated test problems are shown in Figure 4.2, where it is possible to reasonably reconstruct close to the measurement boundary, and the reconstruction is much improved when using prior knowledge about the location of the inclusions (if they are close enough to the measurement boundary).

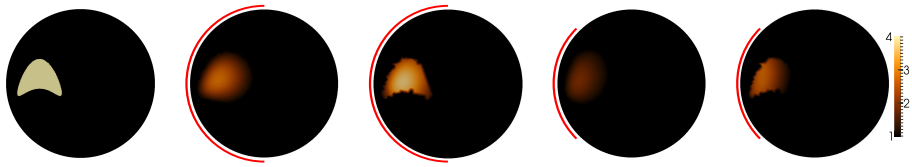

Figure 4.2: 2D sparsity-based reconstruction using noisy simulated partial data from 10 trigonometric current patterns and $\gamma_0 = 1$. **(a):** Numerical phantom. **(b):** Reconstruction from partial data on half of the boundary. **(c):** Reconstruction from partial data on half of the boundary, assuming the support of $\delta\gamma$ is given on a 10% dilation of the true support. **(d):** Reconstruction from partial data on a quarter of the boundary. **(e):** Reconstruction from partial data on a quarter of the boundary, assuming the support of $\delta\gamma$ is given on a 10% dilation of the true support.

4.2 Depth-weighted regularization

From the bounds in Part I there is an inherent depth dependence in the ND-map. This means that there is a depth dependence in the discrepancy terms J_k in (4.4), however we have not taken this into consideration in the penalty term P. The idea of the regularization parameter is to balance the discrepancy and the regularization term. This implies that if we use a fixed regularization parameter $\alpha_j = \alpha$, for all the coefficients, then the regularization is actually not uniformly distributed on the domain due to the depth dependence in the problem. The approximation that is found from the iterative method can therefore be affected by having shape and positioning errors, see e.g. Figure 4.3.

Instead, similar to (4.5), we define $\alpha_j \equiv \alpha\beta_j w_j$ such that it approximates a weighted L^1-norm for a positive and continuous weight function satisfying

$w(x_j) = w_j$

$$\alpha \int_\Omega w(x)|\delta\sigma(x)|\,dx \simeq \alpha \sum_{j=1}^{N} \beta_j w_j |\delta\sigma(x_j)|.$$

Here $w(x)$ is not used to include prior information, but is instead a depth-dependent weight function only depending on Ω. In light of (2.8), where $\lim_{r\to 0} \rho = |C|$, and that it is possible to obtain conditional Lipschitz stability for piecewise constant conductivities [6], we choose the following weight function as a kind of pointwise estimate on the change in distinguishability

$$w(x) \equiv \sqrt{\frac{1+|x|^2}{1-|x|^2}}, \quad x \in \mathbb{D}. \tag{4.6}$$

It is noteworthy that (2.8) is given in terms of DN-maps. Using that estimate is partially justified in the sense that one can obtain estimates in terms of ND-maps using the following identity

$$\Lambda(\gamma_1) - \Lambda(\gamma_2) = \Lambda(\gamma_1)\left(\mathcal{R}(\gamma_2) - \mathcal{R}(\gamma_1)\right)\Lambda(\gamma_2).$$

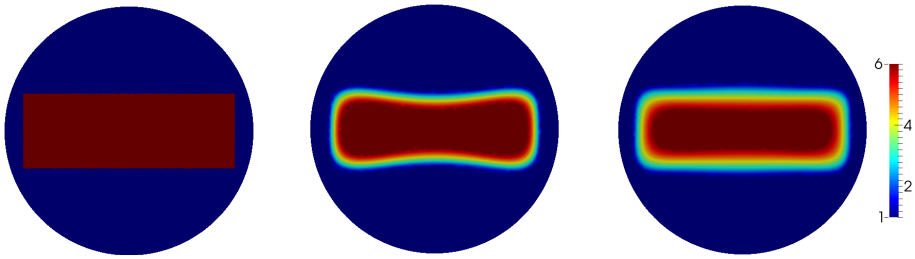

Figure 4.3: 2D sparsity-based reconstruction using noiseless simulated data from 10 trigonometric current patterns and $\gamma_0 = 1$. **(a):** Numerical phantom. **(b):** Reconstruction without using depth-weighted regularization. **(c):** Reconstruction using depth-weighted regularization.

4.2.1 Reconstructions using the CEM

Sparse reconstruction is now considered for the CEM, where both perturbation $\delta\gamma$ and the contact impedances z are estimated. The contact impedances are of no real interest, however it turns out that simultaneous estimation of both $\delta\gamma$

and z yields better reconstructions compared to using a fixed z estimated from the measurements. The corresponding functional for the optimization problem, using K current-voltage measurements $\{(I^k, V^k)\}_{k=1}^K$, is then

$$\Psi^{\mathrm{CEM}}(\delta\sigma, z) \equiv \frac{1}{2}\sum_{k=1}^{K}\|R(\gamma_0 + \delta\sigma, z)I^k - V^k\|_2^2 + \alpha\sum_{j=1}\beta_j w_j|\delta\sigma(x_j)|.$$

The solution of the optimization problem is analogous to (4.2). The only change is in the derivative J' where the maps F are given in terms of the CEM (1.4)-(1.7). If we denote by J^{CEM} the discrepancy term

$$J^{\mathrm{CEM}}(\delta\sigma) \equiv \frac{1}{2}\sum_{k=1}^{K}\|R(\gamma_0 + \delta\sigma, z)I^k - V^k\|_2^2,$$

and by $F_I : \delta\sigma \mapsto v$ the solution to (1.4)-(1.7) with current pattern I and conductivity $\gamma = \gamma_0 + \delta\sigma$, then

$$(J^{\mathrm{CEM}})'(\delta\sigma) = -\sum_{k=1}^{K}\nabla F_{I^k}(\delta\sigma)\cdot\nabla F_{R(\gamma_0+\delta\sigma,z)I^k - V^k}(\delta\sigma),$$

see also [44, 23] for more details. In terms of the contact impedances the optimization is a plain projected steepest descend, where we only assume that $z_j \geq c_z$ for a fixed scalar $c_z > 0$ (in the examples chosen as 10^{-10}).

Due to the estimates in Theorem 3.5 we expect that depth dependence of the CM is also observed for the CEM, at least if there are sufficiently many electrodes. Therefore the weight function (4.6) is used here.

The numerical examples in Figure 4.4 are done using real measurements from the KIT4 device at the University of Eastern Finland in Kuopio, Finland (the same equipment used for real measurements in Paper B). The geometry is a cylindrical tank filled with tap water. The tank has a radius of 14.0 cm and is equipped with 16 equidistantly placed electrodes of width 2.5 cm and height 7.0 cm. The measurement setup is essentially 2D, and the optimization problem is also solved in 2D by dividing the currents by the height of the electrodes. The measurements consist of 60 current patterns; four sets of 15 linearly independent current patterns where each set is enough to construct the measurement map $R(\gamma)$. All of the redundant measurements are used in the reconstruction as they may be influenced by measurement noise and calibration errors.

The background conductivity and initial contact impedances are estimated from a measurement with the tank only filled with water, where contact impedances and a constant conductivity are fitted to the data using a least squares fit.

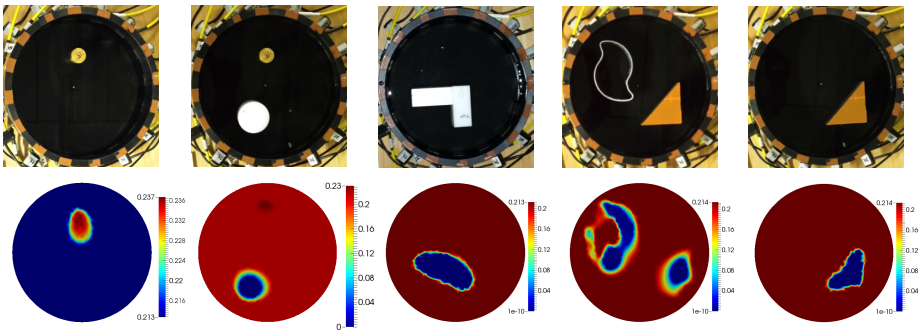

Figure 4.4: 2D sparsity-based reconstruction with depth-weighted regularization using the CEM with 16 equidistant electrodes and 60 current patterns. The measurement equipment is the KIT4 measurement device from the University of Eastern Finland. **Top:** Measurement setup with various metal and plastic objects submerged in water. **Bottom:** Reconstructions.

4.3 Conclusions/discussion

The sparsity reconstruction is reasonably noise robust and generally able to attain a high contrast and relatively high resolution (in terms of EIT), in particular when using full boundary data with either CM or CEM. In all the 2D examples in Paper D we only used 10 current patterns which is quite low. Compared to the monotonicity reconstructions in Paper C where 32 current patterns are used, the reconstruction with the sparsity assumption is still more noise robust. While most of the noise robustness is from the choice of regularization, there is also something to be gained from how the data is represented. For simplicity consider the full boundary problem $\Gamma^{\mathrm{N}} = \Gamma^{\mathrm{D}} = \partial\Omega$, then the data in the sparse reconstruction is

$$\left\{(g_k, f_k) : g_k \in H_\diamond^{-1/2}(\partial\Omega), \;\; f_k = \mathcal{R}(\gamma) g_k\right\}_{k=1}^{K},$$

which for an orthonormal set of current patterns is the graph of the operator

$$\mathcal{R}(\gamma) P_K, \tag{4.7}$$

where P_K is the orthogonal projection onto $\operatorname{span}\{g_k\}_{k=1}^K$. For many direct methods, including the monotonicity method, it is not possible to directly use the graph but instead requires some finite dimensional matrix representation $A \equiv \{\langle \mathcal{R}(\gamma) g_m, g_n \rangle\}_{n,m=1,\dots K}$. Such a matrix is a representation of the operator

$$P_K \mathcal{R}(\gamma) P_K. \tag{4.8}$$

So by simply using different representations of the measured data, which in the infinite dimensional case are equivalent, there is a discrepancy where in (4.7) all the measured data is used while in (4.8) parts of the voltage measurements are *thrown away* in the need to use a matrix representation. For the CEM which is already finite dimensional there is no difference between the two representations, however using the graph still gives the flexibility to use redundant measurements which is very useful in practice.

In terms of how fast it is possible to get a reconstruction the sparse reconstruction usually requires in the magnitude of 50 iterations to converge, and less if additional prior information about the location of the perturbation is included. The method's main computational burden lies in evaluating the forward problem, which involves solving several elliptic PDEs. Solving a linear system of size $N \times N$ requires $O(N^3)$ floating point operations, therefore the method is affected by the *curse of dimensionality* in which 3D reconstructions takes significantly longer than 2D reconstruction because of the much larger FEM system matrix required for a 3D domain. The linear monotonicity method, however, is much less affected by the dimension of the domain, and can therefore be quite useful for obtaining information about the location of the perturbation $\delta\gamma$ to speed up the 3D reconstructions in the sparsity-based method. Further studies on this topic is reserved for future research.

For the depth-weighted regularization a similar approach has been used in [69], where the depth-weighting is done indirectly by changing the mesh discretization to have larger elements near the centre of the domain. It is in this author's opinion that the weighting should be done through the regularization parameter, if possible, since changing the FEM discretization to be less fine in certain areas of the domain can affect the precision in the evaluation of the forward problem. Having a precise solution to the forward problem is essential to obtain a reasonable resolution with iterative methods in EIT (and for inverse problems in general).

Finally, some observations for the general sparse reconstruction method:

(i) The reason that $H_0^1(\Omega)$-regularity is used for $\delta\gamma$, rather than just $L^2(\Omega)$ with a penalty term on the coefficients $\langle \delta\gamma, \psi_j \rangle_{L^2(\Omega)}$, is that the derivative $J'(\delta\sigma)$ of the discrepancy terms is not guaranteed to be in $L^2(\Omega)$. In 2D the derivative is in $L^p(\Omega)$ for some $p > 1$ and in 3D it is in $L^{6/5}(\Omega)$, which in both cases by Sobolev embedding theorems [2] implies that $J'(\delta\sigma)$ is in $H^{-1}(\Omega)$, the dual space of $H_0^1(\Omega)$. Most of the assumptions in the method are related to the existence of a derivative for the corresponding spaces used.

(ii) When using partial data in the sparsity reconstruction it is still assumed

that the boundary shape $\partial\Omega$ is known. In practical measurements, for instance with lung imaging, it is not guaranteed that the boundary shape is known, and it may lead to severe modelling errors that propagate through the solution. There are methods that simultaneously estimate the boundary shape and reconstruct the conductivity (e.g. [21]) which maybe can be adapted to sparse reconstruction.

Bibliography

[1] A. Abubakar, T. M. Habashy, M. Li, and J. Liu, *Inversion algorithms for large-scale geophysical electromagnetic measurements*, Inverse Problems, 25 (2009), p. 123012.

[2] R. A. Adams and J. J. F. Fournier, *Sobolev spaces*, vol. 140 of Pure and Applied Mathematics (Amsterdam), Elsevier/Academic Press, Amsterdam, second ed., 2003.

[3] I. Akduman and R. Kress, *Electrostatic imaging via conformal mapping*, Inverse Problems, 18 (2002), pp. 1659–1672.

[4] G. Alessandrini, *Stable determination of conductivity by boundary measurements*, Applicable Analysis, 27 (1988), pp. 153–172.

[5] ——, *Singular solutions of elliptic equations and the determination of conductivity by boundary measurements*, Journal of Differential Equations, 84 (1990), pp. 252–273.

[6] G. Alessandrini and S. Vessella, *Lipschitz stability for the inverse conductivity problem*, Advances in Applied Mathematics, 35 (2005), pp. 207–241.

[7] K. Astala and L. Päivärinta, *Calderón's inverse conductivity problem in the plane*, Annals of Mathematics, 163 (2006), pp. 265–299.

[8] K. Astala, L. Päivärinta, and M. Lassas, *Calderón's inverse problem for anisotropic conductivity in the plane*, Comm. Partial Differential Equations, 30 (2005), pp. 207–224.

[9] J. Barzilai and J. M. Borwein, *Two-point step size gradient methods*, IMA Journal of Numerical Analysis, 8 (1988), p. 141.

[10] L. Borcea, *Electrical impedance tomography*, Inverse Problems, 18 (2002), pp. 99–136.

[11] A. Borsic, B. Graham, A. Adler, and W. Lionheart, *In vivo impedance imaging with total variation regularization*, IEEE Transactions on Medical Imaging, 29 (2010), pp. 44–54.

[12] K. Bredies and D. A. Lorenz, *Iterated hard shrinkage for minimization problems with sparsity constraints*, SIAM Journal on Scientific Computing, 30 (2006), pp. 657–683.

[13] K. Bredies, D. A. Lorenz, and P. Maass, *A generalized conditional gradient method and its connection to an iterative shrinkage method*, Computational Optimization and Applications, 42 (2007), pp. 173–193.

[14] M. Brühl, *Explicit characterization of inclusions in electrical impedance tomography*, SIAM Journal on Mathematical Analysis, 32 (2001), pp. 1327–1341.

[15] M. Brühl and M. Hanke, *Numerical implementation of two non-iterative methods for locating inclusions by impedance tomography*, Inverse Problems, 16 (2000), pp. 1029–1042.

[16] A. L. Bukhgeim and G. Uhlmann, *Recovering a potential from partial Cauchy data*, Communications in Partial Differential Equations, 27 (2002), pp. 653–668.

[17] A.-P. Calderón, *On an inverse boundary value problem*, in Seminar on Numerical Analysis and its Applications to Continuum Physics (Rio de Janeiro, 1980), Soc. Brasil. Mat., Rio de Janeiro, 1980, pp. 65–73.

[18] M. Cheney and D. Isaacson, *Distinguishability in impedance imaging*, IEEE Transactions on Biomedical Engineering, 39 (1992), pp. 852–860.

[19] M. Cheney, D. Isaacson, and J. C. Newell, *Electrical impedance tomography*, SIAM Review, 41 (1999), pp. 85–101.

[20] H. Cornean, K. Knudsen, and S. Siltanen, *Towards a d-bar reconstruction method for three-dimensional* EIT , Journal of Inverse and Ill-Posed Problems, 14 (2006), pp. 111–134.

[21] J. Dardé, N. Hyvönen, A. Seppänen, and S. Staboulis, *Simultaneous reconstruction of outer boundary shape and admittivity distribution in electrical impedance tomography*, SIAM J. Imaging Sci., 6 (2013), pp. 176–198.

[22] I. Daubechies, M. Defrise, and C. De Mol, *An iterative thresholding algorithm for linear inverse problems with a sparsity constraint*, Communications on pure and applied mathematics, 57 (2004), pp. 1413–1457.

[23] M. Gehre, T. Kluth, A. Lipponen, B. Jin, A. Seppänen, J. P. Kaipio, and P. Maass, *Sparsity reconstruction in electrical impedance tomography: an experimental evaluation*, Journal of Computational and Applied Mathematics, 236 (2012), pp. 2126–2136.

[24] M. Gehre, T. Kluth, C. Sebu, and P. Maass, *Sparse 3D reconstructions in electrical impedance tomography using real data*, Inverse Probl. Sci. Eng., 22 (2014), pp. 31–44.

[25] B. Haberman and D. Tataru, *Uniqueness in Calderón's problem with Lipschitz conductivities*, Duke Math. J., 162 (2013), pp. 497–516.

[26] S. J. Hamilton, A. Hauptmann, and S. Siltanen, *A data-driven edge-preserving d-bar method for electrical impedance tomography*, Inverse Problems and Imaging, 8 (2014), pp. 1053–1072.

[27] M. Hanke and M. Brühl, *Recent progress in electrical impedance tomography*, Inverse Problems, 19 (2003), pp. S65–S90. Special section on imaging.

[28] M. Hanke, L. Harhanen, N. Hyvönen, and E. Schweickert, *Convex source support in three dimensions*, BIT Numerical Mathematics, 52 (2011), pp. 45–63.

[29] M. Hanke, N. Hyvönen, and S. Reusswig, *Convex source support and its application to electric impedance tomography*, SIAM J. Imaging Sci., 1 (2008), pp. 364–378.

[30] L. Harhanen, N. Hyvönen, H. Majander, and S. Staboulis, *Edge-enhancing reconstruction algorithm for three-dimensional electrical impedance tomography*, SIAM J. Sci. Comput., 37 (2015), pp. B60–B78.

[31] B. Harrach and J. K. Seo, *Exact shape-reconstruction by one-step linearization in electrical impedance tomography*, SIAM Journal on Mathematical Analysis, 42 (2010), pp. 1505–1518.

[32] B. Harrach and M. Ullrich, *Monotonicity-based shape reconstruction in electrical impedance tomography*, SIAM Journal on Mathematical Analysis, 45 (2013), pp. 3382–3403.

[33] ——, *Resolution guarantees in electrical impedance tomography*, IEEE Transactions on Medical Imaging, 34 (2015), pp. 1513–1521.

[34] H. Heck and J.-N. Wang, *Stability estimates for the inverse boundary value problem by partial cauchy data*, Inverse Problems, 22 (2006), pp. 1787–1796.

[35] D. S. Holder, ed., *Electrical impedance tomography; methods, history, and applications*, IOP publishing Ltd., 2005.

[36] N. Hyvönen, *Approximating idealized boundary data of electric impedance tomography by electrode measurements.*, Mathematical Models and Methods in Applied Sciences, 19 (2009), pp. 1185–1202.

[37] M. Ikehata, *How to draw a picture of an unknown inclusion from boundary measurements. Two mathematical inversion algorithms*, Journal of Inverse and Ill-Posed Problems, 7 (1999), pp. 255–271.

[38] ——, *Reconstruction of the support function for inclusion from boundary measurements*, Journal of Inverse and Ill-Posed Problems, 8 (2000), pp. 367–378.

[39] M. Ikehata and S. Siltanen, *Numerical method for finding the convex hull of an inclusion in conductivity from boundary measurements*, Inverse Problems, 16 (2000), pp. 1043–1052.

[40] O.Y. Imanuvilov, G. Uhlmann, and M. Yamamoto, *The Calderón problem with partial data in two dimensions*, American Mathematical Society, 23 (2010), pp. 655–691.

[41] D. Isaacson, *Distinguishability of conductivities by electric current computed tomography*, IEEE Transactions on Medical Imaging, 5 (1986), pp. 91–95.

[42] V. Isakov, *On uniqueness in the inverse conductivity problem with local data*, Inverse Problems and Imaging, 1 (2007), pp. 95–105.

[43] B. Jin, T. Khan, and P. Maass, *A reconstruction algorithm for electrical impedance tomography based on sparsity regularization*, Internat. J. Numer. Methods Engrg., 89 (2012), pp. 337–353.

[44] B. Jin and P. Maass, *An analysis of electrical impedance tomography with applications to Tikhonov regularization*, ESAIM: Control, Optimisation and Calculus of Variations, 18 (2012), pp. 1027–1048.

[45] K. Karhunen, A. Seppänen, A. Lehikoinen, J. Blunt, J. P. Kaipio, and P. J. M. Monteiro, *Electrical resistance tomography for assessment of cracks in concrete*, Materials Journal, 107 (2010), pp. 523–531.

[46] K. Karhunen, A. Seppänen, A. Lehikoinen, P. J. M. Monteiro, and J. P. Kaipio, *Electrical resistance tomography imaging of concrete*, Cement and Concrete Research, 40 (2010), pp. 137–145.

[47] C. E. Kenig, J. Sjöstrand, and G. Uhlmann, *The Calderón problem with partial data*, Annals of Mathematics, 165 (2007), pp. 567–591.

[48] K. Knudsen, *The Calderón problem with partial data for less smooth conductivities*, Communications in Partial Differential Equations, 31 (2006), pp. 57–71.

[49] K. Knudsen, M. Lassas, J. L. Mueller, and S. Siltanen, *D-bar method for electrical impedance tomography with discontinuous conductivities*, SIAM Journal on Applied Mathematics, 67 (2007), p. 893.

[50] K. Knudsen, M. Lassas, J. L. Mueller, and S. Siltanen, *Regularized D-bar method for the inverse conductivity problem*, Inverse Problems and Imaging, 3 (2009), pp. 599–624.

[51] R. Kress, *Conformal mapping and impedance tomography*, J. Phys.: Conf. Ser., 290 (2011), p. 012009.

[52] ——, *Inverse problems and conformal mapping*, Complex Variables and Elliptic Equations, 57 (2012), pp. 301–316.

[53] A. Lechleiter, N. Hyvönen, and H. Hakula, *The factorization method applied to the complete electrode model of impedance tomography*, SIAM Journal on Applied Mathematics, 68 (2008), pp. 1097–1121.

[54] A. Logg, K.-A. Mardal, and G. N. Wells, *Automated solution of differential equations by the finite element method*, vol. 84 of Lecture Notes in Computational Science and Engineering, Springer, Heidelberg, 2012. The FEniCS book.

[55] N. Mandache, *Exponential instability in an inverse problem for the Schrödinger equation*, Inverse Problems, 17 (2001), pp. 1435–1444.

[56] J. J. Manfredi and V. Vespri, *n-harmonic morphisms in space are Möbius transformations.*, The Michigan Mathematical Journal, 41 (1994), pp. 135–142.

[57] A. I. Nachman, *Reconstructions from boundary measurements*, Annals of Mathematics, 128 (1988), pp. 531–576.

[58] ——, *Global uniqueness for a two-dimensional inverse boundary value problem*, Annals of Mathematics, 143 (1996), pp. 71–96.

[59] R. G. Novikov, *A multidimensional inverse spectral problem for the equation* $-\delta\psi + (v(x) - eu(x))\psi = 0$, Functional Analysis and Its Applications, 22 (1988), pp. 263–272.

[60] M. Reed and B. Simon, *Methods of modern mathematical physics. IV. Analysis of operators*, Academic Press [Harcourt Brace Jovanovich, Publishers], New York-London, 1978.

[61] B. Saka and A. Yilmaz, *Elliptic cylinder geometry for distinguishability analysis in impedance tomography*, IEEE Transactions on Biomedical Engineering, 51 (2004), pp. 126–132.

[62] S. Siltanen, J. L. Mueller, and D. Isaacson, *An implementation of the reconstruction algorithm of A. Nachman for the 2-D inverse conductivity problem*, Inverse Problems, 16 (2000), pp. 681–699.

[63] E. Somersalo, M. Cheney, and D. Isaacson, *Existence and uniqueness for electrode models for electric current computed tomography*, SIAM Journal on Applied Mathematics, 52 (1992), pp. 1023–1040.

[64] J. Sylvester and G. Uhlmann, *A global uniqueness theorem for an inverse boundary value problem*, Annals of Mathematics, 125 (1987), pp. 153–169.

[65] A. Tamburrino, *Monotonicity based imaging methods for elliptic and parabolic inverse problems*, Journal of Inverse and Ill-posed Problems, 14 (2006), pp. 633–642.

[66] A. Tamburrino and G. Rubinacci, *A new non-iterative inversion method for electrical resistance tomography*, Inverse Problems, 18 (2002), p. 1809.

[67] G. Uhlmann, *Electrical impedance tomography and Calderón's problem*, Inverse Problems, 25 (2009), p. 123011.

[68] M. Vauhkonen, D. Vadász, P. A. Karjalainen, E. Somersalo, and J. P. Kaipio, *Tikhonov regularization and prior information in electrical impedance tomography*, IEEE Transactions on Medical Imaging, 17 (1998), pp. 285–293.

[69] R. Winkler and A. Rieder, *Resolution-controlled conductivity discretization in electrical impedance tomography*, SIAM J. Imaging Sci., 7 (2014), pp. 2048–2077.

[70] R. Winkler and A. Rieder, *Model-aware newton-type inversion scheme for electrical impedance tomography*, Inverse Problems, 31 (2015), p. 045009.

[71] T. York, *Status of electrical tomography in industrial applications*, Journal of Electronic Imaging, 10 (2001), pp. 608–619.

[72] G. Zhang, *Uniqueness in the calderón problem with partial data for less smooth conductivities*, Inverse Problems, 28 (2012), p. 105008.

Part IV

Journal papers and conference proceedings

PAPER A

Depth dependent bounds on distinguishability of inclusions in electrical impedance tomography

Type	Submitted manuscript (2016)
Authors	Henrik Garde and Kim Knudsen
Available from	`http://arxiv.org/abs/1602.03785`

DEPTH DEPENDENT BOUNDS ON DISTINGUISHABILITY OF INCLUSIONS IN ELECTRICAL IMPEDANCE TOMOGRAPHY*

HENRIK GARDE† AND KIM KNUDSEN†

Abstract. The inverse problem of electrical impedance tomography is highly ill-posed, and it is often observed that inclusions far from the boundary are difficult to reconstruct. This paper provides rigorous results supporting the intuition. Indeed, lower and upper bounds on the distinguishability of an inclusion are derived in terms of the data. These bounds depend explicitly on the distance of the inclusion to the boundary, i.e. the depth of the inclusion. The results are obtained for inclusions in a homogeneous background in the unit disk. This corresponds to determining bounds on eigenvalues for difference operators of Dirichlet-to-Neumann maps corresponding to the case of a known homogeneous background and the case where there is an inclusion perturbation to this background. The theoretical bounds are verified numerically using an exact characterization of the forward map as a tridiagonal matrix depending explicitly on the size and location of the inclusion.

Key words. electrical impedance tomography, depth dependence, harmonic morphism, eigenvalue bounds, distinguishability

AMS subject classifications. 35P15, 35R30, 35R05

1. Introduction. The goal of electrical impedance tomography (EIT) is to reconstruct the internal electrical conductivity of an object. This is done from voltage-current boundary measurements through electrodes on the surface. The forward problem of EIT is, given the real-valued conductivity γ, to solve the *conductivity equation*

$$\nabla \cdot (\gamma \nabla u) = 0, \text{ in } \Omega, \tag{1.1}$$

where u models the interior electric potential and $\Omega \subset \mathbb{R}^d$ is a bounded Lipschitz domain for $d \geq 2$ modelling the physical object. Depending on the choice of boundary conditions various models for EIT arise. The simplest model is Calderón's original formulation of the *continuum model* [6] that given a boundary potential $f \in H^{1/2}(\partial\Omega)$ makes use of a Dirichlet boundary condition

$$u|_{\partial\Omega} = f \text{ on } \partial\Omega,$$

where $u|_{\partial\Omega}$ denotes the trace of u. If

$$\gamma \in L^\infty_+(\Omega) \equiv \{w \in L^\infty(\Omega) : \operatorname{ess\,inf} w > 0\}$$

standard elliptic theory for the continuum model gives a unique solution $u \in H^1(\Omega)$. The Dirichlet-to-Neumann (DN) map defined by $\Lambda(\gamma) : u|_{\partial\Omega} \mapsto \nu \cdot \gamma \nabla u$ where ν is a unit normal to $\partial\Omega$, gives a relation between any applied potential f and the corresponding current flux $\nu \cdot \gamma \nabla u$. $\Lambda(\gamma) : H^{1/2}(\partial\Omega) \to H^{-1/2}(\partial\Omega)$ is therefore the maximal boundary datum of voltage-current measurements that can be obtained, and the inverse problem of EIT is given $\Lambda(\gamma)$ to reconstruct γ. Uniqueness for the inverse problem with the continuum model is a well-studied subject [36, 27, 30, 28, 4, 14]; in this paper we focus on 2D where there is uniqueness for general conductivities in $L^\infty_+(\Omega)$ if the domain is simply connected.

*This research is supported by Advanced Grant 291405 HD-Tomo from the European Research Council.

†Department of Applied Mathematics and Computer Science, Technical University of Denmark, 2800 Kgs. Lyngby, Denmark.

The inverse problem in EIT is highly ill-posed, and under reasonable assumptions it is only possible to obtain conditional log-type stability estimates [2, 24]. It is worth noting that these estimates are uniform throughout the domain, and therefore does not depend on the distance to the boundary. In spite of the global estimates, reconstruction algorithms often produce good results close to the boundary (e.g. [11, 10, 13, 37]). Few theoretical results seem to address this depth dependence, for instance in the linearized problem [29, 3]; the results presented in this paper will focus on the non-linear problem.

In this paper we consider conductivities with an inclusion in a homogeneous background. Let $A > -1$ and let $\chi_{B_{C,R}}$ be a characteristic function on the open ball $B_{C,R}$ with centre C and radius R. For the unit disk $\mathbb{D} \equiv \{x \in \mathbb{R}^2 : |x| < 1\}$, we investigate

$$\|\Lambda(1 + A\chi_{B_{C,R}}) - \Lambda(1)\|_{\mathcal{L}(L^2(\partial\mathbb{D}))} \tag{1.2}$$

where $\mathcal{L}(L^2(\partial\mathbb{D}))$ is the space of bounded linear operators from $L^2(\partial\mathbb{D})$ to itself. The difference operator $\Lambda(1 + A\chi_{B_{C,R}}) - \Lambda(1)$ is compact and self-adjoint in $L^2(\partial\mathbb{D})$ (cf. Lemma 3.2), so the norm in (1.2) equals the largest magnitude eigenvalue of $\Lambda(1 + A\chi_{B_{C,R}}) - \Lambda(1)$. Suppose we have a noisy approximation $\Lambda^\delta \equiv \Lambda(1 + A\chi_{B_{C,R}}) + E^\delta$ with a noise level $\|E^\delta\|_{\mathcal{L}(L^2(\partial\mathbb{D}))} = \delta$. If we hope to reconstruct the inclusion $B_{C,R}$ from Λ^δ we need (1.2) to be larger than δ, to be sure that Λ^δ is not a noisy measurement originating from the background conductivity $\gamma = 1$. Therefore, we call (1.2) the *distinguishability* of the inclusion $B_{C,R}$ from the background, as it shows how much noise that can be added to a measurement before the interior information for the inclusion $B_{C,R}$ is completely lost. In [20, 7] the norm

$$\|\mathcal{R}(1 + A\chi_{B_{0,r}}) - \mathcal{R}(1))\|_{\mathcal{L}(L^2_\diamond(\partial\mathbb{D}))},$$

again in the sense of largest eigenvalue, was investigated in the unit disk, where $\mathcal{R}(\gamma)$ is the Neumann-to-Dirichlet (ND) map (the inverse of $\Lambda(\gamma)$) and $B_{0,r}$ is a concentric ball with radius r. This characterization is straightforward, as the eigenvalues of the operator $\mathcal{R}(1 + A\chi_{B_{0,r}}) - \mathcal{R}(1)$ can be found explicitly by separation of variables. The difference in this paper is that we use balls $B_{C,R}$ for any centre C and radius R; here we do not get a full characterization of (1.2) but rather explicit lower and upper bounds in Theorem 3.4, which depend on the distance of $B_{C,R}$ to the boundary, i.e. the depth of the inclusion. The bounds show that the distinguishability is decreasing with the depth of the inclusion, and that sufficiently close to the boundary the distinguishability can be arbitrarily high. Furthermore, the depth dependence can be formulated for inclusions of fixed size but varying distance to the boundary (cf. Corollary 3.5).

For non-concentric ball-inclusions $B_{C,R}$ the spectrum of $\Lambda(1 + A\chi_{B_{C,R}}) - \Lambda(1)$ does not have a known explicit characterization. To relate the spectrum of the non-concentric inclusions to the known spectrum of a concentric inclusion is done by the use of Möbius transformations. These transformations belong to a class of harmonic morphisms that is used widely in EIT for instance in reconstruction [15, 19, 22, 23, 1, 33], and recently for generating spatially varying meshes trying to accommodate for the depth dependence in numerical reconstruction when using electrode models [37].

As a side remark we note that there are bounds for eigenvalues of DN maps as they coincide with so-called Steklov eigenvalues (see e.g. [5, 9]), however for a difference operator of two different DN maps there is no clear relation to the Steklov eigenvalue problem.

We focus on the unit disk $\Omega \equiv \mathbb{D}$. This is a natural choice of domain both in terms of depth dependence, as it is rotationally symmetric, but also in terms of the

Riemann mapping theorem (e.g. [35]) which states that any simply connected domain which is not all of $\mathbb{C}$ can be mapped conformally to the unit disk. In the rest of the paper $(x_1, x_2) \in \mathbb{R}^2$ will be identified with $x_1 + ix_2 \in \mathbb{C}$. Furthermore, $\|\cdot\|$ will denote the $L^2(\partial\mathbb{D})$-norm and $\langle\cdot,\cdot\rangle$ the corresponding inner product.

The paper is organised as follows: in Section 2 we introduce Möbius transformations in the unit disk, and the DN map for non-concentric inclusions are given in terms of these transformations. The distinguishability bounds are derived in Theorem 3.4 in Section 3. Section 4 gives an exact tridiagonal matrix representation of the non-concentric DN maps to accurately and efficiently validate the bounds numerically and demonstrate their tightness. Finally, we conclude in Section 5.

In Appendix B similar results regarding bounds on distinguishability and exact matrix characterization for the Neumann-to-Dirichlet (ND) map are given. While the actual bounds for the ND map are fundamentally different from the DN counterparts, they are placed in the appendix due to the nature of the proofs being very similar to the proofs for the DN map. Furthermore, in particular the lower bound for the ND map is not as sharp as for the DN map.

2. Möbius transformation of the Dirichlet-to-Neumann map. In this section we will relate the DN map of a non-concentric ball inclusion to a DN map for a concentric ball inclusion by the use of Möbius transformations. This relation will in Section 3 be used to obtain bounds on the distinguishability.

2.1. Möbius transformations in the unit disk. Möbius transformations are known to preserve harmonic functions in 2D, which makes them *harmonic morphisms*. On the unit disk $\mathbb{D}$ the harmonic morphisms are uniquely (up to rotation) given by

$$M_a(x) = \frac{x-a}{\bar{a}x-1}, \quad x \in \mathbb{D}, \tag{2.1}$$

for $|a| < 1$ [35]. The transformations in (2.1) are special cases of Möbius transformations, where $M_a : \mathbb{D} \to \mathbb{D}$ and $\partial\mathbb{D} \to \partial\mathbb{D}$. The particular choice of rotation in (2.1) implies that M_a is an involution, i.e. $M_a^{-1} = M_a$. Furthermore, for any ball $B_{C,R} \subset \mathbb{D}$ with centre C and radius $R < 1 - |C|$ there exists a unique $a \in \mathbb{D}$ such that $M_a(B_{C,R}) = B_{0,r}$ for some $r \geq R$.

Let $a \equiv \rho e^{i\zeta}$ with $0 \leq \rho < 1$ and $\zeta \in \mathbb{R}$. Then we can straightforwardly relate the Möbius transformation anywhere in the disk to the transformation along the real line by the following rotations

$$M_{\rho e^{i\zeta}}(x) = e^{i\zeta} M_\rho(e^{-i\zeta}x). \tag{2.2}$$

This is a useful property that often reduces proofs including M_a to the simpler form M_ρ.

The characterization below of how M_a can be used to move ball inclusions in $\mathbb{D}$ while preserving harmonic functions is well-known (cf. [15, 37]). The proof is short and given for completeness for the particular choice of transformation in (2.1).

PROPOSITION 2.1.

(i) *Let $a \equiv \rho e^{i\zeta}$ with $0 \leq \rho < 1$ and $\zeta \in \mathbb{R}$, and let $0 < r < 1$. Then M_a maps $B_{0,r}$ to $B_{C,R}$ with*

$$C = \frac{\rho(r^2-1)}{\rho^2 r^2 - 1} e^{i\zeta}, \qquad R = \frac{r(\rho^2-1)}{\rho^2 r^2 - 1}.$$

(ii) *Let $C \equiv ce^{i\zeta}$ with $0 \leq c < 1$ and $\zeta \in \mathbb{R}$, and let $0 < R < 1 - c$. Then the unique $a \in \mathbb{D}$ such that M_a maps $B_{C,R}$ to a concentric ball $B_{0,r}$ satisfies*

$$r = \frac{1 + R^2 - c^2 - \sqrt{((1-R)^2 - c^2)((1+R)^2 - c^2)}}{2R}, \qquad a = \frac{C}{1 - Rr}. \tag{2.3}$$

Proof. For (i) we first consider the case $\zeta = 0$ so $a = \rho$. From (2.1) it is seen that M_ρ is symmetric about the real axis so the centre of $M_\rho(B_{0,r})$ lies on the real axis. Furthermore, the mapping of $M_\rho(r)$ and $M_\rho(-r)$ gives the following real points on $\partial M_\rho(B_{0,r})$:

$$M_\rho(r) = \frac{r - \rho}{\rho r - 1}, \qquad M_\rho(-r) = \frac{r + \rho}{\rho r + 1},$$

where $M_\rho(-r) > M_\rho(r)$ for all $\rho < 1$. Thus centre c and radius R of $M_\rho(B_{0,r})$ can be found as

$$c = \frac{M_\rho(-r) + M_\rho(r)}{2} = \frac{\rho(r^2 - 1)}{\rho^2 r^2 - 1}, \tag{2.4}$$

$$R = M_\rho(-r) - c = \frac{r(\rho^2 - 1)}{\rho^2 r^2 - 1}. \tag{2.5}$$

Now in the case $\zeta \neq 0$ we note that $M_a(B_{0,r}) = e^{i\zeta} M_\rho(B_{0,r})$ due to (2.2) and that $B_{0,r}$ is rotationally symmetric. So $C = ce^{i\zeta}$ which yields the desired result.

For (ii) we solve (2.4) and (2.5) with respect to r and ρ, which for $h \equiv 1 + R^2 - c^2$ gives

$$r = \frac{h - \sqrt{h^2 - 4R^2}}{2R}, \qquad \rho = \frac{c}{1 - Rr}.$$

By using that $a = \rho e^{i\zeta}$ and expanding the terms in r gives the expressions in (2.3). □

Note from Proposition 2.1 that M_a maps the origin $\mathcal{O}$ to a in the same direction as C, but a little further towards the boundary as illustrated in Figure 1. However, we will always have that $a \in B_{C,R}$ since $c < 1 - R$ and $r < 1$ implies

$$|a - C| = \rho - c = \frac{c}{1 - Rr} - c = \frac{cr}{1 - Rr} R < \frac{(1-R)r}{1 - Rr} R \leq R.$$

Thus there is in (2.3) the asymptotic limit

$$\lim_{r \to 0} a = \lim_{R \to 0} a = C.$$

Writing $M_a(x) = V_1(x) + iV_2(x)$ for real valued V_1 and V_2, and similarly $x = x_1 + ix_2$, then as M_a is holomorphic on $\mathbb{D}$ the Cauchy-Riemann equations hold

$$\tfrac{\partial}{\partial x_1} V_1 = \tfrac{\partial}{\partial x_2} V_2, \quad \tfrac{\partial}{\partial x_2} V_1 = -\tfrac{\partial}{\partial x_1} V_2,$$

so the Jacobian determinant of M_a becomes:

$$J_a(x) = \left(\tfrac{\partial}{\partial x_1} V_1\right)^2 + \left(\tfrac{\partial}{\partial x_1} V_2\right)^2 = |\tfrac{\partial}{\partial x_1} M_a|^2 = \left(\frac{1 - |a|^2}{|\overline{a}x - 1|^2}\right)^2. \tag{2.6}$$

J_a is the Jacobian determinant for the transformation on the whole domain $\mathbb{D}$, but for the purposes of transforming the boundary operator $\Lambda(\gamma)$ it is necessary to determine

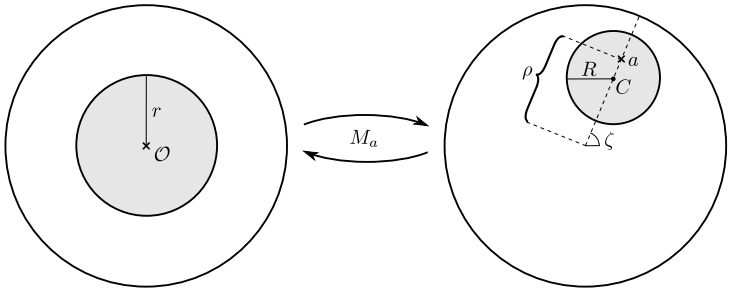

Fig. 1: Illustration of the action of M_a on ball inclusions in the unit disk $\mathbb{D}$ using the notation in Proposition 2.1.

the corresponding transformation on the boundary, i.e. determining the tangential and normal part to the Jacobian matrix on $\partial\mathbb{D}$. Denote for $x \in \mathbb{D}$ the polar coordinates $x = \beta e^{i\theta}$ and $M_a(x) = Be^{i\Theta}$. We have the following relations on $\partial\mathbb{D}$:

$$\begin{aligned} &\frac{\partial B}{\partial \theta}|_{\partial\mathbb{D}} = \frac{\partial \Theta}{\partial \beta}|_{\partial\mathbb{D}} = 0, \\ &\frac{\partial B}{\partial \beta}|_{\partial\mathbb{D}} = \frac{\partial \Theta}{\partial \theta}|_{\partial\mathbb{D}} = J_a^{1/2}|_{\partial\mathbb{D}} = \frac{1-\rho^2}{1+\rho^2-2\rho\cos(\theta-\zeta)}. \end{aligned} \tag{2.7}$$

Deriving the terms in (2.7) involves straightforward computations using that M_a maps $\partial\mathbb{D}$ to itself, along with the following identities which are a consequence of the Cauchy-Riemann equations and (2.2)

$$\begin{aligned} \mathrm{Re}(\tfrac{\partial M_a}{\partial \beta})M_a - \tfrac{\partial M_a}{\partial \beta}\,\mathrm{Re}(M_a) = 0, \quad \text{on } \partial\mathbb{D}, \\ \mathrm{Im}(\tfrac{\partial M_a}{\partial \beta})M_a - \tfrac{\partial M_a}{\partial \beta}\,\mathrm{Im}(M_a) = 0, \quad \text{on } \partial\mathbb{D}. \end{aligned}$$

2.2. Transformation of the DN map. In this section we will write up the DN map for the problem transformed by M_a for disk perturbations. Denote $\gamma_{C,R} \equiv 1 + A\chi_{B_{C,R}}$ for $A > -1$ where $\chi_{B_{C,R}}$ is a characteristic function over the open ball $B_{C,R}$ with centre C and radius R. Furthermore, the notation in Proposition 2.1 will be used throughout, relating a and r to C and R. The background conductivity of 1 is merely for ease of presentation, and can easily be changed to another (constant) background using the identity

$$\Lambda(c\gamma) = c\Lambda(\gamma), \;\; c > 0.$$

By $\mathcal{M}_a$ we denote the operator applying the transformation $\mathcal{M}_a f \equiv f \circ M_a$, where either $f : \mathbb{D} \to \mathbb{C}$ or $f : \partial\mathbb{D} \to \mathbb{C}$. Furthermore, we will use the notation $J_a^{1/2}$ both for the square root of (2.6) and for the multiplication operator $f \mapsto J_a^{1/2}|_{\partial\mathbb{D}} f$, indiscriminately. Before investigating the DN map we list a few basic properties.

Proposition 2.2.

(i) $\mathcal{M}_a(H^{1/2}(\partial\mathbb{D})) = H^{1/2}(\partial\mathbb{D})$ *and* $\mathcal{M}_a(L^2(\partial\mathbb{D})) = L^2(\partial\mathbb{D})$.

(ii) $\mathcal{M}_a$ *and* $J_a^{1/2}\mathcal{M}_a$ *are involutions, i.e. their own inverse.*

(iii) $J_a^{1/2}\mathcal{M}_a = \mathcal{M}_a J_a^{-1/2}$ *and* $J_a^{-1/2}\mathcal{M}_a = \mathcal{M}_a J_a^{1/2}$.

(iv) $\mathcal{M}_a{}^* = J_a^{1/2}\mathcal{M}_a$ *in* $L^2(\partial\mathbb{D})$.

(v) $J_a^{1/2}$ *is on* $\partial\mathbb{D}$ *bounded from below and above by positive constants:*

$$\frac{1-\rho}{1+\rho} \leq J_a^{1/2} \leq \frac{1+\rho}{1-\rho}.$$

Proof. (iii) is a consequence of the inverse function theorem. For (ii) $\mathcal{M}_a$ is an involution since M_a is an involution, and from (iii)

$$J_a^{1/2}\mathcal{M}_a J_a^{1/2}\mathcal{M}_a = \mathcal{M}_a J_a^{-1/2} J_a^{1/2}\mathcal{M}_a = \mathrm{Id}\,.$$

(iv) follows since $M_a^{-1} = M_a$ and $J_a^{1/2}$ is real-valued and is the Jacobian determinant for the boundary integral. For (v) we have

$$\inf_{\theta\in(-\pi,\pi)} J_a^{1/2}(e^{i\theta}) = \inf_{\theta\in(-\pi,\pi)} \frac{1-\rho^2}{|1-\rho e^{i(\theta-\zeta)}|^2} = \frac{1-\rho^2}{(1+\rho)^2} = \frac{1-\rho}{1+\rho},$$
$$\sup_{\theta\in(-\pi,\pi)} J_a^{1/2}(e^{i\theta}) = \sup_{\theta\in(-\pi,\pi)} \frac{1-\rho^2}{|1-\rho e^{i(\theta-\zeta)}|^2} = \frac{1-\rho^2}{(1-\rho)^2} = \frac{1+\rho}{1-\rho}.$$

That M_a is smooth and $J_a^{1/2}$ bounded from below and above by positive constants implies that $\mathcal{M}_a(H^{1/2}(\partial\mathbb{D})) \subseteq H^{1/2}(\partial\mathbb{D})$, and M_a being an involution implies the opposite inclusion $H^{1/2}(\partial\mathbb{D}) \subseteq \mathcal{M}_a(H^{1/2}(\partial\mathbb{D}))$. The same argument is used to show that $\mathcal{M}_a(L^2(\partial\mathbb{D})) = L^2(\partial\mathbb{D})$. □

Applying $\mathcal{M}_a$ to a distribution in $H^{-1/2}(\partial\mathbb{D})$ is done as a generalization of the change of variables through the dual pairing

$$\langle \mathcal{M}_a g, f\rangle \equiv \langle g, J_a^{1/2}\mathcal{M}_a f\rangle,\ \ g \in H^{-1/2}(\partial\mathbb{D}), f \in H^{1/2}(\partial\mathbb{D}).$$

Now we can write up the DN maps for an inclusion transformed with $\mathcal{M}_a$.

Lemma 2.3. *There is the following relation between the DN map for the concentric problem and the DN map for the non-concentric problem:*

$$\Lambda(\gamma_{C,R}) = \Lambda(\mathcal{M}_a(\gamma_{0,r})) = J_a^{1/2}\mathcal{M}_a\Lambda(\gamma_{0,r})\mathcal{M}_a, \tag{2.8}$$

and similarly

$$\Lambda(\gamma_{0,r}) = \Lambda(\mathcal{M}_a(\gamma_{C,R})) = J_a^{1/2}\mathcal{M}_a\Lambda(\gamma_{C,R})\mathcal{M}_a.$$

Proof. For brevity let $\tilde{w}$ be a shorthand notation for $\mathcal{M}_a w$ where w is either a function on $\partial\mathbb{D}$ or on $\mathbb{D}$. Let u be the solution to (1.1) with conductivity $\gamma_{0,r}$ and Dirichlet condition $u|_{\partial\mathbb{D}} = f$. Denote the corresponding Neumann condition $g \equiv \Lambda(\gamma_{0,r})f = \nu\cdot\nabla u|_{\partial\mathbb{D}}$. Furthermore, let $u_1 \equiv u$ in $B_{0,r}$ and $u_2 \equiv u$ in $\mathbb{D}\setminus\overline{B_{0,r}}$. Then as $\gamma_{0,r} = 1+A\chi_{B_{0,r}}$ and $\gamma_{C,R} = 1+A\chi_{B_{C,R}}$ we can write up (1.1), along with Dirichlet- and Neumann-conditions as the following system, alongside with the corresponding transformed problem. This gives the following two transmission problems:

$$\begin{aligned}
\Delta u_1 &= 0 \text{ in } B_{0,r}\\
\Delta u_2 &= 0 \text{ in } \mathbb{D}\setminus\overline{B_{0,r}}\\
u_1 &= u_2 \text{ on } \partial B_{0,r}\\
(1+A)\eta\cdot\nabla u_1 &= \eta\cdot\nabla u_2 \text{ on } \partial B_{0,r}\\
u_2 &= f \text{ on } \partial\mathbb{D}\\
\nu\cdot\nabla u_2 &= g \text{ on } \partial\mathbb{D}
\end{aligned}
\qquad
\begin{aligned}
\Delta \tilde{u}_1 &= 0 \text{ in } B_{C,R}\\
\Delta \tilde{u}_2 &= 0 \text{ in } \mathbb{D}\setminus\overline{B_{C,R}}\\
\tilde{u}_1 &= \tilde{u}_2 \text{ on } \partial B_{C,R}\\
(1+A)\eta\cdot\nabla \tilde{u}_1 &= \eta\cdot\nabla \tilde{u}_2 \text{ on } \partial B_{C,R}\\
\tilde{u}_2 &= \tilde{f} \text{ on } \partial\mathbb{D}\\
\nu\cdot\nabla \tilde{u}_2 &= J_a^{1/2}\tilde{g} \text{ on } \partial\mathbb{D}
\end{aligned}$$

Some notational abuse was used as η is both unit normal to $\partial B_{0,r}$ and to $\partial B_{C,R}$ in the transformed problem. The Laplace-Beltrami operator is preserved as M_a is a harmonic morphism, and the Dirichlet conditions simply apply the change of variable. The only real change occurs in the derivatives, which on the boundary $\partial B_{C,R}$ cancels out as J_a is non-zero, and on the outer boundary $\partial\mathbb{D}$ gives $J_a^{-1/2}\nu\cdot\nabla\tilde{u}_2$ from (2.7) and the property $\mathcal{M}_a J_a^{1/2} = J_a^{-1/2}\mathcal{M}_a$.

Thus we have

$$\Lambda(\gamma_{C,R})\tilde{f} = J_a^{1/2}\mathcal{M}_a g = J_a^{1/2}\mathcal{M}_a\Lambda(\gamma_{0,r})f = J_a^{1/2}\mathcal{M}_a\Lambda(\gamma_{0,r})\mathcal{M}_a\tilde{f},\ \ \forall\tilde{f}\in H^{1/2}(\partial\mathbb{D}).$$

One can interchange $\gamma_{0,r}$ and $\gamma_{C,R}$ above by Proposition 2.2 since $\mathcal{M}_a$ and $J_a^{1/2}\mathcal{M}_a$ are involutions. □

3. Depth dependent bounds on distinguishability of inclusions. In this section we determine lower and upper bounds for the distinguishability of $\Lambda(\gamma_{C,R}) - \Lambda(1)$, in terms of its largest eigenvalue. The bounds are given in Theorem 3.4.

The spectrum of $\Lambda(\gamma_{0,r})$ is given below and is derived from a straightforward application of separation of variables, cf. [26, chapter 12.5.1]. Since the eigenfunctions of $\Lambda(\gamma_{0,r})$ and $\Lambda(1)$ are identical, the eigenvalues of the difference operator $\Lambda(\gamma_{0,r}) - \Lambda(1)$ is just the difference of the eigenvalues for the two respective operators. This simplification of course only holds if the eigenfunctions are identical, i.e. it will not be the case for the non-concentric problem.

PROPOSITION 3.1. *For $\gamma_{0,r} \equiv 1 + A\chi_{B_{0,r}}$ with $0 < r < 1$ and $A > -1$, the eigenfunctions of $\Lambda(\gamma_{0,r})$ are $f_n(\theta) \equiv \frac{1}{\sqrt{2\pi}}e^{in\theta}$, $n\in\mathbb{Z}$. The corresponding eigenvalues are*

$$\lambda_n \equiv \frac{2 + A(1 + r^{2|n|})}{2 + A(1 - r^{2|n|})}|n|,\ \ n\in\mathbb{Z}.$$

The eigenvalues for the difference operator $\Lambda(\gamma_{0,r}) - \Lambda(1)$ are

$$\lambda_n \equiv \frac{2Ar^{2|n|}}{2 + A(1 - r^{2|n|})}|n|,\ \ n\in\mathbb{Z}. \tag{3.1}$$

REMARK 1. *The eigenvalues in* (3.1) *are not necessarily monotonously decaying in $|n|$. This depends on the values of A and r. This is unlike the Neumann-to-Dirichlet operators for which the eigenvalues have monotonous decay as seen in Proposition B.1.*

$\Lambda(\gamma)$ is an unbounded operator on $L^2(\partial\mathbb{D})$ for any $\gamma\in L^\infty_+(\mathbb{D})$, however the difference $\Lambda(\gamma_{C,R}) - \Lambda(1)$ is infinitely smoothing as $\gamma_{C,R} = 1$ in a neighbourhood of $\partial\mathbb{D}$ (see e.g. [8, Lemma 3.1]). In fact $\Lambda(\gamma_{C,R}) - \Lambda(1)$ extends continuously to a compact and self-adjoint operator on all of $L^2(\partial\mathbb{D})$, and it is for this extension that we determine distinguishability bounds. In lack of a proper reference to such a result we give the proof below for our specific scenario.

LEMMA 3.2. *For each centre C and radius R such that $\overline{B_{C,R}}\subset\mathbb{D}$, the operator $\Lambda(\gamma_{C,R}) - \Lambda(1)$ continuously extends to a compact and self-adjoint operator in $\mathcal{L}(L^2(\partial\mathbb{D}))$.*

Proof. The eigenfunctions in Proposition 3.1 comprises the orthonormal Fourier basis $\{f_n\}_{n\in\mathbb{Z}}$ for $L^2(\partial\mathbb{D})$. Using that $\Lambda(\gamma_{0,r})$ and $\Lambda(1)$ are symmetric operators w.r.t.

the $L^2(\partial\mathbb{D})$-inner product, implies that the difference operator $\Lambda(\gamma_{0,r}) - \Lambda(1)$ can be written as below, where λ_n denotes the eigenvalues in (3.1):

$$(\Lambda(\gamma_{0,r}) - \Lambda(1))f = \sum_{n\in\mathbb{Z}} \lambda_n \langle f, f_n\rangle f_n, \quad f \in H^{1/2}(\partial\mathbb{D}). \tag{3.2}$$

Since $\sup_{n\in\mathbb{Z}}|\lambda_n| < \infty$ then (3.2) implies that $\Lambda(\gamma_{0,r}) - \Lambda(1)$ is bounded in terms of the $L^2(\partial\mathbb{D})$-norm:

$$\|(\Lambda(\gamma_{0,r}) - \Lambda(1))f\|_{L^2(\partial\mathbb{D})} \leq \sup_{n\in\mathbb{Z}}|\lambda_n| \|f\|_{L^2(\partial\mathbb{D})}, \quad f \in H^{1/2}(\partial\mathbb{D}),$$

i.e. using the formula in (3.2) the operator $\Lambda(\gamma_{0,r}) - \Lambda(1)$ continuously extends to a self-adjoint operator in $\mathcal{L}(L^2(\partial\mathbb{D}))$.

Note that $|\lambda_n| \leq 2|A||n|r^{2|n|} \to 0$ for $n \to \infty$ implies that the extension is compact. This follows as $\Lambda(\gamma_{0,r}) - \Lambda(1)$ is the limit of the finite rank operators $P_N(\Lambda(\gamma_{0,r}) - \Lambda(1))$, where P_N is the orthogonal projection onto $\text{span}\{f_n\}_{|n|\leq N}$,

$$\begin{aligned}\|(P_N - \text{Id})(\Lambda(\gamma_{0,r}) - \Lambda(1))\|^2_{\mathcal{L}(L^2(\partial\mathbb{D}))} &= \sup_{f\in L^2(\partial\mathbb{D})\setminus\{0\}} \frac{1}{\|f\|^2} \sum_{|n|>N} |\lambda_n|^2 |\langle f, f_n\rangle|^2 \\ &\leq \sup_{|n|>N} |\lambda_n|^2 \to 0 \text{ for } N \to \infty.\end{aligned}$$

Since $\mathcal{M}_a$ and $J_a^{1/2}\mathcal{M}_a$ belong to $\mathcal{L}(L^2(\partial\mathbb{D}))$ implies that through (2.8) then $\Lambda(\gamma_{C,R}) - \Lambda(1)$ extends to a compact and self-adjoint operator in $\mathcal{L}(L^2(\partial\mathbb{D}))$, for any centre C and radius R. □

For brevity we will denote by $\|\cdot\|$ the operator norm on $\mathcal{L}(L^2(\partial\mathbb{D}))$, and it should be straightforward to distinguish it from the $L^2(\partial\mathbb{D})$-norm from the context it is used. It is well known from the spectral theorem that the operator norm of a compact and self-adjoint Hilbert space operator equals the largest magnitude eigenvalue of the operator, and is furthermore given by

$$\begin{aligned}\|\Lambda(\gamma_{C,R}) - \Lambda(1)\| &= \sup_{f\in L^2(\partial\mathbb{D})\setminus\{0\}} \frac{\|(\Lambda(\gamma_{C,R}) - \Lambda(1))f\|}{\|f\|} \\ &= \sup_{f\in L^2(\partial\mathbb{D})\setminus\{0\}} \frac{|\langle(\Lambda(\gamma_{C,R}) - \Lambda(1))f, f\rangle|}{\|f\|^2}.\end{aligned} \tag{3.3}$$

Thus in reality the distinguishability is related to a choice of boundary condition (here Dirichlet condition). Choosing the eigenfunction f_1 to the largest magnitude eigenvalue λ_1 of $\Lambda(\gamma_{C,R}) - \Lambda(1)$ maximises the expression in (3.3). The min-max theorem (see e.g. [32]) furthermore states that in the orthogonal complement to f_1, the maximising function is f_2, the eigenfunction to the second largest eigenvalue λ_2. Continuing the procedure gives an orthonormal set of boundary conditions that in each orthogonal direction maximises the difference $(\Lambda(\gamma_{C,R}) - \Lambda(1))f$.

Suppose that we instead have a noisy approximation $\Lambda^\delta \equiv \Lambda(\gamma_{C,R}) + E^\delta$ with noise level $\|E^\delta\| = \delta$. If we hope to be able to recover the inclusion $B_{C,R}$ from Λ^δ then we need $\|\Lambda(\gamma_{C,R}) - \Lambda(1)\| > \delta$ in order to *distinguish* that the data Λ^δ does not come from the background conductivity $\gamma = 1$, and that there is an inclusion to reconstruct. The distinguishability is therefore a measure of how much noise that can be added before the structural information is completely lost. In particular the

magnitude of the eigenvalues for $\Lambda(\gamma_{C,R}) - \Lambda(1)$ shows whether the corresponding eigenfunctions are able to contribute any distinguishability for a given noise level.

Even though the eigenvalues for the concentric problem are known, this does not imply that Lemma 2.3 directly gives the spectrum of the non-concentric problem. As seen below, an eigenfunction f of $\Lambda(\gamma_{0,r})$ does not yield an eigenfunction $\mathcal{M}_a f$ of $\Lambda(\gamma_{C,R})$ but is instead an eigenfunction of the operator scaled by $J_a^{-1/2}$.

COROLLARY 3.3. *(λ, f) is an eigenpair of $\Lambda(\gamma_{0,r})$ if and only if $(\lambda, \mathcal{M}_a f)$ is an eigenpair of $J_a^{-1/2}\Lambda(\gamma_{C,R})$.*

Proof. From Lemma 2.3 we have:

$$J_a^{-1/2}\Lambda(\gamma_{C,R})\mathcal{M}_a f = \mathcal{M}_a\Lambda(\gamma_{0,r})f. \tag{3.4}$$

If (λ, f) is an eigenpair of $\Lambda(\gamma_{0,r})$ then (3.4) gives $J_a^{-1/2}\Lambda(\gamma_{C,R})\mathcal{M}_a f = \lambda\mathcal{M}_a f$. On the other hand, if $(\lambda, \mathcal{M}_a f)$ is an eigenpair of $J_a^{-1/2}\Lambda(\gamma_{C,R})$ then (3.4) gives $\mathcal{M}_a\Lambda(\gamma_{0,r})f = \lambda\mathcal{M}_a f$ and as $\mathcal{M}_a^{-1} = \mathcal{M}_a$ then (λ, f) is an eigenpair of $\Lambda(\gamma_{0,r})$. □

To the authors' knowledge there is not a known closed-form expression for either eigenvalues or eigenfunctions of the non-concentric problem. However, it is possible to obtain explicit bounds, and for these bounds we will make use of certain weighted norms.

Since $J_a^{1/2}$ is real-valued and bounded as in Proposition 2.2 gives rise to other weighted norms and inner products on $L^2(\partial\mathbb{D})$, namely

$$\langle f, g\rangle_{1/2} \equiv \int_{\partial\mathbb{D}} f\overline{g}J_a^{1/2}\,ds, \qquad \|f\|_{1/2} \equiv \sqrt{\langle f, f\rangle_{1/2}}, \tag{3.5}$$

$$\langle f, g\rangle_{-1/2} \equiv \int_{\partial\mathbb{D}} f\overline{g}J_a^{-1/2}\,ds, \quad \|f\|_{-1/2} \equiv \sqrt{\langle f, f\rangle_{-1/2}}. \tag{3.6}$$

It is clear from Proposition 2.2(v) that these weighted norms are equivalent to the usual $L^2(\partial\mathbb{D})$-norm:

$$\sqrt{\frac{1-\rho}{1+\rho}}\|f\| \le \|f\|_{\pm 1/2} \le \sqrt{\frac{1+\rho}{1-\rho}}\|f\|, \;\; f \in L^2(\partial\mathbb{D}). \tag{3.7}$$

The weighted norms are used below in Theorem 3.4 for determining bounds on the distinguishability. The weighted inner products will turn out to be a natural choice when determining an exact matrix representation for $\Lambda(\gamma_{C,R}) - \Lambda(1)$, as seen in Section 4.

THEOREM 3.4. *Let γ be either $\gamma_{0,r}$ or $\gamma_{C,R}$. From the weighted norms* (3.5) *and* (3.6) *we obtain*

$$\|\Lambda(\gamma) - \Lambda(1)\| = \sup_{f\in L^2(\partial\mathbb{D})\setminus\{0\}} \frac{\|(\Lambda(\mathcal{M}_a\gamma) - \Lambda(1))f\|_{-1/2}}{\|f\|_{1/2}}. \tag{3.8}$$

Furthermore the following bounds hold

$$\frac{1-\rho}{1+\rho}\|\Lambda(\gamma_{C,R}) - \Lambda(1)\| \le \|\Lambda(\gamma_{0,r}) - \Lambda(1)\| \le \sqrt{\frac{1-\rho^2}{1+\rho^2}}\|\Lambda(\gamma_{C,R}) - \Lambda(1)\|. \tag{3.9}$$

Proof. By Lemma 2.3

$$\begin{aligned}\|\Lambda(\gamma) - \Lambda(1)\|^2 &= \|J_a^{1/2}\mathcal{M}_a(\Lambda(\mathcal{M}_a\gamma) - \Lambda(1))\mathcal{M}_a\|^2 \\ &= \sup_{f\in L^2(\partial\mathbb{D})\setminus\{0\}} \frac{\|J_a^{1/2}\mathcal{M}_a(\Lambda(\mathcal{M}_a\gamma) - \Lambda(1))\mathcal{M}_a f\|^2}{\|f\|^2}.\end{aligned}$$

Now applying the change of variables with $\mathcal{M}_a$ in both numerator and denominator, and using that $J_a^{1/2}$ is the Jacobian determinant in the boundary integral along with Proposition 2.2(iii), yields

$$\begin{aligned}\|\Lambda(\gamma)-\Lambda(1)\|^2 &= \sup_{f\in L^2(\partial\mathbb{D})\setminus\{0\}} \frac{\int_{\partial\mathbb{D}} J_a \mathcal{M}_a|(\Lambda(\mathcal{M}_a\gamma)-\Lambda(1))\mathcal{M}_a f|^2\,ds}{\int_{\partial\mathbb{D}}|f|^2\,ds} \\ &= \sup_{f\in L^2(\partial\mathbb{D})\setminus\{0\}} \frac{\int_{\partial\mathbb{D}} J_a^{-1/2}|(\Lambda(\mathcal{M}_a\gamma)-\Lambda(1))\mathcal{M}_a f|^2\,ds}{\int_{\partial\mathbb{D}} J_a^{1/2}|\mathcal{M}_a f|^2\,ds}.\end{aligned}$$

Finally, it is applied that $\mathcal{M}_a f$ can be substituted by f in the supremum since $\mathcal{M}_a(L^2(\partial\mathbb{D})) = L^2(\partial\mathbb{D})$ and $\mathcal{M}_a f = 0 \Leftrightarrow f = 0$

$$\|\Lambda(\gamma)-\Lambda(1)\|^2 = \sup_{f\in L^2(\partial\mathbb{D})\setminus\{0\}} \frac{\int_{\partial\mathbb{D}} J_a^{-1/2}|(\Lambda(\mathcal{M}_a\gamma)-\Lambda(1))f|^2\,ds}{\int_{\partial\mathbb{D}} J_a^{1/2}|f|^2\,ds},$$

which is the expression in (3.8).

Let f_1 be the eigenfunction of $\Lambda(\gamma_{C,R})-\Lambda(1)$ corresponding to the largest eigenvalue λ_1, and similarly let $\hat{f}_1$ be the eigenfunction of $\Lambda(\gamma_{0,r})-\Lambda(1)$ corresponding to the largest eigenvalue $\hat{\lambda}_1$, then

$$|\hat{\lambda}_1| = \|\Lambda(\gamma_{0,r})-\Lambda(1)\| \geq \frac{\|(\Lambda(\gamma_{C,R})-\Lambda(1))f_1\|_{-1/2}}{\|f_1\|_{1/2}} = |\lambda_1|\frac{\|f_1\|_{-1/2}}{\|f_1\|_{1/2}}.$$

Now utilizing the norm equivalence in (3.7)

$$|\hat{\lambda}_1| \geq |\lambda_1|\frac{\|f_1\|_{-1/2}}{\|f_1\|_{1/2}} \geq |\lambda_1|\frac{\sqrt{\frac{1-\rho}{1+\rho}}\|f_1\|}{\sqrt{\frac{1+\rho}{1-\rho}}\|f_1\|} = \frac{1-\rho}{1+\rho}|\lambda_1|,$$

which is the lower bound in (3.9). The same can be done by interchanging $\gamma_{0,r}$ and $\gamma_{C,R}$

$$|\lambda_1| = \|\Lambda(\gamma_{C,R})-\Lambda(1)\| \geq \frac{\|(\Lambda(\gamma_{0,r})-\Lambda(1))\hat{f}_1\|_{-1/2}}{\|\hat{f}_1\|_{1/2}} = |\hat{\lambda}_1|\frac{\|\hat{f}_1\|_{-1/2}}{\|\hat{f}_1\|_{1/2}}.$$

Since $\gamma_{0,r}$ is concentric, then $\hat{f}_1$ may be chosen as a complex exponential by Proposition 3.1 i.e. $|\hat{f}_1| = 1$

$$|\hat{\lambda}_1| \leq |\lambda_1|\sqrt{\frac{\int_{\partial\mathbb{D}} J_a^{1/2}\,ds}{\int_{\partial\mathbb{D}} J_a^{-1/2}\,ds}}. \tag{3.10}$$

Here $\int_{\partial\mathbb{D}} J_a^{1/2}\,ds = \int_{\partial\mathbb{D}} 1\,ds = 2\pi$ as $J_a^{1/2}$ is the Jacobian determinant in the boundary integral. By (2.7)

$$\int_{\partial\mathbb{D}} J_a^{-1/2}\,dx = \frac{1}{1-\rho^2}\int_0^{2\pi}\left[1+\rho^2-2\rho\cos(\theta-\zeta)\right]d\theta = 2\pi\frac{1+\rho^2}{1-\rho^2}, \tag{3.11}$$

which combined with (3.10) gives the upper bound in (3.9)

$$|\hat{\lambda}_1| \leq |\lambda_1|\sqrt{\frac{1-\rho^2}{1+\rho^2}}.$$

□

In the bounds in Theorem 3.4 it is worth noting that both lower and upper bound tends to zero as ρ tends to 1. When ρ approaches 1, $B_{C,R}$ approaches $\partial\mathbb{D}$, and the largest eigenvalue of $\Lambda(\gamma_{C,R})-\Lambda(1)$ tends to infinity corresponding to $\Lambda(\gamma_{C,R})-\Lambda(1)$ diverging in $\mathcal{L}(L^2(\partial\mathbb{D}))$.

Since the constant in the upper bound in (3.9) is smaller than 1 for any $0 \leq \rho < 1$ implies that $\|\Lambda(\gamma_{0,r})-\Lambda(1)\| \leq \|\Lambda(\gamma_{C,R})-\Lambda(1)\|$ for any $a \in \mathbb{D}$. This means that the distinguishability increases as the inclusion is moved closer to the boundary. However it does so even though $B_{C,R}$ is decreasing in size as $\lim_{\rho\to 1} R = 0$. So no matter what the size of $B_{0,r}$ is, it is always possible to construct another arbitrarily small inclusion $B_{C,R}$ sufficiently close to the boundary $\partial\mathbb{D}$ such that $\Lambda(\gamma_{C,R})$ is easier to distinguish from $\Lambda(1)$ than $\Lambda(\gamma_{0,r})$ is, in the presence of noise. In other words, given a noisy measurement we can expect to more stably reconstruct smaller structures of γ near the boundary than larger structures deeper in the domain.

Combining (3.9) with Corollary A.2 in Appendix A directly gives the following upper bound on the distinguishability when then size of the inclusion is fixed.

COROLLARY 3.5. *For $|C| \leq 1-r$ the following bounds hold*

$$\|\Lambda(\gamma_{0,r})-\Lambda(1)\| \leq \sqrt{\frac{1-\rho^2}{1+\rho^2}}\|\Lambda(\gamma_{C,R})-\Lambda(1)\| \leq \sqrt{\frac{1-\rho^2}{1+\rho^2}}\|\Lambda(\gamma_{C,r})-\Lambda(1)\|.$$

4. Comparison of bounds on the dinstinguishability. In this section the bounds from Theorem 3.4 are investigated and verified numerically, to see how tight the bounds are for inclusions of various sizes. Here it is important to determine eigenvalues of the non-concentric problem $\Lambda(\gamma_{C,R})-\Lambda(1)$ accurately. Therefore, we will avoid numerical solution of $f \mapsto \Lambda(\gamma_{C,R})f$ as well as numerical integration, as integration of high frequent trigonometric-like functions requires many sampling points for a usual Gauss-Legendre quadrature rule to be accurate. Instead we will use an orthonormal basis $\{\phi_n\}_{n\in\mathbb{Z}}$ in terms of the inner product $\langle\cdot,\cdot\rangle_{1/2}$ from (3.5), and determine the coefficients

$$\mathcal{A}_{n,m} \equiv \langle(\Lambda(\gamma_{C,R})-\Lambda(1))\phi_m, \phi_n\rangle_{1/2}$$

exactly, based on the known spectrum of the concentric problem $\Lambda(\gamma_{0,r})-\Lambda(1)$ and the transformation $\mathcal{M}_a$ that takes $B_{0,r}$ to $B_{C,R}$. As the basis is orthonormal the infinite dimensional matrix $\mathcal{A}$ is then a matrix representation of $\Lambda(\gamma_{C,R})-\Lambda(1)$. This is understood in the sense that for $f \in H^{1/2}(\partial\mathbb{D})$ where we write $f = \sum_{m\in\mathbb{Z}} v_m\phi_m$ with the coefficients $v_m \equiv \langle f, \phi_m\rangle_{1/2}$ collected in a sequence v, then the n'th component of $\mathcal{A}v$ is by linearity of $\Lambda(\gamma_{C,R})-\Lambda(1)$ and the inner product given by

$$\begin{aligned}(\mathcal{A}v)_n &= \sum_{m\in\mathbb{Z}} \langle f, \phi_m\rangle_{1/2}\langle(\Lambda(\gamma_{C,R})-\Lambda(1))\phi_m, \phi_n\rangle_{1/2} \\ &= \langle(\Lambda(\gamma_{C,R})-\Lambda(1))f, \phi_n\rangle_{1/2}.\end{aligned}$$

Thus $\mathcal{A}$ maps the basis coefficients for f to the corresponding basis coefficients of $(\Lambda(\gamma_{C,R})-\Lambda(1))f$. Furthermore, $\mathcal{A}$ has the same eigenvalues as $\Lambda(\gamma_{C,R})-\Lambda(1)$, and the eigenvectors of $\mathcal{A}$ comprises the basis coefficients for the eigenfunctions of $\Lambda(\gamma_{C,R})-\Lambda(1)$. In practice we can only construct an N-term approximation $\mathcal{A}_N$

using the finite $\{\phi_n\}_{|n|\leq N}$ set of basis functions. Such a matrix is a representation of the operator

$$P_N(\Lambda(\gamma_{C,R}) - \Lambda(1))P_N,$$

where P_N is an orthogonal projection onto $\text{span}\{\phi_n\}_{|n|\leq N}$ in terms of the $\langle\cdot,\cdot\rangle_{1/2}$-inner product. For compact operators it is known from spectral theory (cf. [31, 21]) that eigenvalues and eigenfunctions of such N-term approximations converge as $N \to \infty$. From Figure 2 it is evident that it is possible to estimate the correct eigenvalues to machine precision using very small N if the basis $\{\phi_n\}_{n\in\mathbb{Z}}$ is well-chosen.

Let $f_n(\theta) \equiv \frac{1}{\sqrt{2\pi}} e^{in\theta}$ be the usual Fourier basis for $L^2(\partial\mathbb{D})$. Since $\{f_n\}_{n\in\mathbb{Z}}$ is an orthonormal basis in the usual $L^2(\partial\mathbb{D})$-inner product, it follows straightforwardly that $\phi_n \equiv \mathcal{M}_a f_n$ gives an orthonormal basis in the $\langle\cdot,\cdot\rangle_{1/2}$-inner product. It is a consequence of Proposition 2.2 and that $\mathcal{M}_a$ is bounded; by picking $f \in L^2(\partial\mathbb{D})$ then $\mathcal{M}_a f \in L^2(\partial\mathbb{D})$ so

$$\mathcal{M}_a f = \sum_{n\in\mathbb{Z}} \langle \mathcal{M}_a f, f_n\rangle f_n = \sum_{n\in\mathbb{Z}} \langle f, \phi_n\rangle_{1/2} f_n \Rightarrow f = \sum_{n\in\mathbb{Z}} \langle f, \phi_n\rangle_{1/2}\phi_n.$$

THEOREM 4.1. *Let $\hat{\lambda}_n$ be the n'th eigenvalue of $\Lambda(\gamma_{0,r}) - \Lambda(1)$ (cf. Proposition 3.1). Define the orthonormal basis $\{\phi_n\}_{n\in\mathbb{Z}}$ by*

$$\phi_n \equiv \mathcal{M}_a f_n, \quad f_n(\theta) \equiv \frac{1}{\sqrt{2\pi}} e^{in\theta}, \ \ n \in \mathbb{Z}.$$

Then $\Lambda(\gamma_{C,R}) - \Lambda(1)$ is represented in this basis via the following tridiagonal matrix:

$$\mathcal{A}_{m,n} \equiv \langle(\Lambda(\gamma_{C,R}) - \Lambda(1))\phi_m, \phi_n\rangle_{1/2} = \begin{cases} \frac{1+\rho^2}{1-\rho^2}\hat{\lambda}_m, & m = n, \\ \frac{-a}{1-\rho^2}\hat{\lambda}_m, & m - n = 1, \\ \frac{-\bar{a}}{1-\rho^2}\hat{\lambda}_m, & m - n = -1, \\ 0, & \text{else.} \end{cases}$$

Proof. Utilizing Lemma 2.3 and Proposition 2.2 (and that $\Lambda(\mathcal{M}_a 1) = \Lambda(1)$):

$$\begin{aligned} \langle(\Lambda(\gamma_{C,R}) - \Lambda(1))\phi_m, \phi_n\rangle_{1/2} &= \langle J_a^{1/2}\mathcal{M}_a(\Lambda(\gamma_{0,r}) - \Lambda(1))\mathcal{M}_a\mathcal{M}_a f_m, J_a^{1/2}\mathcal{M}_a f_n\rangle \\ &= \langle(\Lambda(\gamma_{0,r}) - \Lambda(1))f_m, J_a^{-1/2} f_n\rangle. \end{aligned}$$

Now using that f_m is an eigenfunction of $\Lambda(\gamma_{0,r}) - \Lambda(1)$ and the expression (2.7) for $J_a^{1/2}|_{\partial\mathbb{D}}$

$$\begin{aligned} \langle(\Lambda(\gamma_{C,R}) - \Lambda(1))\phi_m, \phi_n\rangle_{1/2} &= \frac{1}{2\pi}\langle(\Lambda(\gamma_{0,r}) - \Lambda(1))e^{im\theta}, J_a^{-1/2}e^{in\theta}\rangle \\ &= \frac{\hat{\lambda}_m}{2\pi}\langle e^{im\theta}, J_a^{-1/2}e^{in\theta}\rangle \\ &= \frac{\hat{\lambda}_m}{2\pi(1-\rho^2)}\int_0^{2\pi} e^{i(m-n)\theta}(1+\rho^2-2\rho\cos(\theta-\zeta))d\theta \\ &= \begin{cases} \frac{1+\rho^2}{1-\rho^2}\hat{\lambda}_m, & m = n, \\ \frac{-a}{1-\rho^2}\hat{\lambda}_m, & m - n = 1, \\ \frac{-\bar{a}}{1-\rho^2}\hat{\lambda}_m, & m - n = -1, \\ 0, & \text{else.} \end{cases} \end{aligned}$$

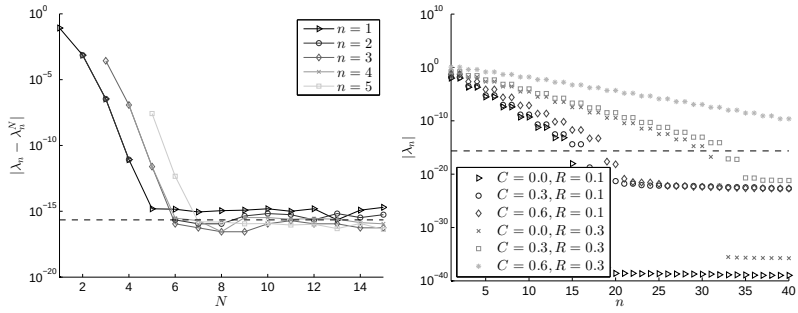

(a) (b)

Fig. 2: **(a):** Difference $|\lambda_n - \lambda_n^N|$ between the $n = 1, 2, \ldots, 5$ largest eigenvalues λ_n of $\Lambda(\gamma_{C,R}) - \Lambda(1)$ with $C = 0.7$ and $R = 0.2$, and the eigenvalues λ_n^N of the N-term approximation $\mathcal{A}_N$ from Theorem 4.1. **(b):** Largest $n = 1, 2, \ldots, 40$ eigenvalues of $\Lambda(\gamma_{C,R}) - \Lambda(1)$ for various values of C and R, estimated to machine precision (dashed line).

So the above calculation gives the matrix representation. □

The basis functions in Theorem 4.1 can explicitly be given in terms of θ. Since $M_a : \partial\mathbb{D} \to \partial\mathbb{D}$ then the angular variable θ is mapped to another angular variable $\psi_a(\theta)$, thus

$$\phi_n(\theta) = \frac{1}{\sqrt{2\pi}} e^{in\psi_a(\theta)} = \frac{1}{\sqrt{2\pi}} M_a(e^{i\theta})^n = \frac{1}{\sqrt{2\pi}} \left(\frac{e^{i\theta} - \rho e^{i\zeta}}{\rho e^{i(\theta-\zeta)} - 1} \right)^n, \quad n \in \mathbb{Z}.$$

REMARK 2. *The matrix $\mathcal{A}$ in Theorem 4.1 is not Hermitian as $\Lambda(\gamma_{C,R}) - \Lambda(1)$ is only self-adjoint in the regular $L^2(\partial\mathbb{D})$-inner product, and not in the weighted $\langle \cdot, \cdot \rangle_{1/2}$-inner product.*

The ratio of the norms in Theorem 3.4 have negligible dependence with respect to the amplitude A, compared to the radius r (note also that ρ in the bounds are independent of A). This can also be seen in terms of the Fréchet derivate of $\gamma \mapsto \Lambda(\gamma)$:

$$\frac{\|\Lambda(1 + A\chi_{B_{0,r}}) - \Lambda(1)\|}{\|\Lambda(1 + A\chi_{B_{C,R}}) - \Lambda(1)\|} = \frac{\|\Lambda'(1)\chi_{B_{0,r}} + o(A)/A\|}{\|\Lambda'(1)\chi_{B_{C,R}} + o(A)/A\|} \xrightarrow[A \to 0]{} \frac{\|\Lambda'(1)\chi_{B_{0,r}}\|}{\|\Lambda'(1)\chi_{B_{C,R}}\|}.$$

Therefore A will be kept fixed $A = 2$ in the following examples.

Figure 3 shows that for large inclusions with r close to 1 the lower bound of Theorem 3.4 comes reasonably close, while for small inclusions with r close to 0 the upper bound is quite tight for $\rho < 0.3$ (meaning inclusions close to the centre). It appears that as $r \to 0$ the distinguishability approaches a fixed curve (the curves for $r = 0.1$ and $r = 0.01$ are indistinguishable in the figure, and even $r = 0.5$ is quite close), lying in the middle of the lower and upper bounds.

The depth dependence of EIT is further exemplified in Figure 4a where the eigenvalues of $\Lambda(\gamma_{C,R}) - \Lambda(1)$ are shown for a fixed radius $R = 0.1$ as increasing functions of the centre $|C|$. Furthermore, the eigenfunction for the largest eigenvalue is shown

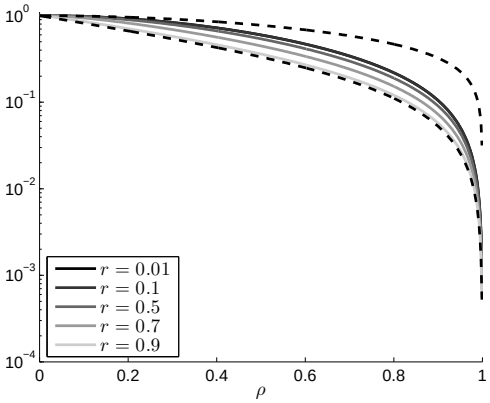

Fig. 3: Ratio $\|\Lambda(\gamma_{0,r}) - \Lambda(1)\|/\|\Lambda(\gamma_{C,R}) - \Lambda(1)\|$ for $|a| = \rho \in [0, 1)$ where R and C are determined from r and ρ by Proposition 2.1, along with the bounds (dashed lines) from Theorem 3.4.

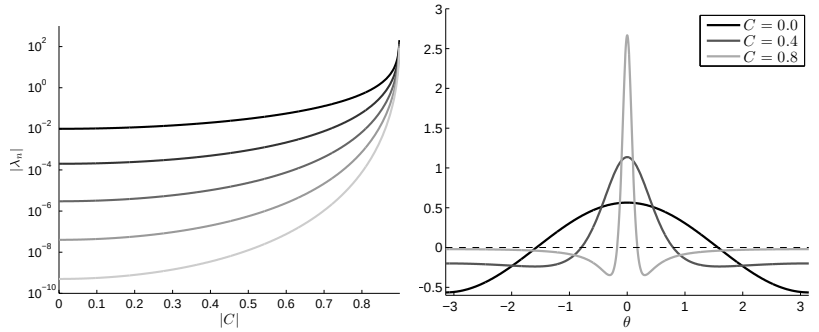

(a) (b)

Fig. 4: **(a):** 10 largest eigenvalues λ_n (each with multiplicity 2) of $\Lambda(\gamma_{C,R}) - \Lambda(1)$ with fixed $R = 0.1$ and $0 \leq |C| < 1 - R$. **(b):** Eigenfunction $f(\theta)$ (normalized in $\|\cdot\|$) corresponding to largest eigenvalue of $\Lambda(\gamma_{C,R}) - \Lambda(1)$ for fixed $R = 0.1$ and various values of C.

in Figure 4b, and how it changes from a cosine to a very localized function as the inclusion is moved closer to the boundary. The eigenfunctions corresponding to the largest eigenvalues are the best choice of (orthonormal) boundary conditions in practice, as they maximize the distinguishability. Therefore reconstruction is expected to be more noise robust when using the eigenfunctions in the measurements. So from the behaviour in Figure 4b it is not surprising that it is possible to numerically obtain

very reasonable local reconstructions in the case of partial data (where only part of the boundary is accessible), close to the measured boundary [11, 10].

5. Conclusions. We have characterized the Dirichlet-to-Neumann map for ball inclusions in the unit disk (and for the Neumann-to-Dirichlet map, cf. Appendix B), and have shown explicit lower and upper bounds on how much the distance of the inclusions to the boundary affects the operator norms. The bounds show a distinct depth dependence that can be utilized in numerical reconstruction, for instance by spatially varying regularization.

It is not known if the bounds are optimal, however through several examples it is demonstrated that the bounds accurately predicts the change in distinguishability. To verify the bounds and test their tightness numerically, exact matrix representations of the boundary operators were derived, where the matrix elements are given explicitly without the need for numerical integration or solution of PDEs.

Other forward models for EIT exists that in practical measurements can reduce modelling errors, such as the *complete electrode model* (CEM) [34]. However, in [18, 12] it was shown that the difference in the forward map of CEM and the continuum model, as well as their Fréchet derivatives, depends linearly on a parameter that characterize how densely the electrodes cover the boundary. It is therefore expected that, for sufficiently many boundary electrodes, any depth dependent properties of the continuum model will also be observed for the CEM.

The analysis was restricted to the 2D case, though it is natural to consider if the same bounds hold for the 3D unit ball. However, in higher dimensions $d \geq 3$ the harmonic morphisms only include orthogonal transformations and translation, while Möbius transformations generally preserve the d-Laplacian [25]. For this reason there is not a straightforward extension to 3D.

Appendix A. A monotonicity property of the DN map.

The results in this appendix are given for completeness due to a lack of proper reference.

For the Neumann-to-Dirichlet map a similar monotonicity relation as below is well-known and is used in reconstruction algorithms [12, 16, 17], where the right hand-side inequality is "flipped". In both cases of DN and ND maps the proof boils down to an application of a generalized Dirichlet principle.

LEMMA A.1. *Let $\gamma_1, \gamma_2 \in L^\infty_+(\Omega)$ be real-valued, then*

$$\gamma_1 \leq \gamma_2 \text{ a.e. in } \Omega \quad \text{implies} \quad \langle \Lambda(\gamma_1) f, f\rangle \leq \langle \Lambda(\gamma_2) f, f\rangle, \ \ \forall f \in H^{1/2}(\partial\Omega).$$

Proof. From the weak form of the continuum model then for any $\gamma \in L^\infty_+(\Omega)$ we have

$$\langle \Lambda(\gamma) f, h\rangle = \int_\Omega \gamma \nabla u \cdot \overline{\nabla v}\, dx, \ \ \forall v \in H^1(\partial\Omega), v|_{\partial\Omega} = h,$$

in particular

$$\int_\Omega \gamma \nabla u \cdot \overline{\nabla v}\, dx = 0, \ \ \forall v \in H^1_0(\partial\Omega). \tag{A.1}$$

So for $v \in H_0^1(\partial\Omega)$ then (A.1) implies

$$\begin{aligned}\int_\Omega \gamma|\nabla(u+v)|^2\,dx &= \int_\Omega \gamma\left(|\nabla u|^2 + |\nabla v|^2 + \nabla u\cdot\overline{\nabla v} + \nabla v\cdot\overline{\nabla u}\right)\,dx \\ &= \int_\Omega \gamma\left(|\nabla u|^2 + |\nabla v|^2\right)\,dx,\end{aligned}$$

or rather

$$\langle\Lambda(\gamma)f, f\rangle = \int_\Omega \gamma|\nabla u|^2\,dx = \inf\left\{\int_\Omega \gamma|\nabla w|^2\,dx : w\in H^1(\Omega), w|_{\partial\Omega} = f\right\}. \tag{A.2}$$

So for any boundary potential $f \in H^{1/2}(\partial\Omega)$, and with u_1 being the solution to (1.1) for γ_1 and u_2 the solution for γ_2. Then using $\gamma_1 \le \gamma_2$ in Ω, and the minimizing property (A.2)

$$\langle\Lambda(\gamma_1)f,f\rangle = \int_\Omega \gamma_1|\nabla u_1|^2\,dx \le \int_\Omega \gamma_1|\nabla u_2|^2\,dx \le \int_\Omega \gamma_2|\nabla u_2|^2\,dx = \langle\Lambda(\gamma_2)f,f\rangle.$$

□

This leads to the very intuitive conclusion that larger inclusions gives larger distinguishability.

COROLLARY A.2. *Let $A > -1$ and $D_1 \subseteq D_2 \subset \tilde{\Omega}$, where $\tilde{\Omega} \subsetneq \Omega$ such that $\operatorname{dist}(\tilde{\Omega}, \partial\Omega) > 0$, then*

$$\|\Lambda(1+A\chi_{D_1}) - \Lambda(1)\| \le \|\Lambda(1+A\chi_{D_2}) - \Lambda(1)\|.$$

Proof. The case $A \equiv 0$ is trivial. Let $A > 0$ then by Lemma A.1

$$\begin{aligned}0 &= \langle(\Lambda(1)-\Lambda(1))f,f\rangle \\ &\le \langle(\Lambda(1+A\chi_{D_1})-\Lambda(1))f,f\rangle \\ &\le \langle(\Lambda(1+A\chi_{D_2})-\Lambda(1))f,f\rangle,\ \ \forall f\in H^{1/2}(\partial\Omega),\end{aligned}$$

and similarly if $-1 < A < 0$:

$$\begin{aligned}0 &= \langle(\Lambda(1)-\Lambda(1))f,f\rangle \\ &\ge \langle(\Lambda(1+A\chi_{D_1})-\Lambda(1))f,f\rangle \\ &\ge \langle(\Lambda(1+A\chi_{D_2})-\Lambda(1))f,f\rangle,\ \ \forall f\in H^{1/2}(\partial\Omega).\end{aligned}$$

Thus for any $A > -1$:

$$|\langle(\Lambda(1+A\chi_{D_1})-\Lambda(1))f,f\rangle| \le |\langle(\Lambda(1+A\chi_{D_2})-\Lambda(1))f,f\rangle|,\ \ \forall f\in H^{1/2}(\partial\Omega). \tag{A.3}$$

Then the claim follows directly from (A.3) and that $H^{1/2}(\partial\Omega)$ is dense in $L^2(\partial\Omega)$

$$\begin{aligned}\|\Lambda(1+A\chi_{D_1})-\Lambda(1)\| &= \sup_{f\in H^{1/2}(\partial\Omega)\setminus\{0\}} \frac{|\langle(\Lambda(1+A\chi_{D_1})-\Lambda(1))f,f\rangle|}{\|f\|^2_{L^2(\partial\Omega)}} \\ &\le \sup_{f\in H^{1/2}(\partial\Omega)\setminus\{0\}} \frac{|\langle(\Lambda(1+A\chi_{D_2})-\Lambda(1))f,f\rangle|}{\|f\|^2_{L^2(\partial\Omega)}} \\ &= \|\Lambda(1+A\chi_{D_2})-\Lambda(1)\|.\end{aligned}$$

□

Appendix B. Distinguishability bounds and matrix characterizations for the Neumann-to-Dirichlet map.

In this appendix we give extensions to the distinguishability bounds as well as matrix representations in terms of the Neumann-to-Dirichlet (ND) map.

The ND map is the operator $\mathcal{R}(\gamma) : \nu \cdot \gamma \nabla u \mapsto u|_{\partial\Omega}$, where u is the solution to the conductivity equation subject to a Neumann boundary condition $g \in H_\diamond^{-1/2}(\partial\Omega)$

$$\nabla \cdot (\gamma \nabla u) = 0 \text{ in } \Omega, \quad \nu \cdot \gamma \nabla u = g \text{ on } \partial\Omega, \quad \int_{\partial\Omega} u \, ds = 0. \tag{B.1}$$

The latter condition in (B.1) is a grounding of the boundary potential, and is required to uniquely solve the PDE. Thus the ND map is an operator from $H_\diamond^{-1/2}(\partial\Omega)$ to $H_\diamond^{1/2}(\partial\Omega)$, where the $\diamond$-symbol indicates distributions/functions with zero mean on $\partial\Omega$. $\mathcal{R}(\gamma)$ is the inverse of $\Lambda(\gamma)$, if $\Lambda(\gamma)$ is restricted to $H_\diamond^{1/2}(\partial\Omega)$.

Returning to the domain $\Omega \equiv \mathbb{D}$ it is in this paper sufficient to consider $\mathcal{R}(\gamma) : L_\diamond^2(\partial\Omega) \to L_\diamond^2(\partial\Omega)$ with

$$L_\diamond^2(\partial\Omega) \equiv \{f \in L^2(\partial\Omega) : \langle f, 1\rangle = 0\},$$

for which $\mathcal{R}(\gamma)$ is compact and self-adjoint (unlike the DN map where a difference of two DN maps were required for compactness).

From the proof of Lemma 2.3 we may expect that $\mathcal{R}(\gamma_{C,R}) = \mathcal{M}_a \mathcal{R}(\gamma_{0,r}) J_a^{1/2} \mathcal{M}_a$, however we need to be slightly more careful. First of all $J_a^{1/2}\mathcal{M}_a(L_\diamond^2(\partial\mathbb{D})) = L_\diamond^2(\partial\mathbb{D})$ which follows from Proposition 2.2 where the boundary integral is preserved and that $J_a^{1/2}\mathcal{M}_a$ is an involution. However, we only have $\mathcal{M}_a(L_\diamond^2(\partial\mathbb{D})) \subset L^2(\partial\mathbb{D})$. What we end up with is an ND operator from $L_\diamond^2(\partial\mathbb{D})$ to $\mathcal{M}_a(L_\diamond^2(\partial\mathbb{D}))$, corresponding to changing the grounding condition in (B.1) to

$$\int_{\partial\mathbb{D}} J_a^{1/2} u|_{\partial\mathbb{D}} \, ds = 0.$$

Since the PDE and Neumann condition in (B.1) gives uniqueness up to a scalar (which is chosen by the grounding condition), we can obtain the correct operator in $\mathcal{L}(L_\diamond^2(\partial\mathbb{D}))$ by

$$\mathcal{R}(\gamma_{C,R}) = P\mathcal{M}_a \mathcal{R}(\gamma_{0,r}) J_a^{1/2} \mathcal{M}_a, \tag{B.2}$$

and similarly

$$\mathcal{R}(\gamma_{0,r}) = P\mathcal{M}_a \mathcal{R}(\gamma_{C,R}) J_a^{1/2} \mathcal{M}_a,$$

where $P \equiv \mathrm{Id} - L$ is the orthogonal projection of $L^2(\partial\mathbb{D})$ onto $L_\diamond^2(\partial\mathbb{D})$, with

$$Lf \equiv \frac{1}{2\pi} \int_{\partial\mathbb{D}} f \, ds, \quad f \in L^2(\partial\mathbb{D}).$$

While the change is minor, the projection is necessary for the transformed ND map $\mathcal{R}(\gamma_{C,R})$ to have any eigenvalues.

PROPOSITION B.1. *For $\gamma_{0,r} \equiv 1 + A\chi_{B_{0,r}}$ with $0 < r < 1$ and $A > -1$, the eigenfunctions of $\mathcal{R}(\gamma_{0,r})$ are $f_n(\theta) \equiv \frac{1}{\sqrt{2\pi}} e^{in\theta}$, $n \in \mathbb{Z} \setminus \{0\}$. The corresponding*

eigenvalues are

$$\lambda_n = \frac{2 + A(1 - r^{2|n|})}{2 + A(1 + r^{2|n|})} \frac{1}{|n|}, \quad n \neq 0.$$

The eigenvalues for the difference operator $\mathcal{R}(\gamma_{0,r}) - \mathcal{R}(1)$ *are*

$$\lambda_n = \frac{-2Ar^{2|n|}}{2 + A(1 + r^{2|n|})} \cdot \frac{1}{|n|}, \quad n \neq 0. \tag{B.3}$$

With the numbering given in (B.3)*, then* $|\lambda_n|$ *decays monotonically with increasing* $|n|$.

Proof. The eigenvalues can be derived from Proposition 3.1. Now define

$$f(x) = \frac{-2Ar^{2x}}{2 + A(1 + r^{2x})} \cdot \frac{1}{x}, \quad x > 0.$$

It follows immediately that

$$f'(x) = \frac{-2Ar^{2x}(2\log(r)x(A+2) - (A + 2 + Ar^{2x}))}{(A + 2 + Ar^{2x})^2 x^2}, \quad x > 0.$$

Since $0 < r < 1$ and $A > -1$ then $\log(r) < 0$, $A + 2 > 0$ and $A + 2 + Ar^{2x} > 0$. In the case $-1 < A < 0$ we have $f' < 0$ so f is a decreasing function, however $f > 0$. In the case $A > 0$ then $f' > 0$ so f is increasing, but $f < 0$. Collected we get that $|f|$ is decreasing. □

While Proposition B.1 seems obvious, the corresponding case for the DN-maps does not hold for all A and r, i.e. the eigenvalues for the DN-map difference does not decay monotonically with the usual numbering of the eigenvalues from the trigonometric basis.

Similar to Section 4 let $f_n(\theta) \equiv \frac{1}{\sqrt{2\pi}} e^{in\theta}$. Defining $\psi_n \equiv J_a^{1/2} \mathcal{M}_a f_n$ makes $\{\psi_n\}_{n \in \mathbb{Z} \setminus \{0\}}$ an orthonormal basis for $L^2_\diamond(\partial\mathbb{D})$ with respect to the $\langle \cdot, \cdot \rangle_{-1/2}$-inner product defined in (3.6).

THEOREM B.2. *Let either* $H(\gamma) \equiv \mathcal{R}(\gamma)$ *or* $H(\gamma) \equiv \mathcal{R}(\gamma) - \mathcal{R}(1)$*. Let* $\hat{\lambda}_n$ *be the* n*'th eigenvalue of* $H(\gamma_{0,r})$ *(cf. Proposition B.1), and denote by* h_n *the* n*'th Fourier coefficient of* $J_a^{1/2}$ *given by*

$$h_n = \begin{cases} 1 & n = 0, \\ \overline{a}^{|n|} & n > 0, \\ a^{|n|} & n < 0. \end{cases} \tag{B.4}$$

Define the orthonormal basis $\{\psi_n\}_{n \in \mathbb{Z} \setminus \{0\}}$ *by*

$$\psi_n \equiv J_a^{1/2} \mathcal{M}_a f_n, \quad f_n(\theta) \equiv \frac{1}{\sqrt{2\pi}} e^{in\theta}, \quad n \in \mathbb{Z} \setminus \{0\}.$$

Then $H(\gamma_{C,R})$ *is represented in this basis via the following matrix:*

$$\mathcal{A}_{n,m} \equiv \langle H(\gamma_{C,R})\psi_m, \psi_n \rangle_{-1/2} = \hat{\lambda}_m (h_{n-m} - \overline{h_m} h_n), \quad m, n \neq 0. \tag{B.5}$$

Proof. First the Fourier series of $J_a^{1/2}$ will be determined. Consider the case $\zeta = 0$:

$$J_\rho^{1/2}|_{e^{i\theta}} = \frac{1-\rho^2}{|\rho e^{i\theta}-1|^2} = 1 + \frac{\rho}{e^{-i\theta}-\rho} + \frac{\rho}{e^{i\theta}-\rho} = 1 + \sum_{n=1}^{\infty} \rho^n e^{in\theta} + \sum_{n=1}^{\infty} \rho^n e^{-in\theta},$$

where the series comes from geometric series of $\rho e^{i\theta}$ and $\rho e^{-i\theta}$, which converge as $0 \le \rho < 1$. Now $\zeta \neq 0$ corresponds to a translation by ζ in the θ-variable:

$$J_a^{1/2}|_{e^{i\theta}} = 1 + \sum_{n=1}^{\infty} \rho^n e^{in(\theta-\zeta)} + \sum_{n=1}^{\infty} \rho^n e^{-in(\theta-\zeta)} = 1 + \sum_{n=1}^{\infty} \overline{a}^n e^{in\theta} + \sum_{n=1}^{\infty} a^n e^{-in\theta},$$

which corresponds to the Fourier coefficients given in (B.4).

The adjoint of the projection operator P with respect to $\langle \cdot, \cdot \rangle_{-1/2}$ is

$$P^* = \mathrm{Id} - J_a^{1/2} L J_a^{-1/2}. \tag{B.6}$$

This follows from the calculation

$$\begin{aligned}
\langle Pf, g\rangle_{-1/2} &= \langle f, g\rangle_{-1/2} - \frac{1}{2\pi}\int_{\partial\mathbb{D}} f\,dx \int_{\partial\mathbb{D}} J_a^{-1/2}\overline{g}\,ds \\
&= \langle f, g\rangle_{-1/2} - \langle f, L J_a^{-1/2} g\rangle \\
&= \langle f, (\mathrm{Id} - J_a^{1/2} L J_a^{-1/2}) g\rangle_{-1/2}.
\end{aligned}$$

Let $m \neq 0$, then by (B.2) the terms of (B.5) can be expanded. Using P^* from (B.6) and the properties in Proposition 2.2 gives

$$\begin{aligned}
\mathcal{A}_{n,m} &= \langle H(\gamma_{C,R})\psi_m, \psi_n\rangle_{-1/2} \\
&= \langle P\mathcal{M}_a H(\gamma_{0,r}) J_a^{1/2}\mathcal{M}_a J_a^{1/2}\mathcal{M}_a f_m, J_a^{1/2}\mathcal{M}_a f_n\rangle_{-1/2} \\
&= \langle \mathcal{M}_a H(\gamma_{0,r}) f_m, J_a^{-1/2}(\mathrm{Id} - J_a^{1/2} L J_a^{-1/2}) J_a^{1/2}\mathcal{M}_a f_n\rangle \\
&= \hat{\lambda}_m \langle \mathcal{M}_a f_m, \mathcal{M}_a f_n\rangle - \hat{\lambda}_m \langle \mathcal{M}_a f_m, L\mathcal{M}_a f_n\rangle,
\end{aligned}$$

where in the last equality it was used that f_m is an eigenfunction of $H(\gamma_{0,r})$. Note that $\mathcal{M}_a L f = L f$ as it is constant, and

$$L\mathcal{M}_a f = \tfrac{1}{2\pi}\langle \mathcal{M}_a f, 1\rangle = \tfrac{1}{2\pi}\langle J_a^{1/2} f, 1\rangle = L J_a^{1/2} f.$$

Thus for $h_n = \frac{1}{\sqrt{2\pi}}\langle J_a^{1/2}, f_n\rangle = \frac{1}{2\pi}\int_0^{2\pi} J_a^{1/2} e^{-in\theta}\,d\theta$ being the n'th Fourier coefficient of $J_a^{1/2}$, then

$$\begin{aligned}
\mathcal{A}_{n,m} &= \frac{\hat{\lambda}_m}{\sqrt{2\pi}}\langle J_a^{1/2}, f_{n-m}\rangle - \hat{\lambda}_m \langle J_a^{1/2} f_m, L J_a^{1/2} f_n\rangle \\
&= \hat{\lambda}_m h_{n-m} - \hat{\lambda}_m \langle J_a^{1/2} f_m, 1\rangle \overline{L J_a^{1/2} f_n} \\
&= \hat{\lambda}_m h_{n-m} - \hat{\lambda}_m \overline{\langle J_a^{1/2}, f_m\rangle} \frac{1}{2\pi}\langle J_a^{1/2}, f_n\rangle \\
&= \hat{\lambda}_m (h_{n-m} - \overline{h_m} h_n), \quad m \neq 0.
\end{aligned}$$

Thereby concluding the proof. □

REMARK 3. *The ND map can also be considered on all of $L^2(\partial\mathbb{D})$ by introducing the null-space* $\operatorname{span}\{1\}$ *such that $\mathcal{A}$ is a matrix representation of $H(\gamma_{C,R})P$ instead of $H(\gamma_{C,R})$. In that case the row $n=0$ and column $m=0$, respectively, becomes*

$$\begin{aligned}\mathcal{A}_{0,m} &= \langle H(\gamma_{C,R})P\psi_m, \psi_0\rangle_{-1/2} = 0,\\ \mathcal{A}_{n,0} &= \langle H(\gamma_{C,R})P\psi_0, \psi_n\rangle_{-1/2} = -\sum_{k\neq 0} h_k \mathcal{A}_{n,k}.\end{aligned}$$

Now we obtain distinguishability bounds analogous to Theorem 3.4.

THEOREM B.3. *Let γ be either $\gamma_{0,r}$ or $\gamma_{C,R}$ and denote by $\|\cdot\|$ the operator norm on $\mathcal{L}(L^2_\diamond(\partial\mathbb{D}))$. From the weighted norms in* (3.5) *and* (3.6) *we have*

$$\|\mathcal{R}(\gamma)-\mathcal{R}(1)\| = \sup_{g\in L^2_\diamond(\partial\mathbb{D})\setminus\{0\}} \frac{\|(\mathrm{Id}-LJ_a^{1/2})(\mathcal{R}(\mathcal{M}_a\gamma)-\mathcal{R}(1))g\|_{1/2}}{\|g\|_{-1/2}}. \tag{B.7}$$

Furthermore the following bounds hold:

$$\frac{1-\rho}{1+\rho}\|\mathcal{R}(\gamma_{C,R})-\mathcal{R}(1)\| \le \|\mathcal{R}(\gamma_{0,r})-\mathcal{R}(1)\| \le \frac{\sqrt{1+\rho^2}}{1-\rho^2}\|\mathcal{R}(\gamma_{C,R})-\mathcal{R}(1)\|. \tag{B.8}$$

Proof. By (B.2)

$$\begin{aligned}\|\mathcal{R}(\gamma)-\mathcal{R}(1)\|^2 &= \sup_{g\in L^2_\diamond(\partial\mathbb{D})\setminus\{0\}} \frac{\|P\mathcal{M}_a(\mathcal{R}(\mathcal{M}_a\gamma)-\mathcal{R}(1))J_a^{1/2}\mathcal{M}_a g\|^2}{\|g\|^2}\\ &= \sup_{g\in L^2_\diamond(\partial\mathbb{D})\setminus\{0\}} \frac{\int_{\partial\mathbb{D}}|P\mathcal{M}_a(\mathcal{R}(\mathcal{M}_a\gamma)-\mathcal{R}(1))J_a^{1/2}\mathcal{M}_a g|^2\,ds}{\int_{\partial\mathbb{D}} J_a^{1/2}|\mathcal{M}_a g|^2\,ds}.\end{aligned}$$

Utilizing that $J_a^{1/2}\mathcal{M}_a(L^2_\diamond(\partial\mathbb{D})) = L^2_\diamond(\partial\mathbb{D})$, we can substitute $J_a^{1/2}\mathcal{M}_a g$ with g, and afterwards use that $P\mathcal{M}_a = \mathcal{M}_a - LJ_a^{1/2}$

$$\begin{aligned}\|\mathcal{R}(\gamma)-\mathcal{R}(1)\|^2 &= \sup_{g\in L^2_\diamond(\partial\mathbb{D})\setminus\{0\}} \frac{\int_{\partial\mathbb{D}}|P\mathcal{M}_a(\mathcal{R}(\mathcal{M}_a\gamma)-\mathcal{R}(1))g|^2\,ds}{\int_{\partial\mathbb{D}} J_a^{-1/2}|g|^2\,ds}\\ &= \sup_{g\in L^2_\diamond(\partial\mathbb{D})\setminus\{0\}} \frac{\int_{\partial\mathbb{D}}|(\mathcal{M}_a - LJ_a^{1/2})(\mathcal{R}(\mathcal{M}_a\gamma)-\mathcal{R}(1))g|^2\,ds}{\int_{\partial\mathbb{D}} J_a^{-1/2}|g|^2\,ds}.\end{aligned}$$

Applying the change of variables $\mathcal{M}_a$ and $\mathcal{M}_a L = L$ yields the expression in (B.7)

$$\begin{aligned}\|\mathcal{R}(\gamma)-\mathcal{R}(1)\|^2 &= \sup_{g\in L^2_\diamond(\partial\mathbb{D})\setminus\{0\}} \frac{\int_{\partial\mathbb{D}} J_a^{1/2}|(\mathrm{Id}-LJ_a^{1/2})(\mathcal{R}(\mathcal{M}_a\gamma)-\mathcal{R}(1))g|^2\,ds}{\int_{\partial\mathbb{D}} J_a^{-1/2}|g|^2\,ds}\\ &= \sup_{g\in L^2_\diamond(\partial\mathbb{D})\setminus\{0\}} \frac{\|(\mathrm{Id}-LJ_a^{1/2})(\mathcal{R}(\mathcal{M}_a\gamma)-\mathcal{R}(1))g\|_{1/2}^2}{\|g\|_{-1/2}^2}.\end{aligned}$$

Now let $\hat{g}_1 \equiv e^{i\theta}$ which by Proposition B.1 is the eigenfunction corresponding to the largest eigenvalue $\hat{\lambda}_1$ for $\mathcal{R}(\gamma_{0,r})-\mathcal{R}(1)$. Let λ_1 be the largest eigenvalue for

$\mathcal{R}(\gamma_{C,R}) - \mathcal{R}(1)$, then (B.7) implies

$$
\begin{aligned}
|\lambda_1|^2 &= \|\mathcal{R}(\gamma_{C,R}) - \mathcal{R}(1)\|^2 \\
&= \sup_{g \in L^2_\diamond(\partial\mathbb{D})\setminus\{0\}} \frac{\int_{\partial\mathbb{D}} J_a^{1/2} |(\mathrm{Id} - L J_a^{1/2})(\mathcal{R}(\gamma_{0,r}) - \mathcal{R}(1))g|^2 \, ds}{\int_{\partial\mathbb{D}} J_a^{-1/2} |g|^2 \, ds} \\
&\geq |\hat{\lambda}_1|^2 \frac{\int_{\partial\mathbb{D}} J_a^{1/2} |(\mathrm{Id} - L J_a^{1/2})\hat{g}_1|^2 \, ds}{\int_{\partial\mathbb{D}} J_a^{-1/2} \, ds} \qquad \text{(B.9)} \\
&= \frac{|\hat{\lambda}_1|^2}{2\pi} \frac{1-\rho^2}{1+\rho^2} \int_{\partial\mathbb{D}} J_a^{1/2} |(\mathrm{Id} - L J_a^{1/2})\hat{g}_1|^2 \, ds, \qquad \text{(B.10)}
\end{aligned}
$$

where the integral of $J_a^{-1/2}$ was calculated in (3.11). Expanding $J_a^{1/2}$ in its Fourier series from (B.4) gives $J_a^{1/2}\hat{g}_1 = \sum_{k\in\mathbb{Z}} h_k e^{i(k+1)\theta}$, thus

$$
L J_a^{1/2} \hat{g}_1 = \frac{1}{2\pi} \int_{\partial\mathbb{D}} J_a^{1/2} \hat{g}_1 \, ds = \frac{1}{2\pi} \sum_{k\in\mathbb{Z}} h_k \int_0^{2\pi} e^{i(k+1)\theta} \, d\theta = h_{-1} = a. \qquad \text{(B.11)}
$$

By inserting (B.11) into (B.10), again applying the Fourier series of $J_a^{1/2}$ from (B.4) and that $\int_{\partial\mathbb{D}} J_a^{1/2} \, ds = 2\pi$ gives the upper bound

$$
\begin{aligned}
|\lambda_1|^2 &\geq \frac{|\hat{\lambda}_1|^2}{2\pi} \frac{1-\rho^2}{1+\rho^2} \int_0^{2\pi} J_a^{1/2} |e^{i\theta} - a|^2 \, d\theta \\
&= \frac{|\hat{\lambda}_1|^2}{2\pi} \frac{1-\rho^2}{1+\rho^2} \int_0^{2\pi} J_a^{1/2} (1 + \rho^2 - \overline{a} e^{i\theta} - a e^{-i\theta}) \, d\theta \\
&= \frac{|\hat{\lambda}_1|^2}{2\pi} \frac{1-\rho^2}{1+\rho^2} \left[2\pi(1+\rho^2) - \int_0^{2\pi} \left(\overline{a} \sum_{k\in\mathbb{Z}} h_k e^{i(k+1)\theta} + a \sum_{k\in\mathbb{Z}} h_k e^{i(k-1)\theta} \right) d\theta \right] \\
&= \frac{|\hat{\lambda}_1|^2}{2\pi} \frac{1-\rho^2}{1+\rho^2} \left[2\pi(1+\rho^2) - 2\pi(\overline{a} h_{-1} + a h_1) \right] \\
&= |\hat{\lambda}_1|^2 \frac{(1-\rho^2)^2}{1+\rho^2}.
\end{aligned}
$$

Thus

$$
\|\mathcal{R}(\gamma_{0,r}) - \mathcal{R}(1)\| = |\hat{\lambda}_1| \leq \frac{\sqrt{1+\rho^2}}{1-\rho^2} |\lambda_1| = \frac{\sqrt{1+\rho^2}}{1-\rho^2} \|\mathcal{R}(\gamma_{C,R}) - \mathcal{R}(1)\|.
$$

Now consider the opposite case for (B.9), and let g_1 be a normalized (in $\|\cdot\|_{L^2(\partial\mathbb{D})}$) eigenfunction corresponding to the largest eigenvalue λ_1 of $\mathcal{R}(\gamma_{C,R}) - \mathcal{R}(1)$. Using the bounds (3.7)

$$
\begin{aligned}
|\hat{\lambda}_1|^2 &= \|\mathcal{R}(\gamma_{0,r}) - \mathcal{R}(1)\|^2 \\
&= \sup_{g \in L^2_\diamond(\partial\mathbb{D})\setminus\{0\}} \frac{\|(\mathrm{Id} - L J_a^{1/2})(\mathcal{R}(\gamma_{C,R}) - \mathcal{R}(1))g\|_{1/2}^2}{\|g\|_{-1/2}^2} \\
&\geq |\lambda_1|^2 \frac{\|(\mathrm{Id} - L J_a^{1/2}) g_1\|_{1/2}^2}{\|g_1\|_{-1/2}^2} \\
&\geq |\lambda_1|^2 \left(\tfrac{1-\rho}{1+\rho} \right)^2 \|(\mathrm{Id} - L J_a^{1/2}) g_1\|^2.
\end{aligned}
$$

Now utilizing that $g_1 \in L^2_\diamond(\partial\mathbb{D})$, so as $LJ_a^{1/2}g_1$ is constant then $\langle LJ_a^{1/2}g_1, g_1\rangle = 0$:

$$\begin{aligned} |\hat{\lambda}_1|^2 &\geq |\lambda_1|^2 \left(\tfrac{1-\rho}{1+\rho}\right)^2 (\|g_1\|^2 + \|LJ_a^{1/2}g_1\|^2) \\ &= |\lambda_1|^2 \left(\tfrac{1-\rho}{1+\rho}\right)^2 (1 + 2\pi|LJ_a^{1/2}g_1|^2) \\ &\geq |\lambda_1|^2 \left(\tfrac{1-\rho}{1+\rho}\right)^2, \end{aligned} \tag{B.12}$$

which gives the lower bound in (B.8). □

Numerically it can be verified (cf. Figure 5a) that

$$\|\mathcal{R}(\gamma_{C,R}) - \mathcal{R}(1)\| \leq \|\mathcal{R}(\gamma_{0,r}) - \mathcal{R}(1)\|,$$

which is a stronger bound than in Theorem B.3. However, in the proof even the bound (B.12) which depends on g_1 does not give $\|\mathcal{R}(\gamma_{C,R}) - \mathcal{R}(1)\| \leq \|\mathcal{R}(\gamma_{0,r}) - \mathcal{R}(1)\|$ in general.

REMARK 4. *It is possible to remove the projection operator P in Theorem B.3, which led to its lengthy proof, by writing the norm as*

$$\|\mathcal{R}(\gamma) - \mathcal{R}(1)\| = \sup_{g \in L^2_\diamond(\partial\mathbb{D})\setminus\{0\}} \frac{|\langle P\mathcal{M}_a(\mathcal{R}(\mathcal{M}_a\gamma) - \mathcal{R}(1))J_a^{1/2}\mathcal{M}_a g, g\rangle|}{\|g\|^2},$$

and abusing that P is self-adjoint in the usual $L^2(\partial\mathbb{D})$-inner product (as it is an orthogonal projection). The proof would give the same lower bound, however it leads to the worse upper bound with the term $(1+\rho^2)/(1-\rho^2)$ instead of $\sqrt{1+\rho^2}/(1-\rho^2)$.

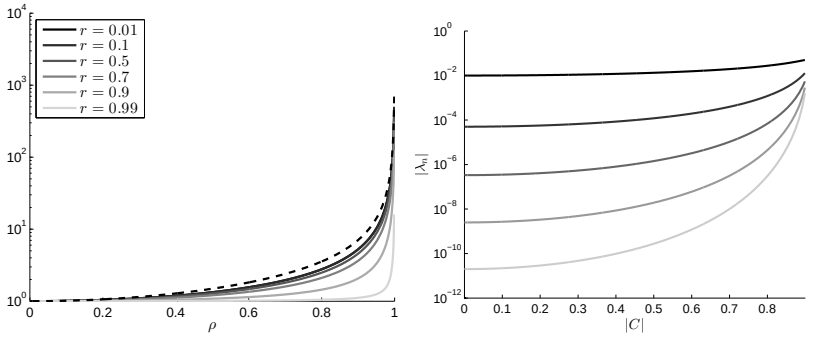

(a) (b)

Fig. 5: **(a):** Ratio $\|\mathcal{R}(\gamma_{0,r}) - \mathcal{R}(1)\|/\|\mathcal{R}(\gamma_{C,R}) - \mathcal{R}(1)\|$ for $|a| = \rho \in [0,1)$ where R and C are determined from r and ρ by Proposition 2.1, along with the upper bound (dashed line) from Theorem B.3. **(b):** 10 largest eigenvalues λ_n (each with multiplicity 2) of $\mathcal{R}(\gamma_{C,R}) - \mathcal{R}(1)$ with fixed $R = 0.1$ and $0 \leq |C| < 1 - R$.

Figure 5a shows that the upper bound in Theorem B.3 is very reasonable for small inclusions with r close to 0. Furthermore, it shows (for the chosen examples) that the distinguishability is decreasing as ρ is increased, meaning $\|\mathcal{R}(\gamma_{C,R}) - \mathcal{R}(1)\| \leq$

$\|\mathcal{R}(\gamma_{0,r}) - \mathcal{R}(1)\|$. This is different from what was observed for the DN map in Figure 3, however it is worth noting that the radius R is decreasing with ρ, and in Figure 5b where the radius is kept fixed, the distinguishability is increasing. Thus, for the ND map the distinguishability is increasing at a slower rate as the distance to the boundary is reduced (compared to the DN map), and is not able to overcome the change in radius from r to R. It is therefore worth noting that reconstruction based on ND- and DN-maps are fundamentally different in terms of depth dependence.

REFERENCES

[1] I. Akduman and R. Kress, *Electrostatic imaging via conformal mapping*, Inverse Problems, 18 (2002), pp. 1659–1672.

[2] G. Alessandrini, *Stable determination of conductivity by boundary measurements*, Applicable Analysis, 27 (1988), pp. 153–172.

[3] H. Ammari, J. Garnier, and K. Sølna, *Partial data resolving power of conductivity imaging from boundary measurements*, SIAM Journal on Mathematical Analysis, 45 (2013), pp. 1704–1722.

[4] K. Astala and L. Päivärinta, *Calderón's inverse conductivity problem in the plane*, Annals of Mathematics, 163 (2006), pp. 265–299.

[5] F. Brock, *An isoperimetric inequality for eigenvalues of the Stekloff problem*, ZAMM Z. Angew. Math. Mech., 81 (2001), pp. 69–71.

[6] A.-P. Calderón, *On an inverse boundary value problem*, in Seminar on Numerical Analysis and its Applications to Continuum Physics (Rio de Janeiro, 1980), Soc. Brasil. Mat., Rio de Janeiro, 1980, pp. 65–73.

[7] M. Cheney and D. Isaacson, *Distinguishability in impedance imaging*, IEEE Transactions on Biomedical Engineering, 39 (1992), pp. 852–860.

[8] H. Cornean, K. Knudsen, and S. Siltanen, *Towards a d-bar reconstruction method for three-dimensional* eit , Journal of Inverse and Ill-Posed Problems, 14 (2006), pp. 111–134.

[9] A. Fraser and R. Schoen, *The first Steklov eigenvalue, conformal geometry, and minimal surfaces*, Adv. Math., 226 (2011), pp. 4011–4030.

[10] H. Garde and K. Knudsen, *3D reconstruction for partial data electrical impedance tomography using a sparsity prior*, in Dynamical Systems and Differential Equations, AIMS Proceedings 2015 Proceedings of the 10th AIMS International Conference (Madrid, Spain), American Institute of Mathematical Sciences (AIMS), nov 2015, pp. 495–504.

[11] ———, *Sparsity prior for electrical impedance tomography with partial data*, Inverse Probl. Sci. Eng., 24 (2016), pp. 524–541.

[12] H. Garde and S. Staboulis, *Convergence and regularization for monotonicity-based shape reconstruction in electrical impedance tomography*, Submitted manuscript. Available from http://arxiv.org/abs/1512.01718, (2016).

[13] M. Gehre, T. Kluth, C. Sebu, and P. Maass, *Sparse 3D reconstructions in electrical impedance tomography using real data*, Inverse Probl. Sci. Eng., 22 (2014), pp. 31–44.

[14] B. Haberman and D. Tataru, *Uniqueness in Calderón's problem with Lipschitz conductivities*, Duke Math. J., 162 (2013), pp. 497–516.

[15] M. Hanke, N. Hyvönen, and S. Reusswig, *Convex source support and its application to electric impedance tomography*, SIAM J. Imaging Sci., 1 (2008), pp. 364–378.

[16] B. Harrach and M. Ullrich, *Monotonicity-based shape reconstruction in electrical impedance tomography*, SIAM Journal on Mathematical Analysis, 45 (2013), pp. 3382–3403.

[17] ———, *Resolution guarantees in electrical impedance tomography*, IEEE Transactions on Medical Imaging, 34 (2015), pp. 1513–1521.

[18] N. Hyvönen, *Approximating idealized boundary data of electric impedance tomography by electrode measurements.*, Mathematical Models and Methods in Applied Sciences, 19 (2009), pp. 1185–1202.

[19] M. Ikehata and S. Siltanen, *Numerical method for finding the convex hull of an inclusion in conductivity from boundary measurements*, Inverse Problems, 16 (2000), pp. 1043–1052.

[20] D. Isaacson, *Distinguishability of conductivities by electric current computed tomography*, IEEE Transactions on Medical Imaging, 5 (1986), pp. 91–95.

[21] T. Kato, *Perturbation theory for linear operators*, vol. 132, Springer Verlag, 1995.

[22] R. Kress, *Conformal mapping and impedance tomography*, J. Phys.: Conf. Ser., 290 (2011), p. 012009.

[23] ———, *Inverse problems and conformal mapping*, Complex Variables and Elliptic Equations,

57 (2012), pp. 301–316.
[24] N. Mandache, *Exponential instability in an inverse problem for the Schrödinger equation*, Inverse Problems, 17 (2001), pp. 1435–1444.
[25] J. J. Manfredi and V. Vespri, *n-harmonic morphisms in space are mbius transformations.*, The Michigan Mathematical Journal, 41 (1994), pp. 135–142.
[26] J. L. Mueller and S. Siltanen, *Linear and Nonlinear Inverse Problems with Practical Applications*, SIAM, oct 2012.
[27] A. I. Nachman, *Reconstructions from boundary measurements*, Annals of Mathematics, 128 (1988), pp. 531–576.
[28] ———, *Global uniqueness for a two-dimensional inverse boundary value problem*, Annals of Mathematics, 143 (1996), pp. 71–96.
[29] S. Nagayasu, G. Uhlmann, and J.-N. Wang, *A depth-dependent stability estimate in electrical impedance tomography*, Inverse Problems, 25 (2009), p. 075001.
[30] R. G. Novikov, *A multidimensional inverse spectral problem for the equation* $-\delta\psi + (v(x) - eu(x))\psi = 0$, Functional Analysis and Its Applications, 22 (1988), pp. 263–272.
[31] J. Osborn, *Spectral approximation for compact operators*, Mathematics of Computation, 29 (1975), pp. 712–725.
[32] M. Reed and B. Simon, *Methods of modern mathematical physics. IV. Analysis of operators*, Academic Press [Harcourt Brace Jovanovich, Publishers], New York-London, 1978.
[33] B. Saka and A. Yilmaz, *Elliptic cylinder geometry for distinguishability analysis in impedance tomography*, IEEE Transactions on Biomedical Engineering, 51 (2004), pp. 126–132.
[34] E. Somersalo, M. Cheney, and D. Isaacson, *Existence and uniqueness for electrode models for electric current computed tomography*, SIAM Journal on Applied Mathematics, 52 (1992), pp. 1023–1040.
[35] E. M. Stein and R. Shakarchi, *Complex analysis*, Princeton Lectures in Analysis, II, Princeton University Press, Princeton, NJ, 2003.
[36] J. Sylvester and G. Uhlmann, *A global uniqueness theorem for an inverse boundary value problem*, Annals of Mathematics, 125 (1987), pp. 153–169.
[37] R. Winkler and A. Rieder, *Resolution-controlled conductivity discretization in electrical impedance tomography*, SIAM J. Imaging Sci., 7 (2014), pp. 2048–2077.

PAPER B

Convergence and regularization for monotonicity-based shape reconstruction in electrical impedance tomography

Type	Submitted manuscript (2016)
Authors	Henrik Garde and Stratos Staboulis
Available from	`http://arxiv.org/abs/1512.01718`

Convergence and regularization for monotonicity-based shape reconstruction in electrical impedance tomography

Henrik Garde · Stratos Staboulis

Abstract The inverse problem of electrical impedance tomography is severely ill-posed, meaning that, only limited information about the conductivity can in practice be recovered from boundary measurements of electric current and voltage. Recently it was shown that a simple monotonicity property of the related Neumann-to-Dirichlet map can be used to characterize shapes of inhomogeneities in a known background conductivity. In this paper we formulate a monotonicity-based shape reconstruction scheme that applies to approximative measurement models, and regularizes against noise and modelling error. We demonstrate that for admissible choices of regularization parameters the inhomogeneities are detected, and under reasonable assumptions, asymptotically exactly characterized. Moreover, we rigorously associate this result with the complete electrode model, and describe how a computationally cheap monotonicity-based reconstruction algorithm can be implemented. Numerical reconstructions from both simulated and real-life measurement data are presented.

Keywords electrical impedance tomography · inverse problems · monotonicity method · regularization · complete electrode model · direct reconstruction methods

Mathematics Subject Classification (2000) 35R30 · 35Q60 · 35R05 · 65N21

1 Introduction

In *electrical impedance tomography* (EIT), the aim is to extract information about the internal properties of a physical object by external measurements of electric current and voltage. In practice, through a set of surface electrodes, currents of

H. Garde · S. Staboulis
Department of Applied Mathematics and Computer Science
Technical University of Denmark
2800 Kgs. Lyngby, Denmark
E-mail: ssta@dtu.dk

H. Garde
E-mail: hgar@dtu.dk

prescribed magnitudes are conducted into the object and the voltages needed for maintaining the currents are recorded. The obtained current-voltage data are used for imaging the internal electrical conductivity distribution of the object. Examples of EIT applications include, among others, monitoring patient lung function, control of industrial processes, non-destructive testing of materials, and locating mineral deposits [3,8,12,42].

In EIT, electricity inside the domain is modelled by the *conductivity equation*

$$\nabla \cdot (\gamma \nabla u) = 0, \quad \text{in } \Omega \tag{1}$$

where $\Omega \subset \mathbb{R}^n$ describes the spatial dimensions of the object, $\gamma = \gamma(x)$ the conductivity (or admittivity) distribution, and $u = u(x)$ the potential of the electric field. The ideal data obtainable by current-voltage measurements are characterized by the *Neumann-to-Dirichlet operator* $\Lambda(\gamma)$ which relates a boundary current density to the corresponding boundary potential through a Neumann-problem for (1).

The *inverse conductivity problem* is stated as "given $\Lambda(\gamma)$, determine γ". The problem has been extensively studied during the past decades [6,35,42] — the known solvability conditions depend on the spatial dimension. In the plane, a general bounded real-valued γ with a positive lower bound is uniquely determined by $\Lambda(\gamma)$ as long as Ω is simply connected [1]. In the three-dimensional space, more regularity of Ω and γ is in general required [39]. Despite the unique solvability, the mapping $\Lambda(\gamma) \mapsto \gamma$ has points of discontinuity in the L^∞-norm [3]. Therefore, the problem of reconstructing a general γ from $\Lambda(\gamma)$ is ill-posed in the sense of Hadamard.

A practical version of the inverse conductivity problem is "given a noisy and discrete approximation of $\Lambda(\gamma)$, reconstruct information about γ". Arguably, the most flexible framework for computational EIT reconstruction is provided by iterative output least-squares type methods [7,21,30,43] which work with realistic measurement models and allow incorporation of prior information into the model. However, in many applications, full-scale imaging may not be the top priority — especially if it is computationally expensive due to high dimensionality of the computational domain. Instead, one may be interested in locating conductivity inhomogeneities in a known and/or uninteresting background medium. A variety of iterative [10,24] and direct inhomogeneity detection methods have been introduced and elaborately studied. Two of the most prominent direct EIT methods relevant to this work are *the factorization method* [4,5,13,14,31] and *the enclosure method* [26,27], which rely on repetitive but computationally very cheap testing of criteria that theoretically characterize shapes of conductivity inhomogeneities.

In this paper we study the *monotonicity method*, the idea of which originates in [19,40,41]. This direct method detects conductivity inhomogeneities by utilizing the fact that the forward map $\gamma \mapsto \Lambda(\gamma)$ is monotonically decreasing. To describe the method's main idea, suppose for simplicity that Ω has a smooth boundary and that the target conductivity is of form $\gamma = 1 + \chi_D$ where $D \subseteq \Omega$ is an unknown open set we would like to reconstruct. The monotonicity property implies that if a ball $B \subseteq D$ then $\Lambda(1+\chi_B) - \Lambda(\gamma) \geq 0$ in the sense of semidefiniteness. Therefore, the collection $\mathcal{M}$ of all open balls satisfying the latter criterion forms a cover for D. Recently, it was shown that, if D has no holes, the converse holds: $\cup\mathcal{M}$ coincides with D. Moreover, the result remains valid even if $\Lambda(1+\chi_B)$ is replaced with the affine approximation $\Lambda(1) + \frac{1}{2}\Lambda'(1)\chi_B$ (note the factor $\frac{1}{2}$) regardless of

the possibly large linearization error [19]. The affine formulation is numerically tempting as the Fréchet derivative can be calculated ahead of time and applied by evaluating computationally cheap matrix-vector products.

A key property of the monotonicity method is that it can be trivially formulated using the realistic *complete electrode model* (CEM) — just by replacing $\Lambda(\gamma)$ by its CEM counterpart. The feasibility of the CEM-based monotonicity method was first considered in [20]. By suitably relaxing the monotonicity test, it was shown that a non-trivial upper bound for D can be obtained from inaccurate CEM data. In this paper, we consider the converse, that is, whether a sequence of suitably regularized reconstructions $\mathcal{M}_\alpha$ in some sense converges to a limit as the discretization error and measurement noise level tend to zero. We study this question by extending the ideas of [19] where *B-dependent* regularization of the monotonicity method is discussed.

Our main theoretical result (Theorem 1) states that, as a suitable sequence of regularization parameters tends to zero, the noisy and discrete semidefiniteness test converges *uniformly* in B to the continuum counterpart. As a corollary, we obtain the set-theoretic convergence of the regularized reconstruction $\mathcal{M}_\alpha$ to the idealistic $\mathcal{M}$. To be more precise, we formulate the above results in terms of a certain class of admissible approximate models for $\Lambda(\gamma)$. However, we also rigorously show how the results apply to the CEM by constructing approximate sequences for a Fréchet derivative of $\gamma \mapsto \Lambda(\gamma)$ of arbitrary order (Theorems 2–3 and Remark 4). The approximation technique generalizes the ideas of [23] which studies the CEM in the limit as the number of electrodes grows towards infinity. All in all, this paper is thematically comparable to [31] where a rigorous asymptotic connection between the factorization method and the CEM is established.

Before describing the structure of this paper, let us make some general comments on the extensions and limitations of the considered reconstruction method. Compared to other direct inhomogeneity detection techniques, the monotonicity method has the advantage that the inhomogeneity characterization results naturally extend to the *indefinite case* [19] (both jumps and drops off the background conductivity). Although fast and easy to implement, a drawback of the standard implementation is that it requires the knowledge of the background conductivity. Fortunately, as in the context of the factorization method [17], this problem can be partly avoided if A/C measurements with different frequencies are available. The appropriate analysis is carried out in [16] where the monotonicity method is generalized to complex-valued admittivities.

The contents of this article are organised as follows. In section 2 the idealized continuum model (CM) of EIT is rigorously defined, and its fundamental monotonicity properties are revised. In section 3 the regularized monotonicity method is formulated and the main result (Theorem 1) of the paper is proven. Section 4 introduces the CEM and demonstrates how it can be used to construct approximations to the CM. Two alternative algorithmic implementations of the monotonicity method are described in section 5. Moreover, a theoretical justification for the algoritmic use of the CEM is given. Finally, in section 6, the CEM-based reconstruction algorithms are tested numerically in two and three spatial dimensions for simulated measurements, and in two dimensions for real-life (cylindrically symmetric) water tank measurement data.

2 Electrical impedance tomography based on monotonicity

In this section we formulate the continuum model (CM) and revise its fundamental monotonicity property that motivates the monotonicity method. For simplicity, we only consider static EIT where all electric quantities are modelled by real-numbers. Generalizations of the method for A/C measurements, that is, complex-valued quantities, can be found in [16].

2.1 Continuum model

Let $\Omega \subset \mathbb{R}^n$, $n = 2$ or 3, be a bounded domain with $\mathscr{C}^\infty$-regular boundary $\partial\Omega$. Consider the elliptic boundary value problem

$$\begin{aligned} &\nabla \cdot (\gamma \nabla u) = 0, \ \text{ in } \Omega, \\ &\nu \cdot \gamma \nabla u = f, \qquad \text{on } \partial\Omega, \end{aligned} \tag{2}$$

where ν denotes the outward-pointing unit normal of $\partial\Omega$ and the real-valued coefficient function $\gamma = \gamma(x)$ belongs to

$$L^\infty_+(\Omega) = \{w \in L^\infty(\Omega) : \operatorname{ess\,inf} w > 0\}.$$

By the Lax–Milgram theorem, for a given Neumann-boundary datum

$$f \in L^2_\diamond(\partial\Omega) = \{w \in L^2(\partial\Omega) : \langle w, \mathbb{1}\rangle = 0\}, \tag{3}$$

problem (2) has a unique weak solution

$$u \in H^1_\diamond(\Omega) = \{w \in H^1(\Omega) : \langle w|_{\partial\Omega}, \mathbb{1}\rangle = 0\}. \tag{4}$$

Above and from here on $\langle\cdot,\cdot\rangle$ denotes the $L^2(\partial\Omega)$-inner product, $w|_{\partial\Omega}$ stands for the trace of w on $\partial\Omega$, and $\mathbb{1} \equiv 1$ on $\partial\Omega$. In electrostatics, u models the electric potential in Ω induced by the electrical conductivity distribution γ and the input current density f. The extra conditions in the function space definitions (3) and (4) correspond to current conservation law and choice of ground level of potential, respectively.

The idealistic infinite precision data related to electric current-voltage boundary measurements are characterized by the *Neumann-to-Dirichlet (ND) map*

$$\Lambda(\gamma) : L^2_\diamond(\partial\Omega) \to L^2_\diamond(\partial\Omega), \qquad f \mapsto u|_{\partial\Omega},$$

where u is the solution to (2). Note that by density, knowledge of $\Lambda(\gamma)$ is tantamount to knowing every boundary current-voltage density pair

$$(f, u|_{\partial\Omega}) \in H^{-1/2}_\diamond(\partial\Omega) \times H^{1/2}_\diamond(\partial\Omega)$$

connected via a more general formulation of (2) for less regular input current densities. The operator $\Lambda(\gamma)$ is linear and bounded, that is, it belongs to the space $\mathcal{L}(L^2_\diamond(\partial\Omega))$ of bounded linear operators from $L^2_\diamond(\partial\Omega)$ to itself. Furthermore, it is straightforward to show that $\Lambda(\gamma)$ is self-adjoint (see e.g. [3]). On the other hand, the mapping

$$\gamma \mapsto \Lambda(\gamma) \colon L^\infty_+(\Omega) \to \mathcal{L}(L^2_\diamond(\partial\Omega))$$

is non-linear since clearly $\Lambda(c\gamma) = \Lambda(\gamma)/c$ for any constant $c > 0$. Despite being non-linear, the mapping is still very regular as it is analytic in $\gamma \in L^\infty_+(\Omega)$ (cf. Appendix B).

Although the CM is feasible in proving interesting solvability and uniqueness results, it should be emphasized that the model is not very accurate in predicting real-life measurements. This is because, in practice, point-wise boundary current densities are out of reach and realistic electrodes cause a shunting effect which the CM does not directly account for [9,38]. Be that as it may, the operator $\Lambda(\gamma) \in \mathcal{L}(L^2_\diamond(\partial\Omega))$ as well as its linearization is compact due to the compact embedding $H^{1/2}(\partial\Omega) \subset\subset L^2(\partial\Omega)$. Therefore, it seems natural that they can be approximated accurately by finite-dimensional electrode model-based matrices. Before returning to this question in section 4, we recapitulate the ideas behind the monotonicity method.

2.2 Monotonicity-based characterization of inclusions

The following principle forms the basis of the monotonicity method in EIT [18,19, 41].

Proposition 1 *For two arbitrary conductivities $\gamma, \tilde\gamma \in L^\infty_+(\Omega)$ it holds*

$$\int_\Omega \frac{\tilde\gamma}{\gamma}(\gamma - \tilde\gamma)|\nabla\tilde u|^2 dx \le \langle(\Lambda(\tilde\gamma) - \Lambda(\gamma))f, f\rangle \le \int_\Omega (\gamma - \tilde\gamma)|\nabla\tilde u|^2 dx \tag{5}$$

where $f \in L^2_\diamond(\partial\Omega)$ is arbitrary and $\tilde u \in H^1_\diamond(\Omega)$ solves

$$\nabla\cdot(\tilde\gamma\nabla\tilde u) = 0 \ \text{ in } \Omega, \qquad \nu\cdot\tilde\gamma\nabla\tilde u = f \ \text{ on } \partial\Omega.$$

Proof See, e.g., [19, Lemma 3.1]. □

In what follows, we focus on detecting (definite) conductivity inhomogeneities, or *inclusions*, lying in a known background. For the ease of presentation, we define the notion of an inclusion.

Definition 1 Consider a conductivity distribution of the form $\gamma = \gamma_0 + \kappa\chi_D$, where $\gamma_0 \in L^\infty_+(\Omega)$ is piecewise analytic, $\kappa \in L^\infty_+(\Omega)$, and D is open with $\overline{D} \subseteq \Omega$. The set D is called a positive *inclusion* with respect to the background conductivity γ_0.

In the rest of the paper, γ is implicitly assumed to be as in Definition 1 unless otherwise mentioned.

Proposition 1 gives rise to the following method for computing upper estimates for the inclusion D. Assume $0 < \beta \le \kappa$ and let $B \subseteq \Omega$ be an arbitrary open ball. As a consequence of Proposition 1 we have

$$B \subseteq D \quad \text{implies} \quad \Lambda(\gamma_0 + \beta\chi_B) - \Lambda(\gamma) \ge 0 \tag{6}$$

in the sense of semidefiniteness. Here χ_B is the characteristic function of B. Denoting the collection of all admissible open balls by

$$\mathcal{M} = \{B \subseteq \Omega \text{ open ball} : \Lambda(\gamma_0 + \beta\chi_B) - \Lambda(\gamma) \ge 0\}, \tag{7}$$

we get the upper estimate

$$D \subseteq \cup\mathcal{M}. \tag{8}$$

Accurate numerical approximation of $\mathcal{M}$ can be costly, as it typically requires computation of a large number of forward solutions to (2).

Faster formulation of the semidefiniteness tests in (7) can be derived by linearizing the operator $\gamma \mapsto \Lambda(\gamma)$ around $\gamma = \gamma_0$. In fact, this modification also yields an upper bound for D analogous to (8). To see this, suppose that γ is as in Definition 1. As a consequence of Proposition 1 and the Fréchet derivative (see (52) in Appendix B), we obtain

$$\langle (\Lambda(\gamma_0) + \beta\Lambda'(\gamma_0)\chi_B - \Lambda(\gamma))f, f\rangle \geq \int_\Omega \left(\frac{\gamma_0\kappa}{\gamma}\chi_D - \beta\chi_B\right)|\nabla u_0|^2 dx$$

for any $f \in L^2_\diamond(\partial\Omega)$ and $u_0 \in H^1_\diamond(\Omega)$ solving

$$\nabla\cdot(\gamma_0\nabla u_0) = 0 \ \text{ in } \Omega, \qquad \nu\cdot\gamma_0\nabla u_0 = f \ \text{ on } \partial\Omega.$$

In particular (cf. (6)) we deduce

$$B \subseteq D \quad \text{implies} \quad \Lambda(\gamma_0) + \beta\Lambda'(\gamma_0)\chi_B - \Lambda(\gamma) \geq 0 \tag{9}$$

provided that $0 < \beta \leq \gamma_0\kappa/\gamma$. By defining

$$\mathcal{M}' = \left\{B \subseteq \Omega \text{ open ball} : \Lambda(\gamma_0) + \beta\Lambda'(\gamma_0)\chi_B - \Lambda(\gamma) \geq 0\right\}, \tag{10}$$

we have

$$D \subseteq \cup\mathcal{M}' \tag{11}$$

which is analogous to (8). Computational approximation of the set $\mathcal{M}'$ is the main idea behind the reconstruction algorithm studied in this paper. A particular advantage of this approach is that the Fréchet derivative $\Lambda'(\gamma_0)$ can be computed ahead of time since it only depends on the (known) background conductivity γ_0 and object Ω but not on B or β. More theoretical plausibility for the monotonicity method is given by the following result which, in a sense, complements relations (6) and (9) [19].

Proposition 2 *Assume that $\gamma \in L^\infty_+(\Omega)$ is as in Definition 1. Then, for any constant $\beta > 0$,*

$$\Lambda(\gamma_0 + \beta\chi_B) - \Lambda(\gamma) \geq 0 \quad \textit{or} \quad \Lambda(\gamma_0) + \beta\Lambda'(\gamma_0)\chi_B - \Lambda(\gamma) \geq 0 \tag{12}$$

implies

$$B \subseteq D^\bullet = \overline{\Omega} \setminus \cup\{U \subseteq \mathbb{R}^n \setminus D \textit{ open and connected} : U \cap \partial\Omega \neq \emptyset\}.$$

Note that $D^\bullet$ corresponds to the smallest closed set containing D and having connected complement. Consequently, by (7) *and* (10)*, the conditions*

$$D \subseteq \cup\mathcal{M} \subseteq D^\bullet \quad \textit{if} \quad 0 < \beta \leq \operatorname{ess\,inf}\kappa, \tag{13}$$

$$D \subseteq \cup\mathcal{M}' \subseteq D^\bullet \quad \textit{if} \quad 0 < \beta \leq \operatorname{ess\,inf}\left(\frac{\gamma_0\kappa}{\gamma}\right). \tag{14}$$

hold true. Note also that if D has connected complement, then $D^\bullet = \overline{D}$.

Proof The claim follows directly from [19, Theorem 4.1 and Theorem 4.3] which are proven using the theory of *localized potentials* [11]. It should be noted that the piecewise analyticity assumption in Definition 1 is a sufficient condition for the existence of such potentials. The intuition behind (12) can roughly be described as follows. If $B \not\subseteq D^\bullet$, then $\gamma_0 + \beta\chi_B \geq \gamma$ in $B \setminus D^\bullet$. Consequently, each of the semidefiniteness conditions in (12) can be contradicted by constructing sequences of potentials having simultaneously very large energy in $B \setminus D^\bullet$ and very small energy in $D^\bullet$. □

Remark 1 In the original version of Proposition 2 [19, Theorem 4.1 and Theorem 4.3], the upper bound in the counterparts of (13) and (14) is formulated as the "outer support" $\mathrm{out}_{\partial\Omega}(\kappa\chi_D)$. Using Definition 1 and [19, Definition 2.3 (c) and (d)], it is easy to point out that this set coincides with $D^\bullet$.

Relations (13) and (14) indicate that both $\mathcal{M}$ and $\mathcal{M}'$ can contain significant information about D. However, due to ill-posedness, the associated semidefiniteness tests can be expected to be sensitive with respect to measurement noise and modelling error. Aiming for stable numerical implementation we introduce a regularized variant of the semidefiniteness tests.

3 Regularized monotonicity-based reconstruction

In practice, the infinite precision measurement $\Lambda(\gamma)$ is out of reach, and moreover, only approximate numerical models are available for computational monotonicity tests. We model a collection of abstract approximate forward models by a family of compact self-adjoint operators $\{\Lambda_h(\gamma)\}_{h>0}$ such that

$$\|\Lambda(\gamma) - \Lambda_h(\gamma)\|_{\mathcal{L}(L^2_\diamond(\partial\Omega))} \leq \omega(h)\|\gamma\|_{L^\infty(\Omega)}, \quad \lim_{h\to 0}\omega(h) = 0 \tag{15}$$

for any $\gamma \in L^\infty_+(\Omega)$, where ω is independent of γ. In addition to systematic modelling error, real-life measurements are also corrupted by noise caused by imperfections of the measurement device. We assume the following additive noise model

$$\Lambda_h^\delta(\gamma) = \Lambda_h(\gamma) + N^\delta,$$

where the noise is modelled by a family of compact and self-adjoint operators

$$N^\delta \colon L^2_\diamond(\partial\Omega) \to L^2_\diamond(\partial\Omega), \qquad \|N^\delta\|_{\mathcal{L}(L^2_\diamond(\partial\Omega))} \leq \delta. \tag{16}$$

Note that, by symmetrizing if necessary, the self-adjointness assumption of the error operator can be made without loss of generality.

To facilitate reading, we use the following abbreviations for certain operators and the related infimal eigenvalues. For a given open set $B \subseteq \Omega$ we denote

$$\begin{aligned} T(B) &= \Lambda(\gamma_0 + \beta\chi_B) - \Lambda(\gamma), \\ T_h(B) &= \Lambda_h(\gamma_0 + \beta\chi_B) - \Lambda_h(\gamma), \\ T_h^\delta(B) &= \Lambda_h(\gamma_0 + \beta\chi_B) - \Lambda_h^\delta(\gamma). \end{aligned} \tag{17}$$

As all operators in (17) are self-adjoint, their spectra are contained in $\mathbb{R}$. Moreover, by Hilbert–Schmidt theorem [36], the eigenvalues of any infinite dimensional, compact and self-adjoint Hilbert space operator S accumulate at zero implying

$$-\|S\| \leq \inf \sigma(S) \leq 0$$

where $\sigma(S)$ denotes the spectrum of S.

To guarantee a meaningful noisy reconstruction, we introduce a regularized version of (7) with the help of the relaxed ball collections

$$\mathcal{M}_\alpha(S) = \{B \subseteq \Omega \text{ open ball} : S(B) + \alpha \operatorname{Id} \geq 0\} \tag{18}$$

where $\alpha \in \mathbb{R}$ is a regularization parameter and $S = S(B)$ is a compact operator for each $B \subseteq \Omega$. Next we investigate in which sense and under which conditions the set $\mathcal{M}_\alpha(T_h^\delta)$ converges to $\mathcal{M}_0(T)$, as the error parameters h and δ tend to zero. To establish an asymptotic relationship, we resort to the following lemma which is a consequence of spectral continuity [29].

Lemma 1 *Let S and T be bounded self-adjoint operators on a Hilbert space H. Then*

$$|\inf \sigma(S) - \inf \sigma(T)| \leq \|S - T\|_{\mathcal{L}(H)} \tag{19}$$

Proof We begin by noting that (19) trivially holds if its left-hand side vanishes. Hence, by symmetry we may assume that $\inf \sigma(S) < \inf \sigma(T)$. There exists a sequence $\{\lambda_j\}_{j=1}^\infty \subseteq \sigma(S)$ such that

$$\lim_{j\to\infty} \lambda_j = \inf \sigma(S)$$

and $\inf \sigma(S) \leq \lambda_j < \inf \sigma(T)$ for all j. By the continuity of the spectrum [29, Chapter V §4, Theorem 4.10], we have

$$\operatorname{dist}(\lambda_j, \sigma(T)) \leq \sup_{\lambda\in\sigma(S)} \operatorname{dist}(\lambda, \sigma(T)) \leq \|S - T\|_{\mathcal{L}(H)}.$$

Consequently

$$\|S - T\|_{\mathcal{L}(H)} \geq \operatorname{dist}(\lambda_j, \sigma(T)) = \inf_{\mu\in\sigma(T)} |\lambda_j - \mu| = \inf \sigma(T) - \lambda_j$$

and hence, by taking the limit, we deduce

$$\inf \sigma(T) - \inf \sigma(S) = \lim_{j\to\infty} \operatorname{dist}(\lambda_j, \sigma(T)) \leq \|S - T\|_{\mathcal{L}(H)}$$

which concludes the proof. □

As a special consequence of Lemma 1, (15), and (16) we obtain

$$|\inf \sigma(T_h^\delta(B)) - \inf \sigma(T(B))| \leq \omega(h) \left(\|\gamma_0\|_{L^\infty(\Omega)} + \beta + \|\gamma\|_{L^\infty(\Omega)}\right) + \delta$$

which implies that

$$\lim_{h,\delta\to 0} \inf \sigma(T_h^\delta(B)) = \inf \sigma(T(B)) \tag{20}$$

uniformly in $B \subseteq \Omega$.

The following theorem shows that, with a suitable sequence of regularization parameters $\alpha \in \mathbb{R}$, the set $\mathcal{M}_0(T)$ can be, in a sense, stably approximated by the sequence $\mathcal{M}_\alpha(T_h^\delta)$.

Theorem 1 *Suppose that the regularization parameter $\alpha = \alpha(h,\delta) \in \mathbb{R}$ satisfies*

$$\delta - \alpha(h,\delta) \leq \inf_{B \in \mathcal{M}_0(T)} \inf \sigma(T_h(B)) \quad \text{and} \quad \lim_{h,\delta \to 0} \alpha(h,\delta) = 0. \tag{21}$$

Then for any given $\lambda > 0$ there exists an $\varepsilon_\lambda > 0$ such that

$$\mathcal{M}_0(T) \subseteq \mathcal{M}_{\alpha(h,\delta)}(T_h^\delta) \subseteq \mathcal{M}_\lambda(T) \tag{22}$$

for all $h, \delta \in (0, \varepsilon_\lambda]$.

Proof Let us start by noting that according to (20) and Lemma 2 of Appendix A, the conditions (21) are not contradictory, and thus, the set of admissible sequences of regularization parameters is not empty.

To prove the left-hand set inclusion in (22), let $B \in \mathcal{M}_0(T)$ be an arbitrary open ball. First we note that, by a basic property of the infimal eigenvalue and (21), we have

$$T_h(B) \geq \inf \sigma(T_h(B)) \operatorname{Id} \geq (\delta - \alpha(h,\delta)) \operatorname{Id}. \tag{23}$$

From (16) we obtain $\delta \operatorname{Id} \geq N^\delta$, which together with (23) yields

$$T_h^\delta(B) + \alpha(h,\delta) \operatorname{Id} = T_h(B) - N^\delta + \alpha(h,\delta) \operatorname{Id} \geq \delta \operatorname{Id} - N^\delta \geq 0.$$

This shows that $B \in \mathcal{M}_{\alpha(h,\delta)}(T_h^\delta)$ for all $h, \delta > 0$. In particular, the left-hand set inclusion in (22) holds.

To prove the right-hand set inclusion in (22), let $\lambda > 0$ be arbitrary. According to (21) and the uniform convergence (20), there exists an $\varepsilon_\lambda > 0$ such that

$$\alpha(h,\delta) \leq \frac{\lambda}{2}, \quad \inf \sigma(T_h^\delta(B)) \leq \inf \sigma(T(B)) + \frac{\lambda}{2}$$

for all $h, \delta \in (0, \varepsilon_\lambda]$ and open balls $B \subseteq \Omega$. Moreover, by definition (18), any open ball $B \in \mathcal{M}_{\alpha(h,\delta)}(T_h^\delta)$ satisfies

$$0 \leq \inf \sigma(T_h^\delta(B)) + \alpha(h,\delta) \leq \inf \sigma(T(B)) + \lambda \tag{24}$$

which implies that $\mathcal{M}_{\alpha(h,\delta)}(T_h^\delta) \subseteq \mathcal{M}_\lambda(T)$ for all $h, \delta \in (0, \varepsilon_\lambda]$. □

Compared to $\mathcal{M}_\alpha(T_h^\delta)$, the family $\mathcal{M}_\lambda(T)$ has the favourable monotone decreasing property

$$0 < \lambda \leq \mu \;\text{ implies }\; \mathcal{M}_\lambda(T) \subseteq \mathcal{M}_\mu(T). \tag{25}$$

This yields the set-theoretic limit (defined as in e.g. [37])

$$\lim_{\lambda \to 0} \mathcal{M}_\lambda(T) = \bigcap_{\lambda > 0} \mathcal{M}_\lambda(T) = \mathcal{M}_0(T) \tag{26}$$

where the left and right equalities follow from the monotone decreasing property (25) and the definition of $\mathcal{M}_\lambda(T)$, respectively. As a consequence of (26) and Theorem 1, we obtain a corresponding limit for $\mathcal{M}_\alpha(T_h^\delta)$.

Corollary 1 *Let the regularization parameter be as in* (21)*. Then we have the set-theoretic limit*

$$\lim_{h,\delta \to 0} \mathcal{M}_{\alpha(h,\delta)}(T_h^\delta) = \mathcal{M}_0(T) = \bigcap_{h,\delta > 0} \mathcal{M}_{\alpha(h,\delta)}(T_h^\delta). \tag{27}$$

Proof The fact that the set-theoretic limit exists and coincides with $\mathcal{M}_0(T)$ is a direct consequence of the "squeeze principle" enforced by (22) and (26). Note that the considered family of sets is not necessarily decreasing; hence, the right-hand equality in (27) has to be proven separately. In the proof of Theorem 1 it is shown that $\mathcal{M}_0(T) \subseteq \mathcal{M}_{\alpha(h,\delta)}(T_h^\delta)$ for all $h, \delta > 0$, implying the "$\supseteq$"-direction. The "$\subseteq$"-direction follows from (24) by letting $h, \delta \to 0$ and recalling (20). □

Remark 2 Suppose that the inclusion D has a connected complement, and that $|D| = |\overline{D}|$. Assume further that the approximate operator family satisfies the monotonicity property: $\gamma \geq \tilde{\gamma}$ implies $\Lambda_h(\tilde{\gamma}) - \Lambda_h(\gamma) \geq 0$ for all $\gamma, \tilde{\gamma} \in L^\infty_+(\Omega)$. By Proposition 2 we have $\cup\mathcal{M}_0(T) \subseteq \overline{D}$. Hence, by monotonicity and choosing β as in (13) yields

$$T_h(B) \geq T_h(\cup\mathcal{M}_0(T)) \geq T_h(\overline{D}) = T_h(D) \geq 0$$

for any $B \in \mathcal{M}_0(T)$. Consequently, the choice $\alpha(h, \delta) = \delta$ is in this case sufficient for obtaining (27).

Remark 3 The results indicated by Theorem 1, Corollary 1, and Remark 2 straightforwardly adapt to the linearized version (11). To complete the proofs it is sufficient, in addition to (15), to assume that we have

$$\|\Lambda'(\gamma)\eta - \Lambda'_h(\gamma)\eta\|_{\mathcal{L}(L^2_\diamond(\partial\Omega))} \leq \omega(h)\|\gamma\|_{L^\infty(\Omega)}\|\eta\|_{L^\infty(\Omega)} \tag{28}$$

for all $\eta \in L^\infty(\Omega)$. Furthermore, the definitions (17) have to be modified accordingly.

While the above asymptotic results are formulated between the somewhat abstract ball collections, a relevant question is whether an analogue of (27) holds for their unions which — according to Proposition 2 — can be directly compared to conductivity inclusions. In particular, such a result would imply

$$D \subseteq \lim_{h,\delta\to 0} \cup\mathcal{M}_{\alpha(h,\delta)}(T_h^\delta) \subseteq D^\bullet$$

with the convergence in the sense of the Lebesgue measure. With straightforward modifications, the proof of Theorem 1 can be adapted to the case where the ball collections are replaced with the unions

$$\cup\mathcal{M}_\lambda(T) \quad \text{and} \quad \cup\,\mathcal{M}_\alpha(T_h^\delta).$$

Moreover, the former family is monotonously decreasing (cf. (25)) allowing a set-theoretic limit and convergence in the Lebesgue measure. However, currently we are not aware of a non-trivial relationship between (cf (26))

$$\bigcap_{\lambda>0} \cup\mathcal{M}_\lambda(T) \quad \text{and} \quad \cup\,\mathcal{M}_0(T).$$

To demonstrate the present difficulty, pick a point x that belongs to $\cup\mathcal{M}_\lambda(T)$ for all $\lambda > 0$. Then for each $\lambda > 0$ there exists an open ball $B_\lambda \in \mathcal{M}_\lambda(T)$ which contains x. However, without further specifications, this does not imply the existence of a *fixed* ball B that would contain x and lie in $\mathcal{M}_\lambda(T)$ for all $\lambda > 0$.

4 Approximating infinite-precision data by realistic models

The most widely used model for real-life EIT measurements is the CEM which is capable of predicting measurement data up to instrument precision [8,9,38]. In this section, we define the CEM and review its fundamental monotonicity property analogous to (5). Subsequently, we point out that — under some reasonable regularity assumptions — the CEM can be used to construct sequences of approximate operators of type (15) and (28) for both $\Lambda(\gamma)$ and $\Lambda'(\gamma)$, respectively.

4.1 Complete electrode model

The CEM is formally defined by the boundary value problem

$$\begin{aligned} &\nabla\cdot(\gamma\nabla v)=0, && \text{in } \Omega,\\ &\nu\cdot\gamma\nabla v=0, && \text{on } \partial\Omega\setminus\textstyle\bigcup_{j=1}^{k}\overline{E_j},\\ &v+z_j\nu\cdot\gamma\nabla v=V_j, && \text{on } E_j,\\ &\displaystyle\int_{E_j}\nu\cdot\gamma\nabla v\,dS=I_j, && j=1,2,\dots k, \end{aligned} \tag{29}$$

where the open, connected and mutually disjoint sets $E_j\subseteq\partial\Omega$ model the electrode patches attached to the outer boundary of the object. For a given conductivity $\gamma\in L^\infty_+(\Omega)$, contact impedance $z\in\mathbb{R}^k_+$, and net input current pattern

$$I\in\mathbb{R}^k_\diamond=\left\{W\in\mathbb{R}^k:\sum_{j=1}^{k}W_j=0\right\},$$

a unique weak solution pair

$$(v,V)\in H^1(\Omega)\oplus\mathbb{R}^k_\diamond$$

to problem (29) exists [38,22]. The electrode measurement data related to γ (and z) are fully characterized by the bounded, linear, and self-adjoint [38] *measurement map*

$$R(\gamma):\mathbb{R}^k_\diamond\to\mathbb{R}^k_\diamond,\qquad I\mapsto V.$$

Here I and V model the net input currents and the net voltages perceived by the electrodes, respectively. Note that $R(\gamma)$ depends also on the contact impedance z. However, this dependence will be omitted except in Proposition 3 where its values may vary.

Compared to the CM (2), the CEM has a more complicated mathematical formulation (29). Partly due to this, CEM-based EIT is not theoretically well-understood. In particular, virtually all known uniqueness and stability results — and the related reconstruction techniques — for the inverse conductivity problem are formulated in terms of the CM. However, by the following proposition, the monotonicity principle (5) extends quite naturally to the CEM framework [20].

Proposition 3 *Consider two arbitrary conductivities $\gamma, \tilde{\gamma} \in L^\infty_+(\Omega)$ and contact impedances $z, \tilde{z} \in \mathbb{R}^k_+$. Denote*

$$c_0 = \int_\Omega \frac{\tilde{\gamma}}{\gamma}(\gamma - \tilde{\gamma})|\nabla \tilde{v}|^2 dx + \sum_{j=1}^k \int_{E_j} \frac{z_j}{\tilde{z}_j}\Big(\frac{1}{z_j} - \frac{1}{\tilde{z}_j}\Big)|\tilde{v} - \tilde{V}_j|^2 dS,$$
$$c_1 = \int_\Omega (\gamma - \tilde{\gamma})|\nabla \tilde{v}|^2 dx + \sum_{j=1}^k \int_{E_j} \Big(\frac{1}{z_j} - \frac{1}{\tilde{z}_j}\Big)|\tilde{v} - \tilde{V}_j|^2 dS,$$

where $(\tilde{v}, \tilde{V})$ is the solution pair to (29) corresponding to the input current $I \in \mathbb{R}^k_\diamond$, conductivity $\tilde{\gamma}$, and contact impedance $\tilde{z} \in \mathbb{R}^k_+$. Then it holds

$$c_0 \leq I^{\mathrm{T}}(R(\tilde{\gamma}, \tilde{z}) - R(\gamma, z))I \leq c_1.$$

Proof See [20, Theorem 2]. □

Proposition 3 implies, in particular, that counterparts of (6) and (9) hold in the CEM framework.

4.2 Approximating $\Lambda(\gamma)$ using the measurement map $R(\gamma)$

The relationship between $\Lambda(\gamma) \in \mathcal{L}(L^2_\diamond(\partial\Omega))$ and $R(\gamma) \in \mathcal{L}(\mathbb{R}^k_\diamond)$ has been studied e.g. in [31,23]. In what follows, we review the approach in [23] because it is simple to formulate, and it gives a good error estimate. The method relies on the concept of open and mutually disjoint *extended electrodes* $\{E_j^+\}_{j=1}^k$ that are assumed (together with the actual electrodes) to satisfy

$$E_j \subseteq E_j^+ \subseteq \partial\Omega, \quad \bigcup_{j=1}^k \overline{E_j^+} = \partial\Omega, \quad \min_{j=1,\ldots,k} \frac{|E_j|}{|E_j^+|} \geq c \tag{30}$$

where $c > 0$ is a constant independent of the set of electrodes in question. The mappings $\Lambda(\gamma)$ and $R(\gamma)$ can be compared with the help of the adjoint pair $Q\colon \mathbb{R}^k \to L^2(\partial\Omega)$ and $Q^*\colon L^2(\partial\Omega) \to \mathbb{R}^k$ defined via

$$QW = \sum_{j=1}^k W_j \chi_j^+, \quad (Q^* f)_j = \int_{E_j^+} f dS$$

where χ_j^+ denotes the characteristic function of E_j^+. A thorough motivation of the notion of extended electrodes can be found in [23].

As indicated by the following theorem, under reasonable assumptions on the regularity of E_j^+ and $\partial\Omega$, the infinite precision EIT data can be approximated using the CEM with an error directly proportional to the maximal extended electrode width.

Theorem 2 *Let $P\colon L^2(\partial\Omega) \to \mathbb{R}^k$ and $L\colon L^2(\partial\Omega) \to L^2_\diamond(\partial\Omega)$ be the orthogonal projectors*[1] *defined via*

$$(Pf)_j = \fint_{E_j} f\,dS, \quad Lf = f - \fint_{\partial\Omega} f dS, \tag{31}$$

and denote the maximal extended electrode diameter by $h = \max_j \operatorname{diam}(E_j^+)$. Assume that the extended electrodes are regular enough[2] *so that the Poincaré inequality-type estimate*

$$\|(\mathrm{Id} - QP)f\|_{L^2(\partial\Omega)} \leq Ch \inf_{c\in\mathbb{R}} \|f + c\|_{H^1(\partial\Omega)}, \tag{32}$$

holds for all $f \in H^1(\partial\Omega)$ with a constant $C > 0$ independent of h. Then we have

$$\|\Lambda(\gamma) - LQ(R(\gamma) - Z)Q^*\|_{\mathcal{L}(L^2_\diamond(\partial\Omega))} \leq Ch\|\gamma\|_{L^\infty(\Omega)} \tag{33}$$

for any γ as in Definition 1 with a constant $C > 0$ independent of γ and h. Here $Z \in \mathbb{R}^{k\times k}$ is the diagonal matrix with the non-zero entries $Z_{jj} = z_j/|E_j|$.

Proof The claim follows from [23, Proof of Theorem 4.1] with the following minor modifications. First of all, note that the projector Q^* and the matrix Z are defined slightly differently here because [23] formulates (29) in terms of mean electrode currents instead of the total currents used in this paper. Moreover, for the proof, it is essential that QZQ^* is uniformly bounded with respect to h. This is ensured by assuming the rightmost condition in (30). Finally, in [23] the forward models are formulated in the quotient space framework, that is, choice of ground level potential is circumvented by letting $\Lambda(\gamma)$ and $R(\gamma)$ take values in spaces $L^2(\partial\Omega)/\mathbb{R}$ and $\mathbb{R}^k/\mathbb{R}$, respectively. With the above modifications to Q and Z, it is straightforward to see that the whole difference operator in (33) equals its counterpart in [23] up to an isometry between $L^2(\partial\Omega)/\mathbb{R}$ and $L^2_\diamond(\partial\Omega)$.

Above it was pointed out that, under suitable assumptions, the CEM provides a linearly convergent approximation to the CM as the number of electrodes grows in a suitable manner. Next we point out that the same holds true also for the linearized versions of the models.

Theorem 3 *Let $\eta \in L^\infty(\Omega)$ be compactly supported in Ω. Under the same assumptions as in Theorem 2, there holds*

$$\|\Lambda'(\gamma)\eta - LQ(R'(\gamma)\eta)Q^*\|_{\mathcal{L}(L^2_\diamond(\partial\Omega))} \leq Ch\|\gamma\|_{L^\infty(\Omega)}\|\eta\|_{L^\infty(\Omega)},$$

where h is the maximal diameter of E_j^+ and $C > 0$ is a constant independent of h, γ, and η.

[1] The former in the sense in which $\mathbb{R}^k$ is identified with the subspace of $L^2(\partial\Omega)$ consisting of piecewise constant functions of form $a = \sum_j a_j\chi_j$ where χ_j is the characteristic function of E_j.

[2] Estimate (32) could be enforced by assuming E_j^+ are regular enough to allow a "scaling argument" resulting in a Poincaré inequality with a constant bounded by $C\operatorname{diam}(E_j^+)$ [23,33, 2].

Proof Let u be the solution to (2) with boundary condition $f \in L^2_\diamond(\partial\Omega)$ and let (v, V) solve (29) with the input current $I = Q^*f$. Denote by u' the solution to the sensitivity problem (52) and by (v', V') the solution to (53). In the following, the operator L is also considered an operator from $H^1(\Omega)$ to $H^1_\diamond(\Omega)$ in the sense of subtracting the mean of the trace; cf. (31).

By the boundary conditions of (53), we have

$$QV' = \sum_{j=1}^{k} \chi_j^+ \fint_{E_j} (v' + z_j \nu \cdot \gamma \nabla v') dS = \sum_{j=1}^{k} \chi_j^+ \fint_{E_j} v' dS = QPv'. \tag{34}$$

By (34), the triangle inequality, and by applying the trace theorem and the fact $\|L\|_{\mathcal{L}(L^2(\partial\Omega))} = 1$, we get

$$\begin{aligned} \|u' - LQV'\|_{L^2(\partial\Omega)} &\leq \|u' - Lv'\|_{L^2(\partial\Omega)} + \|L(\mathrm{Id} - QP)v'\|_{L^2(\partial\Omega)} \\ &\leq C\|u' - Lv'\|_{H^1(\Omega)} + \|(\mathrm{Id} - QP)v'\|_{L^2(\partial\Omega)}. \end{aligned} \tag{35}$$

Next we estimate the first term on the right side of (35). By coercivity of the bilinear form associated with (2), we have

$$\|u' - Lv'\|^2_{H^1(\Omega)} \leq C \int_\Omega \gamma |\nabla(u' - v')|^2 \, dx. \tag{36}$$

Furthermore, using the variational formulations of the sensitivity problems (52) and (53), we obtain

$$\begin{aligned} \int_\Omega \gamma |\nabla(u' - v')|^2 \, dx = &\int_\Omega \eta \nabla(Lv - u) \cdot \nabla(u' - Lv') \, dx \\ &+ \sum_{j=1}^{k} \int_{E_j} \frac{1}{z} (v' - V_j')(u' - Lv') \, dS. \end{aligned} \tag{37}$$

Note that, in the three instances above, v has been replaced by Lv and v' by Lv', respectively. While in the interior term the replacements are trivially justified, the boundary term follows from the fact that — by the boundary conditions (53) — we have

$$\int_{E_j} \frac{1}{z} (v' - V_j') c \, dS = c \int_{E_j} \nu \cdot \gamma \nabla v' dS = 0$$

for all scalars c. Inserting (37) into (36), and applying Cauchy–Schwartz inequality and trace theorem to the right-hand quantity results in

$$\|u' - Lv'\|_{H^1(\Omega)} \leq C\Big(\|\eta\|_{L^\infty(\Omega)} \|u - Lv\|_{H^1(\Omega)} + \sum_{j=1}^{k} \|v' - V_j'\|_{L^2(E_j)} \Big). \tag{38}$$

The first term on the right side of (38) can be estimated suitably by using

$$\|u - Lv\|_{H^1(\Omega)} \leq Ch \|\gamma\|_{L^\infty(\Omega)} \|f\|_{L^2(\partial\Omega)} \tag{39}$$

which follows from the proof of Theorem 2. Since by (34) we have

$$\|v' - V_j'\|_{L^2(E_j)} = \|v' - QV'\|_{L^2(E_j)} \leq \|(\mathrm{Id} - QP)v'\|_{L^2(\partial\Omega)},$$

the second term on the right side of (38) can be handled by working out an appropriate upper bound for $\|(\mathrm{Id}-QP)v'\|_{L^2(\partial\Omega)}$.

At this point, to guarantee sufficient regularity for v', we need the assumptions that γ is as in Definition 1 and η is compactly supported in Ω (cf. (53)). Under these hypotheses, an analogous argument to [25, Theorem 2.1] — ultimately based on elliptic regularity theory [34] and the boundary conditions (53) — implies that there exists a relatively open connected set $U \subseteq \overline{\Omega}$ such that

$$\partial\Omega \subseteq \partial U, \quad \overline{U} \cap (\operatorname{supp}\eta \cup \overline{D}) = \emptyset, \quad \|\nu \cdot \gamma \nabla v'\|_{L^2(\partial U)} \leq C\|v'\|_{H^1(\Omega)}. \tag{40}$$

Consequently, applying (32), the trace theorem for quotient spaces [22], continuous dependence on Neumann-data [34, §1 Theorem 7.4], the rightmost estimate of (40), and continuity properties of (53) leads us to the estimate

$$\begin{aligned}
\|(\mathrm{Id}-QP)v'\|_{L^2(\partial\Omega)} &\leq Ch \inf_{c\in\mathbb{R}} \|v' + c\|_{H^1(\partial\Omega)} \\
&\leq Ch \inf_{c\in\mathbb{R}} \|v' + c\|_{H^{3/2}(U)} \\
&\leq Ch\|\nu \cdot \gamma \nabla v'\|_{L^2(\partial U)} \\
&\leq Ch\|v'\|_{H^1(\Omega)} \\
&\leq Ch\|\gamma\|_{L^\infty(\Omega)}\|\eta\|_{L^\infty(\Omega)}\|f\|_{L^2(\partial\Omega)}.
\end{aligned} \tag{41}$$

In conclusion, using (35)–(41) we have shown that

$$\begin{aligned}
&\|(\Lambda(\gamma)'\eta)f - LQ(R'(\gamma)\eta)Q^*f\|_{L^2(\partial\Omega)} \\
&\qquad \leq C\|u' - Lv'\|_{H^1(\Omega)} + \|(\mathrm{Id}-QP)v'\|_{L^2(\partial\Omega)} \\
&\qquad \leq C\left(\|\eta\|_{L^\infty(\Omega)}\|u - Lv\|_{H^1(\Omega)} + \|(\mathrm{Id}-QP)v'\|_{L^2(\partial\Omega)}\right) \\
&\qquad \leq Ch\|\gamma\|_{L^\infty(\Omega)}\|\eta\|_{L^\infty(\Omega)}\|f\|_{L^2(\partial\Omega)}
\end{aligned}$$

and the proof is concluded. □

Remark 4 Analogous argumentation can be used to generalize Theorem 3 for higher order Fréchet derivatives; cf. Proposition 5 in Appendix B.

According to Theorems 2–3, the operators of the form

$$\Lambda_h(\gamma) = LQ(R(\gamma) - Z)Q^*, \quad \Lambda_h'(\gamma) = LQR'(\gamma)Q^*$$

satisfy (15) and (28), respectively. Given a noisy measurement map $R^\delta(\gamma)$, the semidefiniteness test applied to the operators

$$LQ(R(\gamma_0 + \beta\chi_B) - R^\delta(\gamma))Q^*, \quad LQ(R(\gamma_0) + \beta R'(\gamma_0)\chi_B + R^\delta(\gamma))Q^*$$

where $B \subseteq \Omega$ is an open ball, satisfies the asymptotic characterization property of Theorem 1. Note also that the noise does not get amplified since the operator norms of Q (and Q^*) and L are obviously bounded by $\max_{j=1,\ldots,k} |E_j^+|^{1/2}$ and 1, respectively.

The following lemma shows that equivalent semidefiniteness tests can be carried out without constructing the projection operators, but instead, just using the electrode measurement map.

Proposition 4 *Let $A : \mathbb{R}^k_\diamond \to \mathbb{R}^k_\diamond$ be arbitrary. Then for any $f, g \in L^2_\diamond(\partial\Omega)$ we have*

$$\langle LQAQ^* f, g\rangle = AQ^* f \cdot Q^* g. \tag{42}$$

As a consequence, the conditions

$$LQAQ^* \geq 0 \quad \textit{and} \quad A \geq 0$$

are equivalent.

Proof Clearly, L is self-adjoint when considered an operator from $L^2(\partial\Omega)$ to itself. Moreover, since $L|_{L^2_\diamond(\partial\Omega)} = \mathrm{Id}$, we have

$$\langle LQAQ^* f, g\rangle = AQ^* f \cdot Q^* Lg = AQ^* f \cdot Q^* g.$$

for any $f, g \in L^2_\diamond(\partial\Omega)$, that is, (42). In particular, it follows that $A \geq 0$ implies $LQAQ^* \geq 0$.

To show the converse, assume that $LQAQ^* \geq 0$. As a consequence of (42), it is sufficient to show that for any $I \in \mathbb{R}^k_\diamond$ there exists an $f_I \in L^2_\diamond(\partial\Omega)$ such that $I = Q^* f_I$. For example, the function defined by

$$f_I = \sum_{j=1}^{k} \frac{\chi_j^+}{|E_j^+|} I_j,$$

has the desired property. □

Let us finish the section with a short recap. We have demonstrated that, under the assumption (32), the CEM can be used to construct a sequence of monotonicity reconstructions that converge to the infinite precision counterpart in the sense of Theorem 1. Although the assumptions of Theorem 1 do not require the approximative operators to satisfy a monotonicity principle, Proposition 3 shows that the CEM measurement map nevertheless has this favourable property (cf. Remark 2). We also emphasize that, by Proposition 4, the operators Q and L do not have a practical role in terms of implementing the algorithm — they are only needed for forming a theoretical connection between the CEM and CM-based semidefiniteness tests.

5 Algorithmic implementation

In this section we formulate two slightly different algorithms for reconstructing strictly positive (or negative) conductivity inclusions. The modifications that enable reconstructing indefinite inclusions are left for future studies. To highlight the fact that in practice the "true" conductivity is unknown, we denote the noisy measurement data by R^δ omitting the dependence on γ. Moreover, let us remind that we make the arguably restrictive assumption that the background conductivity γ_0 is known a priori.

Algorithm 1 (Monotonicity method for the CEM)

0. Fix the collection of balls $\mathcal{B}$, choose the regularization parameter $\alpha > 0$, and compute $R(\gamma_0)$ and $R'(\gamma_0)$.

1. *For all $B = B(x, r) \in \mathcal{B}$, construct the indicator*

$$\mathrm{Ind}(x) := \max\{0, \min \sigma(R(\gamma_0) + \beta R'(\gamma_0)\chi_B - R^\delta + \alpha\,\mathrm{Id})\} \tag{43}$$

2. *Return* Ind.

A logical choice for the probing scalar is

$$\beta = \operatorname{ess\,inf}\Big(\frac{\gamma_0\kappa}{\gamma}\Big).$$

In practice a scalar satisfying $\beta \leq \operatorname{ess\,inf}(\gamma_0\kappa/\gamma)$ can be constructed from knowledge of a lower bound on κ. Moreover, we propose constructing the regularization parameter in the form

$$\alpha = \alpha(h, \delta) = -\mu \min \sigma(R(\gamma_0) - R^\delta), \quad \mu \approx 1. \tag{44}$$

The value of μ is to be tuned — according to our numerical results typically very close to 1. The idea behind this choice comes from the following heuristic argument. According to the adaptation of Theorem 1 to the linearized monotonicity method, the following holds. If the regularization parameter satisfies

$$\alpha(h, \delta) \geq \delta - \inf_{B \in \mathcal{M}_0'} \inf \sigma(\Lambda_h(\gamma_0) + \beta\Lambda_h'(\gamma_0)\chi_B - \Lambda_h(\gamma)),$$

then the reconstruction forms an upper bound for $\mathcal{M}_0'$. However, recalling that $\beta\Lambda_h'(\gamma_0)\chi_B \leq 0$ [19, Corollary 3.4] and $N^\delta \leq \delta$, we see that

$$\begin{aligned} -\inf \sigma(\Lambda_h(\gamma_0) - \Lambda_h^\delta(\gamma)) &\leq \delta - \inf \sigma(\Lambda_h(\gamma_0) - \Lambda_h(\gamma)) \\ &\leq \delta - \inf_{B \in \mathcal{M}_0'} \inf \sigma(\Lambda_h(\gamma_0) + \beta\Lambda_h'(\gamma_0)\chi_B - \Lambda_h(\gamma)). \end{aligned} \tag{45}$$

The idea is to barely reverse the inequality (45) by multiplying with a suitable μ such that the resulting regularization parameter α satisfies (21) while being small enough. Rigorous association of (44) with the reversal of (45) would of course require taking the operators L, Q and Q^* into the consideration. Further elaboration of the choice of the regularization parameter is left for future studies.

According to our numerical tests, the output of Algorithm 1 is very sensitive to the choice of the regularization parameter: Choosing slightly too large α tends to result in crudely overestimated supports, whereas even a bit too small α yields vanishing reconstructions. An idea for increasing the flexibility of the method is to fix sufficiently large α, and probe monotonicity using various values of β. Intuitively this seems natural, as increasing β will tighten the monotonicity test and in turn (hopefully) sharpen up the reconstruction. This gives rise to the following algorithm.

Algorithm 2 (A flexible monotonicity method for the CEM)

0. *Fix the collection of balls $\mathcal{B}$ and choose the regularization parameter $\alpha > 0$, and compute $R(\gamma_0)$ and $R'(\gamma_0)$. Fix a collection $\{\beta_j\}_{j=1}^m \subset \mathbb{R}$ of increasing values for probing semidefiniteness, and set $j = 1$.*

1. *For all* $B = B(x, r) \in \mathcal{B}$*, construct*

$$\mathrm{Ind}_j(x) := \begin{cases} 1, & \text{if } \min \sigma(R(\gamma_0) + \beta_j R'(\gamma_0)\chi_B - R^\delta + \alpha \,\mathrm{Id}) \geq 0, \\ 0, & \text{otherwise.} \end{cases} \tag{46}$$

2. *Set* $j \to j + 1$*, redefine* $\mathcal{B} \to \mathcal{B} \setminus \{B(x, r) \in \mathcal{B} : \mathrm{Ind}_j(x) = 0\}$*, and go back to step 1.*

3. *If* $\mathcal{B} = \emptyset$*, return the indicator*

$$\mathrm{Ind} := \sum_{j=1}^{m} \mathrm{Ind}_j.$$

Observe that the idea of "Step 2" in Algorithm 2 is to speed up the computations by discarding excess test balls — this is justified by the monotonicity property of the CEM measurement map. We also remark that, instead of using the counter function as in (46), an analogous stability improvement for Algorithm 2 can be achieved by defining the indicator at each point as the maximal β for which the respective positive-semidefiniteness holds [15]. Typically, if $\alpha > 0$ is not very large and the inclusions are small, the running times of the Algorithms 1–2 are essentially the same.

6 Numerical experiments

We proceed with four numerical examples which test the implementation of Algorithms 1–2 from the following point of views. The idea of the first example is to test whether the reconstruction of a fixed (non-convex) inclusion sharpens up as the number of measurement electrodes increase. Here, for comparison, adaptations of Algorithms 1–2 are applied also in the CM framework. In the second example, the algorithms are applied in a two-dimensional geometrical setting to synthetic data with and without additive artificial random noise. In the third example Algorithm 2 is applied to real-life data measured on a cylindrically symmetric water tank phantom. Due to the symmetry, the reconstruction is carried out in two spatial dimensions. The last example is an application of Algorithm 1 to synthetic exact data simulated in three spatial dimensions.

In all of the two-dimensional experiments the object Ω is unit disk-shaped, and the electrodes are equispaced and of equal length, covering in total half of the boundary. In the three-dimensional experiment, the domain is a unit ball with spherical cap-shaped electrodes that are placed approximately equidistantly. Moreover, in all simulated examples, the contact impedance is given a constant value $z_j = 0.01$, $j = 1, 2, \ldots, k$.

The numerical implementation of Algorithms 1–2 is based on the following linear algebra. Let $\{I^{(j)}\}_{j=1}^{k-1}$ be a basis of $\mathbb{R}^k_\diamond$ and denote

$$\mathbf{I} = [I^{(1)}, I^{(2)}, \ldots, I^{(k-1)}].$$

Then a matrix representation of $R(\gamma_0) + \beta R'(\gamma_0)\chi_B - R(\gamma)$ in this basis is given by

$$\mathbf{A} = \mathbf{I}^\dagger(\mathbf{X} + \mathbf{V}) \in \mathbb{R}^{(k-1)\times(k-1)},$$

where $\mathbf{I}^\dagger = (\mathbf{I}^{\mathrm{T}}\mathbf{I})^{-1}\mathbf{I}^{\mathrm{T}}$ is the Moore–Penrose pseudoinverse of $\mathbf{I}$,

$$\mathbf{X} = [X^{(1)}, X^{(2)}, \ldots, X^{(k-1)}], \quad \mathbf{V} = [V^{(1)}, V^{(2)}, \ldots, V^{(k-1)}],$$

with $X^{(j)} = (R(\gamma_0) + \beta R'(\gamma_0)\chi_B)I^{(j)}$ and $V^{(j)} = R(\gamma)I^{(j)}$. Evaluation of the indicator functions in (43) and (46) is based on computing the smallest eigenvalue of

$$\mathbf{A}^\delta = \mathbf{I}^\dagger(\mathbf{X} + \mathbf{V}^\delta),$$

where

$$\mathbf{V}^\delta = \mathrm{Sym}(\widetilde{\mathbf{V}}^\delta \mathbf{I}^\dagger)\mathbf{I}$$

and $\widetilde{\mathbf{V}}^\delta$ is the noisy measurement data. Here Sym denotes the symmetric part, and it is applied to ensure that the underlying noisy data comprise a symmetric matrix. In addition, each column of $\widetilde{\mathbf{V}}^\delta$ and $\mathbf{V}^\delta$ is enforced to be in $\mathbb{R}^k_\diamond$. Noise is simulated by setting

$$\widetilde{\mathbf{V}}^\delta = \mathbf{V} + \mathbf{N}, \tag{47}$$

where each entry of $\mathbf{N}$ is given by $N_{ij} = V_i^{(j)} Y_{ij}$ and Y_{ij} is a drawn from normal distribution of mean zero and standard deviation $5 \cdot 10^{-3}$. In the simulated noisy examples the ratio

$$\|\mathbf{V} - \mathbf{V}^\delta\|_F / \|\mathbf{V}\|_F$$

of Frobenius norms is called the "relative error".

The measurement maps and their Fréchet derivatives are approximated by a standard finite element method [28] using piecewise quadratic ($\mathbb{P}_2$) and piecewise affine ($\mathbb{P}_1$) elements, in two and three spatial dimensions, respectively. Moreover, the conductivity distribution is discretized by simplex-wise constant ($\mathbb{P}_0$) elements. The computational domain is a polygonal discretization of a unit disk/ball. In the two-dimensional examples, the meshes used in simulations and reconstructions consist of approximately 2.7×10^6 nodes and 1.3×10^6 triangles, and 7.5×10^5 nodes and 3.7×10^5 triangles, respectively. In the three-dimensional examples the simulations are performed on a mesh with 1.2×10^5 nodes and 6.9×10^5 tetrahedrons, while the reconstructions are computed using a mesh with 4.9×10^4 nodes and 2.9×10^5 tetrahedrons. With the above dimensions, an average reconstruction computation time using a laptop with two Intel Core 2 processors with CPU clock rate 2.4 Ghz was around five seconds.

As our FEM model is based on $\mathbb{P}_0$-discretization of the conductivity, the characteristic functions of the test sets B are approximated by

$$\chi_B \approx \sum_{K \subseteq B} \chi_K, \tag{48}$$

where K are simplices in the mesh. While carrying out the computations, some subtlety regarding to the choice of the test sets was observed. In particular, using very small balls yields artifactual reconstructions. This is not surprising since, for a fixed mesh, (48) is a bad approximation when the radius of B is small. To ease visualization of the results, we do not use disks/balls as computational test sets. In two-dimensions, the test sets are chosen from a regular hexagonal tiling of the plane. In the three-dimensional computations, we use voxels. We emphasize that convergence result analogous to Theorem 1 can be generalized to various types of measurable subsets of Ω.

Example 1 In this numerical example we compute linearized monotonicity reconstructions with respect to different numbers of electrodes. For comparison, we use both CEM and discretized CM as forward models. No extra artificial noise is added to the synthesized data.

The (noiseless) discretized CM is formulated as a truncated matrix approximation as follows. For a set of linearly independent boundary current densities $\{f^{(m)}\}_{m=1}^{p} \subseteq L^2_\diamond(\partial\Omega)$, we set

$$A_{\ell m} = \int_\Omega (\gamma_0 - \beta\chi_B)\nabla u_0^{(\ell)} \cdot \nabla u_0^{(m)} dx - \langle \Lambda(\gamma) f_\ell, f_m \rangle$$

where $u_0^{(m)}$ solves (2) for the conductivity γ_0 and the current density $f^{(m)}$, $m = 1, 2, \ldots, p$. By (2), (52), and Green's formula, the matrix $\mathbf{A} = \{A_{\ell m}\}_{\ell,m=1}^{p}$ is a discretization of $\Lambda(\gamma_0) + \beta\Lambda'(\gamma_0)\chi_B - \Lambda(\gamma)$. Figure 1 shows the reconstructions

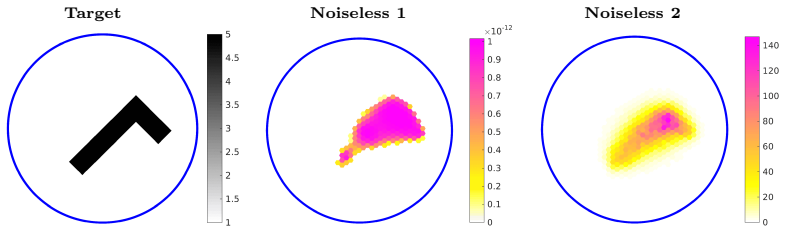

Fig. 1 Two-dimensional CM reconstructions from synthetic exact datum using 64 linearly independent boundary current densities. Reconstructions "**Noiseless 1**" and "**2**" are calculated using Algorithms 1 and 2, respectively. For more information on the FE mesh, see the beginning of section 6.

Parameter	**Noiseless 1** (CM)	**Noiseless 2** (CM)
$\mathrm{diam}(B)$	0.053	0.053
β	0.8	$0.1 + 0.5\mathbb{N}$
μ	1.00003	1.01

Tbl. 1 Parameter values used in the computations; $\mathrm{diam}(B)$ is the diameter of the hexagons in the hexagonal reconstruction mesh (48), β is the probing scalar(s) in the semidefiniteness test, and μ is the regularization parameter (44).

produced by Algorithms 1–2 using the discretized CM model. No random noise is added to the data which are simulated using a target conductivity with an L-shaped conductive inclusion. The model uses a fairly high number $p = 64$ linearly independent boundary current density inputs of form

$$f_m(\theta) = \frac{1}{\sqrt{\pi}} \begin{cases} \cos(m\theta), & m = 1, 2, \ldots, p/2, \\ \sin((m - p/2)\theta), & m - p/2 = 1, 2, \ldots, p/2, \end{cases}, \quad \theta \in [0, 2\pi).$$

Figure 2 displays noiseless reconstructions using the CEM with increasing numbers of electrodes. In this example, current inputs of form

$$I_j^{(m)} = \begin{cases} \cos(m2\pi j/k), & m = 1, 2, \ldots, k/2, \\ \sin((m - k/2)2\pi j/k), & m - k/2 = 1, 2, \ldots, k/2 - 1, \end{cases}$$

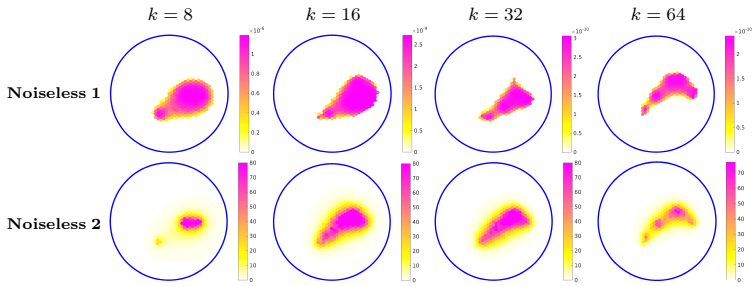

Fig. 2 Two-dimensional CEM reconstructions from synthetic noiseless data using $k = 8, 16, 32$ and 64 equispaced electrodes of equal width. Reconstructions in the table rows "**Noiseless 1**" and "**2**" are calculated using Algorithms 1 and 2, respectively. For more information on the FE mesh, see the beginning of section 6.

	Parameter	**Noiseless 1**	**Noiseless 2**
$k = 8$	$\mathrm{diam}(B)$	0.053	0.053
	β	0.8	$0.1 + 0.5\mathbb{N}$
	μ	1.4	1.4
$k = 16$	$\mathrm{diam}(B)$	0.053	0.053
	β	0.8	$0.1 + 0.5\mathbb{N}$
	μ	1.001	1.01
$k = 32$	$\mathrm{diam}(B)$	0.053	0.053
	β	0.8	$0.1 + 0.5\mathbb{N}$
	μ	1.00001	1.01
$k = 64$	$\mathrm{diam}(B)$	0.053	0.053
	β	0.8	$0.1 + 0.5\mathbb{N}$
	μ	1.00001	1.0001

Tbl. 2 Parameter values used in the computations; $\mathrm{diam}(B)$ is the diameter of the hexagons in the hexagonal reconstruction mesh (48), β is the probing scalar(s) in the semidefiniteness test, and μ is the regularization parameter (44).

are used. Intuitively, the results should not depend too much on the choice of the current basis if the noise level is low. We observe that increasing the number of electrodes seems to improve the reconstruction to the extent that the non-convexity of the target is revealed.

Example 2 The second example considers three different test objects in which the conductivity consists of a constant background with various convex-shaped inclusions. Both noisy and noiseless measurements are simulated using $k = 16$ electrodes. The reconstructions computed with both Algorithms 1–2 are displayed in Figure 3. In the rightmost target, the inclusions are less conductive than the background, i.e., $\gamma = \gamma_0 - \kappa\chi_D$ where $\gamma_0 > \kappa > 0$. In this case, the suitable semidefiniteness test is

$$\min \sigma(R^\delta + \beta R'(\gamma_0)\chi_B - R(\gamma_0) + \alpha\,\mathrm{Id}) \geq 0.$$

Using the right-hand side of (5), one can deduce that a sufficient condition for the probe constant is $\beta \leq \operatorname{ess\,inf}(-\kappa)$. In the noiseless case we observe that (44) yields a negative α. However, we emphasize that negative regularization parameters are allowed by the adaptation of (21) to the case with resistive inclusions. The results indicate that interesting information about the inclusion locations can be retrieved in a relatively realistic simulated setting. Moreover, we notice that Algorithm 2 is more flexible in the sense that it enables compensating bad choices of α by increasing β.

Example 3 In this example we verify that, in principle, Algorithm 2 can provide reasonable reconstructions from real-life measurement data. The measurement data are gathered at the laboratory of the Applied Physics Department at University of Eastern Finland in Kuopio. The test object consists of a cylinder tank filled with regular tap water and iron objects. There are 16 rectangular electrodes on the lateral surface of the tank, and they are homogeneous along the symmetry axis of the tank. Moreover, the water surface is set along the top edge of the electrodes. Thus, the measurement geometry is essentially two-dimensional. The radius of the tank cross-section is 14.0 cm, and the electrode width and height are 2.5 cm and 7.0 cm, respectively. The measurements were performed using a dipole current basis $I^{(m)} = (\mathrm{e}^{(1)} - \mathrm{e}^{(m+1)}) \times 1.0$ mA, $m = 1, 2, \ldots, k-1$.

The results obtained with a planar computational model are presented in Figure 4. Both reconstructions were computed using Algorithm 2 with the trial-and-error estimated values

$$\gamma_0 = 0.0243\,\mathrm{S/m}, \quad z = 0.005\,\mathrm{m}^2/\mathrm{S}$$

for the background conductivity and contact impedance, respectively.

It was observed that the reconstruction procedure is very sensitive with respect to the values of γ_0 and z — a few percent perturbation in their values was enough to ruin the whole reconstruction. This is not surprising as the measurement operator (when interpreted as a function of the conductivity and the contact resistance) satisfies

$$\frac{1}{c} R(\gamma_0, z) = R(c\gamma_0, z/c) \tag{49}$$

for any constant $c > 0$. By (49), a few percent error on γ_0 and z can cause a few percent error on the measurement operator. Due to ill-posedness, such error levels are enough to suppress the signal entirely. However, the results show that with sufficiently good estimates for γ_0 and z, the proposed method can yield reconstructions that are comparable in quality to virtually any existing EIT reconstruction method.

Example 4 The final example is a simulated three-dimensional example. The object is a unit ball, and there are $k = 32$ approximately equidistantly placed electrodes which all are spherical caps of radius 0.1. An orthonormal current basis $\{I^{(m)}\}_{m=1}^{k-1}$, defined by

$$I_j^{(m)} = \begin{cases} \sqrt{\frac{1}{m(m+1)}} & j = 1, 2, \ldots, m, \\ -\sqrt{\frac{m}{m+1}} & j = m+1, \\ 0 & j = m+2, m+3, \ldots, k, \end{cases} \tag{50}$$

is used. Note that (50) is the Gram-Schmidt orthonormalization of the standard $e^{(1)} - e^{(m+1)}$ basis used in many measurement setups, including the setup in Example 3.

The results are shown in Figure 5; for the ease of presentation only Algorithm 1 is considered. It is observed that, with suitable choices of regularization parameters, the algorithm can separate the reconstructed inclusions. We stress that, after precomputing an approximation of $R'(\gamma_0)$ and fixing the χ_B's, the implementation of the method is independent of the spatial dimension.

7 Conclusions

We have extended previous works on the regularization analysis as well as the implementation of the monotonicity method. The leading idea of this reconstruction technique is to perform semidefiniteness tests on certain linear combinations of (noisy and discrete) current-to-voltage operators. We have proven that, as a suitably chosen sequence of regularization parameters tends to zero, the approximative test criterion converges uniformly to the idealistic one. Moreover, we rigorously justified the use of the CEM as an approximate model.

To complement the theoretical study, two reconstruction algorithms were formulated and implemented. Numerical examples were carried out using both simulated CEM data and real-life measurement data. The tests indicate that the monotonicity method can very efficiently provide relatively good images on conductivity inhomogeneities if the homogeneous background conductivity and the electrode contact resistances are sufficiently accurately known.

Acknowledgements Henrik Garde is supported by advanced grant no. 291405 *HD-Tomo* from the European Research Council. Stratos Staboulis is supported by grant no. 4002-00123 *Improved Impedance Tomography with Hybrid Data* from The Danish Council for Independent Research — Natural Sciences.

The authors are grateful to Professor Jari Kaipio's research group at the University of Eastern Finland (Kuopio) for granting us access to their EIT devices. We thank Marcel Ullrich at University of Stuttgart for his valuable insight on the implementation details of the presented method.

References

1. Astala, K., Päivärinta, L.: Calderón's inverse conductivity problem in the plane. Annals of Mathematics **163**(1), 265–299 (2006)
2. Bebendorf, M.: A note on the poincaré inequality for convex domains (2003)
3. Borcea, L.: Electrical impedance tomography. Inverse Problems **18**, 99–136 (2002)
4. Brühl, M.: Explicit characterization of inclusions in electrical impedance tomography. SIAM Journal on Mathematical Analysis **32**, 1327–1341 (2001)
5. Brühl, M., Hanke, M.: Numerical implementation of two non-iterative methods for locating inclusions by impedance tomography. Inverse Problems **16**, 1029–1042 (2000)
6. Calderón, A.P.: On an inverse boundary value problem. In: Seminar on Numerical Analysis and its Applications to Continuum Physics (Rio de Janeiro, 1980), pp. 65–73. Sociedade Brasileira de Matemática, Rio de Janeiro (1980)
7. Cheney, M., Isaacson, D., Newell, J., Simske, S., Goble, J.: Noser: An algorithm for solving the inverse conductivity problem. International Journal of Imaging Systems and Technology **2**(2), 66–75 (1990)
8. Cheney, M., Isaacson, D., Newell, J.C.: Electrical impedance tomography. SIAM Review **41**(1), 85–101 (1999)

9. Cheng, K., Isaacson, D., Newell, J., Gisser, D.: Electrode models for electric current computed tomography. IEEE Transactions on Biomedical Engineering **36**(9), 918–924 (1989)
10. Chung, E.T., Chan, T.F., Tai, X.C.: Electrical impedance tomography using level set representation and total variation regularization. Journal of Computational Physics **205**(1), 357–372 (2005)
11. Gebauer, B.: Localized potentials in electrical impedance tomography. Inverse Problems and Imaging **2**(2), 251–269 (2008)
12. Hanke, M., Brühl, M.: Recent progress in electrical impedance tomography. Inverse Problems **19**(6), S65–S90 (2003). Special section on imaging
13. Hanke-Bourgeois, M., Kirsch, A.: Sampling Methods. Springer (2015)
14. Harrach, B.: Recent progress on the factorization method for electrical impedance tomography. Computational and mathematical methods in medicine **2013** (2013)
15. Harrach, B.: Interpolation of missing electrode data in electrical impedance tomography. Inverse Problems **31**(11), 115,008 (2015)
16. Harrach, B., Lee, E., Ullrich, M.: Combining frequency-difference and ultrasound modulated electrical impedance tomography. Inverse Problems **31**(9), 095,003 (2015)
17. Harrach, B., Seo, J.K.: Detecting inclusions in electrical impedance tomography without reference measurements. SIAM Journal on Applied Mathematics **69**(6), 1662–1681 (2009)
18. Harrach, B., Seo, J.K.: Exact shape-reconstruction by one-step linearization in electrical impedance tomography. SIAM Journal on Mathematical Analysis **42**(4), 1505–1518 (2010)
19. Harrach, B., Ullrich, M.: Monotonicity-based shape reconstruction in electrical impedance tomography. SIAM Journal on Mathematical Analysis **45**(6), 3382–3403 (2013)
20. Harrach, B., Ullrich, M.: Resolution guarantees in electrical impedance tomography. IEEE Transactions on Medical Imaging **34**(7), 1513–1521 (2015)
21. Heikkinen, L.M., Vilhunen, T., West, R.M., Vauhkonen, M.: Simultaneous reconstruction of electrode contact impedances and internal electrical properties: II. Laboratory experiments. Measurement Science and Technology **13**, 1855–1861 (2002)
22. Hyvönen, N.: Complete electrode model of electrical impedance tomography: Approximation properties and characterization of inclusions. SIAM Journal on Applied Mathematics **64**(3), 902–931 (2004)
23. Hyvönen, N.: Approximating idealized boundary data of electric impedance tomography by electrode measurements. Mathematical Models and Methods in Applied Sciences **19**(7), 1185–1202 (2009)
24. Hyvönen, N., Karhunen, K., Seppänen, A.: Fréchet derivative with respect to the shape of an internal electrode in electrical impedance tomography. SIAM Journal on Applied Mathematics **70**(6), 1878–1898 (2010)
25. Hyvönen, N., Seppänen, A., Staboulis, S.: Optimizing electrode positions in electrical impedance tomography. SIAM Journal on Applied Mathematics **74**(6), 1831–1851 (2014)
26. Ikehata, M.: How to draw a picture of an unknown inclusion from boundary measurements. Two mathematical inversion algorithms. Journal of Inverse and Ill-Posed Problems **7**(3), 255–271 (1999)
27. Ikehata, M.: Reconstruction of the support function for inclusion from boundary measurements. Journal of Inverse and Ill-Posed Problems **8**, 367–378 (2000)
28. Kaipio, J., Kolehmainen, V., Somersalo, E., Vauhkonen, M.: Statistical inversion and monte carlo sampling methods in electrical impedance tomography. Inverse Problems **16**(5), 1487–1522 (2000)
29. Kato, T.: Perturbation theory for linear operators, vol. 132. Springer Verlag (1995)
30. Lechleiter, A.: A regularization technique for the factorization method. Inverse problems **22**, 1605 (2006)
31. Lechleiter, A., Hyvönen, N., Hakula, H.: The factorization method applied to the complete electrode model of impedance tomography. SIAM Journal on Applied Mathematics **68**, 1097–1121 (2008)
32. Lechleiter, A., Rieder, A.: Newton regularizations for impedance tomography: convergence by local injectivity. Inverse Problems **24**, 065,009 (2008)
33. Lieb, E.H., Seiringer, R., Yngvason, J.: Poincaré inequalities in punctured domains. Annals of Mathematics **158**, 1067–1080 (2003)
34. Lions, J.L., Magenes, E.: Non-homogeneous boundary value problems and applications, Vol. 1. Springer–Verlag, New York–Heidelberg (1972)
35. Nachman, A.I.: Global uniqueness for a two-dimensional inverse boundary value problem. Annals of Mathematics **143**, 71–96 (1996)

36. Reed, M., Simon, B.: Methods of modern mathematical physics. Vol I: Functional analysis. Academic Press Inc., New York (1990)
37. Resnick, S.I.: A Probability Path. Birkhäuser (2014)
38. Somersalo, E., Cheney, M., Isaacson, D.: Existence and uniqueness for electrode models for electric current computed tomography. SIAM Journal on Applied Mathematics **52**(4), 1023–1040 (1992)
39. Sylvester, J., Uhlmann, G.: A global uniqueness theorem for an inverse boundary value problem. Annals of Mathematics **125**, 153–169 (1987)
40. Tamburrino, A.: Monotonicity based imaging methods for elliptic and parabolic inverse problems. Journal of Inverse and Ill-posed Problems **14**(6), 633–642 (2006)
41. Tamburrino, A., G., R.: A new non-iterative inversion method for electrical resistance tomography. Inverse Problems **18**(6), 1809 (2002)
42. Uhlmann, G.: Electrical impedance tomography and Calderón's problem. Inverse Problems **25**(12), 123,011 (2009)
43. Vauhkonen, M., Vadász, D., Karjalainen, P.A., Somersalo, E., Kaipio, J.P.: Tikhonov regularization and prior information in electrical impedance tomography. IEEE Transactions on Medical Imaging **17**, 285–293 (1998)

A Appendix: a lemma on the convergence of infima/suprema

Lemma 2 *Let J be an arbitrary index set and $\{a_j\}_{j\in J}, \{a_j(h)\}_{j\in J} \subset \mathbb{R}$, $h > 0$, be sequences such that $\inf_{j\in J} a_j > -\infty$ and*

$$\lim_{h\to 0} \sup_{j\in J} |a_j - a_j(h)| = 0.$$

Denoting $a = \inf_{j\in J} a_j$ and $a(h) = \inf_{j\in J} a_j(h)$ we have

$$\lim_{h\to 0} a(h) = a. \tag{51}$$

Proof Let us first show that the limit in (51) exists. Given an arbitrary $\varepsilon > 0$, there exists an $h_\varepsilon > 0$ such that $\sup_{j\in J} |a_j - a_j(h)| \le \varepsilon/2$ for all $h \in (0, h_\varepsilon)$. Let $h, h' \in (0, h_\varepsilon)$ then $\sup_{j\in J} |a_j(h) - a_j(h')| \le \varepsilon$, and fix a sequence $\{j(k)\}_{k=1}^\infty \subseteq J$ such that $a_{j(k)}(h)$ converges to $a(h)$. Hence

$$a(h') \le \liminf_{k\to\infty} a_{j(k)}(h') \le \liminf_{k\to\infty} a_{j(k)}(h) + \varepsilon = a(h) + \varepsilon.$$

By symmetry with respect to h and h', it follows that $\{a(h)\}_{h>0}$ is a Cauchy sequence.

It still remains to show that the limit coincides with a. For any $\varepsilon > 0$, there exists $j_\varepsilon \in J$ and $h_\varepsilon > 0$ such that $|a_{j_\varepsilon} - a| \le \varepsilon/2$ and $\sup_{j\in J} |a_j - a_j(h)| \le \varepsilon/2$ for $h \in (0, h_\varepsilon)$, respectively. Thus for $h \in (0, h_\varepsilon)$

$$a(h) \le a_{j_\varepsilon}(h) \le a_{j_\varepsilon} + \varepsilon/2 \le a + \varepsilon.$$

For $h \in (0, h_\varepsilon)$ pick j'_ε such that $|a_{j'_\varepsilon}(h) - a(h)| \le \varepsilon/2$ then

$$a \le a_{j'_\varepsilon} \le a_{j'_\varepsilon}(h) + \varepsilon/2 \le a(h) + \varepsilon.$$

Altogether we have shown for any $\varepsilon > 0$ that $|a(h) - a| \le \varepsilon$ for $h \in (0, h_\varepsilon)$. □

B Appendix: linearization of the CEM and the CM

Proposition 5 *The operators $\Lambda(\gamma) \in \mathcal{L}(L^2_\diamond(\partial\Omega))$ and $R(\gamma) \in \mathcal{L}(\mathbb{R}^k_\diamond)$ are analytic in $\gamma \in L^\infty_+(\Omega)$. In particular, they are infinitely many times Fréchet differentiable. Furthermore, if*

η is compactly supported in Ω, then the boundary value problems

$$\begin{cases} \nabla \cdot (\gamma \nabla u') = -\nabla \cdot (\eta \nabla u) & \text{in } \Omega, \\ \nu \cdot \gamma \nabla u' = 0 & \text{on } \partial\Omega, \end{cases} \tag{52}$$

$$\begin{cases} \nabla \cdot (\gamma \nabla v') = -\nabla \cdot (\eta \nabla v) & \text{in } \Omega, \\ \nu \cdot \gamma \nabla v' = 0 & \text{on } \partial\Omega \setminus \bigcup_{j=1}^{k} \overline{E_j}, \\ v' + z\nu \cdot \gamma \nabla v' = V_j' & \text{on } E_j, \\ \displaystyle\int_{E_j} \nu \cdot \gamma \nabla v' \, dS = 0, & j = 1, 2, \dots k, \end{cases} \tag{53}$$

uniquely determine the Fréchet derivatives via

$$\Lambda'(\gamma)\eta = u'|_{\partial\Omega}, \quad R'(\gamma)\eta = V',$$

respectively. Above u and (v, V) are the unique weak solutions of (2) *and* (29)*, respectively.*

Proof For clarity, we only consider the CEM case as the CM can be handled analogously [6]. Given $(v, V) \in H^1(\Omega) \oplus \mathbb{R}^k_\diamond$ and $\eta \in L^\infty_+(\Omega)$, the variational problem

$$\int_\Omega \gamma \nabla v' \cdot \nabla w \, dx + \sum_{j=1}^{k} \int_{E_j} \frac{1}{z}(v' - V_j')(w - W_j) \, dS = -\int_\Omega \eta \nabla v \cdot \nabla w \, dx \tag{54}$$

for all $(w, W) \in H^1(\Omega) \oplus \mathbb{R}^k_\diamond$, is uniquely solvable. Moreover, if (v, V) weakly solves (29), then $V' = R'(\gamma)I$ [32]. Clearly, if η is compactly supported, the right-hand side of (54) does not induce any boundary terms and hence (v', V') satisfies (53).

Define the mapping

$$D = D(\eta) \colon \mathbb{R}^k_\diamond \to \mathbb{R}^k_\diamond, \quad V \mapsto V'$$

as the solution operator to (54). Consider the expansion

$$V(\gamma + \eta) = V(\gamma) + \tilde{V}(\eta),$$

where we denote $V(\gamma) = R(\gamma)I$ and $V(\gamma + \eta) = R(\gamma + \eta)I$. A direct calculation using the variational formulation with the associated internal potentials reveals

$$\tilde{V}(\eta) = D(\eta)V(\gamma + \eta) = D(\eta)\tilde{V}(\eta) + D(\eta)V(\gamma).$$

As $\|D(\eta)\| \leq C\|\eta\|_{L^\infty(\Omega)}$, the associated Neumann-series converges for small enough η. Consequently,

$$V(\gamma + \eta) = V(\gamma) + \tilde{V}(\eta) = V(\gamma) + (\mathrm{Id} - D(\eta))^{-1} D(\eta) V(\gamma) = \sum_{m=0}^{\infty} D(\eta)^m V(\gamma). \tag{55}$$

Different order Fréchet derivatives can be inductively derived using (55) and the fact that $D(\eta)$ is linear. □

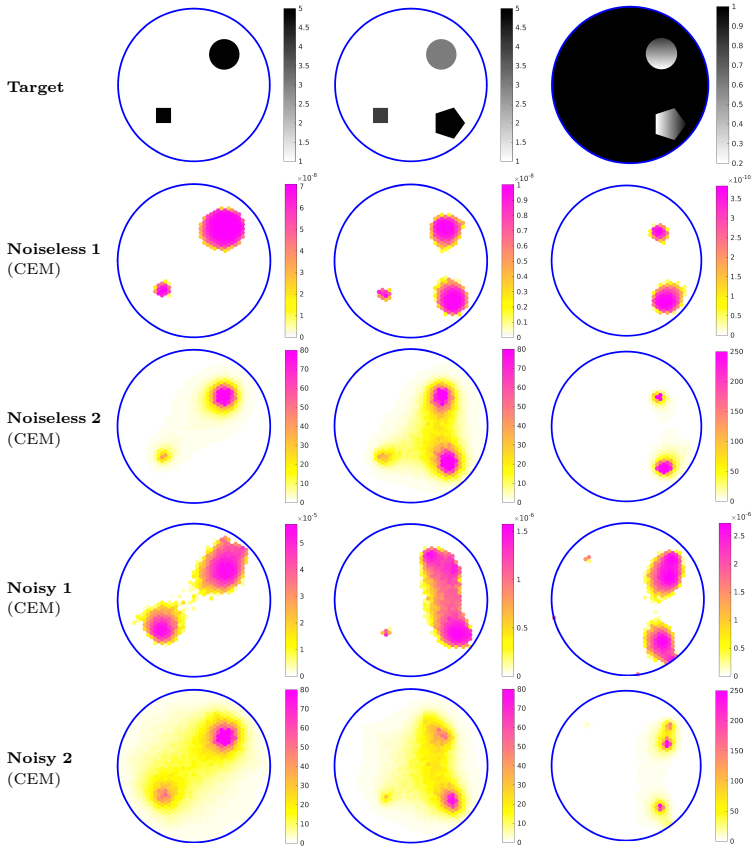

Fig. 3 Two-dimensional reconstructions on a unit disk with 16 equispaced and equidistant electrodes that cover 50% of the boundary. Reconstructions in the table rows "**Noiseless/Noisy 1**" and "**2**" are calculated using Algorithms 1 and 2, respectively. In each column, the noisy reconstructions are computed from a single dataset that contains around 0.5% pseudorandom noise; see (47) for details on the noise simulation. For more information on the FE mesh, see the beginning of section 6.

	Parameter	**Noiseless 1**	**Noiseless 2**	**Noisy 1**	**Noisy 2**
Left	$\mathrm{diam}(B)$	0.053	0.053	0.053	0.053
	β	0.8	$0.1 + 0.5\mathbb{N}$	0.8	$0.1 + 0.5\mathbb{N}$
	μ	1.001	1.01	1.01	1.01
Middle	$\mathrm{diam}(B)$	0.053	0.053	0.053	0.053
	β	0.66	$0.1 + 0.5\mathbb{N}$	0.66	$0.1 + 0.5\mathbb{N}$
	μ	1.0002	1.01	1.01	1.01
Right	$\mathrm{diam}(B)$	0.053	0.053	0.053	0.053
	β	-0.1	$-0.01 - 0.02\mathbb{N}$	-0.01	$-0.01 - 0.02\mathbb{N}$
	μ	0.99998	0.99998	1.001	1.001

Tbl. 3 Parameter values used in the computations; $\mathrm{diam}(B)$ is the diameter of the hexagons in the hexagonal reconstruction mesh (48), β is the probing scalar(s) in the semidefiniteness test, and μ is the regularization parameter (44).

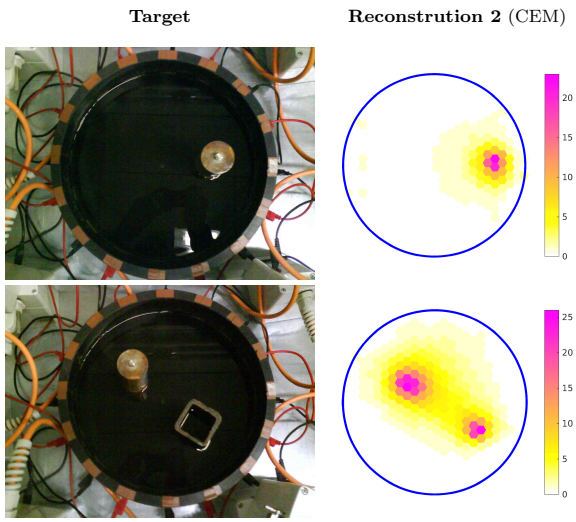

Fig. 4 Reconstructions from water tank measurement data computed using a planar computational model and Algorithm 2. The tank is cylindrically symmetric with cross-sectional radius 14 cm. The measurements are done using 16 identical rectangular equispaced electrodes of 2.5 cm width and 7 cm height, and the depth of the water is 7 cm. For more information on the FE mesh, see the beginning of section 6.

Parameter	**Reconstruction 2**
$\mathrm{diam}(B)$	0.093
β	$0.1 + 0.1\mathbb{N}$
μ	1.02

Tbl. 4 Parameter values used in the computations; $\mathrm{diam}(B)$ is the diameter of the hexagons in the hexagonal reconstruction mesh (48), β is the probing scalar(s) in the semidefiniteness test, and μ is the regularization parameter (44).

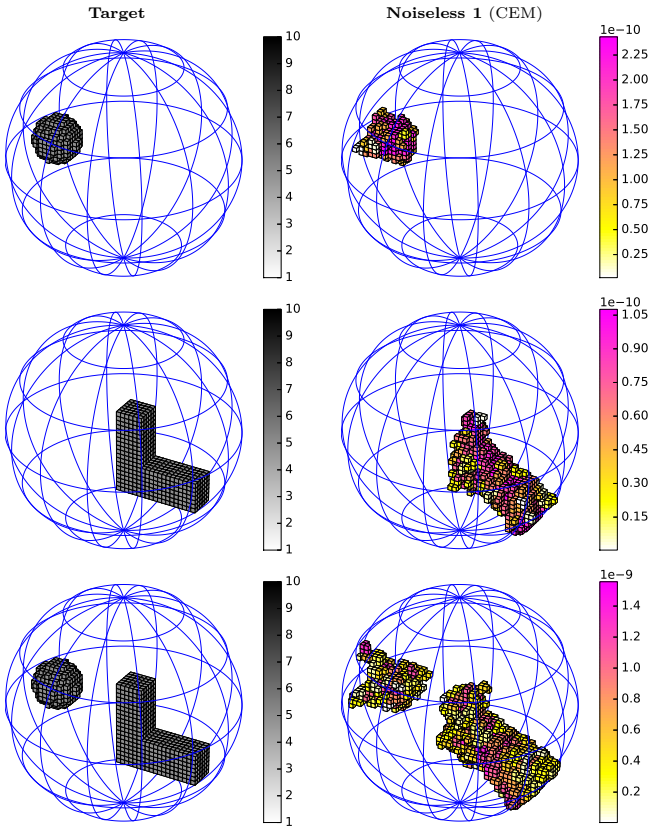

Fig. 5 Three-dimensional reconstructions from simulated noise-free measurements with 32 electrodes. The test sets B are cubes. Reconstructions in the table column "**Noiseless 1**" are calculated using Algorithm 1. For more information on the FE mesh, see the beginning of section 6.

	Parameter	**Noiseless 1**
Top	diam(B)	0.069
	β	0.8
	μ	1.023
Middle	diam(B)	0.069
	β	0.8
	μ	1.002
Bottom	diam(B)	0.069
	β	0.8
	μ	0.9966

Tbl. 5 Parameter values used in the computations; diam(B) is the diameter of the voxels in the reconstruction mesh (48), β is the probing scalar(s) in the semidefiniteness test, and μ is the regularization parameter (44).

PAPER C

Comparison of linear and non-linear monotonicity-based shape reconstruction using exact matrix characterizations

Type	Submitted manuscript (2016)
Author	Henrik Garde
Available from	`http://arxiv.org/abs/1602.04053`

Comparison of linear and non-linear monotonicity-based shape reconstruction using exact matrix characterizations

Henrik Garde*

Department of Applied Mathematics and Computer Science, Technical University of Denmark, 2800 Kgs. Lyngby, Denmark

(*March 2016*)

Detecting inhomogeneities in the electrical conductivity is a special case of the inverse problem in electrical impedance tomography, that leads to fast direct reconstruction methods. One such method can, under reasonable assumptions, exactly characterize the inhomogeneities based on monotonicity properties of either the Neumann-to-Dirichlet map (non-linear) or its Fréchet derivative (linear). We give a comparison of the non-linear and linear approach in the presence of measurement noise, and show numerically that the two methods gives essentially the same reconstruction. For a fair comparison, exact matrix characterizations are used when probing the monotonicity relations to avoid errors from numerical solution to PDEs and numerical integration. Using a special factorization of the Neumann-to-Dirichlet map also makes the non-linear method as fast as the linear method in the unit disk geometry.

Keywords: Electrical impedance tomography; monotonicity method; inverse boundary value problem; ill-posed problem; direct reconstruction

AMS Subject Classifications: 65N21; 35R30; 35Q60; 35R05

1. Introduction

In electrical impedance tomography (EIT) the internal electrical conductivity γ, inside a bounded Lipschitz domain $\Omega \subset \mathbb{R}^d$ for $d \geq 2$, is determined from boundary current-voltage measurements through electrode patches. The underlying mathematical problem, also known as the Calderón problem [1], is an inverse problem. A common mathematical formulation of EIT is the *continuum model*

$$\nabla \cdot (\gamma \nabla u) = 0 \text{ in } \Omega, \quad \nu \cdot \gamma \nabla u = g \text{ on } \partial\Omega, \quad \int_{\partial\Omega} u|_{\partial\Omega}\, ds = 0, \tag{1.1}$$

where u is the internal electrical potential, ν is an outwards pointing unit normal, and g is the applied current. The latter condition in (1.1) is a grounding of the total electrical potential at the boundary. If $\gamma \in L^\infty_+(\Omega)$ and $g \in H^{-1/2}_\diamond(\partial\Omega)$ with

$$L^\infty_+(\Omega) \equiv \{w \in L^\infty(\Omega) : \operatorname{ess\,inf} w > 0\},$$
$$H^{-1/2}_\diamond(\partial\Omega) \equiv \left\{w \in H^{-1/2}(\partial\Omega) : \langle w, 1\rangle = 0\right\},$$

*Corresponding author. Email: hgar@dtu.dk

then standard elliptic theory gives rise to a unique solution $u \in H^1_\diamond(\Omega)$ to (1.1), where the $\diamond$-symbol implies functions with zero mean on the boundary

$$H^{1/2}_\diamond(\partial\Omega) \equiv \left\{ w \in H^{1/2}(\partial\Omega) : \int_{\partial\Omega} w\, ds = 0 \right\},$$
$$H^1_\diamond(\Omega) \equiv \left\{ w \in H^1(\partial\Omega) : w|_{\partial\Omega} \in H^{1/2}_\diamond(\partial\Omega) \right\}.$$

The forward problem of EIT is the Neumann-to-Dirichlet (ND) map $\mathcal{R}(\gamma) : \nu \cdot \gamma\nabla u \to u|_{\partial\Omega}$ which relates any applied current to the corresponding boundary potential. In general $\mathcal{R}(\gamma)$ is a map from $H^{-1/2}_\diamond(\partial\Omega)$ to $H^{1/2}_\diamond(\partial\Omega)$, however in this paper it suffices to restrict it to a map in $\mathcal{L}(L^2_\diamond(\partial\Omega))$, the space of linear and bounded operators from $L^2_\diamond(\partial\Omega)$ to itself, where

$$L^2_\diamond(\partial\Omega) \equiv \left\{ w \in L^2(\partial\Omega) : \int_{\partial\Omega} w\, ds = 0 \right\}.$$

In this sense $\mathcal{R}(\gamma)$ is both compact and self-adjoint in the usual $L^2(\partial\Omega)$-inner product. The inverse problem of EIT is from knowledge of $\mathcal{R}(\gamma)$ and Ω to reconstruct γ. Uniqueness has been shown with various regularity assumptions depending on the dimension d [2–6] and for $d = 2$ there is uniqueness for general $L^\infty_+(\Omega)$-conductivities when the domain Ω is simply connected [7].

The inverse problem of EIT is severely ill-posed and with reasonable assumptions it is only possible to get conditional logarithmic stability [8, 9]. It is therefore not always of interest to perform a full reconstruction of γ, but rather reconstruct inclusions/inhomogeneities from a known or uninteresting background, which is an easier problem. Here it is assumed that

$$\gamma \equiv \gamma_0 + \kappa\chi_{\mathcal{D}},$$

where $\gamma_0 \in L^\infty_+(\Omega)$ is known and $\chi_{\mathcal{D}}$ is a characteristic function over the sought inclusion $\mathcal{D} \subset \Omega$, on which γ_0 is perturbed by κ. Direct reconstruction methods for such inclusion detection are prominently the factorization method [10–12] and the enclosure method [13, 14]. In this paper we investigate the more recent monotonicity method [15–19] that makes use of a monotonicity property of $\gamma \mapsto \mathcal{R}(\gamma)$. The basic idea of the method is to determine whether or not a chosen ball B is inside the inclusion $\mathcal{D}$, for instance in the simple case $\gamma \equiv 1 + \chi_{\mathcal{D}}$, then

$$B \subseteq \mathcal{D} \quad \text{implies} \quad \mathcal{R}(1 + \chi_B) - \mathcal{R}(1 + \chi_{\mathcal{D}}) \geq 0, \tag{1.2}$$

where the inequality is in terms of positive semi-definiteness. Checking the positive semi-definiteness for all balls in Ω gives an upper bound on $\mathcal{D}$, and in [15] it was shown that it completely characterizes $\mathcal{D}$ under reasonable regularity assumptions.

The map $\gamma \mapsto \mathcal{R}(\gamma)$ is non-linear and thus the evaluation of $\mathcal{R}(1 + \chi_B)$ is costly as each evaluation requires solving (1.1) for several Neumann conditions. In [15] it was shown that, without loss of shape information, the non-linear part could be replaced by a linearisation

$$B \subseteq \mathcal{D} \quad \text{implies} \quad \mathcal{R}(1) + \tfrac{1}{2}\mathcal{R}'(1)\chi_B - \mathcal{R}(1 + \chi_{\mathcal{D}}) \geq 0. \tag{1.3}$$

Using the Fréchet derivative is attractive as it only requires one evaluation of the deriva-

tive, and can be evaluated beforehand.

In this paper we compare reconstructions based on the non-linear approach (1.2) and the linear approach (1.3). In [17] resolution bounds for stable reconstruction were determined based on the non-linear and linear approach, which for the linear method were much more pessimistic, though the bounds were not shown to be optimal. With various levels of noise added to the measurements, the numerical examples in section 4 surprisingly shows that there is essentially no difference in the reconstructions based on the non-linear and the linear approach.

We focus on the unit disk domain $\Omega \equiv \mathbb{D}$ in $\mathbb{R}^2$. For a fair comparison of the non-linear and linear method, exact matrix representations are determined for $\mathcal{R}(1 + \beta\chi_B)$ and $\mathcal{R}'(1)\chi_B$ for any ball in $\mathbb{D}$, in order to avoid errors from numerical solution to PDEs and numerical integration. In this specific geometry the non-linear method furthermore becomes as fast as the linear method, by use of an explicit factorization derived from Möbius transformations.

More precise forward models for EIT exists for practical measurements, such as the *complete electrode model* (CEM). It was recently shown in [16] that the monotonicity method can be regularized against noise and generalizes to various approximations of the continuum model, including the CEM. By simply replacing the ND map with the CEM counterpart gives a reconstruction that is interlaced between two reconstructions from the continuum model; one without regularization and one with regularization. Thus, in this sense, the comparison made here also directly applies to the CEM variant of the monotonicity method.

The contents of this paper is organised as follows: in section 2 the monotonicity method is outlined and Möbius transformations are introduced to relate non-concentric ball inclusions to concentric ones. In section 3 the exact matrix representations of the ND map and its Fréchet derivatives are derived, and their matrix structures are elaborated on. Implementation details and numerical examples are given in section 4, and finally we conclude in section 5.

2. Monotonicity-based shape reconstruction

Let $\gamma_0 \in L^\infty_+(\Omega)$ be a known background conductivity and let $\kappa \in L^\infty_+(\Omega)$, and for an inclusion $\mathcal{D} \subset \Omega$ define the conductivity as

$$\gamma \equiv \gamma_0 + \kappa\chi_{\mathcal{D}}, \tag{2.1}$$

where $\chi_{\mathcal{D}}$ is a characteristic function on $\mathcal{D}$. As $\kappa > 0$ we call the inclusion in (2.1) positive (or definite). The monotonicity method can also be formulated for negative inclusions and for a combination of both positive and negative inclusions (indefinite) [15, 16]. We denote for $\beta > 0$ the monotonicity-based reconstructions by

$$\begin{aligned}\mathcal{T} &\equiv \{B \subseteq \Omega \text{ open ball} : \mathcal{R}(\gamma_0 + \beta\chi_B) - \mathcal{R}(\gamma) \geq 0\},\\ \mathcal{T}' &\equiv \left\{B \subseteq \Omega \text{ open ball} : \mathcal{R}(\gamma_0) + \beta\mathcal{R}'(\gamma_0)\chi_B - \mathcal{R}(\gamma) \geq 0\right\}.\end{aligned}$$

Here the Fréchet derivative $\mathcal{R}'(\gamma_0)$ of $\gamma \mapsto \mathcal{R}(\gamma)$ evaluated at γ_0 and in direction $\eta \in L^\infty(\Omega)$ is given by

$$\langle \mathcal{R}'(\gamma_0)[\eta]f, g\rangle = -\int_\Omega \eta\nabla w_f \cdot \overline{\nabla w_g}\, dx, \tag{2.2}$$

where w_f and w_g are solutions to (1.1) with conductivity γ_0 and Neumann condition f and g, respectively.

Using the formulation in [16], if we assume that γ_0 is furthermore piecewise analytic, $\overline{\mathcal{D}} \subseteq \Omega$ and $\mathcal{D}$ has connected complement (no holes in the inclusions), then

$$\mathcal{D} \subseteq \cup\mathcal{T} \subseteq \overline{\mathcal{D}} \quad \text{if} \quad 0 < \beta \leq \operatorname{ess\,inf} \kappa, \tag{2.3}$$

$$\mathcal{D} \subseteq \cup\mathcal{T}' \subseteq \overline{\mathcal{D}} \quad \text{if} \quad 0 < \beta \leq \operatorname{ess\,inf} \left(\frac{\gamma_0 \kappa}{\gamma} \right). \tag{2.4}$$

Given bounds $\beta_0^{\mathrm{L}} \leq \gamma_0 \leq \beta_0^{\mathrm{U}}$ and assuming prior knowledge of bounds on the inclusion $\beta^{\mathrm{L}} \leq \kappa \leq \beta^{\mathrm{U}}$, then an admissible choice for the β-value in (2.3) and (2.4) can be guaranteed by

$$\beta^{\mathrm{nonlin}} \equiv \beta^{\mathrm{L}}, \qquad \beta^{\mathrm{lin}} \equiv \frac{\beta_0^{\mathrm{L}} \beta^{\mathrm{L}}}{\beta_0^{\mathrm{U}} + \beta^{\mathrm{U}}}. \tag{2.5}$$

The main advantage of the linear method is that $\mathcal{R}'(\gamma_0)$ can be evaluated cheaply and prior to reconstruction. While the $\mathcal{R}(\gamma_0 + \beta\chi_B)$-maps can also be evaluated prior to reconstruction it requires knowledge of the β-value beforehand, and different β-values requires new evaluations. The non-linear method has the advantage that choosing β as in (2.5) only requires prior knowledge of a lower bound on κ, while the linear method requires both a lower and upper bound.

Given a noisy perturbation $E^\delta \in \mathcal{L}(L^2_\diamond(\partial\Omega))$ with noise level $\|E^\delta\|_{\mathcal{L}(L^2_\diamond(\partial\Omega))} \leq \delta$, then the noisy datum $\mathcal{R}^\delta(\gamma)$ is modelled with additive noise

$$\mathcal{R}^\delta(\gamma) \equiv \mathcal{R}(\gamma) + E^\delta. \tag{2.6}$$

For regularization parameter choice $\alpha(\delta) \geq \delta$ with $\lim_{\delta\to 0} \alpha(\delta) = 0$ it was proved in [16] that the following regularized reconstructions are upper bounds for $\mathcal{D}$, and that they converge as the noise level tends to zero, $\delta \to 0$:

$$\mathcal{T}_\alpha \equiv \left\{ B \subseteq \Omega \text{ open ball} : \mathcal{R}(\gamma_0 + \beta\chi_B) + \alpha \operatorname{Id} - \mathcal{R}^\delta(\gamma) \geq 0 \right\}, \tag{2.7}$$

$$\mathcal{T}'_\alpha \equiv \left\{ B \subseteq \Omega \text{ open ball} : \mathcal{R}(\gamma_0) + \beta\mathcal{R}'(\gamma_0)\chi_B + \alpha \operatorname{Id} - \mathcal{R}^\delta(\gamma) \geq 0 \right\}. \tag{2.8}$$

In the rest of the paper we will consider $\Omega \equiv \mathbb{D}$ the unit disk in $\mathbb{R}^2$, furthermore we will throughout identify $(x_1, x_2) \in \mathbb{R}^2$ with $x_1 + ix_2 \in \mathbb{C}$. The background conductivity will be chosen as $\gamma_0 \equiv 1$, however this choice is merely for ease of presentation, and other (constant) background conductivities can be used with the identity

$$\mathcal{R}(c\gamma) = \frac{1}{c}\mathcal{R}(\gamma), \quad c > 0.$$

2.1. *Möbius transformations and additional notation*

To get a precise and fast evaluation of $\mathcal{R}(1 + \beta\chi_B)$, we use Möbius transformations to move non-concentric balls $B_{C,R}$ to concentric balls $B_{0,r}$, and abuse that the spectrum of $\mathcal{R}(1 + \beta\chi_{B_{0,r}})$ is known. To shorten notation we will use the abbreviation

$$\gamma_{C,R} \equiv 1 + \beta\chi_{B_{C,R}},$$

where $B_{C,R}$ is an open ball with centre C and radius R. Denote by M_a for any $a \in \mathbb{D}$ the Möbius transformation

$$M_a(x) \equiv \frac{x-a}{\overline{a}x-1}, \ \ x \in \mathbb{D}.$$

Here $M_a : \mathbb{D} \to \mathbb{D}$ and $\partial\mathbb{D} \to \partial\mathbb{D}$, and is furthermore an involution i.e. its own inverse $M_a^{-1} = M_a$. Using the notation in [20] let $a \equiv \rho e^{i\zeta}$ for $0 \leq \rho < 1$ and $\zeta \in \mathbb{R}$. For $0 < r < 1$ then $M_a(B_{0,r}) = B_{C,R}$ with

$$C = \frac{\rho(r^2-1)}{\rho^2 r^2 - 1} e^{i\zeta}, \quad R = \frac{r(\rho^2-1)}{\rho^2 r^2 - 1}.$$

Furthermore, for $C = ce^{i\zeta}$ with $0 \leq c < 1$ and $0 < R < 1 - c$, then there is a unique $a \in \mathbb{D}$ such that $M_a(B_{C,R}) = B_{0,r}$ where r and a satisfies

$$r = \frac{1 + R^2 - c^2 - \sqrt{((1-R)^2 - c^2)((1+R)^2 - c^2)}}{2R}, \quad a = \frac{C}{1 - Rr}.$$

The above notation for the relation between a non-concentric ball $B_{C,R}$ and a concentric ball $B_{0,r}$ will be used in the remainder of the paper, and it is also illustrated in figure 2.1.

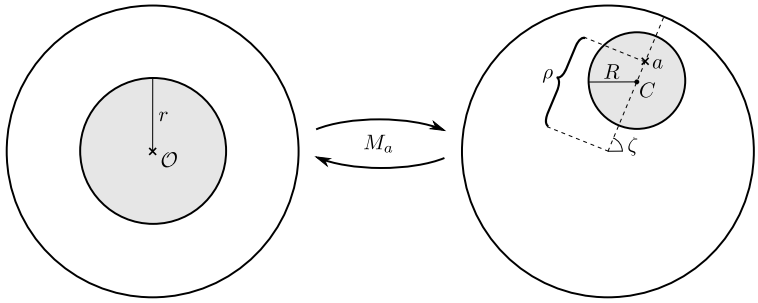

Figure 2.1. Illustration of M_a acting on balls $B_{0,r}$ and $B_{C,R}$.

Let $\mathcal{M}_a f \equiv f \circ M_a$, then the Jacobian determinant for the change of variables on $\mathbb{D}$ is

$$J_a \equiv \left(\frac{1-\rho^2}{|\overline{a} \cdot -1|^2} \right)^2.$$

The Jacobian determinant for the integral on $\partial\mathbb{D}$ is $J_a^{1/2}|_{\partial\mathbb{D}}$, and there is the following factorization of $\mathcal{R}(\gamma_{C,R})$ (cf. [20, Appendix B])

$$\mathcal{R}(\gamma_{C,R}) = P\mathcal{M}_a \mathcal{R}(\gamma_{0,r}) J_a^{1/2} \mathcal{M}_a. \tag{2.9}$$

Here $P : L^2(\partial\mathbb{D}) \to L^2_\diamond(\partial\mathbb{D})$ is the orthogonal projection given by $Pf \equiv f - \frac{1}{2\pi}\int_{\partial\mathbb{D}} f \, ds$, and $J_a^{1/2} : L^2(\partial\mathbb{D}) \to L^2(\partial\mathbb{D})$ is the multiplication operator $f \mapsto J_a^{1/2}|_{\partial\mathbb{D}} f$.

The operator $\mathcal{R}(\gamma_{0,r})$ for the concentric ball has the Fourier basis

$$f_n(\theta) \equiv \frac{1}{\sqrt{2\pi}} e^{in\theta}, \ \ n \in \mathbb{Z} \setminus \{0\}, \tag{2.10}$$

as eigenfunctions with eigenvalues

$$\lambda_n \equiv \frac{2+\beta(1-r^{2|n|})}{2+\beta(1+r^{2|n|})}\frac{1}{|n|}, \quad n \in \mathbb{Z}\setminus\{0\}. \tag{2.11}$$

So the factorization in (2.9) implies that the β-dependence of $\mathcal{R}(\gamma_{C,R})$ is given explicitly through a diagonalization of $\mathcal{R}(\gamma_{0,r})$ with the eigenvalues (2.11). Here $P\mathcal{M}_a$ and $J_a^{1/2}\mathcal{M}_a$ only depends on the transformation parameter a, and can be determined prior to reconstruction, thus making the non-linear and linear methods have identical computational complexity.

In order to determine matrix representations of $P\mathcal{M}_a$ and $J_a^{1/2}\mathcal{M}_a$ in the Fourier basis it is relevant to investigate the action of M_a on a trigonometric function, utilizing that it maps $\partial\mathbb{D}$ to itself:

$$M_a(e^{in\theta}) = e^{in\psi_a(\theta)} = M_a(e^{i\theta})^n = \left(\frac{e^{i\theta}-\rho e^{i\zeta}}{\rho e^{i(\theta-\zeta)}-1}\right)^n, \tag{2.12}$$

where ψ_a is the corresponding transformation in the angular variable on $\partial\mathbb{D}$.

LEMMA 2.1 *The map ψ_a in (2.12) is given by*

$$\psi_a(\theta) \equiv \pi + \zeta + 2\arctan\left(\frac{1+\rho}{1-\rho}\tan\left(\frac{\theta-\zeta}{2}\right)\right).$$

Proof. By standard trigonometric identities it follows that

$$e^{iz} = \frac{1+i\tan(z/2)}{1-i\tan(z/2)}, \quad z \in (-\pi,\pi),$$

thus

$$e^{i(\pi+2\arctan(z))} = \frac{-1-iz}{1-iz}, \quad z \in \mathbb{R}. \tag{2.13}$$

Since $M_a(e^{i\theta}) = e^{i\zeta}M_\rho(e^{i(\theta-\zeta)})$ we get

$$\psi_a(\theta) = \zeta + \psi_\rho(\theta-\zeta), \tag{2.14}$$

so it is sufficient to consider $\zeta = 0$. Writing $\psi_\rho(\theta)$ on the form (2.13) gives

$$e^{i\psi_\rho(\theta)} = \frac{e^{i\theta}-\rho}{\rho e^{i\theta}-1} = \frac{-1-iz}{1-iz} \Rightarrow z = \frac{(1+\rho)(1-e^{i\theta})}{(1-\rho)(1+e^{i\theta})}i = \frac{1+\rho}{1-\rho}\tan(\theta/2). \tag{2.15}$$

Now combining (2.15) with (2.13) and (2.14) yields the desired result. □

3. Matrix structures and characterizations

For a general real-valued $\gamma \in L_+^\infty(\mathbb{D})$ it holds that $\mathcal{R}(\gamma)\overline{f} = \overline{\mathcal{R}(\gamma)f}$. Defining $\{f_n\}_{n\in\mathbb{Z}\setminus\{0\}}$ as the usual Fourier basis for $L^2_\diamond(\partial\mathbb{D})$ as in (2.10) gives the identity $\mathcal{R}(\gamma)f_n = \overline{\mathcal{R}(\gamma)f_{-n}}$,

i.e.

$$\mathcal{A}_{n,m} \equiv \langle \mathcal{R}(\gamma) f_m, f_n \rangle = \overline{\langle \mathcal{R}(\gamma) f_{-m}, f_{-n} \rangle} = \overline{\mathcal{A}_{-n,-m}}, \;\; n, m \in \mathbb{Z} \setminus \{0\}. \tag{3.1}$$

So by arranging the row and column indices in the matrix representation $\mathcal{A}$ from negative to positive gives a *centrohermitian* matrix [21], meaning that there is symmetry (similar to a Hermitian matrix) across the centre of the matrix. The centrohermitian property can be written as in (3.1) for that particular choice of indices (which will used throughout this paper), or in general as

$$\mathcal{A} = \mathcal{J}\overline{\mathcal{A}}\mathcal{J},$$

where $\mathcal{J}$ is the *exchange matrix* which has zeroes in all entries except on the anti-diagonal (from bottom left to top right) where its entries equals 1. Since $\mathcal{R}(\gamma)$ is self-adjoint also makes $\mathcal{A}$ Hermitian in addition to being centrohermitian.

In [20] an explicit matrix representation of $\mathcal{R}(\gamma_{C,R})$ was determined by the use of basis functions orthonormal in weighted L^2-inner products. This matrix representation cannot be used for the monotonicity method as the basis functions depends on the transformation M_a, and here we need a fixed basis namely the same used for the datum $\mathcal{R}(\gamma)$. A common choice of orthonormal basis for the unit disk is the Fourier basis (2.10) for $L^2_\diamond(\partial\mathbb{D})$, which will also be used here. Now a matrix representation of $P\mathcal{M}_a$ and $J_a^{1/2}\mathcal{M}_a$ from (2.9) can be found in terms of the Fourier basis.

THEOREM 3.1 *Recall that $a = \rho e^{i\zeta}$ and define the matrix H_a by*

$$(H_a)_{n,m} \equiv \langle f_m, \mathcal{M}_a f_n \rangle, \;\; n, m \in \mathbb{Z} \setminus \{0\}, \tag{3.2}$$

then H_a has the following properties (note in particular that (iv)-(vii) *explicitly defines the entire matrix):*

(i) H_a *is a matrix representation of* $J_a^{1/2}\mathcal{M}_a$.
(ii) $(H_a)^*$ *is a matrix representation of* $P\mathcal{M}_a$.
(iii) H_a *is involutory, i.e.* $H_a = H_a^{-1}$.
(iv) $(H_a)_{n,m} = e^{i(m-n)\zeta}(H_\rho)_{n,m}, \;\; \forall n, m.$
(v) H_a *is centrohermitian, i.e.* $(H_a)_{n,m} = \overline{(H_a)_{-n,-m}}, \;\; \forall n, m.$
(vi) H_a *is block diagonal with* $(H_a)_{n,m} = 0$ *for* $n < 0, m > 0$ *and for* $n > 0, m < 0$.
(vii) There is the following formula for $n > 0, m > 0$*:*

$$(H_\rho)_{n,m} = \sum_{k=\max\{n-m,0\}}^{n} (-1)^{n-k} \binom{k+m-1}{k+m-n} \binom{n}{k} \rho^{2k+m-n}. \tag{3.3}$$

Proof. Since $J_a^{1/2}$ is the Jacobian determinant for the change of variables $\mathcal{M}_a$ we get

$$(H_a)_{n,m} = \langle J_a^{1/2}\mathcal{M}_a f_m, f_n \rangle,$$

which shows (i). (iii) follows directly from (i) as $J^{1/2}\mathcal{M}_a$ is an involution on $L^2_\diamond(\partial\mathbb{D})$ (cf. [20]). Furthermore, as P is self-adjoint in the $L^2(\partial\mathbb{D})$-inner product (as it is an orthogonal projection), then

$$\langle J_a^{1/2}\mathcal{M}_a f, g \rangle = \langle f, \mathcal{M}_a g \rangle = \langle Pf, \mathcal{M}_a g \rangle = \langle f, P\mathcal{M}_a g \rangle, \;\; \forall f, g \in L^2_\diamond(\partial\mathbb{D}),$$

i.e. the adjoint of $P\mathcal{M}_a$ (in terms of maps from $L^2_\diamond(\partial\mathbb{D})$ to itself) is $J_a^{1/2}\mathcal{M}_a$, which shows (ii).

Proof of (iv) and (v): from Lemma 2.1 and (2.14) where ψ_ρ is 2π-periodic, then a change of variable from θ to $\theta+\zeta$ gives

$$\begin{aligned}\langle f_m, \mathcal{M}_a f_n\rangle &= \frac{1}{2\pi}\int_0^{2\pi} e^{i(m\theta - n\zeta - n\psi_\rho(\theta-\zeta))}\,d\theta = \frac{1}{2\pi}\int_0^{2\pi} e^{i(m\theta + m\zeta - n\zeta - n\psi_\rho(\theta))}\,d\theta \\ &= e^{i(m-n)\zeta}\frac{1}{2\pi}\int_0^{2\pi} e^{i(m\theta - n\psi_\rho(\theta))}\,d\theta = e^{i(m-n)\zeta}\langle f_m, \mathcal{M}_\rho f_n\rangle.\end{aligned}$$

This shows (iv). Furthermore,

$$\langle f_m, \mathcal{M}_a f_n\rangle = \frac{1}{2\pi}\int_0^{2\pi} e^{i(m\theta - n\psi_a(\theta))}\,d\theta = \overline{\frac{1}{2\pi}\int_0^{2\pi} e^{-i(m\theta - n\psi_a(\theta))}\,d\theta} = \overline{\langle f_{-m}, \mathcal{M}_a f_{-n}\rangle}.$$

Proof of (vi): first notice the identity

$$\begin{aligned}\overline{\mathcal{M}_\rho f_n} &= \frac{1}{\sqrt{2\pi}}\overline{\left(\frac{e^{i\theta}-\rho}{\rho e^{i\theta}-1}\right)^n} = \frac{1}{\sqrt{2\pi}}\left(\frac{\rho e^{-i\theta}-1}{e^{-i\theta}-\rho}\right)^{-n} = \frac{1}{\sqrt{2\pi}}\left(\frac{e^{i\theta}-\rho}{\rho e^{i\theta}-1}\right)^{-n} \\ &= \frac{1}{\sqrt{2\pi}}(e^{i\theta}-\rho)^{-n}(\rho e^{i\theta}-1)^n.\end{aligned}$$

Assume $n>0$, then using the binomial theorem for both $(e^{i\theta}-\rho)^{-n}$ and $(\rho e^{i\theta}-1)^n$ (which for $(e^{i\theta}-\rho)^{-n}$ converges as $\rho<1$) and using that the negative binomial coefficient can be written as

$$\binom{-n}{k'} = (-1)^{k'}\binom{n+k'-1}{k'},$$

gives

$$\begin{aligned}\overline{\mathcal{M}_\rho f_n} &= \frac{1}{\sqrt{2\pi}}\left[\sum_{k'=0}^{\infty}(-1)^{k'}\binom{n+k'-1}{k'}(-\rho)^{k'}e^{-i(k'+n)\theta}\right]\cdot\left[\sum_{k=0}^{n}\binom{n}{k}(-1)^{n-k}\rho^k e^{ik\theta}\right] \\ &= \frac{1}{\sqrt{2\pi}}\sum_{k'=0}^{\infty}\sum_{k=0}^{n}(-1)^{n-k}\binom{n+k'-1}{k'}\binom{n}{k}\rho^{k+k'}e^{i(k-k'-n)\theta},\ \ n>0.\end{aligned}$$

Thus

$$\langle f_m, \mathcal{M}_\rho f_n\rangle = \frac{1}{2\pi}\sum_{k'=0}^{\infty}\sum_{k=0}^{n}(-1)^{n-k}\binom{n+k'-1}{k'}\binom{n}{k}\rho^{k+k'}\int_0^{2\pi}e^{i(m+k-k'-n)\theta}\,d\theta. \quad (3.4)$$

So if $m<0$ and $n>0$ then $m+k-k'-n<0$ for all $k=0,1,\dots,n$ and $k'\geq 0$ so $\int_0^{2\pi}e^{i(m+k-k'-n)\theta}\,d\theta = 0$, i.e.

$$\langle f_m, \mathcal{M}_\rho f_n\rangle = 0,\ \ m<0, n>0. \quad (3.5)$$

Now (vi) follows from (3.5), (iv), and (v).

Proof of (vii): Assume $n > 0$ and $m > 0$. We have

$$\frac{1}{2\pi}\int_0^{2\pi} e^{i(m+k-k'-n)\theta}\, d\theta = \delta_{m+k-k'-n,0},$$

so to find the non-zero coefficients in (3.4) we need to determine when $m+k-k'-n = 0$, i.e. set $k' = m+k-n$ and find $m+k-n \geq 0$ (as we have $k' \geq 0$). Since $k \geq 0$ we need $k' = m+k-n$ and $k \geq \max\{n-m, 0\}$. Thus (3.4) becomes

$$\langle f_m, \mathcal{M}_\rho f_n\rangle = \sum_{k=\max\{n-m,0\}}^{n} (-1)^{n-k}\binom{k+m-1}{k+m-n}\binom{n}{k}\rho^{2k+m-n}, \;\; n>0, m>0.$$

□

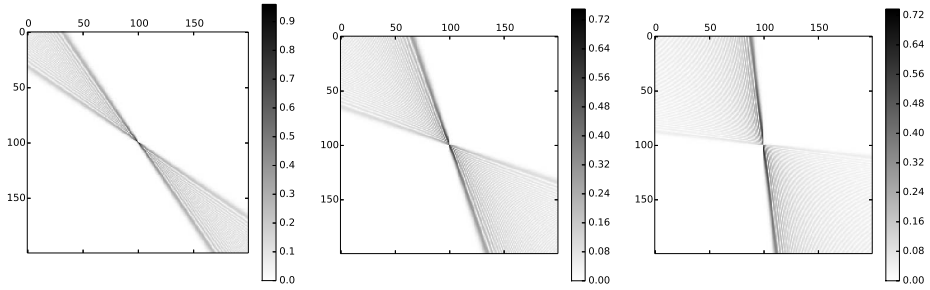

(a) $a = 0.2$ (b) $a = 0.5$ (c) $a = 0.8$

Figure 3.1. Plot of absolute value $|(H_a)_{n,m}|$ for $|n|, |m| = 1, 2, \ldots, 100$.

Figure 3.1 shows the structure of the H_a-matrices for different choice of a. It is evident that as $a \to 1$, and thereby M_a maps $B_{0,r}$ to a ball $B_{C,R}$ close to the boundary, the representation H_a becomes less sparse in the Fourier basis.

If we denote the matrix representation of $\mathcal{R}(\gamma_{C.R})$ by

$$A_{n,m} \equiv \langle \mathcal{R}(\gamma_{C,R}) f_m, f_n\rangle,$$

and for $\mathcal{R}(\gamma_{0,r})$ the matrix representation is a diagonal matrix D with $D_{n,n} \equiv \lambda_n$ from (2.11), then from Theorem 3.1 and (2.9) we have

$$A = (H_a)^* D H_a. \tag{3.6}$$

Due to the centrohermitian and block diagonal properties of both H_a and D they have the block structure

$$H_a = \begin{pmatrix} \mathcal{J}\overline{H_a^+}\mathcal{J} & 0 \\ 0 & H_a^+ \end{pmatrix}, \quad D = \begin{pmatrix} \mathcal{J}D^+\mathcal{J} & 0 \\ 0 & D^+ \end{pmatrix}, \tag{3.7}$$

where $\mathcal{J}$ is the previously defined exchange matrix, H_a^+ is the lower right part of H_a i.e. for $n > 0, m > 0$, and similarly D^+ is the lower right part of D. Therefore we get the

following structure for A:

$$A = \begin{pmatrix} \mathcal{J}\overline{(H_a^+)^* D^+ H_a^+}\mathcal{J} & 0 \\ 0 & (H_a^+)^* D^+ H_a^+ \end{pmatrix}. \tag{3.8}$$

That the matrix representation of $\mathcal{R}(\gamma_{C,R})$, for any ball inclusion $B_{C,R}$, is a block diagonal matrix of the form (3.8) is a non-trivial result of the factorization (3.6). For a general $\gamma \in L_+^\infty(\mathbb{D})$ the matrix representation of $\mathcal{R}(\gamma)$ is not block diagonal. Furthermore, it also means that we only need to evaluate and save the H_a^+-part for constructing A.

An explicit formula can also be obtained for the Fréchet derivative $\mathcal{R}'(1)$ on ball inclusions.

PROPOSITION 3.2 *Denote by A' the matrix representation of $\mathcal{R}'(1)[\chi_{B_{C,R}}]$, i.e.*

$$A'_{n,m} \equiv \langle \mathcal{R}'(1)[\chi_{B_{C,R}}] f_m, f_n \rangle, \quad n, m \in \mathbb{Z} \setminus \{0\}, \tag{3.9}$$

then

(i) A' is Hermitian, i.e. $A' = (A')^*$.
(ii) A' is centrohermitian, i.e. $A'_{n,m} = \overline{A'_{-n,-m}}$.
(iii) A' is block diagonal with $A'_{n,m} = 0$ for $n < 0, m > 0$ and for $n > 0, m < 0$.
(iv) There is the following formula for $n > 0, m > 0$, recalling that $C = ce^{i\zeta}$:

$$A'_{n,m} = -e^{i(m-n)\zeta} \sum_{k=0}^{\min\{n,m\}-1} \frac{1}{k+1} \binom{m-1}{k} \binom{n-1}{k} c^{m+n-2k-2} R^{2k+2}. \tag{3.10}$$

Proof. (i) and (ii) follows directly from (2.2), and the proof of (iii) can be done in an analogous way to the proof of Theorem 3.1. These three properties can also be derived from the fact that the matrix representations of both $\mathcal{R}(\gamma_{C,R})$ and $\mathcal{R}(1)$ have the same properties.

Now proving (iv). Let $n > 0, m > 0$ and for $x \in \mathbb{D}$ write $x \equiv x_1 + ix_2$ for real-valued x_1 and x_2. Then the solution to (1.1) with $\gamma \equiv 1$ and Neumann boundary condition f_n from (2.10) is

$$w_n(x) \equiv \frac{1}{n\sqrt{2\pi}} x^n, \quad n > 0.$$

From (2.2) we get

$$A'_{n,m} = -\int_{B_{C,R}} \nabla w_m \cdot \overline{\nabla w_n}\, dx = -\frac{1}{\pi} \int_{B_{C,R}} x^{m-1} \overline{x}^{n-1}\, dx.$$

Applying a change of variables from x to $x + C$ and writing $x = \eta e^{i\theta}$ in polar coordinates yields

$$\begin{aligned} A'_{n,m} &= -\frac{1}{\pi} \int_{B_{0,R}} (x + C)^{m-1} \overline{(x + C)}^{n-1}\, dx \\ &= -\frac{1}{\pi} \int_0^R \int_0^{2\pi} (\eta e^{i\theta} + C)^{m-1} (\eta e^{-i\theta} + \overline{C})^{n-1} \eta\, d\theta\, d\eta. \end{aligned}$$

Now using the binomial theorem for $(\eta e^{i\theta} + C)^{m-1}$ and $(\eta e^{-i\theta} + \overline{C})^{n-1}$

$$A'_{n,m} = -\frac{1}{\pi} \sum_{k=0}^{m-1} \sum_{k'=0}^{n-1} \binom{m-1}{k} \binom{n-1}{k'} C^{m-k-1} \overline{C}^{n-k'-1} \int_0^R \eta^{k+k'+1} \, d\eta \int_0^{2\pi} e^{i(k-k')\theta} \, d\theta.$$

Here the term $\int_0^{2\pi} e^{i(k-k')\theta} \, d\theta$ is only non-zero for $k' = k$, which can only hold for k up to $\min\{n, m\} - 1$. Also recalling that $C = ce^{i\zeta}$ gives the expression in (3.10)

$$\begin{aligned} A'_{n,m} &= -2 \sum_{k=0}^{\min\{n,m\}-1} \binom{m-1}{k} \binom{n-1}{k} C^{m-k-1} \overline{C}^{n-k-1} \int_0^R \eta^{2k+1} \, d\eta \\ &= -e^{i(m-n)\zeta} \sum_{k=0}^{\min\{n,m\}-1} \frac{1}{k+1} \binom{m-1}{k} \binom{n-1}{k} c^{m+n-2k-2} R^{2k+2}. \end{aligned}$$

□

Analogous to (3.7) the matrix structure of A' is

$$A' = \begin{pmatrix} \mathcal{J} \overline{A'^{+}} \mathcal{J} & 0 \\ 0 & A'^{+} \end{pmatrix},$$

thus we only need to evaluate the lower right part A'^{+}, and as A' is Hermitian it is sufficient to evaluate the upper triangular part of A'^{+}.

4. Implementation details and numerical results

In this section we will shortly discuss the implementation details for the algorithms (2.7) and (2.8), and apply the linear and non-linear approach to the three examples in figure 4.1. These three examples are difficult scenarios for EIT reconstruction. Example A will demonstrate if the algorithms can reconstruct very non-convex shapes, in particular where the non-convex part is oriented away from the closest boundary. Example B will test if the algorithms can separate relatively small convex inclusions. Since the monotonicity method cannot detect holes in inclusions [15], the point of Example C will be to test whether one wide inclusion can partially shield another inclusion, potentially making it difficult to separate the two in the presence of noise. The β-values for the reconstructions are chosen as in (2.5) which for the examples in figure 4.1 are $\beta^{\text{nonlin}} = 4$ and $\beta^{\text{lin}} = 0.8$.

For the numerical implementation we will use a regular hexagonal tiling of the plane, where each hexagon has a centre C and radius R such that its corners are placed on the ball $B_{C,R}$. Here the resolution is controlled by the radius R which is kept fixed; it is chosen as $R = 0.025$ for the given examples. In terms of the monotonicity-based reconstructions (2.7) and (2.8) a hexagon is included in the reconstruction if the corresponding ball $B_{C,R}$ yields a positive semi-definite operator in the monotonicity test. The positive semi-definiteness is determined from the sign of the smallest eigenvalue, which are real-valued as all the involved operators are self-adjoint.

In practice we can only use finite dimensional approximations to the matrix representations in (3.6) and (3.9), so we have $|n|, |m| = 1, 2, \ldots, N$ which gives $2N \times 2N$ matrices. For any compact operator $\mathcal{F} : L^2_\diamond(\partial\mathbb{D}) \to L^2_\diamond(\partial\mathbb{D})$ the corresponding N-term

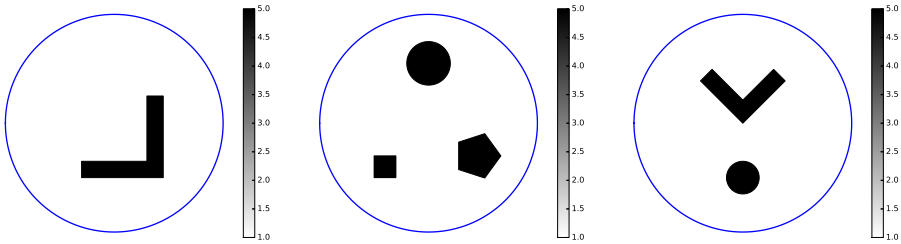

(a) Example A (b) Example B (c) Example C

Figure 4.1. Numerical phantoms.

matrix approximation is

$$F^N_{n,m} \equiv \langle \mathcal{F} f_m, f_n \rangle, \quad |n|, |m| = 1, 2, \ldots, N.$$

As $\{f_n\}_{n\in\mathbb{Z}\setminus\{0\}}$ is an orthonormal basis for $L^2_\diamond(\partial\mathbb{D})$ then F^N is a matrix representation of $P_N\mathcal{F}P_N$, where P_N is the orthogonal projection onto $\operatorname{span}\{f_n\}_{|n|=1,2,\ldots,N}$. It is straightforward to show that the eigenvalues of F^N and $P_N\mathcal{F}P_N$ coincide, and from spectral theory of compact operators (e.g. [22, 23]) it is well known that the spectrum of $P_N\mathcal{F}P_N$ converge to that of $\mathcal{F}$ as $N \to \infty$.

In the numerical examples below we use $N = 16$ which implies 32 orthonormal current patterns; more than 32 current patterns for a 2D reconstruction is often considered excessive. Since the factorization (3.6) holds in terms of infinite matrices, we use a much larger $\tilde{N} > N$ to generate the H_a-matrices for which we according to (3.8) only construct the $\tilde{N} \times \tilde{N}$ matrices H_a^+. Afterwards we use (3.8) to construct the larger $2\tilde{N} \times 2\tilde{N}$ matrix $A^{\tilde{N}}$ and extract the central $2N \times 2N$ matrix A^N to use for the monotonicity tests in the non-linear case. For the following examples $\tilde{N} = 200$ was used, and that sufficient accuracy is attained is checked through the involution property of H_a; namely how large a central $2N \times 2N$ part of $H_a^{\tilde{N}} H_a^{\tilde{N}}$ that equals an identity matrix.

From Theorem 3.1.(vii) it is observed that $(H_\rho)_{n,m}$ is a polynomial in ρ with at most m non-zero terms. The coefficients of the polynomial are independent of a, and can therefore be precomputed and reused for the evaluation of H_a for each a. Since the coefficients in the polynomial are binomial coefficients, and that we need to evaluate them up to a very high index $\tilde{N} = 200$, the summation in (3.3) quickly becomes numerically unstable. For this purpose the Python library gmpy2 [24] is used, which has a very fast implementation for exact evaluation of binomial coefficients, and has data structures that supports much higher precision (in terms of no. of digits) and is able to accurately evaluate the expressions in (3.3). Alternatively, a more stable approach which would not require gmpy2 or the equivalent, is to apply Gauss-Legendre quadrature to the inner products (3.2) with weights $\mathbf{w}$ and sample points $\boldsymbol{\theta}$, which from Lemma 2.1 gives

$$(H_a)_{n,m} \simeq \frac{(-1)^n e^{-in\zeta}}{2\pi} \mathbf{w}^{\mathrm{T}} \exp\left[i \left(m\boldsymbol{\theta} - 2n \arctan\left(\frac{1+\rho}{1-\rho} \tan\left[\frac{1}{2}(\boldsymbol{\theta} - \zeta) \right] \right) \right) \right]. \quad (4.1)$$

It should be noted that using (4.1) was about 30 times slower than (3.3) when the binomial coefficients were reused, in order to attain the same precision for $\tilde{N} = 200$.

The involved PDEs to simulate the data $\mathcal{R}(\gamma)$, for the three examples in figure 4.1, are solved with a finite element method with piecewise affine elements. The applied mesh is excessively fine ($1.3{\cdot}10^5$ nodes) and is aligned with the inclusions, such that we can expect

that only the applied noise and the finite dimensional truncation $2N$ has an influence in the comparison.

The added noise is a matrix E^δ cf. (2.6), which is constructed in the following way: for each index (n, m) let $E^1_{n,m}$ be a realization from a normal $\mathcal{N}(0, 1)$-distribution, and take the Hermitian and centrohermitian parts:

$$E^2 \equiv \frac{1}{2}\left[E^1 + (E^1)^*\right], \quad E^3 \equiv \frac{1}{2}\left[E^2 + \mathcal{J}\overline{E^2}\mathcal{J}\right]. \tag{4.2}$$

If $\mathcal{A}$ is the matrix representation of the noiseless data $\mathcal{R}(\gamma)$, then we scale

$$E^4_{n,m} \equiv E^3_{n,m}\mathcal{A}_{n,m}.$$

Finally, the noise is scaled to have a specified norm δ in the operator norm

$$E^\delta \equiv \frac{\delta}{\|E^4\|}E^4.$$

A different noise realization is used for each noise level δ, however the same noisy data $\mathcal{R}^\delta(\gamma)$ is used for both the linear and non-linear reconstruction. It should be noted that the measured data $\mathcal{R}^\delta(\gamma)$ can in practice be symmetrized to achieve (4.2), which often reduces the noise level significantly below δ. How much the noise level is reduced completely depends on the particular noise realization. The way the noise is added in this paper makes the reconstructions less dependent on whether we were *lucky* enough that part of the noise cancels out, and the reconstructions are in this sense a worst-case scenario for a specified noise level δ.

It was shown in [16] that the regularization parameter could be chosen as $\alpha = \delta$, however it is no guarantee for the best choice of regularization parameter. Furthermore, there is also the truncation of the dimension to $2N$ which implies that slightly more regularization is required. In [16] it was suggested that a good choice of regularization parameter in both linear and non-linear cases is

$$\alpha = -\mu \inf \sigma(\mathcal{R}(\gamma_0) - \mathcal{R}^\delta(\gamma)), \tag{4.3}$$

where γ_0 is the background conductivity (in this case constant 1), σ denotes the spectrum of the operators, and μ is a parameter that must be tuned; typically very close to 1. The values of μ for the numerical experiments are shown in table 4.1.

	Example A		Example B		Example C	
δ	linear	non-linear	linear	non-linear	linear	non-linear
0	0.999200	0.998600	0.999750	0.999660	0.999300	0.998900
10^{-5}	0.999600	0.999200	0.999750	0.999400	0.999600	0.999400
10^{-4}	0.999200	0.998400	0.999800	0.999700	0.999600	0.999200
10^{-3}	1.000040	1.000050	1.000002	1.000004	1.000040	1.000070
10^{-2}	1.000100	1.000200	1.000050	1.000050	1.000002	1.000002

Table 4.1. Choice of regularization parameter μ from (4.3) for the examples in figure 4.1 with different levels of noise δ.

The reconstruction is very fast as it only requires computation of eigenvalues for $2N \times 2N$ Hermitian matrices, and it is suited for parallel computing as the monotonicity tests for different balls can be done completely independently.

From figure 4.2 and 4.3 it is clear that there is hardly any difference in the reconstructions based on the linear and non-linear methods. It is observed that for 32 current

patterns it is difficult to reconstruct non-convex shapes, in particular the large L-shaped inclusion in Example A where the non-convex part is pointed away from the closest boundary. For the non-convex inclusion in Example C the reconstruction is reasonable in the noiseless case, where for increased noise the separation of the two inclusions is lost. This is a common feature of the monotonicity reconstructions when one larger inclusion partially shields another.

For Example B there is a reasonable separation of the inclusions even for the highest noise level, and both shapes and locations are found well in the cases $\delta = 0, 10^{-5}, 10^{-4}$. A slight positioning error is present in Example B even in the noiseless case, this can sometimes happen when there are multiple inclusions of various sizes placed asymmetrically. The positioning error as well as shape errors can be improved by either increasing the pixel size (this affects the size of the balls in the test inclusions) or by increasing the number of current patterns used.

The ball inclusions $B_{C,R}$ are small enough that we might consider if $\mathcal{R}(1) + \beta^{\text{lin}}\mathcal{R}'(1)\chi_{B_{C,R}}$ is a good approximation to $\mathcal{R}(1 + \beta^{\text{nonlin}}\chi_{B_{C,R}})$, and therefore leads to similar reconstructions. Firstly, the Fréchet derivative is given in terms of L^∞ which only relates to the β-values here, and not the radius of the ball inclusions, secondly the values of β^{lin} and β^{nonlin} in this case are quite different. Furthermore, tests from both smaller and larger R gives comparable results.

5. Conclusions

The linear and non-linear algorithms for monotonicity-based shape reconstruction in EIT were compared, and surprisingly found to essentially yield the same reconstructions both for noiseless and for noisy data. Exact matrix characterizations were derived for the Neumann-to-Dirichlet map and its Fréchet derivative for the ball inclusions used in the monotonicity tests. These matrix characterizations ensures that the sources of errors in the reconstructions are limited to the finite dimensional truncation and the added noise.

It is clear that the monotonicity method performs best for detecting small convex shapes, and here it is often possible to separate inclusions quite well in the presence of noise. For non-convex shapes, one usually obtains something that resembles a convex approximation to the shape either due to noise or the limited number of current patterns.

Funding

This research is supported by Advanced Grant No. 291405 HD-Tomo from the European Research Council.

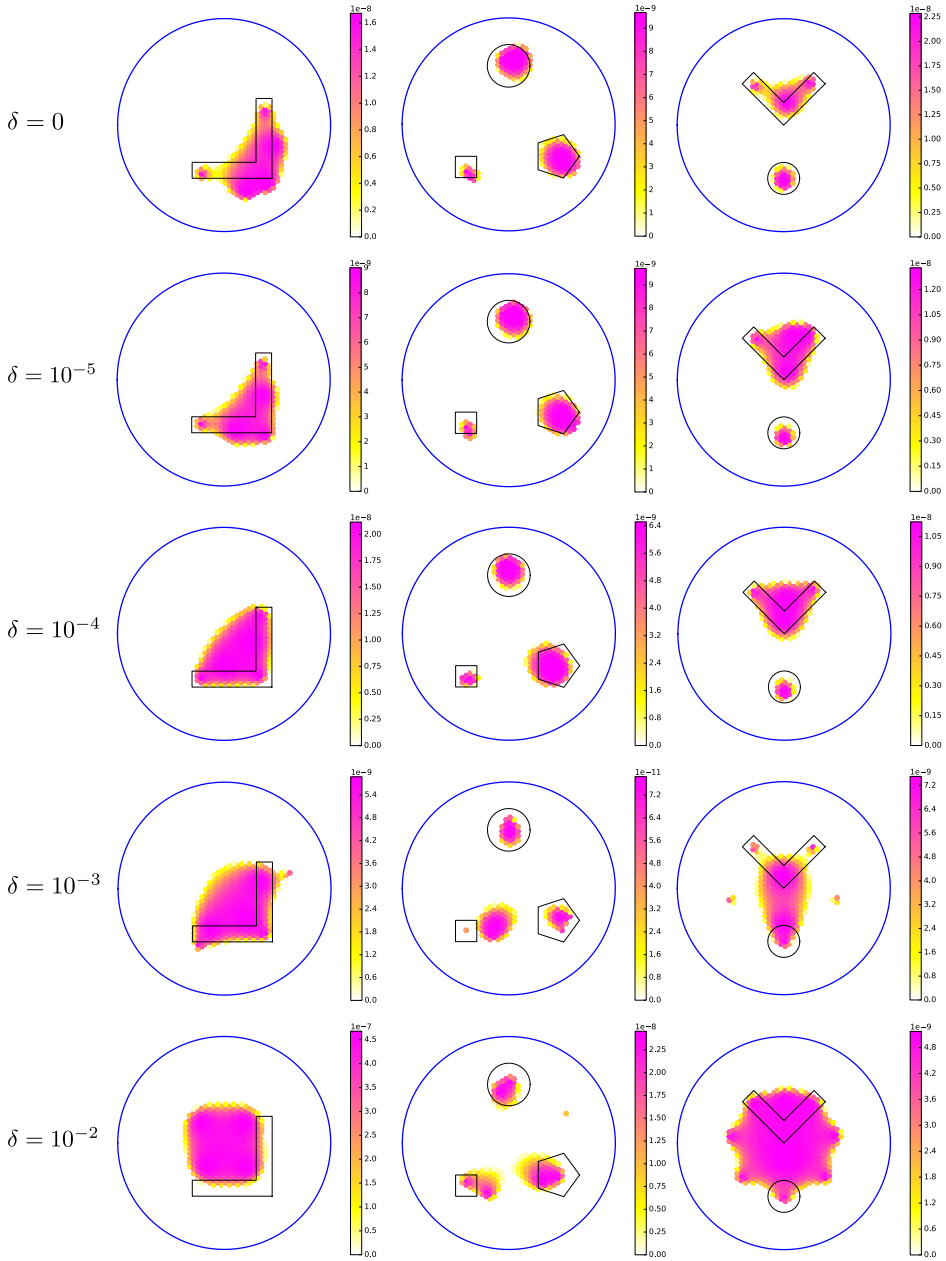

Figure 4.2. Monotonicity reconstruction using the linear algorithm for the examples in figure 4.1 with various levels of noise δ. The regularization parameters are chosen as in table 4.1. The smallest eigenvalues are plotted for the hexagons where the inclusions are detected. The correct targets are outlined with a solid black line.

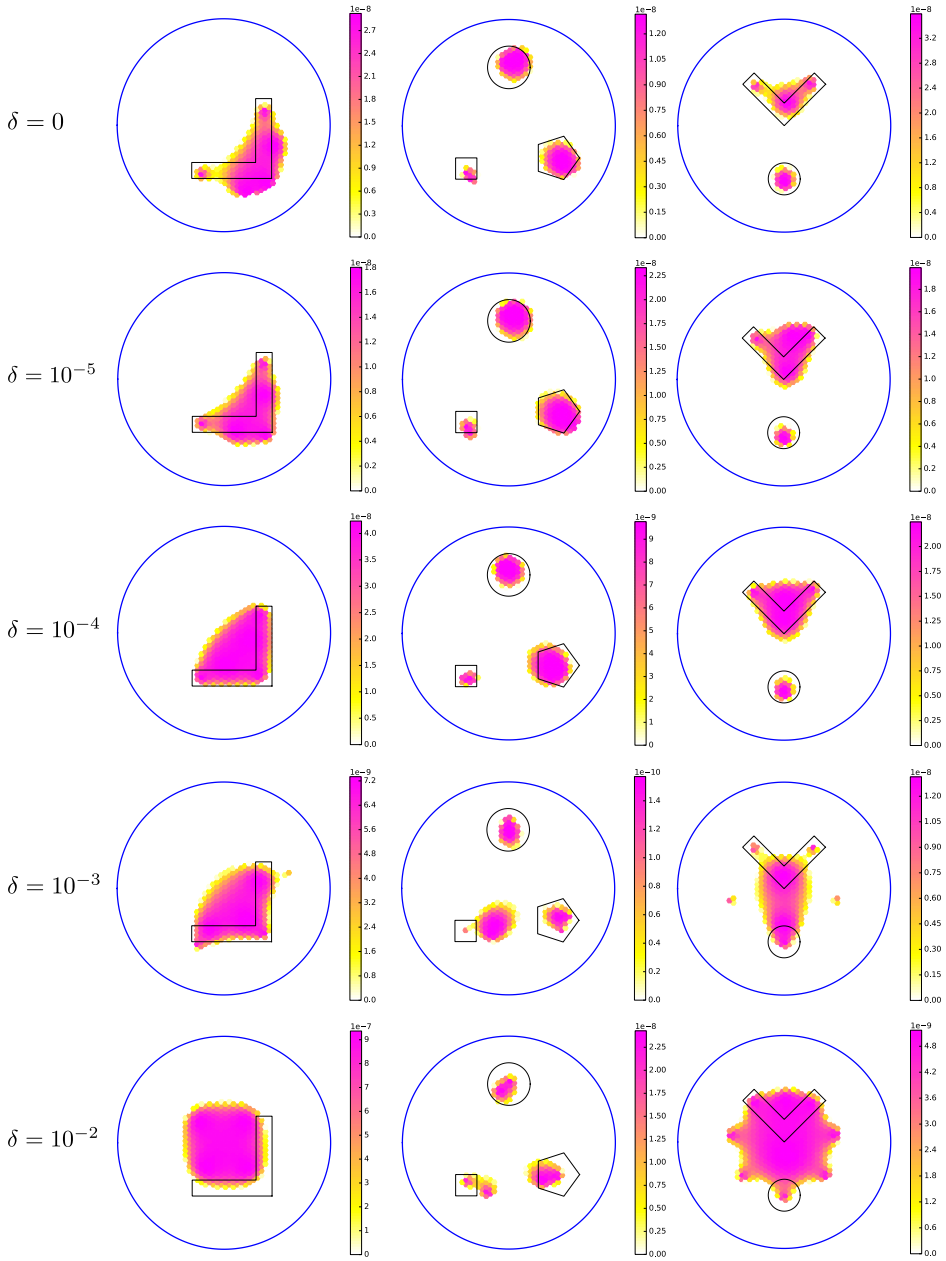

Figure 4.3. Monotonicity reconstruction using the non-linear algorithm for the examples in figure 4.1 with various levels of noise δ. The regularization parameters are chosen as in table 4.1. The smallest eigenvalues are plotted for the hexagons where the inclusions are detected. The correct targets are outlined with a solid black line.

References

[1] Calderón AP. On an inverse boundary value problem. In: Seminar on Numerical Analysis and its Applications to Continuum Physics (Rio de Janeiro, 1980). Rio de Janeiro: Soc. Brasil. Mat.; 1980. p. 65–73.

[2] Sylvester J, Uhlmann G. A global uniqueness theorem for an inverse boundary value problem. Annals of Mathematics. 1987;125:153–169.

[3] Nachman AI. Reconstructions from boundary measurements. Annals of Mathematics. 1988; 128:531–576.

[4] Novikov RG. A multidimensional inverse spectral problem for the equation $-\delta\psi + (v(x) - eu(x))\psi = 0$. Functional Analysis and Its Applications. 1988;22(4):263–272.

[5] Nachman AI. Global uniqueness for a two-dimensional inverse boundary value problem. Annals of Mathematics. 1996;143:71–96.

[6] Haberman B, Tataru D. Uniqueness in Calderón's problem with Lipschitz conductivities. Duke Math J. 2013 feb;162(3):497–516.

[7] Astala K, Päivärinta L. Calderón's inverse conductivity problem in the plane. Annals of Mathematics. 2006;163(1):265–299.

[8] Alessandrini G. Stable determination of conductivity by boundary measurements. Applicable Analysis. 1988;27:153–172.

[9] Mandache N. Exponential instability in an inverse problem for the Schrödinger equation. Inverse Problems. 2001;17(5):1435–1444.

[10] Brühl M. Explicit characterization of inclusions in electrical impedance tomography. SIAM Journal on Mathematical Analysis. 2001;32:1327–1341.

[11] Brühl M, Hanke M. Numerical implementation of two non-iterative methods for locating inclusions by impedance tomography. Inverse Problems. 2000;16:1029–1042.

[12] Lechleiter A, Hyvönen N, Hakula H. The factorization method applied to the complete electrode model of impedance tomography. SIAM Journal on Applied Mathematics. 2008; 68:1097–1121.

[13] Ikehata M. How to draw a picture of an unknown inclusion from boundary measurements. Two mathematical inversion algorithms. Journal of Inverse and Ill-Posed Problems. 1999; 7(3):255–271.

[14] Ikehata M. Reconstruction of the support function for inclusion from boundary measurements. Journal of Inverse and Ill-Posed Problems. 2000;8:367–378.

[15] Harrach B, Ullrich M. Monotonicity-based shape reconstruction in electrical impedance tomography. SIAM Journal on Mathematical Analysis. 2013;45(6):3382–3403.

[16] Garde H, Staboulis S. Convergence and regularization for monotonicity-based shape reconstruction in electrical impedance tomography. Submitted manuscript. 2016;Available from: http://arxiv.org/abs/1512.01718.

[17] Harrach B, Ullrich M. Resolution guarantees in electrical impedance tomography. IEEE Transactions on Medical Imaging. 2015;34(7):1513–1521.

[18] Tamburrino A. Monotonicity based imaging methods for elliptic and parabolic inverse problems. Journal of Inverse and Ill-posed Problems. 2006;14(6):633–642.

[19] Tamburrino A, Rubinacci G. A new non-iterative inversion method for electrical resistance tomography. Inverse Problems. 2002;18(6):1809.

[20] Garde H, Knudsen K. Depth dependent bounds on distinguishability of inclusions in electrical impedance tomography. Preprint. 2016;Available from: http://arxiv.org/abs/1602.03785.

[21] Pressman IS. Matrices with multiple symmetry properties: applications of centro-Hermitian and per-Hermitian matrices. Linear Algebra Appl. 1998;284(1-3):239–258; iLAS Symposium on Fast Algorithms for Control, Signals and Image Processing (Winnipeg, MB, 1997).

[22] Osborn J. Spectral approximation for compact operators. Mathematics of Computation. 1975 July;29(131):712–725.

[23] Kato T. Perturbation theory for linear operators. Vol. 132. Springer Verlag; 1995.

[24] Horsen CV. gmpy2 v2.0.7 C-coded Python extension. 2015; Available from: https://pypi.python.org/pypi/gmpy2.

PAPER D

Sparsity prior for electrical impedance tomography with partial data

Type	Journal paper
Authors	Henrik Garde and Kim Knudsen
Journal	Inverse Problems in Science and Engineering
Year	2016
Volume	24
Pages	524–541
Available from	http://dx.doi.org/10.1080/17415977.2015.1047365

Inverse Problems in Science and Engineering, 2016
Vol. 24, No. 3, 524–541, http://dx.doi.org/10.1080/17415977.2015.1047365

Taylor & Francis
Taylor & Francis Group

Sparsity prior for electrical impedance tomography with partial data

Henrik Garde* and Kim Knudsen

Department of Applied Mathematics and Computer Science, Technical University of Denmark, Lyngby, Denmark

(*Received 22 December 2014; final version received 28 April 2015*)

This paper focuses on prior information for improved sparsity reconstruction in electrical impedance tomography with partial data, i.e. Cauchy data measured on subsets of the boundary. Sparsity is enforced using an ℓ_1 norm of the basis coefficients as the penalty term in a Tikhonov functional, and prior information is incorporated by applying a spatially distributed regularization parameter. The resulting optimization problem allows great flexibility with respect to the choice of measurement subsets of the boundary and incorporation of prior knowledge. In fact, the measurement subsets can be chosen completely arbitrary. The problem is solved using a generalized conditional gradient method applying soft thresholding. Numerical examples with noisy simulated data show that the addition of prior information in the proposed algorithm gives vastly improved reconstructions, even for the partial data problem. Moreover, numerical examples show that a reliable reconstruction for the partial data problem can only be found close to the measurement subsets. The method is in addition compared to a total variation approach.

Keywords: electrical impedance tomography; inverse boundary value problem; ill-posed problem; partial data; sparsity

AMS Subject Classifications: 65N20; 65N21

1. Introduction

The inverse problem in electrical impedance tomography (EIT) consists of reconstructing an electrical conductivity distribution in the interior of an object from electrostatic boundary measurements on the surface of the object. EIT is an emerging technology with applications in medical imaging,[1] geophysics [2] and industrial tomography.[3] The underlying mathematical problem is known as the Calderón problem in recognition of Calderón's seminal paper.[4]

Consider a bounded domain $\Omega \subset \mathbb{R}^n$, $n \geq 2$, with smooth boundary $\partial\Omega$. In order to consider partial boundary measurements, we introduce the subsets $\Gamma^{\mathrm{N}}, \Gamma^{\mathrm{D}} \subseteq \partial\Omega$ for the Neumann and Dirichlet data, respectively. Let $\sigma \in L^\infty(\Omega)$ with $0 < c \leq \sigma$ a.e. denote the real-valued conductivity distribution in Ω. Applying a boundary current flux g (Neumann condition) through $\Gamma^{\mathrm{N}} \subseteq \partial\Omega$ gives rise to the interior electric potential u characterized as the solution to

*Corresponding author. Email: hgar@dtu.dk

$$\nabla \cdot (\sigma \nabla u) = 0 \text{ in } \Omega, \quad \sigma \frac{\partial u}{\partial \nu} = g \text{ on } \partial\Omega, \quad \int_{\Gamma^{\mathrm{D}}} u|_{\partial\Omega}\, \mathrm{d}s = 0, \tag{1.1}$$

where ν is an outward unit normal to $\partial\Omega$. The latter condition in (1.1) is a grounding of the total electric potential along the subset $\Gamma^{\mathrm{D}} \subseteq \partial\Omega$. To be precise, we define the spaces

$$L^2_\diamond(\partial\Omega) \equiv \left\{ g \in L^2(\partial\Omega) \mid \int_{\partial\Omega} g\, \mathrm{d}s = 0 \right\},$$
$$H^{-1/2}_\diamond(\partial\Omega) \equiv \{ g \in H^{-1/2}(\partial\Omega) \mid \langle g, 1 \rangle = 0 \},$$

consisting of boundary functions with mean zero, and the spaces

$$H^1_{\Gamma^{\mathrm{D}}}(\Omega) \equiv \{ u \in H^1(\Omega) \mid u|_{\partial\Omega} \in H^{1/2}_{\Gamma^{\mathrm{D}}}(\partial\Omega) \},$$
$$H^{1/2}_{\Gamma^{\mathrm{D}}}(\partial\Omega) \equiv \left\{ f \in H^{1/2}(\partial\Omega) \mid \int_{\Gamma^{\mathrm{D}}} f\, \mathrm{d}s = 0 \right\},$$

consisting of functions with mean zero on Γ^{D} designed to encompass the partial boundary data. Since σ is real valued, it is sufficient to consider the above spaces as real vector spaces, for the use of real-valued Cauchy data in the measurements. Using standard elliptic theory, it follows that (1.1) has a unique solution $u \in H^1_{\Gamma^{\mathrm{D}}}(\Omega)$ for any $g \in H^{-1/2}_\diamond(\partial\Omega)$. This defines the Neumann-to-Dirichlet map (ND-map) R_σ as an operator from $H^{-1/2}_\diamond(\partial\Omega)$ into $H^{1/2}_{\Gamma^{\mathrm{D}}}(\partial\Omega)$ by $g \mapsto u|_{\partial\Omega}$, and the partial ND-map as $g \mapsto (R_\sigma g)|_{\Gamma^{\mathrm{D}}}$.

The data for the classical Calderón problem is the full operator R_σ with $\Gamma^{\mathrm{D}} = \Gamma^{\mathrm{N}} = \partial\Omega$. The problem is well studied and there are numerous publications addressing different aspects of its solution; we mention only a few: the uniqueness and reconstruction problem was solved in [5–10] using the so-called complex geometrical optics (CGO) solutions; for a recent survey see [11]. Stability estimates of log type were obtained in [12,13] and shown to be optimal in [14]. Thus any computational algorithm must rely on regularization. Such computational regularization algorithms following the CGO approach were designed, implemented and analysed in [15–19].

Recently, the partial data Calderón problem have been studied intensively. In 3D uniqueness has been proved under certain conditions on Γ^{D} and Γ^{N},[20–24] and in 2D the general problem with localized data i.e. $\Gamma^{\mathrm{D}} = \Gamma^{\mathrm{N}} = \Gamma$ for some, possibly small, subset $\Gamma \subseteq \partial\Omega$ has been shown to possess uniqueness.[25] Also stability estimates of log–log type have been obtained for the partial data problem [26]; this suggests that the partial data problem is even more ill-posed and hence requires more regularization than the full data problem. Recently, a computational algorithm for the partial data problem in 2D was suggested and investigated in [27].

The boundary condition in (1.1) is the continuum model which is related to the above-mentioned uniqueness results, and actual electrode measurements can be seen as an approximation to this model, see for instance [28]. Another more realistic model is the Complete Electrode Model (CEM) introduced in [29]. The approach to the reconstruction problem in EIT considered here can be formulated with CEM as well, see [30,31].

A general approach to linear inverse problems with sparsity regularization was given in [32], and in [33,34] the method was adapted to non-linear problems using a so-called generalized conditional gradient method. In [30,35,36], the method was applied to the reconstruction problem in EIT with full boundary data. A study was made in [31] with 3D sparse reconstruction with current injection and voltage measurements on disjoint sets of

electrodes on a planar EIT device, where it was possible to reconstruct a 2D position of an inclusion close to the measured boundary. In this paper, we seek a general approach with regards to the measurement boundaries Γ^{D} and Γ^{N}, and the use of prior information to improve the reconstruction further away from the measured boundary. In the numerical examples in Section 4 we consider the case of local data, with Cauchy data on the same part of the boundary. For other approaches to EIT using optimization methods, we refer to [37].

In this paper, we will focus on the partial data problem for which we develop a reconstruction algorithm based on a least squares formulation with sparsity regularization. The results are twofold: first we extend the full data algorithm of [36] to the case of partial data, second we show how prior information about the spatial location of the perturbation in the conductivity can be used in the design of a spatially varying regularization parameter. We will restrict the treatment to 2D, however everything extends to 3D with some minor assumptions on the regularity of the Neumann data.[38]

The data considered here consist of a finite number of Cauchy data, corresponding to the number of applied current patterns, taken on the subsets Γ^{D} and Γ^{N}, i.e.

$$\{(f_k, g_k) \mid g_k \in H_\diamond^{-1/2}(\partial\Omega),\ \operatorname{supp}(g_k) \subseteq \Gamma^{\mathrm{N}},\ f_k = R_\sigma g_k|_{\Gamma^{\mathrm{D}}}\}_{k=1}^K,\ K \in \mathbb{N}. \tag{1.2}$$

We assume that the true conductivity is given as $\sigma = \sigma_0 + \delta\sigma$, where σ_0 is a known background conductivity. Define the closed and convex subset

$$\mathcal{A}_0 \equiv \{\delta\gamma \in H_0^1(\Omega) \mid c \le \sigma_0 + \delta\gamma \le c^{-1} \text{ a.e. in } \Omega\} \tag{1.3}$$

for some $c \in (0, 1)$, and $\sigma_0 \in H^1(\Omega)$ where $c \le \sigma_0 \le c^{-1}$. Similarly define

$$\mathcal{A} \equiv \{\delta\gamma + \sigma_0 \mid \delta\gamma \in \mathcal{A}_0\} = \{\gamma \in H^1(\Omega) \mid c \le \gamma \le c^{-1} \text{ a.e. in } \Omega,\ \gamma|_{\partial\Omega} = \sigma_0|_{\partial\Omega}\}.$$

The inverse problem is then to approximate $\delta\sigma \in \mathcal{A}_0$ given the data (1.2).

Let $\{\psi_j\}_{j=1}^\infty$ denote a chosen orthonormal basis for $H_0^1(\Omega)$. For sparsity regularization, we approximate $\delta\sigma$ by $\operatorname{argmin}_{\delta\gamma\in\mathcal{A}_0} \Psi(\delta\gamma)$ using the following Tikhonov functional [36]

$$\Psi(\delta\gamma) \equiv \sum_{k=1}^K J_k(\delta\gamma) + P(\delta\gamma),\quad \delta\gamma \in \mathcal{A}_0, \tag{1.4}$$

with

$$J_k(\delta\gamma) \equiv \frac{1}{2}\|R_{\sigma_0+\delta\gamma} g_k - f_k\|^2_{L^2(\Gamma^{\mathrm{D}})},\qquad P(\delta\gamma) \equiv \sum_{j=1}^\infty \alpha_j |c_j|,$$

for $c_j \equiv \langle\delta\gamma, \psi_j\rangle_{H^1(\Omega)}$. The regularization parameter $\alpha_j > 0$ for the sparsity-promoting ℓ_1 penalty term P is distributed such that each basis coefficient can be regularized differently; we will return to this in Section 3. It should be noted how easy and natural the use of partial data is introduced in this way, simply by only minimizing the discrepancy on Γ^{D} on which the Dirichlet data are known and ignoring the rest of the boundary.

This paper is organized as follows: in Section 2 we derive the Fréchet derivative of J_k and reformulate the optimization problem using the generalized conditional gradient method as a sequence of linearized optimization problems. In Section 3, we explain the idea of the spatially dependent regularization parameter designed for the use of prior information. Then, in Section 4 we show the feasibility of the algorithm by several numerical examples, and finally we conclude in Section 5.

2. Sparse reconstruction

In this section, the sparse reconstruction of $\delta\sigma$ based on the optimization problem (1.4) is investigated for a bounded domain $\Omega \subset \mathbb{R}^2$ with smooth boundary $\partial\Omega$. The penalty term emphasizes that $\delta\sigma$ should only be expanded by few basis functions in a given orthonormal basis, and the level of sparsity is controlled by the regularization parameter. Using a distributed regularization parameter, it is possible to further apply prior information about which basis functions that should be included in the expansion of $\delta\sigma$. The partial data problem comes into play in the discrepancy term, in which we only fit the data on part of the boundary. Ultimately, this leads to the algorithm given in Algorithm 1 at the end of this section.

Denote by $F_g(\sigma)$ the unique solution to (1.1) and let $\mathcal{F}_g(\sigma)$ be its trace (note that $R_\sigma g = \mathcal{F}_g(\sigma)$). Let $\gamma \in \mathcal{A}$, $g \in L^p(\partial\Omega) \cap H_\diamond^{-1/2}(\partial\Omega)$ for $p > 1$, then following the proofs of Theorem 2.2 and Corollary 2.1 in [35] whilst applying the partial boundary Γ^{D} we have

$$\lim_{\substack{\|\eta\|_{H^1(\Omega)}\to 0 \\ \gamma+\eta\in\mathcal{A}}} \frac{\|\mathcal{F}_g(\gamma+\eta) - \mathcal{F}_g(\gamma) - (\mathcal{F}_g)'_\gamma \eta\|_{H^{1/2}_{\Gamma^{\mathrm{D}}}(\partial\Omega)}}{\|\eta\|_{H^1(\Omega)}} = 0. \tag{2.1}$$

Here $(\mathcal{F}_g)'_\gamma$ is the linear map that maps η to $w|_{\partial\Omega}$, where w is the unique solution to

$$-\nabla\cdot(\gamma\nabla w) = \nabla\cdot(\eta\nabla F_g(\gamma)) \text{ in } \Omega, \quad \sigma\frac{\partial w}{\partial \nu} = 0 \text{ on } \partial\Omega, \quad \int_{\Gamma^{\mathrm{D}}} w|_{\partial\Omega}\,\mathrm{d}s = 0. \tag{2.2}$$

It is noted that $(\mathcal{F}_g)'_\gamma$ resembles a Fréchet derivative of $\mathcal{F}_g$ evaluated at γ due to (2.1), however $\mathcal{A}$ is not a linear vector space, thus the requirement $\gamma, \gamma+\eta \in \mathcal{A}$.

The first step in minimizing Ψ using a gradient descent-type iterative algorithm is to determine a derivative to the discrepancy terms J_k.

LEMMA 2.1 *Let $\gamma = \sigma_0 + \delta\gamma$ for $\delta\gamma \in \mathcal{A}_0$, and $\chi_{\Gamma^{\mathrm{D}}}$ be a characteristic function on Γ^{D}. Then*

$$E_k \equiv -\nabla F_{g_k}(\gamma)\cdot\nabla F_{\chi_{\Gamma^{\mathrm{D}}}(R_\gamma g_k - f_k)}(\gamma) \in L^r(\Omega) \subset H^{-1}(\Omega) \tag{2.3}$$

for some $r > 1$, and the Fréchet derivative $(J_k)'_{\delta\gamma}$ of J_k on $H_0^1(\Omega)$ evaluated at $\delta\gamma$ is given by

$$(J_k)'_{\delta\gamma}\eta = \int_\Omega E_k\eta\,\mathrm{d}x, \quad \delta\gamma+\eta \in \mathcal{A}_0. \tag{2.4}$$

Proof For the proof, the index k is suppressed. First it is proved that $E \in L^r(\Omega)$ for some $r > 1$, which is shown by estimates on $F_g(\gamma)$ and $F_h(\gamma)$ where $h \equiv \chi_{\Gamma^{\mathrm{D}}}(R_\gamma g - f)$. Note that $R_\gamma g \in H^{1/2}_{\Gamma^{\mathrm{D}}}(\partial\Omega)$ and $f \in L^2_\diamond(\Gamma^{\mathrm{D}})$, i.e. $h \in L^2_\diamond(\partial\Omega) \subset L^2(\partial\Omega) \cap H_\diamond^{-1/2}(\partial\Omega)$. Now using [35, Theorem 3.1], there exists $Q > 2$ such that

$$\|F_h(\gamma)\|_{W^{1,q}(\Omega)} \le C\|h\|_{L^2(\partial\Omega)}, \tag{2.5}$$

where $q \in (2, Q) \cap [2, 4]$. Since $F_g(\gamma) \in H^1_{\Gamma^{\mathrm{D}}}(\Omega)$ then $|\nabla F_g(\gamma)| \in L^2(\Omega)$. It has already been established in (2.5) that $F_h(\gamma) \in W^{1,q}(\Omega)$ for $q \in (2, \min\{Q, 4\})$, so $|\nabla F_h(\gamma)| \in L^q(\Omega)$. By Hölder's generalized inequality

$$E = -\nabla F_g(\gamma)\cdot\nabla F_h(\gamma) \in L^r(\Omega), \quad \tfrac{1}{r} = \tfrac{1}{2} + \tfrac{1}{q},$$

and as $q > 2$ then $r > 1$. Let r' be the conjugate exponent to r, then $r' \in [1, \infty)$, i.e. the Sobolev imbedding theorem [39] implies that $H^1(\Omega) \hookrightarrow L^{r'}(\Omega)$ as $\Omega \subset \mathbb{R}^2$. Thus $E \in (L^{r'}(\Omega))' \subset (H^1(\Omega))' \subset (H_0^1(\Omega))' = H^{-1}(\Omega)$.

Now it will be shown that $J'_{\delta\gamma}$ can be identified with E. $J'_{\delta\gamma}\eta$ is by the chain rule (utilizing that $R_\gamma g = \mathcal{F}_g(\gamma)$) given as

$$J'_{\delta\gamma}\eta = \int_{\partial\Omega} \chi_{\Gamma^D}(R_\gamma g - f)(\mathcal{F}_g)'_\gamma \eta \, \mathrm{d}s, \tag{2.6}$$

where χ_{Γ^D} is enforcing that the integral is over Γ^D. The weak formulations of (1.1), with Neumann data $\chi_{\Gamma^D}(R_\gamma g - f)$, and (2.2) are

$$\int_\Omega \gamma \nabla F_{\chi_{\Gamma^D}(R_\gamma g - f)}(\gamma) \cdot \nabla v \, \mathrm{d}x = \int_{\partial\Omega} \chi_{\Gamma^D}(R_\gamma g - f) v|_{\partial\Omega} \, \mathrm{d}s, \quad \forall v \in H^1(\Omega), \tag{2.7}$$

$$\int_\Omega \gamma \nabla w \cdot \nabla v \, \mathrm{d}x = -\int_\Omega \eta \nabla F_g(\gamma) \cdot \nabla v \, \mathrm{d}x, \quad \forall v \in H^1(\Omega). \tag{2.8}$$

Now by letting $v \equiv w$ in (2.7) and $v \equiv F_{\chi_{\Gamma^D}(R_\gamma g - f)}(\gamma)$ in (2.8), we obtain using the definition $w|_{\partial\Omega} = (\mathcal{F}_g)'_\gamma \eta$ that

$$\begin{aligned} J'_{\delta\gamma}\eta &= \int_{\partial\Omega} \chi_{\Gamma^D}(R_\gamma g - f)(\mathcal{F}_g)'_\gamma \eta \, \mathrm{d}s = \int_\Omega \gamma \nabla F_{\chi_{\Gamma^D}(R_\gamma g - f)}(\gamma) \cdot \nabla w \, \mathrm{d}x \\ &= -\int_\Omega \eta \nabla F_g(\gamma) \cdot \nabla F_{\chi_{\Gamma^D}(R_\gamma g - f)}(\gamma) \, \mathrm{d}x = \int_\Omega E\eta \, \mathrm{d}x. \end{aligned}$$

□

Remark 2.2 It should be noted that $(J_k)'_{\delta\gamma}$ is related to the Fréchet derivative R'_γ of $\gamma \mapsto R_\gamma$ evaluated at γ, by $(J_k)'_{\delta\gamma}\eta = \int_{\Gamma^D}(R_\gamma g_k - f_k) R'_\gamma[\eta] g_k \, \mathrm{d}s$.

Define

$$J'_{\delta\gamma} \equiv \sum_{k=1}^{K} (J_k)'_{\delta\gamma} = -\sum_{k=1}^{K} \nabla F_{g_k}(\gamma) \cdot \nabla F_{\chi_{\Gamma^D}(R_\gamma g_k - f_k)}(\gamma).$$

For a gradient-type descent method, we seek to find a direction η for which the discrepancy decreases. As $J'_{\delta\gamma} \in H^{-1}(\Omega)$ it is known from Riesz' representation theorem that there exists a unique function in $H_0^1(\Omega)$, denoted by $G(\delta\gamma)$, such that

$$J'_{\delta\gamma}\eta = \langle G(\delta\gamma), \eta \rangle_{H^1(\Omega)}, \quad \eta \in H_0^1(\Omega). \tag{2.9}$$

Now $\eta \equiv -G(\delta\gamma)$ points in the direction of steepest descend among the viable directions. Furthermore, since $G(\delta\gamma)|_{\partial\Omega} = 0$ the boundary condition $\delta\sigma|_{\partial\Omega} = 0$ will automatically be fulfilled for the approximation. In [40], $G(\delta\gamma)$ is called a Sobolev gradient, and it is the unique solution to

$$(-\Delta + 1)v = J'_{\delta\gamma} \text{ in } \Omega, \quad v = 0 \text{ on } \partial\Omega,$$

for which (2.9) is the weak formulation.

In each iteration step, we need to determine a step size s_i for an algorithm resembling a steepest descent $\delta\gamma_{i+1} = \delta\gamma_i - s_i G(\delta\gamma_i)$. Here a Barzilai–Borwein step size rule [36,41,42]

will be applied, for which we determine s_i such that $\frac{1}{s_i}(\delta\gamma_i - \delta\gamma_{i-1}) = \frac{1}{s_i}(\gamma_i - \gamma_{i-1}) \simeq G(\delta\gamma_i) - G(\delta\gamma_{i-1})$ in the least squares sense

$$s_i \equiv \underset{s}{\operatorname{argmin}} \|s^{-1}(\delta\gamma_i - \delta\gamma_{i-1}) - (G(\delta\gamma_i) - G(\delta\gamma_{i-1}))\|^2_{H^1(\Omega)}. \tag{2.10}$$

Assuming that $\langle \delta\gamma_i - \delta\gamma_{i-1}, G(\delta\gamma_i) - G(\delta\gamma_{i-1})\rangle_{H^1(\Omega)} \neq 0$ yields

$$s_i = \frac{\|\delta\gamma_i - \delta\gamma_{i-1}\|^2_{H^1(\Omega)}}{\langle \delta\gamma_i - \delta\gamma_{i-1}, G(\delta\gamma_i) - G(\delta\gamma_{i-1})\rangle_{H^1(\Omega)}}. \tag{2.11}$$

A maximum step size $s_{\max}$ is enforced to avoid the situations where $\langle \delta\gamma_i - \delta\gamma_{i-1}, G(\delta\gamma_i) - G(\delta\gamma_{i-1})\rangle_{H^1(\Omega)} \simeq 0$.

With inspiration from [42], s_i will be initialized by (2.11), after which it is thresholded to lie in $[s_{\min}, s_{\max}]$, for positive constants $s_{\min}$ and $s_{\max}$. It is noted in [42] that Barzilai–Borwein step rules lead to faster convergence if we do not restrict Ψ to decrease in every iteration. Allowing an occasional increase in Ψ can be used to avoid places where the method has to take many small steps to ensure the decrease of Ψ. Therefore, one makes sure that the following so called weak monotonicity is satisfied, which compares $\Psi(\delta\gamma_{i+1})$ with the most recent M steps. Let $\tau \in (0, 1)$ and $M \in \mathbb{N}$, then s_i is said to satisfy the weak monotonicity with respect to M and τ if the following is satisfied [42]

$$\Psi(\delta\gamma_{i+1}) \leq \max_{i-M+1\leq j\leq i} \Psi(\delta\gamma_j) - \frac{\tau}{2s_i}\|\delta\gamma_{i+1} - \delta\gamma_i\|^2_{H^1(\Omega)}. \tag{2.12}$$

If (2.12) is not satisfied, the step size s_i is reduced until this is the case. To solve the non-linear minimization problem for (1.4), we iteratively solve the following linearized problem

$$\begin{aligned} \zeta_{i+1} &\equiv \underset{\delta\gamma\in H^1_0(\Omega)}{\operatorname{argmin}} \left[\frac{1}{2}\|\delta\gamma - (\delta\gamma_i - s_i G(\delta\gamma_i))\|^2_{H^1(\Omega)} + s_i \sum_{j=1}^{\infty} \alpha_j |c_j|\right], \\ \delta\gamma_{i+1} &\equiv \mathcal{P}_{\mathcal{A}_0}(\zeta_{i+1}). \end{aligned} \tag{2.13}$$

Here $\{\psi_j\}_{j=1}^{\infty}$ is an orthonormal basis for $H^1_0(\Omega)$ in the H^1-metric, and $\mathcal{P}_{\mathcal{A}_0}$ is the projection of $H^1_0(\Omega)$ onto $\mathcal{A}_0$ to ensure that (1.1) is solvable (note that $H^1_0(\Omega)$ does not imbed into $L^\infty(\Omega)$, i.e. ζ_{i+1} may be unbounded). By use of the map $\mathcal{S}_\beta : \mathbb{R} \to \mathbb{R}$ defined below, known as the soft shrinkage/thresholding map with threshold $\beta > 0$,

$$\mathcal{S}_\beta(x) \equiv \operatorname{sgn}(x)\max\{|x| - \beta, 0\}, \quad x \in \mathbb{R}, \tag{2.14}$$

the solution to (2.13) is easy to find directly (see also [32, Section 1.5]):

$$\zeta_{i+1} = \sum_{j=1}^{\infty} \mathcal{S}_{s_i\alpha_j}(d_j)\psi_j, \tag{2.15}$$

where $d_j \equiv \langle \delta\gamma_i - s_i G(\delta\gamma_i), \psi_j\rangle_{H^1(\Omega)}$ are the basis coefficients for $\delta\gamma_i - s_i G(\delta\gamma_i)$.

Remark 2.3 The soft threshold in (2.15) assumes that the coefficients $\{d_j\}_{j=1}^{\infty}$ are real valued, as in this case with real-valued conductivity σ and Cauchy-data. For

complex-valued admittivity σ, appropriate use of complex conjugation is required for the derivative in Lemma 2.1, and a minimizer for (2.13) can be found in [42].

The projection $\mathcal{P}_{\mathcal{A}_0} : H_0^1(\Omega) \to \mathcal{A}_0$ is defined as

$$\mathcal{P}_{\mathcal{A}_0}(v) \equiv T_c(\sigma_0 + v) - \sigma_0, \quad v \in H_0^1(\Omega), \tag{2.16}$$

where T_c is the following truncation that depends on the constant $c \in (0, 1)$ in (1.3)

$$T_c(v) \equiv \begin{cases} c & \text{where } v < c \text{ a.e.,} \\ c^{-1} & \text{where } v > c^{-1} \text{ a.e.,} \\ v & \text{else.} \end{cases}$$

Since $\sigma_0 \in H^1(\Omega)$ and $c \leq \sigma_0 \leq c^{-1}$, it follows directly from [43, Lemma 1.2] that T_c and $\mathcal{P}_{\mathcal{A}_0}$ are well defined, and it is easy to see that $\mathcal{P}_{\mathcal{A}_0}$ is a projection.

Remark 2.4 In the numerical examples in Section 4, the value of c is chosen small enough that the truncation in $\mathcal{P}_{\mathcal{A}_0}$ does not occur during the iterations. If tight bounds on σ are known a priori, the truncation may lead to improved rate of convergence and gives reconstructions in the correct dynamic range.

It should also be noted that $0 \in \mathcal{A}_0$ since $c \leq \sigma_0 \leq c^{-1}$, thus we may choose $\delta\gamma_0 \equiv 0$ as the initial guess in the algorithm. The algorithm is summarized in Algorithm 1. In this paper, the stopping criterion is when the step size s_i gets below a threshold s_{stop}.

Remark 2.5 Note that $\sum_j \langle \delta\gamma_i - s_i G(\delta\gamma_i), \psi_j \rangle_{H^1(\Omega)} \psi_j$ corresponds to only having the discrepancy term in (2.13), while the penalty term $s_i \sum_{j=1}^{\infty} \alpha_j |\langle \delta\gamma, \psi_j \rangle_{H^1(\Omega)}|$ leads to the soft thresholding in (2.15).

Remark 2.6 The functional Ψ in (1.4) is non-convex. Thus, the best we can hope is to find a local minimum. The quality of the reconstruction depends on the initial guess, and as we expect the reconstruction to be sparse, then $\delta\gamma_0 \equiv 0$ is a reasonable initial guess.

Algorithm 1 Sparse reconstruction for partial data EIT.

Set $\delta\gamma_0 := 0$.
while stopping criteria not reached **do**
  Set $\gamma_i := \sigma_0 + \delta\gamma_i$.
  Compute $\Psi(\delta\gamma_i)$ by (1.4).
  Compute $J'_{\delta\gamma_i} := -\sum_{k=1}^{K} \nabla F_{g_k}(\gamma_i) \cdot \nabla F_{\chi_{\Gamma_D}(R_{\gamma_i} g_k - f_k)}(\gamma_i)$.
  Compute $G(\delta\gamma_i) \in H_0^1(\Omega)$ such that $J'_{\delta\gamma_i} \eta = \langle G(\delta\gamma_i), \eta \rangle_{H^1(\Omega)}$.
  Compute step length s_i by (2.11), and decrease it till (2.12) is satisfied.
  Compute the basis coefficients $\{d_j\}_{j=1}^{\infty}$ for $\delta\gamma_i - s_i G(\delta\gamma_i)$.
  Update $\delta\gamma_{i+1} := \mathcal{P}_{\mathcal{A}_0}\left(\sum_{j=1}^{\infty} \mathcal{S}_{s_i\alpha_j}(d_j)\psi_j\right)$ using (2.14) and (2.16).
end while
Return final iterate of $\delta\gamma$.

Remark 2.7 The main computational cost lies in computing $J'_{\delta\gamma_i}$, which involves solving $2K$ well-posed PDE's (note that $F_{g_k}(\gamma_i)$ can be reused from the evaluation of Ψ), where K is the number of current patterns used in the measurements. It should be noted that each of the $2K$ problems consists of solving the same problem, but with different boundary conditions, which leads to only having to assemble and factorize the finite element method (FEM) matrix once per iteration.

3. Prior information

Prior information is typically introduced in the penalty term P for Tikhonov-like functionals, and here the regularization parameter determines how much this prior information is enforced. In the case of sparsity regularization, this implies knowledge of how sparse we expect the solution is in general. Instead of applying the same prior information for each basis function, a distributed parameter is applied. Let

$$\alpha_j \equiv \alpha\mu_j,$$

where α is the usual regularization parameter, corresponding to the case where no prior information is considered about specific basis functions. The $\mu_j \in (0, 1]$ will be used to weight the penalty depending on whether a specific basis function should be included in the expansion of $\delta\sigma$. The μ_j are chosen as

$$\mu_j = \begin{cases} 1, & \text{no prior on } c_j, \\ \sim 0, & \text{prior that } c_j \neq 0, \end{cases}$$

i.e. if we know that a coefficient in the expansion of $\delta\sigma$ should be non-zero, we can choose to penalize that coefficient less. Using a basis with localized support, the sparsity assumption translates to an assumption on the support of the inclusion.

3.1. *Applying the FEM basis*

In order to improve the sparsity solution for finding small inclusions, it seems appropriate to include prior information about the support of the inclusions. There are different methods available for obtaining such information assuming piecewise constant conductivity [44,45] or real-analytic conductivity.[46] An example of the reconstruction of supp $\delta\sigma$ is shown in Figure 1, where it is observed that numerically it is possible to reconstruct a reasonable convex approximation to the support. Thus, it is possible to acquire estimates of supp $\delta\sigma$ *for free*, in the sense that it is gained directly from the data without further assumptions on the location.

Another approach is to consider other reconstruction methods such as total variation (TV) regularization that tends to give good approximations to the support, but has issues with reconstructing the contrast if the amplitude of $\delta\sigma$ is large as seen in Section 4.3. The idea is to be able to apply such information in the sparsity algorithm in order to get good contrast in the reconstruction while maintaining the correct support, even for the partial data problem.

Suppose that as a basis we consider a FEM basis $\{\psi_j\}_{j=1}^N$ for the subspace $V_h \subseteq H_0^1(\Omega)$ of piecewise affine elements. This basis comprises basis functions that are piecewise affine with degrees of freedom at the mesh nodes, i.e. $\psi_j(x_k) = \delta_{j,k}$ at mesh node x_k

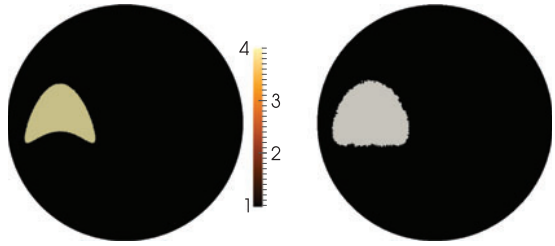

(a) (b)

Figure 1. (a) Phantom with kite-shaped piecewise constant inclusion $\delta\sigma$. (b) Reconstruction of supp $\delta\sigma$ using monotonicity relations from the approach in [45] by use of simulated noiseless data.

in the applied mesh. Let $\delta\sigma \in V_h$, then $\delta\sigma(x) = \sum_j \delta\sigma(x_j)\psi_j(x)$, i.e. for each node there is a basis function for which the coefficient contains local information about the expanded function; this is convenient when applying prior information about the support of an inclusion. Note that the FEM basis functions are not mutually orthogonal, since basis functions corresponding to neighbouring nodes are non-negative and have overlapping support. However, for any non-neighbouring pair of nodes the corresponding basis functions are orthogonal.

When applying the FEM basis for mesh nodes $\{x_j\}_{j=1}^N$, the corresponding functional is

$$\Psi(\delta\gamma) = \frac{1}{2}\sum_{k=1}^{K} \| R_{\sigma_0+\delta\gamma} g_k - f_k \|^2_{L^2(\Gamma^D)} + \sum_{j=1}^{N} \alpha_j |\delta\gamma(x_j)|.$$

It is evident that the penalty corresponds to determining inclusions with small support, and prior information on the sparsity corresponds to prior information on the support of $\delta\sigma$. We cannot directly utilize (2.15) due to the FEM basis not being an orthonormal basis for $H_0^1(\Omega)$, and instead we suggest the following iteration step:

$$\begin{aligned} \zeta_{i+1}(x_j) &= \mathcal{S}_{s_i \alpha_j / \|\psi_j\|_{L^1(\Omega)}}(\delta\gamma_i(x_j) - s_i G(\delta\gamma_i)(x_j)), \quad j = 1, 2, \ldots, N, \\ \delta\gamma_{i+1} &= \mathcal{P}_{\mathcal{A}_0}(\zeta_{i+1}). \end{aligned} \tag{3.1}$$

Note that the regularization parameter will depend quite heavily on the discretization of the mesh, i.e. for the same domain a good regularization parameter α will be much larger on a coarse mesh than on a fine mesh. This is quite inconvenient, and instead we can weight the regularization parameter according to the mesh cells, by having $\alpha_j \equiv \alpha\beta_j\mu_j$. This leads to a discretization of a weighted L^1-norm penalty term:

$$\alpha \int_\Omega f_\mu |\delta\gamma| \, \mathrm{d}x \simeq \alpha \sum_{j=1}^{N} \beta_j \mu_j |\delta\gamma(x_j)|,$$

where $f_\mu : \Omega \to (0, 1]$ is continuous and $f_\mu(x_j) = \mu_j$. For a triangulated mesh, the weights β_j consists of the node area computed in 2D as 1/3 of the area of supp ψ_j. This corresponds to splitting each cell's area evenly amongst the nodes, and it will not lead to

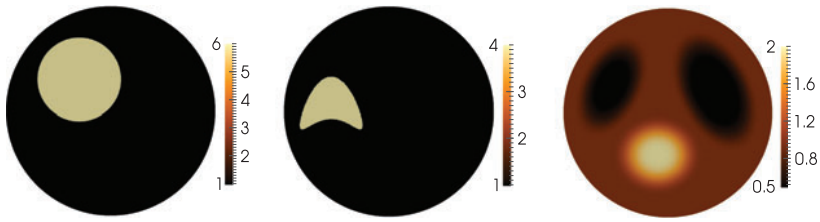

Figure 2. Numerical phantoms. (a) Circular piecewise constant inclusion. (b) Kite-shaped piecewise constant inclusion. (c) Multiple C^2 inclusions.

instability on a regular mesh. This will make the choice of α almost independent of the mesh, and is used in the numerical examples in the following section.

Remark 3.1 The corresponding algorithm with the FEM basis is the same as Algorithm 1, except that the update is applied via (3.1) instead of (2.13).

4. Numerical examples

In this section we illustrate, through several examples, the numerical algorithm implemented using the finite element library FEniCS.[47] We consider the full data case $\Gamma^{\mathrm{D}} = \Gamma^{\mathrm{N}} = \partial\Omega$ first without prior information and then with prior information, and afterwards we do the same for the partial data case. Finally, a brief comparison is made with another sparsity promoting method based on TV.

For the following examples Ω is the unit disk in $\mathbb{R}^2$ (however, the algorithm can be applied to any bounded domain with smooth boundary). The regularization parameter α is chosen manually by trial and error. The other parameters are $\sigma_0 \equiv 1$, $M = 5$, $\tau = 10^{-5}$, $s_{\min} = 1$, $s_{\max} = 1000$, and the stopping criteria are when the step size is below $s_{\text{stop}} = 10^{-3}$. We take $K = 10$ with the applied Neumann data of the form $g_n^{\mathrm{c}}(\theta) \equiv \cos(n\theta)$ and $g_n^{\mathrm{s}}(\theta) \equiv \sin(n\theta)$ for $n = 1, \ldots, 5$ and θ being the angular variable. Such trigonometric current patterns are realistic approximations to electrode measurements, see for instance [28]. For the partial data, an interval $\Gamma = \Gamma^{\mathrm{N}} = \Gamma^{\mathrm{D}} = \{\theta \in (\theta_1, \theta_2)\}$ is considered, and g_n^{c} and g_n^{s} are scaled and translated such that they have n periods in the interval.

When applying prior information, the coefficients μ_j are chosen as 10^{-2} where the support of $\delta\sigma$ is assumed, and 1 elsewhere. It should be noted that in order to get fast transitions for sharp edges when prior information is applied, a local mesh refinement is used during the iterations to refine the mesh where $|\nabla\delta\gamma_i|$ is large.

For the simulated Dirichlet data, the forward problem is computed on a very fine mesh, and afterwards interpolated onto a different much coarser mesh (with roughly 2800 triangle elements) in order to avoid inverse crimes. White Gaussian noise has been added to the Dirichlet data $\{f_k\}_{k=1}^K$ on the discrete nodes on the boundary of the mesh. The standard deviation of the noise is chosen as $\epsilon \max_k \max_{x_j \in \Gamma^{\mathrm{D}}} |f_k(x_j)|$ as in [36], where the noise level is fixed as $\epsilon = 10^{-2}$ (corresponding to 1% noise) unless otherwise stated.

Figure 2 shows the numerical phantoms: where one is a simple circular inclusion, another is the non-convex kite-shaped phantom. Finally, we also shortly investigate the case of multiple smoother inclusions.

4.1. *Full boundary data*

For $\Gamma^D = \Gamma^N = \partial\Omega$, it is possible to get quite good reconstructions of both shape and contrast for the convex inclusions as seen in Figure 3, and for the case with multiple inclusions there is a reasonable separation of the inclusions.

For the kite-shaped phantom, we only get what seems like a convex approximation of the shape. It is seen in [36] that the algorithm is able to reconstruct some types of non-convex inclusions such as the hole in a ring-shaped phantom, however those inclusions are much larger which makes it easier to distinguish from similar convex inclusions.

We note that the method is very noise robust. Figure 4 demonstrates that even unreasonably large amounts of noise lead to only small deformations in the shape of the reconstructed inclusion.

In order to investigate the use of prior information, we consider the phantom in Figure 2(a), and let $B(r)$ denote a ball centred at the correct inclusion and with radius r. Now we can investigate reconstructions with prior information assuming that the support of the inclusion is $\overline{B((1+\delta r)r^*)}$ for r^* being the correct radius of the inclusion. Figure 5 shows that underestimating the support of the inclusion $\delta r < 0$ is heavily enforced, and the contrast is vastly overestimated in the reconstruction as shown in Figure 6 (note that this cannot be seen in Figure 5 as the color scale for the phantom is applied).

Interestingly, when overestimating the support, the contrast and support of the reconstructed inclusion does not suffer particularly. Intuitively, this corresponds to increasing δr such that the assumed support of $\delta\sigma$ contains the entire domain Ω, which corresponds to the case with no prior information. Denote by $\sigma_B \equiv |B(r^*)|^{-1} \int_{B(r^*)} \sigma \, \mathrm{d}x$ the average of the reconstruction σ on $\overline{B(r^*)}$, the correct support of the inclusion, and by σ_{B^C} the average of σ on the complement to $B(r^*)$. Denote by $\sigma_{\max} \equiv \max_j |\sigma(x_j)|$ the maximum of σ on the mesh nodes. Then Figure 6 gives a good indication of the aforementioned intuition, where around $\delta r = 0$ both σ_B and $\sigma_{\max}$ level off around the correct contrast of the inclusion (the red line) and stays there for $\delta r > 0$. It should be noted that even a 25% overestimation of the support leads to a better contrast in the reconstruction than if no prior information was applied, as seen in Figure 5.

Having an overestimation of the support for $\delta\sigma$ also seems to be a reasonable assumption. Definitely there is the case of no prior information which means that $\operatorname{supp}\delta\sigma$ is assumed to be Ω. If the estimation comes from another method such as TV regularization, then the support is typically slightly overestimated while the contrast suffers.[48] Thus, we

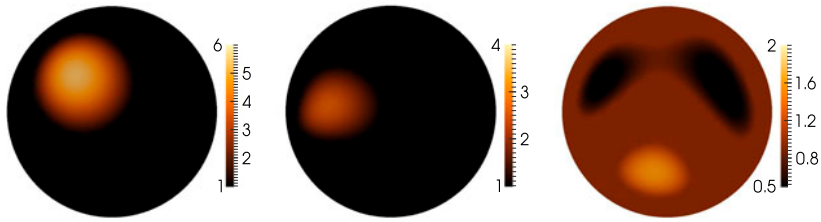

(a) $\alpha = 10^{-3}$ **(b)** $\alpha = 5 \cdot 10^{-4}$ **(c)** $\alpha = 6.5 \cdot 10^{-4}$

Figure 3. Full data sparse reconstruction of the phantoms in Figure 2 without prior information on the support of inclusions.

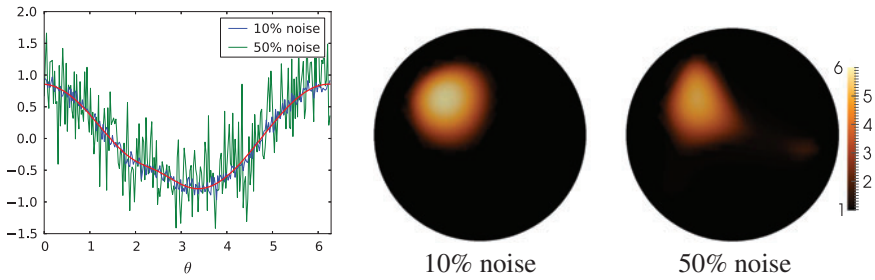

Figure 4. Left: Dirichlet data corresponding to $g = \cos(\theta)$ for the phantom in Figure 2(a), with 10% and 50% noise level. Middle: full data reconstruction for 10% noise level. Right: full data reconstruction for 50% noise level.

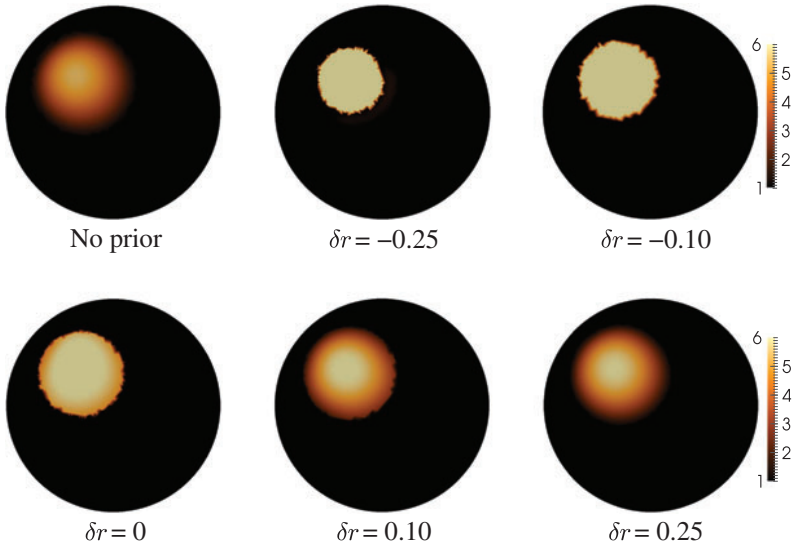

Figure 5. Full data sparse reconstruction of the phantom in Figure 2(a) varying the assumed support given by a dilation δr. The colour bar is truncated at [1, 6]. For $\delta r < 0$, the contrast in the reconstruction is higher than in the phantom.

can use the overestimated support to get a good localization and contrast reconstruction simultaneously.

Figure 7 shows how the reconstruction of the kite-shaped phantom can be vastly improved. Note that not only is supp $\delta\sigma$ better approximated, but the contrast is also highly improved. It is not surprising that we can achieve an almost perfect reconstruction if supp $\delta\sigma$ is exactly known, however it is a good benchmark to compare the cases for the overestimated support as it shows how well the method can possibly do.

4.2. *Partial boundary data*

For the partial data problem we choose $\Gamma = \Gamma^{\mathrm{D}} = \Gamma^{\mathrm{N}} = \{\theta \in (\theta_1, \theta_2)\}$ for $0 \leq \theta_1 < \theta_2 \leq 2\pi$.

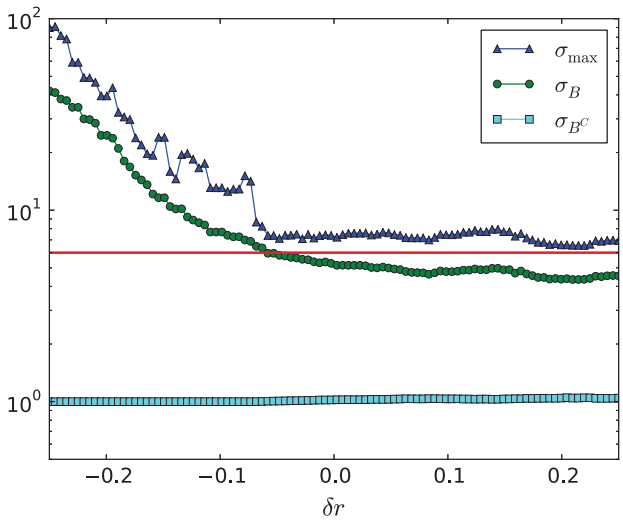

Figure 6. Behaviour of full data sparsity reconstruction based on the phantom in Figure 2(a) by varying δr characterizing the assumed support. The correct support of the inclusion is a ball $\overline{B(r^*)}$ while the assumed support is $\overline{B((1+\delta r)r^*)}$. σ_B is the average of reconstruction σ over $B(r^*)$ and σ_{B^C} is the average on the complement of $B(r^*)$. $\sigma_{\max}$ is the maximum of σ on the mesh nodes.

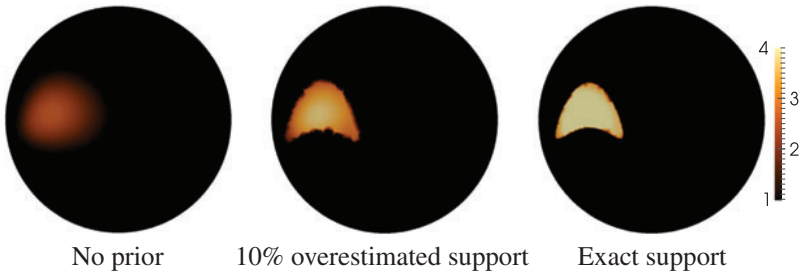

Figure 7. Full data sparse reconstruction of the phantom in Figure 2(b). The applied prior information for the overestimated support is a 10% dilation of the correct shape.

In Figure 8 we observe that with data on the top half of the unit circle, it is actually possible to get very good contrast and also reasonable localization of the two large inclusions. There is still a clear separation of the inclusions, while the small inclusion is not reconstructed at all. With data on the bottom half, the small inclusion is reconstructed almost as well as with full boundary data, but the larger inclusions are only vaguely visible. This is the kind of behaviour that is expected from partial data EIT, and in practice it implies that we can only expect reasonable reconstruction close to where the measurements are taken.

In the rightmost reconstruction in Figure 8, there is a small artefact to the left in a region where a reliable reconstruction is expected. This may be due to the partial data problem being very noise sensitive and the low number of current patterns ($K = 10$).

In Figures 9 and 10 panels (a) and (c) it is observed that as the length of Γ becomes smaller, the reconstructed shape of the inclusion is rapidly deformed. By including prior

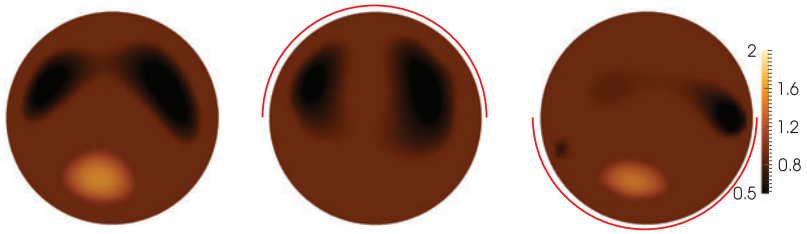

Figure 8. Sparse reconstruction of the phantom in Figure 2(c). Left: $\Gamma = \partial\Omega$. Middle: $(\theta_1, \theta_2) = (0, \pi)$. Right: $(\theta_1, \theta_2) = (\pi, 2\pi)$.

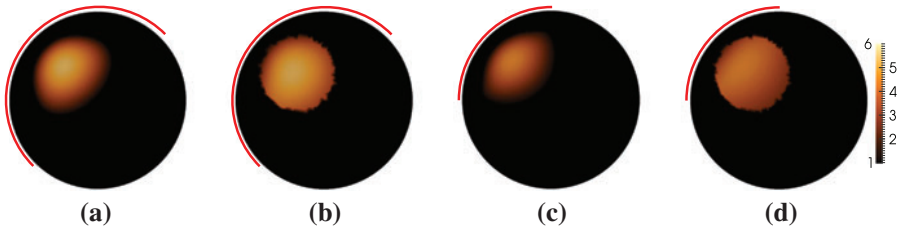

Figure 9. Sparse reconstruction of the phantom with a ball inclusion in Figure 2(a). (a) 50% boundary data, no prior. (b): 50% boundary data with 5% overestimated support. (c): 25% boundary data, no prior. (d): 25% boundary data with 5% overestimated support.

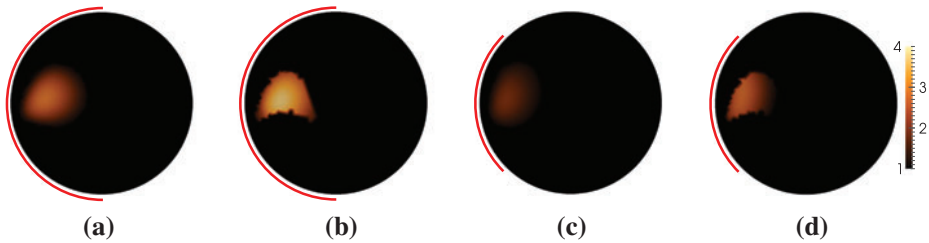

Figure 10. Sparse reconstruction of the phantom with a kite-shaped inclusion in Figure 2(b). (a) 50% boundary data, no prior. (b) 50% boundary data with 10% overestimated support. (c) 25% boundary data, no prior. (d) 25% boundary data with 10% overestimated support.

information about the support of $\delta\sigma$, it is possible to rectify the deformation of the shape, and get reconstructions with almost the correct shape but with a slightly worse reconstructed contrast compared to full boundary data reconstructions. This is observed for the ball- and kite-shaped inclusions in Figures 9 and 10, respectively.

4.3. *Comparison with TV regularization*

Another sparsity promoting method is TV regularization, which promotes a sparse gradient in the solution. This can be achieved by minimizing the functional

$$\Psi_{\mathrm{TV}}(\delta\gamma) \equiv \sum_{k=1}^{K} J_k(\delta\gamma) + P_{\mathrm{TV}}(\delta\gamma), \quad \delta\gamma \in \mathcal{A}_0, \tag{4.1}$$

where the discrepancy terms J_k remain the same as in (1.4), but the penalty term is now given by

$$P_{\mathrm{TV}}(\delta\gamma) \equiv \alpha \int_\Omega \sqrt{|\nabla\delta\gamma|^2 + b}\,\mathrm{d}x. \tag{4.2}$$

Here $b > 0$ is a constant that implies that P_{TV} is differentiable, but chosen small such that P_{TV} approximates $\alpha \int_\Omega |\nabla\delta\gamma|\,\mathrm{d}x$. The computational cost for determining the derivative of Ψ_{TV} is the same as for the sparsity regularization in (1.4), as it is dominated by the same $2K$ PDE's (see Remark 2.7). Minimizing the functional (4.1) is implemented numerically using a plain steepest descend method.

For the numerical examples, the piecewise constant phantoms in Figure 2 panels (a) and (b) are used, with the same noise level as in the previous sections. The value $b = 10^{-5}$ is used for the penalty term in all the examples.

It should be noted that the colour scale in the following examples is not the same scale as for the phantoms, unlike the previous reconstructions. This is because the TV reconstructions have a significantly lower contrast, in particular for the partial data reconstructions, and would be visually difficult to distinguish from the background conductivity in the correct colour scale.

As seen from Figures 11 and 12, the support of the inclusion is slightly overestimated in the case of full boundary data, and for the partial data cases the support is slightly larger than the counterparts in Figures 9 and 10. It is also noticed that the TV reconstructions have a much lower contrast than the ℓ_1 sparsity reconstructions, and the contrast for the TV reconstructions is severely reduced when partial data are used. It is also observed that the same type of shape deformation occurs for both methods in case of partial data.

A typical feature of the TV regularization is piecewise constant reconstructions; however, the reconstructions seen here have constant contrast levels with a smooth transition between them. This is partly due to the slight smoothing of the penalty term with the

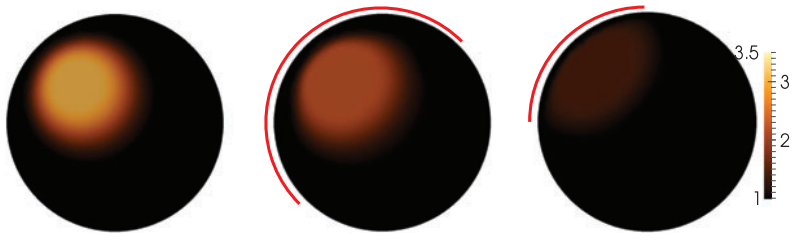

Figure 11. TV reconstruction of the phantom with a ball inclusion in Figure 2(a). (a) Full boundary data. (b) 50% boundary data. (c) 25% boundary data.

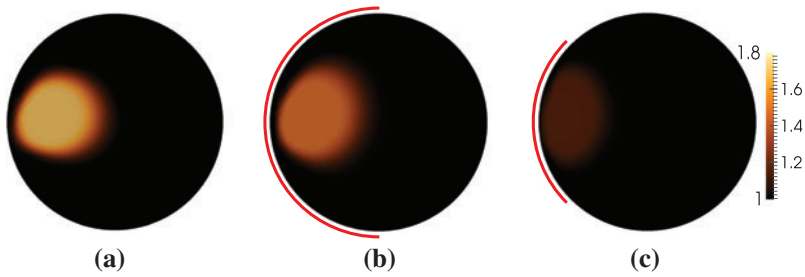

Figure 12. TV reconstruction of the phantom with a kite-shaped inclusion in Figure 2(b). (a) Full boundary data. (b) 50% boundary data. (c) 25% boundary data.

parameter $b > 0$ to make it differentiable, but mostly because the discrepancy terms are not convex which may lead to local minima. The same kind of smooth transitions is also observed in TV-based methods for EIT in [48].

5. Conclusions

We have extended the algorithm developed in [36], for sparse reconstruction in electrical impedance tomography, to the case of partial data. Furthermore, we have shown how a distributed regularization parameter can be applied to utilize spatial prior information. This lead to numerical results showing improved reconstructions for the support of the inclusions and the contrast simultaneously. The use of the distributed regularization parameter enables sharper edges in the reconstruction and vastly reduces the deformation of the inclusions in the partial data problem, even when the prior is overestimated.

The optimization problem is non-convex and the suggested algorithm is therefore only expected to find a local minimum. Initializing with the background conductivity in the numerical examples yields acceptable reconstructions for both full boundary data and partial boundary data.

The algorithm can be generalized for 3D reconstruction, under further assumptions on the boundary conditions $\{g_k\}_{k=1}^K$ and the amplitude of the perturbation $\delta\sigma$. This will be considered in a forthcoming paper [38].

Disclosure statement

No potential conflict of interest was reported by the authors.

Funding

This research is supported by the European Research Council [advanced grant number 291405 HD-Tomo].

References

[1] Holder DS. Electrical impedance tomography: methods, history and applications. Bristol: IOP Publishing Ltd; 2005.

[2] Abubakar A, Habashy TM, Li M, Liu J. Inversion algorithms for large-scale geophysical electromagnetic measurements. Inverse Prob. 2009;25:30 p. Article ID 123012.
[3] York TA. Status of electrical tomography in industrial applications. Proc. SPIE Int. Soc. Opt. Eng. 2001;4188:175–190.
[4] Calderón AP. On an inverse boundary value problem. In: Seminar on numerical analysis and its applications to continuum physics (Rio de Janeiro, 1980). Rio de Janeiro: Sociedade Brasiliera de Matemática; 1980. p. 65–73.
[5] Sylvester J, Uhlmann G. A global uniqueness theorem for an inverse boundary value problem. Ann. Math. (2). 1987;125:153–169.
[6] Nachman AI. Reconstructions from boundary measurements. Ann. Math. (2). 1988;128: 531–576.
[7] Novikov RG. A multidimensional inverse spectral problem for the equation $-\Delta\psi + (v(x) - Eu(x))\psi = 0$. Funktsional. Anal. i Prilozhen. 1988;22:11–22, 96.
[8] Nachman AI. Global uniqueness for a two-dimensional inverse boundary value problem. Ann. Math. (2). 1996;143:71–96.
[9] Astala K, Päivärinta L. Calderón's inverse conductivity problem in the plane. Ann. Math. (2). 2006;163:265–299.
[10] Haberman B, Tataru D. Uniqueness in Calderón's problem with Lipschitz conductivities. Duke Math. J. 2013;162:496–516.
[11] Uhlmann G. Electrical impedance tomography and Calderón's problem. Inverse Prob. 2009;25:39 p. Article ID 123011.
[12] Alessandrini G. Stable determination of conductivity by boundary measurements. Appl. Anal. 1988;27:153–172.
[13] Alessandrini G. Singular solutions of elliptic equations and the determination of conductivity by boundary measurements. J. Differ. Equ. 1990;84:252–272.
[14] Mandache N. Exponential instability in an inverse problem for the Schrödinger equation. Inverse Prob. 2001;17:1435–1444.
[15] Siltanen S, Mueller J, Isaacson D. An implementation of the reconstruction algorithm of A. Nachman for the 2D inverse conductivity problem. Inverse Prob. 2000;16:681–699.
[16] Knudsen K, Lassas M, Mueller JL, Siltanen S. Regularized D-bar method for the inverse conductivity problem. Inverse Prob. Imaging. 2009;3:599–624.
[17] Bikowski J, Knudsen K, Mueller JL. Direct numerical reconstruction of conductivities in three dimensions using scattering transforms. Inverse Prob. 2011;27:015002, 19.
[18] Delbary F, Hansen PC, Knudsen K. Electrical impedance tomography: 3D reconstructions using scattering transforms. Appl. Anal. 2012;91:737–755.
[19] Delbary F, Knudsen K. Numerical nonlinear complex geometrical optics algorithm for the 3D Calderón problem. Inverse Prob. Imaging. 2014;8:991–1012.
[20] Bukhgeim AL, Uhlmann G. Recovering a potential from partial Cauchy data. Comm. Partial Differ. Equ. 2002;27:653–668.
[21] Kenig CE, Sjöstrand J, Uhlmann G. The Calderón problem with partial data. Ann. Math (2). 2007;165:567–591.
[22] Knudsen K. The Calderón problem with partial data for less smooth conductivities. Comm. Partial Differ. Equ. 2006;31:57–71.
[23] Zhang G. Uniqueness in the Calderón problem with partial data for less smooth conductivities. Inverse Prob. 2012;28:105008, 18.
[24] Isakov V. On uniqueness in the inverse conductivity problem with local data. Inverse Prob. Imaging. 2007;1:95–105.
[25] Imanuvilov OY, Uhlmann G, Yamamoto M. The Calderón problem with partial data in two dimensions. J. Am. Math. Soc. 2010;23:655–691.
[26] Heck H, Wang JN. Stability estimates for the inverse boundary value problem by partial Cauchy data. Inverse Prob. 2006;22:1787–1796.

[27] Hamilton SJ, Siltanen S. Nonlinear inversion from partial EIT data: computational experiments. In: Stefanov P, Zworski M, editors. Inverse problems and applications. Vol. 615, Contemporary mathematics. Providence (RI): American Mathematical Society; 2014. p. 105–129.
[28] Mueller JL, Siltanen S. Linear and nonlinear inverse problems with practical applications. Vol. 10, Computational science & engineering. Philadelphia (PA): Society for Industrial and Applied Mathematics (SIAM); 2012.
[29] Somersalo E, Cheney M, Isaacson D. Existence and uniqueness for electrode models for electric current computed tomography. SIAM J. Appl. Math. 1992;52:1023–1040.
[30] Gehre M, Kluth T, Lipponen A, Jin B, Seppänen A, Kaipio JP, Maass P. Sparsity reconstruction in electrical impedance tomography: an experimental evaluation. J. Comput. Appl. Math. 2012;236:2126–2136.
[31] Gehre M, Kluth T, Sebu C, Maass P. Sparse 3D reconstructions in electrical impedance tomography using real data. Inverse Prob. Sci. Eng. 2014;22:31–44.
[32] Daubechies I, Defrise M, De Mol C. An iterative thresholding algorithm for linear inverse problems with a sparsity constraint. Comm. Pure Appl. Math. 2004;57:1413–1457.
[33] Bredies K, Lorenz DA, Maass P. A generalized conditional gradient method and its connection to an iterative shrinkage method. Comput. Optim. Appl. 2009;42:173–193.
[34] Bonesky T, Bredies K, Lorenz DA, Maass P. A generalized conditional gradient method for nonlinear operator equations with sparsity constraints. Inverse Prob. 2007;23:2041–2058.
[35] Jin B, Maass P. An analysis of electrical impedance tomography with applications to Tikhonov regularization. ESAIM: Control Optim. Calcul. Varia. 2012;18:1027–1048.
[36] Jin B, Khan T, Maass P. A reconstruction algorithm for electrical impedance tomography based on sparsity regularization. Int. J. Numer. Methods Eng. 2012;89:337–353.
[37] Borcea L. Electrical impedance tomography. Inverse Prob. 2002;18:R99–R136.
[38] Garde H, Knudsen K. 3D reconstruction for partial data electrical impedance tomography using a sparsity prior. Submitted, 2014. Available from: http://arxiv.org/abs/1412.6288
[39] Adams RA, Fournier JJF. Sobolev spaces. 2nd ed. Vol. 140, Pure and applied mathematics (Amsterdam). Amsterdam: Elsevier/Academic Press; 2003.
[40] Neuberger JW. Sobolev gradients and differential equations. 2nd ed. Vol. 1670, Lecture notes in mathematics. Berlin: Springer-Verlag; 2010.
[41] Barzilai J, Borwein JM. Two-point step size gradient methods. IMA J. Numer. Anal. 1988;8: 141–148.
[42] Wright SJ, Nowak RD, Figueiredo MAT. Sparse reconstruction by separable approximation. IEEE Trans. Signal Process. 2009;57:2479–2493.
[43] Stampacchia G. Le problème de dirichlet pour les équations elliptiques du second ordre à coefficients discontinus. Ann. lnst. Fourier. 1965;15:189–257.
[44] Kirsch A, Grinberg N. The factorization method for inverse problems. Vol. 36, Oxford lecture series in mathematics and its applications. Oxford: Oxford University Press; 2008.
[45] von Harrach B, Ullrich M. Monotonicity-based shape reconstruction in electrical impedance tomography. SIAM J. Math. Anal. 2013;45:3382–3403.
[46] von Harrach B, Seo JK. Exact shape-reconstruction by one-step linearization in electrical impedance tomography. SIAM J. Math. Anal. 2010;42:1505–1518.
[47] Logg A, Mardal KA, Wells GN. Automated solution of differential equations by the finite element method. Vol. 84, Lecture notes in computational science and engineering. Heidelberg: Springer; 2012; the FEniCS book.
[48] Borsic A, Graham BM, Adler A, Lionheart W. In vivo impedance imaging with total variation regularization. IEEE Trans. Med. Imaging. 2010;29:44–54.

PAPER E

3D reconstruction for partial data electrical impedance tomography using a sparsity prior

Type	Peer reviewed conference proceeding
Authors	Henrik Garde and Kim Knudsen
Journal	Proceedings of the 10th AIMS International Conference
Year	2015
Pages	495–504
Available from	http://dx.doi.org/10.3934/proc.2015.0495

Dynamical Systems, Differential Equations and Applications
AIMS Proceedings, 2015

doi:10.3934/proc.2015.0495
pp. **495–504**

3D RECONSTRUCTION FOR PARTIAL DATA ELECTRICAL IMPEDANCE TOMOGRAPHY USING A SPARSITY PRIOR

Henrik Garde and Kim Knudsen

Department of Applied Mathematics and Computer Science
Technical University of Denmark
2800 Kgs. Lyngby, Denmark

Abstract. In electrical impedance tomography the electrical conductivity inside a physical body is computed from electro-static boundary measurements. The focus of this paper is to extend recent results for the 2D problem to 3D: prior information about the sparsity and spatial distribution of the conductivity is used to improve reconstructions for the partial data problem with Cauchy data measured only on a subset of the boundary. A sparsity prior is enforced using the ℓ_1 norm in the penalty term of a Tikhonov functional, and spatial prior information is incorporated by applying a spatially distributed regularization parameter. The optimization problem is solved numerically using a generalized conditional gradient method with soft thresholding. Numerical examples show the effectiveness of the suggested method even for the partial data problem with measurements affected by noise.

1. **Introduction.** Sparse reconstruction for electrical impedance tomography (EIT) with full boundary data has been utilized in [9, 14, 15] and are based on algorithms from [3, 4]. A similar approach was used for the 2D partial data problem in [8] by applying a spatially varying regularization parameter; this paper extends the algorithm to the 3D partial data problem. The main contributions are in deriving the Fréchet derivative for the algorithm and in the numerical results in 3D.

The inverse problem in EIT consists of reconstructing an electrical conductivity distribution in the interior of an object from electro-static boundary measurements on the surface of the object. The underlying mathematical problem is known as the Calderón problem in recognition of Calderón's seminal paper [6]. While the Calderón problem can also be considered in two dimensions, physical electric fields are intrinsically three dimensional, and thus the reconstruction problem in EIT should ideally use a 3D reconstruction algorithm to reduce modelling errors in the reconstruction.

Consider a bounded domain $\Omega \subset \mathbb{R}^3$ with smooth boundary $\partial\Omega$. In order to consider partial boundary measurements we introduce the subsets $\Gamma^{\mathrm{N}}, \Gamma^{\mathrm{D}} \subseteq \partial\Omega$ for the Neumann and Dirichlet data respectively. Let $\sigma \in L^\infty(\Omega)$ with $0 < c \leq \sigma$ a.e. denote the conductivity distribution in Ω. Applying a boundary current flux g (Neumann condition) through $\Gamma^{\mathrm{N}} \subseteq \partial\Omega$ gives rise to the interior electric potential u characterized as the solution to

$$\nabla \cdot (\sigma \nabla u) = 0 \text{ in } \Omega, \quad \sigma \frac{\partial u}{\partial \nu} = g \text{ on } \partial\Omega, \quad \int_{\Gamma^{\mathrm{D}}} u|_{\partial\Omega}\, ds = 0, \tag{1}$$

2010 *Mathematics Subject Classification.* Primary: 65N20, 65N21.
Key words and phrases. Impedance tomography, sparsity, partial data, prior information, numerical reconstruction.
The authors are supported by ERC project High-Definition Tomography, Advanced Grant No. 291405.

where ν is an outward unit normal to $\partial\Omega$. The latter condition in (1) is a grounding of the total electric potential along the subset $\Gamma^{\mathrm{D}} \subseteq \partial\Omega$. To be precise we define the spaces

$$L^2_\diamond(\partial\Omega) \equiv \left\{ g \in L^2(\partial\Omega) \;\middle|\; \int_{\partial\Omega} g\, ds = 0 \right\},$$
$$H^{-1/2}_\diamond(\partial\Omega) \equiv \left\{ g \in H^{-1/2}(\partial\Omega) \;\middle|\; \langle g, 1\rangle = 0 \right\},$$

consisting of boundary functions with mean zero (here $\langle\cdot,\cdot\rangle$ denotes the dual pairing), and the spaces

$$H^1_{\Gamma^{\mathrm{D}}}(\Omega) \equiv \left\{ u \in H^1(\Omega) \;\middle|\; u|_{\partial\Omega} \in H^{1/2}_{\Gamma^{\mathrm{D}}}(\partial\Omega) \right\},$$
$$H^{1/2}_{\Gamma^{\mathrm{D}}}(\partial\Omega) \equiv \left\{ f \in H^{1/2}(\partial\Omega) \;\middle|\; \int_{\Gamma^{\mathrm{D}}} f\, ds = 0 \right\},$$

consisting of functions with mean zero on Γ^{D}. Using standard elliptic theory it follows that (1) has a unique solution $u \in H^1_{\Gamma^{\mathrm{D}}}(\Omega)$ for any $g \in H^{-1/2}_\diamond(\partial\Omega)$. This defines the Neumann-to-Dirichlet map (ND-map) $R_\sigma : H^{-1/2}_\diamond(\partial\Omega) \to H^{1/2}_{\Gamma^{\mathrm{D}}}(\partial\Omega)$ by $R_\sigma g = u|_{\partial\Omega}$, and the partial ND-map as $(R_\sigma g)|_{\Gamma^{\mathrm{D}}}$ for $\mathrm{supp}(g) \subseteq \Gamma^{\mathrm{N}}$.

Recently the partial data Calderón problem has been studied intensively. In 3D uniqueness has been proved under certain conditions on Γ^{D} and Γ^{N} [5, 13, 16, 18]. Also stability estimates of log-log type have been obtained for the partial data problem [12]; this suggests that the partial data problem is even more ill-posed and hence requires more regularization than the full data problem which has log type estimates [2].

The data considered here consist of K pairs of Cauchy data taken on the subsets Γ^{D} and Γ^{N}, i.e.

$$\{(f_k, g_k) \mid g_k \in H^{-1/2}_\diamond(\partial\Omega),\ \mathrm{supp}(g_k) \subseteq \Gamma^{\mathrm{N}}, f_k = (R_\sigma g_k)|_{\Gamma^{\mathrm{D}}}\}_{k=1}^K. \tag{2}$$

We assume that the unknown conductivity is given as $\sigma = \sigma_0 + \delta\sigma$, where σ_0 is a known background conductivity. For some fixed $c \in (0,1)$ and $\sigma_0 \in H^1(\Omega)$ where $c \le \sigma_0 \le c^{-1}$, define the closed and convex subset

$$\mathcal{A}_0 \equiv \{\delta\gamma \in H^1_0(\Omega) \mid c \le \sigma_0 + \delta\gamma \le c^{-1} \text{ a.e. in } \Omega\}. \tag{3}$$

Similarly define

$$\mathcal{A} \equiv \mathcal{A}_0 + \sigma_0 = \{\gamma \in H^1(\Omega) \mid c \le \gamma \le c^{-1} \text{ a.e. in } \Omega, \gamma|_{\partial\Omega} = \sigma_0|_{\partial\Omega}\}.$$

The inverse problem is then to approximate $\delta\sigma \in \mathcal{A}_0$ given the data (2).

Let $\{\psi_j\}_{j=1}^\infty$ denote a chosen orthonormal basis for $H^1_0(\Omega)$. For sparsity regularization we approximate $\delta\sigma$ by $\mathrm{argmin}_{\delta\gamma\in\mathcal{A}_0}\Psi(\delta\gamma)$ using the following Tikhonov functional

$$\Psi(\delta\gamma) \equiv \sum_{k=1}^K J_k(\delta\gamma) + P(\delta\gamma), \quad \delta\gamma \in \mathcal{A}_0, \tag{4}$$

with the discrepancy terms J_k and penalty term P given by

$$J_k(\delta\gamma) \equiv \frac{1}{2}\|R_{\sigma_0+\delta\gamma}g_k - f_k\|^2_{L^2(\Gamma^{\mathrm{D}})}, \quad P(\delta\gamma) \equiv \sum_{j=1}^\infty \alpha_j |c_j|,$$

for $c_j \equiv \langle\delta\gamma, \psi_j\rangle_{H^1(\Omega)}$. The regularization parameter α_j for the sparsity-promoting ℓ_1 penalty term P is distributed such that each basis coefficient can be regularized differently; we will return to this in Section 3. It should be noted how easy and natural the use of partial data is introduced in this way, simply by only minimizing the discrepancy on Γ^{D} where the Dirichlet data is known and ignoring the rest of the boundary.

Remark 1. The non-linearity of $\sigma \mapsto R_\sigma$ leads to a non-convex discrepancy term, i.e. Ψ is non-convex. When applying a gradient based optimization method, the best we can hope is to find a local minimum.

This paper is organised as follows: in Section 2 we derive the Fréchet derivative of J_k and reformulate the optimization problem using the generalized conditional gradient method as a sequence of linearized optimization problems. In Section 3 we explain the idea of the spatially dependent regularization parameter designed for the use of prior information. Finally, in Section 4 we show the feasibility of the algorithm by numerical examples.

2. Sparse Reconstruction.

In this section the sparse reconstruction of $\delta\sigma$ based on the optimization problem (4) is investigated for a bounded domain $\Omega \subset \mathbb{R}^3$ with smooth boundary. The penalty term emphasizes that $\delta\sigma$ should only be expanded by few basis functions in the given orthonormal basis. The partial data problem comes into play in the discrepancy term, in which we only fit the data on part of the boundary. Ultimately, this leads to Algorithm 1 at the end of this section.

For fixed g let u be the unique solution to (1). Define the solution operator $F_g : \sigma \mapsto u$ and further its trace $\mathcal{F}_g : \sigma \mapsto u|_{\partial\Omega}$ (note that $R_\sigma g = \mathcal{F}_g(\sigma)$). In order to compute the derivative of $\mathcal{F}_g$, let $\gamma \in \mathcal{A}$ and $g \in L^p(\partial\Omega) \cap H_\diamond^{-1/2}(\partial\Omega)$ for $p \geq \frac{8}{5}$. Then following the proofs of Theorem 2.2 and Corollary 2.1 in [15] whilst applying the partial boundary Γ^{D} we have

$$\lim_{\substack{\|\eta\|_{H^1(\Omega)} \to 0 \\ \gamma+\eta \in \mathcal{A}}} \frac{\|\mathcal{F}_g(\gamma+\eta) - \mathcal{F}_g(\gamma) - (\mathcal{F}_g)'_\gamma \eta\|_{H^{1/2}_{\Gamma^{\mathrm{D}}}(\partial\Omega)}}{\|\eta\|_{H^1(\Omega)}} = 0. \tag{5}$$

The linear map $(\mathcal{F}_g)'_\gamma$ maps η to $w|_{\partial\Omega}$, where w is the unique solution to

$$-\nabla\cdot(\gamma\nabla w) = \nabla\cdot(\eta\nabla F_g(\gamma)) \text{ in } \Omega, \quad \gamma\frac{\partial w}{\partial \nu} = 0 \text{ on } \partial\Omega, \quad \int_{\Gamma^{\mathrm{D}}} w|_{\partial\Omega}\, ds = 0. \tag{6}$$

Note that $(\mathcal{F}_g)'_\gamma$ resembles a Fréchet derivative of $\mathcal{F}_g$ evaluated at γ due to (5), however $\mathcal{A}$ is not a linear vector space, thus the requirement $\gamma, \gamma+\eta \in \mathcal{A}$.

The first step in minimizing Ψ using a gradient descent type iterative algorithm is to determine a derivative to the discrepancy terms J_k. For this purpose the following proposition is applied, and is a special case of [15, Theorem 3.1].

Proposition 1. *Let $\Omega \subset \mathbb{R}^3$ be open and bounded with smooth boundary $\partial\Omega$. For $\gamma \in \mathcal{A}$ there exists $Q(c) > 2$ depending continuously on the bound c from $\mathcal{A}$, such that $\lim_{c\to 1} Q(c) = \infty$. For $q \in (2, Q(c)) \cap [\frac{3}{2}, \frac{3}{2}p]$ and $g \in L^p(\partial\Omega) \cap H_\diamond^{-1/2}(\partial\Omega)$, there is the following estimate with C only depending on c, Ω and q:*

$$\|F_g(\gamma)\|_{W^{1,q}(\Omega)} \leq C\|g\|_{L^p(\partial\Omega)}. \tag{7}$$

Now we can formulate the Fréchet derivative of J_k.

Lemma 2.1. *Let $g_k \in L^p(\partial\Omega) \cap H_\diamond^{-1/2}(\partial\Omega)$ with $p \geq \frac{8}{5}$, and $\chi_{\Gamma^{\mathrm{D}}}$ be a characteristic function on Γ^{D}. Then there exists $c \in (0,1)$ as the bound in $\mathcal{A}_0$ sufficiently close to 1, such that $\gamma = \sigma_0 + \delta\gamma$ with $\delta\gamma \in \mathcal{A}_0$ implies*

$$E_k \equiv -\nabla F_{g_k}(\gamma)\cdot\nabla F_{\chi_{\Gamma^{\mathrm{D}}}(R_\gamma g_k - f_k)}(\gamma) \in L^{6/5}(\Omega) \subset H^{-1}(\Omega), \tag{8}$$

and the Fréchet derivative $(J_k)'_{\delta\gamma}$ of J_k on $H_0^1(\Omega)$ evaluated at $\delta\gamma$ is given by

$$(J_k)'_{\delta\gamma}\eta = \int_\Omega E_k \eta\, dx, \quad \delta\gamma + \eta \in \mathcal{A}_0. \tag{9}$$

Proof. For the proof the index k is suppressed. First it is proved that $E \in L^{6/5}(\Omega)$. Write $h \equiv \chi_{\Gamma^{\mathrm{D}}}(R_\gamma g - f)$ and note that $R_\gamma g \in H^{1/2}_{\Gamma^{\mathrm{D}}}(\partial\Omega)$ and $f \in L^2_\diamond(\Gamma^{\mathrm{D}})$, i.e. $h \in L^2_\diamond(\partial\Omega) \subset L^2(\partial\Omega) \cap H^{-1/2}_\diamond(\partial\Omega)$. Now using Proposition 1, there exists $Q(c) > 2$ such that

$$\|F_h(\gamma)\|_{W^{1,q}(\Omega)} \leq C\|h\|_{L^2(\partial\Omega)}, \tag{10}$$

where $q \in (2, Q(c)) \cap [\frac{3}{2}, 3]$. Since $g \in L^{8/5}(\partial\Omega) \cap H^{-1/2}_\diamond(\partial\Omega)$ then Proposition 1 implies

$$\|F_g(\gamma)\|_{W^{1,\tilde{q}}(\Omega)} \leq \tilde{C}\|g\|_{L^{8/5}(\Omega)}, \tag{11}$$

for $\tilde{q} \in (2, Q(c)) \cap [\frac{3}{2}, \frac{12}{5}]$. Choosing c sufficiently close to 1 leads to $Q(c) > \frac{12}{5}$. By (10) and (11) then $|\nabla F_h(\gamma)|, |\nabla F_g(\gamma)| \in L^{12/5}(\Omega)$, and Hölder's generalized inequality entails that $E \in L^r(\Omega)$ with $\frac{1}{r} = \frac{5}{12} + \frac{5}{12}$, i.e. $r = \frac{6}{5}$,

$$E = -\nabla F_g(\gamma) \cdot \nabla F_h(\gamma) \in L^{6/5}(\Omega).$$

The Sobolev embedding theorem [1] implies the embedding $H^1(\Omega) \hookrightarrow L^6(\Omega)$ as $\Omega \subset \mathbb{R}^3$. Thus $E \in L^{6/5}(\Omega) = (L^6(\Omega))' \subset (H^1(\Omega))' \subset (H^1_0(\Omega))' = H^{-1}(\Omega)$.

Next we prove (9). $J'_{\delta\gamma}\eta$ is by the chain rule (utilizing that $R_\gamma g = \mathcal{F}_g(\gamma)$) given as

$$J'_{\delta\gamma}\eta = \int_{\partial\Omega} \chi_{\Gamma^{\mathrm{D}}}(R_\gamma g - f)(\mathcal{F}_g)'_\gamma \eta \, ds, \tag{12}$$

where $\chi_{\Gamma^{\mathrm{D}}}$ is enforcing that the integral is over Γ^{D}. The weak formulations of (1), with Neumann data $\chi_{\Gamma^{\mathrm{D}}}(R_\gamma g - f)$, and (6) are

$$\int_\Omega \gamma \nabla F_{\chi_{\Gamma^{\mathrm{D}}}(R_\gamma g - f)}(\gamma) \cdot \nabla v \, dx = \int_{\partial\Omega} \chi_{\Gamma^{\mathrm{D}}}(R_\gamma g - f) v|_{\partial\Omega} \, ds, \ \ \forall v \in H^1(\Omega), \tag{13}$$

$$\int_\Omega \gamma \nabla w \cdot \nabla v \, dx = -\int_\Omega \eta \nabla F_g(\gamma) \cdot \nabla v \, dx, \ \ \forall v \in H^1(\Omega). \tag{14}$$

Now by letting $v \equiv w$ in (13) and $v \equiv F_{\chi_{\Gamma^{\mathrm{D}}}(R_\gamma g - f)}(\gamma)$ in (14), we obtain using the definition $w|_{\partial\Omega} = (\mathcal{F}_g)'_\gamma \eta$ that

$$\begin{aligned} J'_{\delta\gamma}\eta &= \int_{\partial\Omega} \chi_{\Gamma^{\mathrm{D}}}(R_\gamma g - f)(\mathcal{F}_g)'_\gamma \eta \, ds = \int_\Omega \gamma \nabla F_{\chi_{\Gamma^{\mathrm{D}}}(R_\gamma g - f)}(\gamma) \cdot \nabla w \, dx \\ &= -\int_\Omega \eta \nabla F_g(\gamma) \cdot \nabla F_{\chi_{\Gamma^{\mathrm{D}}}(R_\gamma g - f)}(\gamma) \, dx = \int_\Omega E\eta \, dx. \end{aligned}$$

□

Define

$$J'_{\delta\gamma} \equiv \sum_{k=1}^K (J_k)'_{\delta\gamma} = -\sum_{k=1}^K \nabla F_{g_k}(\gamma) \cdot \nabla F_{\chi_{\Gamma^{\mathrm{D}}}(R_\gamma g_k - f_k)}(\gamma).$$

We seek to find a direction η for which the discrepancy decreases. As $J'_{\delta\gamma} \in H^{-1}(\Omega)$ it is known from Riesz' representation theorem that there exists a unique function in $H^1_0(\Omega)$, denoted by $G(\delta\gamma)$, such that

$$J'_{\delta\gamma}\eta = \langle G(\delta\gamma), \eta \rangle_{H^1(\Omega)}, \ \ \eta \in H^1_0(\Omega). \tag{15}$$

Now $\eta \equiv -G(\delta\gamma)$ points in the direction of steepest descend among the viable directions. Furthermore, since $G(\delta\gamma)|_{\partial\Omega} = 0$ the boundary condition $\delta\sigma|_{\partial\Omega} = 0$ for the approximation will automatically be fulfilled. Note that $G(\delta\gamma)$ is the unique solution to

$$(-\Delta + 1)v = J'_{\delta\gamma} \text{ in } \Omega, \quad v = 0 \text{ on } \partial\Omega,$$

for which (15) is the weak formulation. In each iteration step we need to determine a step size s_i for an algorithm resembling a steepest descent $\delta\gamma_{i+1} = \delta\gamma_i - s_i G(\delta\gamma_i)$. As in [8] a Barzilai-Borwein step size rule is applied

$$s_i = \frac{\|\delta\gamma_i - \delta\gamma_{i-1}\|^2_{H^1(\Omega)}}{\langle \delta\gamma_i - \delta\gamma_{i-1}, G(\delta\gamma_i) - G(\delta\gamma_{i-1})\rangle_{H^1(\Omega)}}. \tag{16}$$

A maximum step size $s_{\max}$ is enforced to avoid problems in the situation where $\langle \delta\gamma_i - \delta\gamma_{i-1}, G(\delta\gamma_i) - G(\delta\gamma_{i-1})\rangle_{H^1(\Omega)} \simeq 0$.

With inspiration from [21], s_i will be initialized by (16), after which it is thresholded to lie in $[s_{\min}, s_{\max}]$ for two chosen positive constants $s_{\min}$ and $s_{\max}$. It is noted in [21] that Barzilai-Borwein type step rules lead to faster convergence if we do not restrict Ψ to decrease in every iteration. Therefore, one makes sure that the following so-called weak monotonicity is satisfied, which compares $\Psi(\delta\gamma_{i+1})$ with the most recent M steps. Let $\tau \in (0,1)$ and $M \in \mathbb{N}$, then s_i is said to satisfy the weak monotonicity with respect to M and τ if the following is satisfied

$$\Psi(\delta\gamma_{i+1}) \leq \max_{i-M+1\leq j\leq i} \Psi(\delta\gamma_j) - \frac{\tau}{2s_i}\|\delta\gamma_{i+1} - \delta\gamma_i\|^2_{H^1(\Omega)}. \tag{17}$$

If (17) is not satisfied, the step size s_i is reduced until this is the case.

To solve the non-linear minimization problem (4) we iteratively solve the following linearized problem

$$\zeta_{i+1} \equiv \operatorname{argmin}_{\delta\gamma\in H^1_0(\Omega)} \left[\frac{1}{2}\|\delta\gamma - (\delta\gamma_i - s_i G(\delta\gamma_i))\|^2_{H^1(\Omega)} + s_i \sum_{j=1}^{\infty} \alpha_j |c_j|\right], \tag{18}$$

$$\delta\gamma_{i+1} \equiv \mathcal{P}_{\mathcal{A}_0}(\zeta_{i+1}).$$

Here $\{\psi_j\}_{j=1}^{\infty}$ is an orthonormal basis for $H^1_0(\Omega)$ in the H^1-metric, and $\mathcal{P}_{\mathcal{A}_0}$ is a projection of $H^1_0(\Omega)$ onto $\mathcal{A}_0$ to ensure that (1) is solvable (note that $H^1_0(\Omega)$ does not embed into $L^\infty(\Omega)$, i.e. ζ_{i+1} may be unbounded). By use of the map $\mathcal{S}_\beta : \mathbb{R} \to \mathbb{R}$ defined below, known as the soft shrinkage/thresholding map with threshold $\beta > 0$,

$$\mathcal{S}_\beta(x) \equiv \operatorname{sgn}(x)\max\{|x| - \beta, 0\}, \quad x \in \mathbb{R}, \tag{19}$$

the solution to (18) is easy to find directly (see also [7, Section 1.5])

$$\zeta_{i+1} = \sum_{j=1}^{\infty} \mathcal{S}_{s_i\alpha_j}(d_j)\psi_j, \tag{20}$$

where $d_j \equiv \langle \delta\gamma_i - s_i G(\delta\gamma_i), \psi_j\rangle_{H^1(\Omega)}$ are the basis coefficients for $\delta\gamma_i - s_i G(\delta\gamma_i)$.

The projection $\mathcal{P}_{\mathcal{A}_0} : H^1_0(\Omega) \to \mathcal{A}_0$ is defined as

$$\mathcal{P}_{\mathcal{A}_0}(v) \equiv T_c(\sigma_0 + v) - \sigma_0, \quad v \in H^1_0(\Omega),$$

where T_c is the following truncation that depends on the constant $c \in (0,1)$ in (3)

$$T_c(v) \equiv \begin{cases} c & \text{where } v < c \text{ a.e.,} \\ c^{-1} & \text{where } v > c^{-1} \text{ a.e.,} \\ v & \text{else.} \end{cases}$$

Since $\sigma_0 \in H^1(\Omega)$ and $c \leq \sigma_0 \leq c^{-1}$, it follows directly from [20, Lemma 1.2] that T_c and $\mathcal{P}_{\mathcal{A}_0}$ are well-defined, and it is easy to see that $\mathcal{P}_{\mathcal{A}_0}$ is a projection. It should also be noted that $0 \in \mathcal{A}_0$ since $c \leq \sigma_0 \leq c^{-1}$, thus we may choose $\delta\gamma_0 \equiv 0$ as the initial guess in the algorithm, which is appropriate as we expect the solution to be sparse.

The algorithm is summarized in Algorithm 1. In the numerical experiments in Section 4 the stopping criterion is when the step size s_i gets below a threshold s_{stop}.

Algorithm 1 Sparse Reconstruction for Partial Data EIT

Set $\delta\gamma_0 := 0$.
While stopping criteria not reached
  Set $\gamma_i := \sigma_0 + \delta\gamma_i$.
  Compute $\Psi(\delta\gamma_i)$.
  Compute $J'_{\delta\gamma_i} := -\sum_{k=1}^{K} \nabla F_{g_k}(\gamma_i) \cdot \nabla F_{\chi_{\Gamma^D}(R_{\gamma_i} g_k - f_k)}(\gamma_i)$.
  Compute $G(\delta\gamma_i) \in H_0^1(\Omega)$ such that $J'_{\delta\gamma_i}\eta = \langle G(\delta\gamma_i), \eta\rangle_{H^1(\Omega)}$.
  Compute step length s_i by (16), and decrease it till (17) is satisfied.
  Compute the basis coefficients $\{d_j\}_{j=1}^{\infty}$ for $\delta\gamma_i - s_i G(\delta\gamma_i)$.
  Update $\delta\gamma_{i+1} := \mathcal{P}_{\mathcal{A}_0}\left(\sum_{j=1}^{\infty} \mathcal{S}_{s_i\alpha_j}(d_j)\psi_j\right)$.
end while
Return final iterate of $\delta\gamma$.

3. **Prior Information.** Prior information is intrinsically linked to the penalty term P for Tikhonov-like functionals, and the regularization parameter determines how much this prior information is enforced. In the case of sparsity regularization this implies knowledge of how sparse we expect the solution is in general. Instead of applying the same prior information for each basis function, a distributed parameter is applied. Let

$$\alpha_j \equiv \alpha\mu_j,$$

where α is a usual regularization parameter, corresponding to the case where no prior information is considered about specific basis functions. The $\mu_j \in (0, 1]$ will be used to weight the penalty depending on whether a specific basis function should be included in the expansion of $\delta\sigma$. The μ_j are chosen as

$$\mu_j = \begin{cases} 1, & \text{no prior on } c_j, \\ \sim 0, & \text{prior that } c_j \neq 0, \end{cases}$$

i.e. if we know that a coefficient in the expansion of $\delta\sigma$ should be non-zero, we can choose to penalize that coefficient less.

3.1. **Applying the FEM Basis.** In order to improve the sparsity solution for finding small inclusions, it seems appropriate to include prior information about the support of the inclusions. There are different methods available for obtaining such information assuming piecewise constant conductivity [11, 17] or real analytic conductivity [10]. The idea is to be able to apply such information in the sparsity algorithm in order to get good contrast in the reconstruction while maintaining the correct support, even for the partial data problem.

Suppose that as a basis we consider a finite element method (FEM) basis $\{\psi_j\}_{j=1}^{N}$ for the subspace $V_h \subseteq H_0^1(\Omega)$ of piecewise affine functions on each element. Let $\delta\gamma \in V_h$ with mesh nodes $\{x_j\}_{j=1}^{N}$, then $\delta\gamma(x) = \sum_{j=1}^{N} \delta\gamma(x_j)\psi_j(x)$ and $\psi_j(x_k) = \delta_{j,k}$, i.e. for each node there is a basis function for which the coefficient contains local information about the expanded function; this is convenient when applying prior information about the support of an inclusion.

When applying the FEM basis for mesh nodes $\{x_j\}_{j=1}^{N}$, the corresponding functional is

$$\Psi(\delta\gamma) = \frac{1}{2}\sum_{k=1}^{K} \|R_{\sigma_0+\delta\gamma} g_k - f_k\|^2_{L^2(\Gamma^D)} + \sum_{j=1}^{N} \alpha_j |\delta\gamma(x_j)|.$$

It is evident that the penalty corresponds to determining inclusions with small support, and prior information on the sparsity corresponds to prior information on the support of $\delta\sigma$. We cannot directly utilize (20) due to the FEM basis not being an orthonormal basis for

$H_0^1(\Omega)$, and instead we suggest the following iteration step as in [8]:

$$\begin{aligned}\zeta_{i+1}(x_j) &= \mathcal{S}_{s_i\alpha_j/\|\psi_j\|_{L^1(\Omega)}}(\delta\gamma_i(x_j) - s_i G(\delta\gamma_i)(x_j)), \quad j = 1, 2, \ldots, N, \\ \delta\gamma_{i+1} &= \mathcal{P}_{\mathcal{A}_0}(\zeta_{i+1}).\end{aligned} \tag{21}$$

Note that the regularization parameter will depend quite heavily on the discretization of the mesh, i.e. for the same domain a good regularization parameter α will be much larger on a coarse mesh than on a fine mesh. Instead we can weight the regularization parameter according to the mesh cells, by having $\alpha_j \equiv \alpha\beta_j\mu_j$. This leads to a discretization of a weighted L^1-norm penalty term:

$$\alpha \int_\Omega f_\mu |\delta\gamma| \, dx \simeq \alpha \sum_j \beta_j \mu_j |\delta\gamma(x_j)|,$$

where $f_\mu : \Omega \to (0, 1]$ is continuous and $f_\mu(x_j) = \mu_j$. The weights β_j consists of the node volume computed in 3D as 1/4 of the volume of $\text{supp}(\psi_j)$ (if using a mesh of tetrahedrons). This corresponds to splitting each cell's volume evenly amongst the nodes, and it will not lead to instability on a regular mesh. This will make the choice of α almost independent of the mesh, and will be used in the numerical examples in the following section.

Remark 2. The corresponding algorithm with the FEM basis is the same as Algorithm 1, except that the update is applied via (21).

4. **Numerical Examples.** In this section we illustrate, through a few examples, the numerical algorithm implemented by use of the finite element library FEniCS [19]. First we consider the full data case $\Gamma^{\text{D}} = \Gamma^{\text{N}} = \partial\Omega$ both without and with prior information, and then we do the same for the partial data case.

For the following examples Ω is the unit ball in $\mathbb{R}^3$. The numerical phantom consists of a background conductivity with value 1, a smaller ball inclusion with value 2 centred at $(-0.09, -0.55, 0)$ and with radius 0.35, and two large ellipsoid inclusions with value 0.5. One ellipsoid is centred at $(-0.55\sin(\frac{5}{12}\pi), 0.55\cos(\frac{5}{12}\pi), 0)$ and with semi-axes of length $(0.6, 0.3, 0.3)$. The other ellipsoid is centred at $(0.45\sin(\frac{5}{12}\pi), 0.45\cos(\frac{5}{12}\pi), 0)$ and with semi-axes of length $(0.7, 0.35, 0.35)$. The two ellipsoids are rotated respectively $\frac{5}{12}\pi$ and $-\frac{5}{12}\pi$ about the axis parallel to the Z-axis and through the centre of the ellipsoids; see Figure 1.

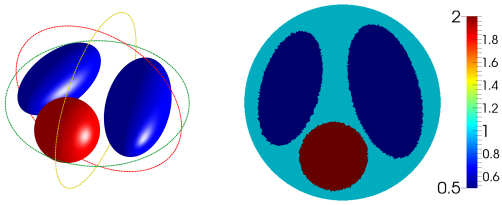

FIGURE 1. **Left:** 3D illustration of the numerical phantom. **Right**: 2D slice ($z = 0$) of the numerical phantom.

In this paper we do not consider choice rules for α; it is chosen manually by trial and error. The parameters are chosen as $\sigma_0 \equiv 1$, $M = 5$, $\tau = 10^{-5}$, $s_{\min} = 1$, $s_{\max} = 1000$, and the stopping criteria is when the step size is reduced below $s_{\text{stop}} = 10^{-3}$. Let Y_n^m denote

Laplace's spherical harmonics of degree n and order m, with real form

$$\tilde{Y}_n^m = \begin{cases} \frac{i}{\sqrt{2}}(Y_n^m - (-1)^m Y_n^{-m}) & \text{for } m < 0, \\ Y_n^0 & \text{for } m = 0, \\ \frac{1}{\sqrt{2}}(Y_n^{-m} + (-1)^m Y_n^m) & \text{for } m > 0. \end{cases} \tag{22}$$

The Neumann data consists of $\tilde{Y}_n^m$ for $-n \leq m \leq n$ and $n = 1, 2, \ldots, 5$, i.e. a total of $K = 35$ current patterns. For the partial data examples a half-sphere is used for local data $\Gamma = \Gamma^{\mathrm{N}} = \Gamma^{\mathrm{D}}$, and the corresponding Neumann data are scaled to have the same number of periods as the full data examples.

When applying prior information, the coefficients μ_j are chosen as 10^{-2} where the support of $\delta\sigma$ is assumed, and 1 elsewhere. The assumed support is a 10% dilation of the true support, to show that this inaccuracy in the prior information still leads to improved reconstructions.

For the simulated Dirichlet data, the forward problem is solved on a very fine mesh, and afterwards interpolated onto a different much coarser mesh in order to avoid inverse crimes. White Gaussian noise has been added to the Dirichlet data $\{f_k\}_{k=1}^K$ on the discrete nodes on the boundary of the mesh. The standard deviation of the noise is chosen as $\epsilon \max_k \max_{x_j \in \Gamma^{\mathrm{D}}} |f_k(x_j)|$ as in [8], where $\epsilon = 10^{-2}$ corresponding to 1% noise.

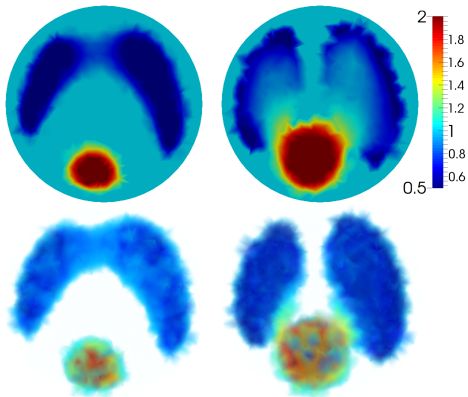

FIGURE 2. **Top:** 2D slices ($z = 0$) through centre of ball domain. **Bottom:** 3D volume plot where the background value of 1 is made transparent. **Left:** reconstruction with full data and no spatial prior information. **Right:** reconstruction with full data and overestimated support as additional prior information.

Figure 2 shows 2D slices of reconstructions from full boundary data. It is seen that the reconstructions attain the correct contrast, and close to the boundary gives good approximations to the correct support for the inclusions. Using the overestimated support as prior information gives vastly improved reconstruction further away from the boundary. This holds for the entire 3D reconstruction as seen in the bottom part of Figure 2, and makes it possible to get a reasonable separation of the inclusions.

From Figure 3 2D slices of partial data reconstructions are shown, and it is evident that far from the measured boundary the reconstructions suffer severely. Reconstructing with data on the lower part of the sphere gives a reasonable reconstruction with correct contrast for the ball inclusion, however the larger inclusions are hardly reconstructed at all.

With data on the top half of the sphere yields a reconstruction with no clear separation of the ellipsoid inclusions, which is much improved by use of the overestimated support.

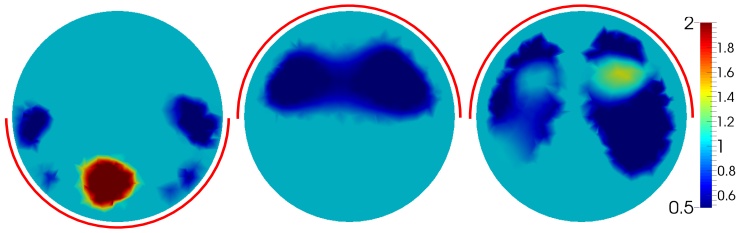

FIGURE 3. 2D slices ($z = 0$) through centre of ball domain **Left:** reconstruction with data on lower half-sphere and no spatial prior information. **Middle:** reconstruction with data on upper half-sphere and no spatial prior information. **Right:** reconstruction with data on upper half-sphere and overestimated support as additional prior information.

There is however an artefact in one of the reconstructed inclusions that could correspond to data from the ball inclusion, which is not detected in the reconstruction even when the additional prior information is used.

The reconstructions shown here are consistent with what was observed in [8] for the 2D problem, and it is possible to reconstruct the correct contrast even in the partial data case, and also get decent local reconstruction close to the measured boundary. However, the partial data reconstructions seems to be slightly worse in 3D when no prior information about the support is applied.

REFERENCES

[1] R. A. Adams and J. J. F. Fournier, *Sobolev Spaces*, 2^{nd} edition, Pure and Applied Mathematics, Amsterdam, 2003.

[2] G. Alessandrini, Stable determination of conductivity by boundary measurements, *Appl. Anal.*, **27** (1988), 153–172.

[3] T. Bonesky, K. Bredies, D. A. Lorenz and P. Maass, A generalized conditional gradient method for nonlinear operator equations with sparsity constraints, *Inverse Problems*, **23** (2007), 2041–2058.

[4] K. Bredies, D. A. Lorenz and P. Maass, A generalized conditional gradient method and its connection to an iterative shrinkage method, *Comput. Optim. Appl.*, **42** (2009), 173–193.

[5] A. L. Bukhgeim and G. Uhlmann, Recovering a potential from partial Cauchy data, *Comm. Partial Differential Equations*, **27** (2002), 653–668.

[6] A.-P. Calderón, On an inverse boundary value problem, in Seminar on Numerical Analysis and its Applications to Continuum Physics, *Soc. Brasil. Mat.*, (1980), 65–73.

[7] I. Daubechies, M. Defrise and C. De Mol, An iterative thresholding algorithm for linear inverse problems with a sparsity constraint, *Comm. Pure Appl. Math.*, **57** (2004), 1413–1457.

[8] H. Garde and K. Knudsen, Sparsity prior for electrical impedance tomography with partial data, *Inverse Probl. Sci. Eng.*, (2015), DOI: 10.1080/17415977.2015.1047365.

[9] M. Gehre, T. Kluth, A. Lipponen, B. Jin, A. Seppänen, J. P. Kaipio and P. Maass, Sparsity reconstruction in electrical impedance tomography: an experimental evaluation, *J. Comput. Appl. Math.*, **236** (2012), 2126–2136.

[10] B. von Harrach and J. K. Seo, Exact shape-reconstruction by one-step linearization in electrical impedance tomography, *SIAM J. Math. Anal.*, **42** (2010), 1505–1518.

[11] B. von Harrach and M. Ullrich, Monotonicity-based shape reconstruction in electrical impedance tomography, *SIAM J. Math. Anal.*, **45** (2013), 3382–3403.

[12] H. Heck and J.-N. Wang, Stability estimates for the inverse boundary value problem by partial Cauchy data, *Inverse Problems*, **22** (2006), 1787–1796.

[13] V. Isakov, On uniqueness in the inverse conductivity problem with local data, *Inverse Probl. Imaging*, **1** (2007), 95–105.

[14] B. Jin, T. Khan and P. Maass, A reconstruction algorithm for electrical impedance tomography based on sparsity regularization, *Internat. J. Numer. Methods Engrg.*, **89** (2012), 337–353.

[15] B. Jin and P. Maass, An analysis of electrical impedance tomography with applications to Tikhonov regularization, *ESAIM: Control, Optimisation and Calculus of Variations*, **18** (2012), 1027–1048.

[16] C. E. Kenig, J. Sjöstrand and G. Uhlmann, The Calderón problem with partial data, *Ann. of Math. (2)*, **165** (2007), 567–591.
[17] A. Kirsch and N. Grinberg, *The Factorization Method for Inverse Problems*, Oxford University Press, Oxford, 2008.
[18] K. Knudsen, The Calderón problem with partial data for less smooth conductivities, *Comm. Partial Differential Equations*, **31** (2006), 57–71.
[19] A. Logg, K.-A. Mardal and G. N. Wells, *Automated Solution of Differential Equations by the Finite Element Method*, Springer, Heidelberg, 2012.
[20] G. Stampacchia, Le problème de Dirichlet pour les équations elliptiques du second ordre à coefficients discontinus, *Ann. Inst. Fourier (Grenoble)*, **15** (1965), 189–257.
[21] S. J. Wright, R. D. Nowak and M. A. T. Figueiredo, Sparse reconstruction by separable approximation, *IEEE Trans. Signal Process.*, **57** (2009), 2479–2493.

Received September 2014; revised August 2015.

E-mail address: hgar@dtu.dk
E-mail address: kiknu@dtu.dk